6-23-2015

A Computationally Efficient Moment-Preserving Monte Carlo Electron Transport Method with Implementation in Geant4

David Dixon

David Andrew Dixon

Candidate

Nuclear Engineering

Department

This dissertation is approved, and it is acceptable in quality and form for publication:

Approved by the Dissertation Committee:

Prof. Anil Prinja, Chair

Dr. Forrest Brown

Dr. Brian Franke

Dr. Chadwick Lindstrom

Prof. Sean Luan

Prof. Cassiano De Oliviera

A Computationally Efficient Moment-Preserving Monte Carlo Electron Transport Method with Implementation in Geant4

by

David A. Dixon

B.S., Nuclear Engineering, University of New Mexico, 2010

DISSERTATION

Submitted in Partial Fulfillment of the
Requirements for the Degree of

Doctor of Philosophy
Engineering

The University of New Mexico

Albuquerque, New Mexico

May, 2015

Dedication

To my incredible wife, Jessie, and our two wonderful daughters, Maren and Charlie, a true source of inspiration.

Acknowledgments

Foremost, I would like to thank my advisor, Prof. Anil Prinja, for sharing his ideas with me, in particular, the Moment-Preserving method. I am truely grateful to have had such a great mentor and I am hopeful that this is just the beginning of many exciting and productive collaborations. As a researcher, I can only hope to achieve half as much as you have during your career and you will always remain as the standard of excellence that I use to guide myself throughout my career in science.

I would also like to thank my committee members for their participation in this pivotal stage of my life. In particular, I would like to thank Dr. Brian Franke for all of his thoughtful input throughout my experience working on the Moment-Preserving method. I should also thank both committee members Dr. Brian Franke and and Dr. Forrest Brown for their support while determining the next step in my career. They have both been instrumental in helping promote my work and myself at both SNL and LANL, and also provided me with some much needed perspective on careers in the national labs. Finally, I would like to thank the remaining committee members Prof. Sean Luan, Dr. Chadwick Lindstrom, and Prof. Cassiano De Oliveira for their valuable input and their patience throughout the entire process.

In addition to my advisor and committee members, I would like to give a special thanks to friend and mentor Dr. Stan Woolf for setting everything in motion. I was really spoiled as a graduate student to get the opportunity to learn from you and it is such a great privilege to have you as a friend.

Lastly, I want to thank my family for your enduring support. None of this would have been possible without you and I will forever remain indebted to you all.

A Computationally Efficient Moment-Preserving Monte Carlo Electron Transport Method with Implementation in Geant4

by

David A. Dixon

B.S., Nuclear Engineering, University of New Mexico, 2010

Ph.D., Engineering, University of New Mexico, 2015

Abstract

The subject of this dissertation is a moment-preserving Monte Carlo electron transport method that is more efficient than analog or detailed Monte Carlo simulations, yet provides accuracy that is statistically indistinguishable from the detailed simulation. Moreover, the Moment-Preserving (MP) method is formulated such that it is distinctly different than Condensed History (CH) methods making the MP method free of the limitations inherent to CH and proving a viable alternative for transporting electrons. Analog, or detailed, Monte Carlo simulations of charged particle transport is computationally intensive; thus, it is impractical for routine calculations. The computational cost of analog Monte Carlo is directly attributed to the underlying charged particle physics characterized by extremely short mean free paths (mfp) and highly peaked differential cross sections (DCS). As a result, a variety of efficient, although approximate solution methods were developed over the past 60 years. The most prolific method is referred to as the Condensed History method. However, CH is widely known to suffer from inconsistencies between the underlying

theory and the application of the method to real, physical problems. Therefore, it is of interest to develop an alternative method that is both efficient and accurate, but also a completely different approach to solving the charged particle transport equation that is free of the limitations inherent to CH. This approach arose from the development of a variety of reduced order physics (ROP) methods that utilize approximate representations of the collision operators. The purpose of this dissertation is the theoretical development and numerical demonstration of an alternative to CH referred to as the Moment-Preserving method. The MP method poses a transport equation with reduced order physics models characterized by less-peaked DCS with longer mfps. Utilizing pre-existing single-scatter algorithms for transporting particles, a solution to the aforementioned transport equation is obtained efficiently with analog level accuracy. The process of constructing ROP models and their properties are presented in detail. A wide variety of theoretical and applied charged particle transport problems are studied including: calculation of angular distributions and energy spectra, longitudinal and lateral distributions, energy deposition in one and two dimensions, a validation of the method for energy deposition and charge deposition calculations, and response function calculations for full three-dimensional detailed detector geometries. It is shown that the accuracy of the MP method is systematically controllable through refinement of the ROP models. In many cases, efficiency gains of two to three orders of magnitude over analog Monte Carlo are demonstrated, while maintaining analog level accuracy. That is, solutions generated sufficient ROP DCS models are statistically indistinguishable from the analog solution. To maintain analog level accuracy under strict problem conditions, small efficiency gains are realized. However, loss of efficiency under these conditions is true of all approximate methods, but the MP method remains accurate where other methods may fail. That is not to say the MP method does not suffer from limitations because the MP method will result in discrete artifacts when the problems conditions are strict. However, where limitations of the method arise, they are overcome

through systematic refinement of the ROP DCS models required by the method. In addition to accuracy and efficiency results, it is shown that the MP method does not require a boundary crossing or pathlength correction algorithm, which is in great contrast to the CH method. Finally, implementation and maintenance of the MP method was found to be straightforward and requires significantly less effort than CH when measured by the number of lines of code required for each method. In particular, as compared with the class II CH method utilized in the Geant4 standard electromagnetic physics list. Ultimately, the MP is shown to be accurate, efficient, versatile, and simple to implement and maintain.

Contents

List of Figures

List of Figures

List of Tables

Chapter 1

Introduction

The need for computational charged particle transport developed from early work in charged particle transport theory, which emerged as a flourishing subbranch of mathematical physics when fast charged particles became available to the experimentalist [2]. As computer technology improved, the problems of interest to charged particle computational physicist expanded to areas including:

- Accelerator Physics,
- Medical Physics,
- Health Physics,
- Space Physics,
- Electro-magnetic pulses.

The advantage of computational charged particle transport over analytical transport is the possibility of simulating complicated geometries and sophisticated boundary conditions or source configurations, which are all characteristics of real world applications. In other words, it is possible to simulate real, physical phenomena using

charged particle transport codes. An example of such a code is the Geant4 toolkit [3] which is used frequently on problems including: design of full-scale experiments such as the Large Hadron Collider [4, 5], design of radiation therapy machines [6] as well as treatment planning systems [7], estimation of detector geometric factors [8], shielding calculations [9], and EMP calculations [10]. It is undisputed that particle transport codes play an important role in the research and development of charged particle applications and reasonable to suggest that particle transport codes will continue to play an important role into future. Therefore, algorithmic improvements to particle transport codes are critical to improving the field of computational charged particle transport.

To make clear the impact of this work and the importance of the remaining chapters, it is necessary to provide, at least, a cursory discussion on what is meant by charged particle transport codes and the associated challenges. First, the purpose of charged particle transport codes is to obtain solutions to the Boltzmann transport equation [11] using stochastic methods like Monte Carlo [12] or deterministic methods like S_N [13]. The Boltzmann transport equation is a balance equation for particles in a six-dimensional phase-space including space, angle, and energy. The solution to this equation describes the particle population and is referred to as the angular flux. For a given analog DCS model, the corresponding transport equation is referred to as the analog model and the angular flux is assumed to be exact. Analog, (detailed, step by step), simulation is feasible under strict circumstances (relatively low energies, thin targets,...), but for high-energy electrons (above a few hundred keV), the number of interactions suffered by an electron along its trajectory is too large for detailed simulations [14]. For this reason, numerous computationally efficient approximate methods have emerged over the past 60 years. The most notable and prolific approximate method is Condensed History (CH). Berger describes CH as an (artificially constructed) random walk, each step of which takes into account the combined effects of many collisions [2]. The distances between collisions or the

steps are significantly longer than those associated with the analog problem, making CH efficient. However, the theoretical basis and practical implementation of the CH algorithm introduces inherent and irreducible limitations that are unique to the method [15].

It is of interest to develop a method free of such limitations. That is, an efficient moment-preserving method for Monte Carlo electron transport, which is the subject of this dissertation. The central question addressed herein is whether the efficiency and accuracy associated with the Moment-Preserving (MP) method are sufficient to recommend this method as an alternative to the CH method. This is addressed in two ways. First, theoretical development of the method is discussed in great detail to emphasize how elements of accuracy and efficiency are inherent to the method. The theoretical development is followed up with an extensive numerical demonstration of the method including calculations of angular distributions, energy spectra, lateral and longitudinal distributions, one-dimension and two-dimension dose deposition, one-dimension charge deposition, and a multi-dimensional space physics application. In addition, specific results are presented that demonstrate how the moment-preserving method is free from the limitations inherent to CH. State-of-the-art tabulated elastic DCSs generated using the ELSEPA code system were used to demonstrate the versatility of the method. Finally, all of the algorithmic development was completed within the Geant4 toolkit [3] to demonstrate the simplicity of the method from a code implementation and maintenance standpoint. Through demonstration of the accuracy, efficiency, versatility, and simplicity of the method, the question central to this dissertation is addressed.

The remainder of the dissertation provides the background information necessary to understand the results, a discussion of the Geant4 toolkit and implementation details specific to the MP method, results, conclusions, and future work. The remaining chapters are organized as follows:

- Chapter 2: Literature Review
- Chapter 3: Electron Interaction Physics
- Chapter 4: The Analog Problem
- Chapter 5: Differential Cross-Section Moments
- Chapter 6: The Condensed History Method
- Chapter 7: The Moment-Preserving Method)
- Chapter 8: The Geant4 Toolkit
- Chapter 9: Results
- Chapter 10: Conclusions and Future Work

Chapter 2

Literature Review

This chapter provides a qualitative discussion of the literature relevant to the analog problem and the associated analog differential cross-sections (DCS) (detailed in chapter 3 and chapter 4), the Condensed History (CH) method (detailed in chapter 6), and the Moment-Preserving (MP) method (detailed in chapter 7). The analog problem is the point of departure for both CH and ROP models, so we begin with a discussion of the analog problem.

2.1 The Analog Problem

The analog description of transport can be mathematically expressed in terms of the linear Boltzmann or transport equation for the angular flux, where the interaction physics are represented through total cross sections (inverse mfp) and the DCSs for angular deflection and energy loss [15]. The total cross sections and DCSs appear in the elastic and inelastic collision operators, which are integral operators or Boltzmann-type operators. Though electrons can undergo several different elec-

tromagnetic interactions[1], the dominant interactions are elastic collisions with nuclei and inelastic collisions with atomic electrons. Typical DCSs for elastic nuclear scattering include relativistic screened Rutherford, Wentzel, or the partial-wave expansion [16, 17, 18], while typical DCSs for inelastic electronic scattering include Rutherford, Möller, or the Evaluated Electron Data Library [19, 20]. These DCSs are highly peaked about small changes in direction and small energy losses and the associated total cross sections are very large resulting in extremely short mfps. Interaction physics of this nature present a difficult computational task.

Boundary conditions for the transport equation depend on the application, but typically include vacuum, pencil beams, or sources distributed in space, energy, and angle. However, mono-energetic pencil beams are very common in electron transport and further complicate the computational challenges because pencil beams are singular in space, energy, and angle.

The problem of computational inefficiencies associated with the analog physics was recognized immediately by early charged particle computational physicists. In fact, Berger [2] acknowledged that a direct analog Monte Carlo procedure would be quite costly, because of the enormous number of collisions that must be sampled. For example, it takes on the order of tens of thousands of collisions for an electron with energy of roughly 1-MeV to slow down to 1-keV, while only 20 to 30 Compton scatterings will reduce the energy of a photon from several MeV down to 1-keV or 18 elastic collisions in hydrogen will reduce a neutron from 2-MeV to thermal energies [2]. In 1963, only one calculation by direct analog Monte Carlo was reported [21]. Since then, several analog Monte Carlo electron transport codes have been developed [14, 22] and a few production codes have included analog physics options [23, 24, 25]. Solutions to the analog problem are exact for a given DCS; therefore,

[1]Bremsstrahlung is an important interaction for relativistic electrons. However, bremsstrahlung does is not a computationally intensive process, so it is neglected in this work. It should be noted that use of preexisting bremsstrahlung physics with the moment-preserving method will not impact the efficacy of the method.

it is understandable that analog physics options were implemented, despite the fact that analog Monte Carlo is computationally inefficient. Moreover, it is feasible to use analog Monte Carlo for occasional calculations if significant computing resources are available. However, analog Monte Carlo remains impractical for routine calculations with exception of very restrictive problems like transport through optically thin materials. For this reason, approximate methods remain a critical component of most Monte Carlo electron transport codes.

2.2 Condensed History

Condensed history has been the prevailing approximate method in computational charged particle transport since the emergence of the field. The usual practice is to use "condensed" (class I) simulation methods, in which the global effect of multiple interactions is described by means of approximate multiple scattering theories. Alternatively, one can use "mixed" (class II) schemes in which hard (catastrophic) interactions, with energy loss or angular deflection above given thresholds, are simulated individually. For a given set of DCSs, class II schemes are intrinsically more accurate than class I simulations [14]. Some examples of codes containing class I schemes are ETRAN, ITS, MCNP, while examples of production codes containing class II CH schemes are EGS4, PENELOPE, Geant4 [26, 27, 3]. Both class I and class II schemes utilize various results from multiple scattering theory, which is a subbranch of mathematical physics developed around the solution of the transport equation with limited applicability resulting from severe restrictions required to obtain analytical solutions [28, 29, 30, 31]. The analytical solutions or multiple scattering distributions describe the angular or energy distributions of electrons after traveling some distance s or a step, that are on the order of hundreds of analog mfps.

The major distinction between class I and class II schemes is how the grouping of

collisions is handled. That is, class I schemes utilize precomputed multiple-scattering (MS) distributions [32, 33, 34, 35] determined for fixed step-sizes on a fixed energy grid. For this reason, energy straggling is sampled from a MS distribution [34, 35] and secondaries are accounted for on an average basis. Therefore, it is not possible to distinguish between inelastic collisions resulting in secondary production (hard) and those that do not (soft). In contrast, a class II scheme like EGS allows all physical processes and boundaries to affect the choice of step size [36]. Thus, distance to hard collision is exponentially distributed and secondary production is treated exactly by sampling energy-loss from the inelastic DCS above the secondary production threshold.

Regardless of the choice in the scheme, substantial efficiency gains over analog Monte Carlo can be realized with CH. However, the accuracy of early forms of CH was strongly dependent on step-size and while it was found that reducing the electron step-size causes the results to converge to the correct values, the computing time increases rapidly in proportion to the inverse of the step-size [37, 38, 39]. Therefore, special algorithms like PRESTA [40] were developed to select the optimal step-size during the process of a Monte Carlo simulation. Without an algorithm like PRESTA, one must resort to a tedious study to determine the optimal step-size such that acceptable accuracy and efficiency is achieved. However, this optimization may not be universal. The various production codes currently available differ in this optimization issue. Some codes, like ITS, have pre-determined step-size parameters, while codes like EGS utilize the PRESTA algorithm [40] or random hinging combined with lateral corrections found in PENELOPE. In addition to step-size limitations, condensed history suffers from inconsistent handling of the material and free surface boundaries. Material interfaces are a fundamental challenge for condensed history because the MS distributions are infinite medium solutions and are not valid for heterogenous regions. Therefore, if a material interface is encountered, a special algorithm like the Jordan-Mack algorithm [41] or PRESTA is required. Another issue specific to class

I schemes that utilize the Goudsmit-Saunderson distribution [32, 33] for sampling angular deflection is that the numerical methods required to generate the Goudsmit-Saunderson distribution are sensitive to small step-sizes. The backwards recurrence used to generate the Goudsmit-Saunderson is unstable for small steps. Even if the step-size is sufficiently long that the backwards recurrence is stable, it is possible that more than the pre-scripted number of recurrence coefficients are required to accurately resolve the Goudsmit-Saunderson distribution [42].

There are many forms of MS theory that are fundamental to CH, but one of particular importance to all approximate methods is referred to as Lewis theory [43]. A concise description of Lewis theory is given by Prinja [44]:

> Consider an infinite medium in which charged particles undergo scattering collisions resulting in angular deflection but no energy losses. Let the differential scattering cross section be given by $\Sigma_s^{(A)}(\vec{\Omega}' \cdot \vec{\Omega})$ with $\vec{\Omega}'$ and $\vec{\Omega}$ being pre- and post-collision unit direction vectors and where the label A denotes a specific configuration of this problem. The Legendre moments of this cross-section are defined by $\Sigma_{s,n}^{(A)} = \int_{4\pi} \Sigma_s^{(A)}(\vec{\Omega} \cdot \vec{\Omega}') P_n(\vec{\Omega} \cdot \vec{\Omega}') d^2\Omega$, where $P_n(\mu)$, $-1 \leq \mu \leq 1$, are the Legendre polynomials. The cross-section or its associated moments and the charged particle source completely characterize this problem. Consider now, a second configuration, labeled B, that is characterized by the same source but a different differential scattering cross-section $\Sigma_s^{(B)}(\vec{\Omega}' \cdot \vec{\Omega})$ and hence different moments $\Sigma_{s,n}^{(B)}$. In general, the particle angular distributions or angular fluxes for the two problems, $\psi_{A,B}(\vec{r}, \vec{\Omega})$, will be different. However, if the cross-sections are related such that $\Sigma_{s,n}^{(A)} = \Sigma_{s,n}^{(B)},\ n = 1, 2, ...N$, for some fixed order N and $\Sigma_{s,n}^{(A)} \neq \Sigma_{s,n}^{(B)},\ n \geq N+1$,then a classic result due to Lewis [43] states that space-angle moments of the two angular fluxes defined by $M_{j,k,l}^{m_x,m_y,m_z} = \int_V \int_{|\vec{\Omega}|=1} x^j y^k z^l \Omega_x^{m_x} \Omega_y^{m_y} \Omega_z^{m_z} \psi_{A,B}(\vec{r}, \vec{\Omega}) d^2\Omega dV$ and com-

monly referred to as Lewis-moments, are identical through any order satisfying $j + k + l + m_x + m_y + m_z = N$, where $(\Omega_x, \Omega_y, \Omega_z)$ are the direction cosines with respect to the Cartesian axes (x, y, z).

The significance of this observation is that if $\Sigma_s^{(A)}(\vec{\Omega}' \cdot \vec{\Omega})$ is the true or exact differential cross-section for scattering of the charged particle by the target nucleus, also referred to as the analog differential cross-section, and $\Sigma_s^{(B)}(\vec{\Omega}' \cdot \vec{\Omega})$ is an approximation to it, Lewis' result points to a sharp link between accuracy of the approximate model, as measure by linear functionals (moments) of the angular flux, and number of Legendre moments of the differential cross-section that are exactly reproduced in the approximate model.

2.3 Reduced Order Physics Models

For the reasons stated above, various alternatives to the CH method were developed. Of particular interest are alternatives referred to as Reduced Order Physics (ROP) models, which are a family of transport-based approximations. ROP models include various approximate representations of the analog collision operators that are of both integral and differential forms. ROP models are obtained through some type of regularization procedure that removes reduce the nearly-singular behavior of the analog DCS, while systematically capturing the key physics through preservation of angular and energy-loss moments of the analog DCSs. Moreover, the zeroth or the total cross section is not preserved, rather it is determined self-consistently by the method. The resulting ROP model is then characterized by less peaked scattering with mfps longer than the analog mfp. Efficiency is achieved by not preserving the total cross section, while accuracy is achieved by preserving the necessary number of moments beyond the zeroth. There are numerous approximations that qualify as ROP models

including Fokker-Planck, Boltzmann Fokker-Planck, Generalized Fokker-Planck, and Generalized Boltzmann Fokker-Planck. The remainder of this chapter is devoted to introducing each of these approximations and indicating how these methods contributed to the development of the MP method.

The classical Fokker-Planck operator is obtained by Taylor expanding the scattering kernels. This is a reasonable approach, assuming the angular flux is sufficiently smooth, because the DCSs fall off rapidly away from small deflection cosines and energy-losses. The resulting operator is differential in angle and energy and models elastic and inelastic scattering as diffusive processes. As a result, the Fokker-Planck operator does not capture large-angle scatter and can lead to energy gains. Pomraning confirmed these inconsistencies by showing that the Fokker-Planck operator is an asymptotic limit of the Boltzmann collision operator and only valid for unrealistically peaked scattering [45]. That is, the FP approximation is strictly valid in the limit that the total scattering cross section goes to infinity and the mean deflection cosine goes to unity such that the transport cross section remains bounded [46]. Under these conditions, large angle scattering is negligible and the FP operator is equivalent to the Boltzmann integral collision operator. Clearly, there is a limitation on the type of physics for which the classical FP operator is valid. Regardless, various implementations of Fokker-Planck operator were studied for in deterministic settings[47, 48, 49, 50].

In efforts to incorporate large-angle scattering, a kernel decomposition approach was introduced by Ligou and is referred to as the Boltzmann-Fokker-Planck (BFP) equation [51, 52, 53]. Ligou recognized that it is easier to numerically treat forward-peaked elastic scattering and small energy losses associated with such scattering using Fokker-Planck (FP) differential operators [49] rather than Boltzmann integral operators. However, the FP operator does not accurately capture large angle scattering. Therefore, it is necessary to decompose the scattering cross section into its

singular and smooth components and apply the FP approximation to the singular component while leaving the smooth operator intact [54]. One important feature of the decomposition process is that there is no rigorous definition of the components so there are infinite decompositions. The key, as indicated by Landesman and Morel [54], is to select a decomposition that is not only accurate and efficient, but also easily integrated into existing transport codes. The early methods for solving the BFP equation were deterministic, but Morel and Sloan [55, 56] developed a hybrid multigroup/continuous-energy Monte Carlo method for solving the BFP equation or the MGBFP method. Morel described the MGBFP method as a new form of condensed history with the major distinction being that path lengths between collision sites are exponentially distributed.

In retrospect, application of kernel decomposition serves to stabilize the divergent behavior of the Fokker-Planck expansion [57] by effectively renormalizing the expansion coefficients. This renormalization process is central to the Generalized Fokker-Planck (GFP) method [58, 59] and resulted after attempting to generalize the FP operator to a broad class of physics with higher order FP operators [57]. In principle, the FP approximation can be improved by retaining higher order terms in the Taylor expansion of the collision operators. Thus, leading to a more accurate description of large angle scattering, but this is only true for specific kernels. For example, it is known that there are no valid FP operators for the Henyey-Greenstein kernel [45] and that the standard FP operator is only marginally valid for screened Rutherford or screened Mott [46]. However, Pomraning [57] completed the same kernel analysis for the exponential and delta function and showed that higher order FP operators are valid for kernels such as these, but they are unphysical. In addition to characterizing the stability of higher order FP operators with respect to specific scattering kernels, this analysis revealed the explicit role of the analog DCS moments to developing approximations. That is, higher order FP expansions suggest that the accuracy of the approximation is improved by incorporating higher order moments.

GFP approaches provide a means to stabilize higher-order FP operators through renormalization of the various terms that appear in the operator. The renormalization process, in essence, allows for an arbitrary ordered FP operator; hence, the approach referred to as generalized FP. Lastly, work on GFP showed that the key to a stable ROP model is preserving the integral form of the collision operator and retaining an arbitrary number of low order moments while approximating all of the higher order moments.

Insight gained from the foregoing approximations - FP, BFP, and GFP - combined with Lewis theory and practical experience from implementing and testing CH led to the development of the Generalized Boltzmann Fokker-Planck (GBFP) method [60]. Like the other ROP models, the GBFP method is a transport-based approximation. However, the GBFP method is more appropriate for Monte Carlo calculations like CH. The emphasis of GBFP method is the development of stable, moment-preserving representations of the collision operators. This is achieved by constructing ROP DCSs that are moment-preserving, per Lewis theory, while leaving the collision operators intact by simply replacing the analog DCSs with the ROP DCSs. Another key feature of the GBFP approach is that angular deflection and energy-loss interactions depend only on Legendre moments and energy-loss moments, not the detailed form of the analog DCSs. Therefore, the GBFP method is applicable to both continuous DCSs [61] and tabulated DCS data [62] and code modifications are not required for physics refinements because this is accomplished by providing moments of the desirable analog model through input data. The bulk of the work on the GBFP method to date emphasizes the most simple, but also the most effective ROP DCSs referred to as the discrete and hybrid models. The discrete model [63] is a superposition of discrete points and weights over the full range of the DCS, while the hybrid model [64] is a superposition of discrete points and weights over the peaked portion of the DCS and the tail is represented exactly by the analog DCS. Recently, the name Moment-Preserving method was adopted in place of the GBFP

method to distinguish the method from Fokker-Planck and to emphasize the concept most fundamental to the method - moment preservation.

Chapter 3

Electron Interaction Physics

In this chapter, interactions of electrons are detailed. Differential cross-sections (DCS) appropriate for moderate to high energies above roughly 10-keV are considered. At these energies, electrons are treated as point particles where they are assumed free streaming between collisions. The medium is assumed amorphous and for a single element with atomic number Z and density ρ the material properties are given by the number density $\mathcal{N}$. The extension to compounds, and mixtures, is normally done on the basis of the additivity approximation, i.e., the molecular DCS is approximated as an incoherent sum of the atomic DCSs of all of the atoms in a molecule [27]. Electron interactions include elastic scattering with atomic nuclei, inelastic scattering with atomic electrons, bremsstrahlung emission, and elastic collisions with atomic electrons. However, the subject of this work is the treatment of Coulomb collisions that contribute significantly to the computational inefficiencies associated with analog transport (specifically, elastic and inelastic collisions as in Fig. 3.1). The analog elastic and inelastic DCSs utilized in this work include analytical functions and tabulated DCS data and are described in the following sections. Moments of analog DCSs are central to the moment-preserving method, so the last section defines the elastic and inelastic DCS moments and discusses the physical

meaning of the moments where it is possible to do so.

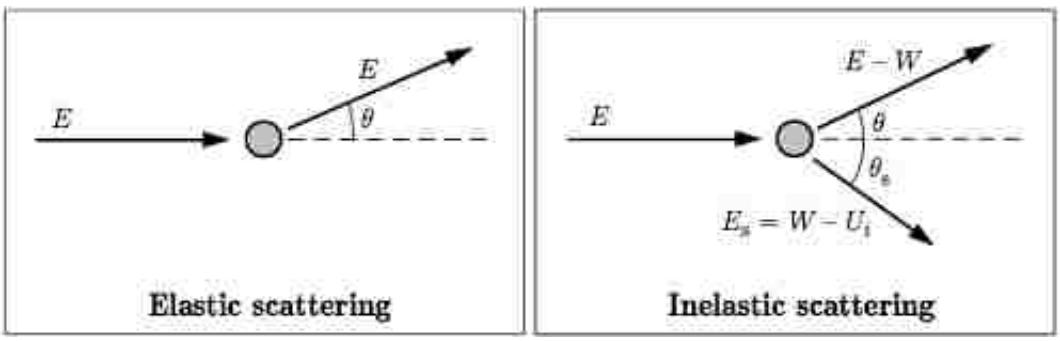

Figure 3.1: Electron interaction diagrams for elastic and inelastic scattering [27].

3.1 Nomenclature

In this dissertation, the term electron (e^-) is used to designate incident electrons, while targets are referred to as atomic nuclei and atomic electrons. The microscopic elastic and inelastic DCSs are designated by σ_{el} or σ_{in} with units of cm^2sr^{-1} and cm^2MeV^{-1} respectively, while the macroscopic elastic and inelastic DCSs are designated as Σ_{el} or Σ_{in} with units of $cm^{-1}sr^{-1}$ and $cm^{-1}MeV^{-1}$ respectively. The number density of a single element, $\mathcal{N}$, has units of atoms per cm^3 and is given by $\mathcal{N} = \rho N_A/A$ where N_A is Avogadro's number and A is the atomic mass. The following is a list of fundamental constants and definitions of frequently used parameters:

Speed of Light	c	=	2.99792458×10^{8} m/s
Reduced Planck's Constant	$\hbar$	=	$6.58211928 \times 10^{-16}$ eV· s
Electron Rest Mass	$m_e c^2$	=	0.510998910 MeV
Classical Electron Radius	r_0	=	$2.8179403267 \times 10^{-13}$ cm^2
Avogadro's Number	N_A	=	6.0221413×10^{23} atoms/mole
Energy Per Rest Mass	τ	=	$E/m_e c^2$ (unitless)
Lorentz Factor	γ	=	$1 + \tau$ (unitless)
Ratio of Electron Velocity to c	β	=	$\sqrt{1 - 1/\gamma^2}$ (unitless)

3.2 Elastic Collisions with a Nucleus

The basic quantity describing the elastic scattering of electrons by a target system is the elastic DCS that can be accurately described by a static central potential $V(r)$. Given an idealized scattering experiment where a mono-directional, mono-energetic beam of electrons with a current $\vec{j}_{inc}$ of electrons passing through a surface area per unit time are scattered through some differential solid angle $d\Omega$ into a detector measuring counts per unit time $\dot{N}_{count}$, the microscopic elastic DCS is defined as

$$\sigma_{el} \equiv \frac{\dot{N}_{count}}{|\vec{j}_{inc}| d\Omega}. \tag{3.1}$$

Though the DCS can be determined experimentally, accurate theoretical expressions for the count rate and the current can be derived. A comprehensive review of such theoretical expressions is described in great detail in the ICRU Report 77 [65]. However, some attention is given to the theoretical development of the DCSs that are utilized in this dissertation.

Herein, incident electrons in the regime of kinetic energies higher than $\approx$ 10-keV are considered, where the interaction with the target atom is likely sudden, i.e., the interaction time is so small that the atomic electron cloud is not appreciably distorted by the interaction [65]. Under these conditions, the target atom is considered a

frozen distribution of electric charge (static-field approximation) and treated as a point nucleus. Elastic scattering is then assumed to be the scattering of the incident electron by the electric field of the atom. The electric field of an atom is assumed spherical and therefore it is a good approximation to assume the interaction potential $V(r)$ depends only on the distance r between the incident electron and the nucleus of the atom. Given these assumptions several forms of the elastic DCS are reviewed.

3.2.1 Non-relativistic theory

The mathematical description of the scattering experiment presented earlier is given by a differential equation for a distorted plane wave (DPW). The DPW is related to scattering amplitude, which completely determines the DCS [65]. There are various theories with fundamental equations used to derive DCSs including the non-relativistic (Schrödinger) theory, Klein-Gordon (relativistic Schrödinger) theory, and one-electron Dirac theory[1]. For example, the time-independent Schrödinger equation is given by

$$\left[-\frac{\hbar^2}{2m_e}\nabla^2 + V(r)\right]\psi_k(\vec{r}) = E\psi_k(\vec{r}),\ E = \frac{(\hbar\vec{k})^2}{2m_e} \tag{3.2}$$

where $\hbar\vec{k}$ and $\hbar\vec{k'}$ are the electron momentum before and after the collision respectively. It can be shown that the the current of incident particles is

$$\vec{j}_{inc} = (2\pi)^{-3}\frac{\hbar\vec{k}}{m_e} \tag{3.3}$$

and the current of scattered particles is

$$\vec{j}_{sc} = (2\pi)^{-3}|f(\vec{k'},\vec{k})|^2 r^{-2}\frac{\hbar\vec{k}}{m_e}\hat{r}, \tag{3.4}$$

[1]Dirac theory is the appropriate theoretical framework for deriving DCSs and includes effects from spin-polarization [65].

where the scattered current is related to the count rate by $\dot{N}_{count} = (\vec{j}_{sc} \cdot \hat{r})r^2$. Therefore, for non-relativistic (Schrödinger) theory, Eq. (3.1) becomes

$$\sigma_{el} = \frac{\dot{N}_{count}}{|\vec{j}_{inc}|d\Omega} = |f(\vec{k}', \vec{k})|^2, \tag{3.5}$$

where $f(\vec{k}', \vec{k})$ is the scattering amplitude and $\theta = \arccos(\vec{k}' \cdot \vec{k})$ is the angle through which the electron was scattered. Under these conditions, the scattering amplitude is

$$f(\vec{k}', \vec{k}) = -\frac{4\pi m_e}{\hbar^2} \int \phi^*_{k'}(\vec{r}) V(r) \psi_k(\vec{r}) d\vec{r}, \tag{3.6}$$

where the interaction potential and the DPW appear again. Eq. (3.6) indicates that the scattering amplitude, which completely determines the elastic DCS, is strongly dependent on the scattering potential. Therefore, the most accurate representation of the scattering potential possible is ideal. However, in the following sections one will find that analytical expressions for the elastic DCS requires relatively simple scattering potentials.

3.2.2 Screened Rutherford and classical Rutherford

It is impractical to obtain solutions to Eq. (3.2), so an alternative is to use the Born Approximation. In the Born approximation, the Schrödinger equation is transformed into an integral equation or

$$\psi_k(r) = \phi(r) + \int dr' G_0(E, r, r') V(r') \psi_k(r), \tag{3.7}$$

with the Green function

$$G_0(E, r, r') = -\frac{m_e}{2\pi\hbar^2} \frac{\exp(ik|r - r'|)}{|r - r'|}. \tag{3.8}$$

The Born approximation starts with the zeroth-order approximation to Eq. (3.7) or $\psi_k^{B0}(r) = \phi(r)$. This is substituted into Eq. (3.7) to get the first order approximation

or

$$\psi_k^{B1}(r) = \phi(r) + \int dr' G_0(E, r, r') V(r') \psi_k^{B0}(r). \tag{3.9}$$

This process is repeated to any order, but first and second order Born approximations are the most common because beyond second order the approximation becomes unmanageable. To obtain a familiar DCS, i.e. the screened Rutherford DCS, we begin by applying the first-order Born approximation to the time-independent Schrödinger equation. From this, the Schrödinger-Born scattering amplitude is obtained which is given by

$$f^{(SB)}(\theta) = -\frac{2m_e}{\hbar^2} \int_0^\infty \frac{sin(qr')}{qr'} V(r') r'^2 dr'. \tag{3.10}$$

We then assume the Wentzel potential for a screening radius of $R = a_0 Z^{-1/3}$ or

$$V_W(r) = \frac{Z_0 Z e^2}{r} \exp(-r/R). \tag{3.11}$$

This results in the corresponding Born scattering amplitude or

$$f_W^{(SB)}(\theta) = -\frac{2Ze^2 m_e}{\hbar^2} \frac{1}{(1/R)^2 + q^2}, \tag{3.12}$$

where

$$q = 2k\sqrt{\frac{1-\cos\theta}{2}} \tag{3.13}$$

for potential scattering. Therefore, the Wentzel or the "screened Rutherford" DCS is

$$\sigma_{el}^W(\theta) = |f_W^{(SB)}(\vec{k}', \vec{k})|^2 = \left(\frac{Ze^2}{2E}\right)^2 \frac{1}{[(2kR)^{-2} + (1-\cos\theta)]^2} \tag{3.14}$$

where $(2kR)^{-2}$ accounts for the screening of nucleus by the atomic electrons and k is the electron wave number, Z atomic number of the target and e is the electron charge. The classical Rutherford DCS is obtained by letting $R \to \infty$, which reduces the Wentzel potential to a Coulomb potential, $V_C(r) = Ze^2/r$, where the effects of nuclear screening are neglected. This gives,

$$\sigma_{el}^C(\theta) = |f_W^{(SB)}(\vec{k}', \vec{k})|^2 = \left(\frac{Ze^2}{2E}\right)^2 \frac{1}{(1-\cos\theta)^2} \tag{3.15}$$

3.2.3 Relativistic screened Rutherford

In practice, the classical Rutherford DCS is not used as it is singular about $\theta = 0$. The screened Rutherford DCS is not typically used either as it is non-relativistic. However, Eq. (3.14) is easily generalizable to the relativistic formulation. At this stage, it is convenient to define a new variable, the deflection cosine, or $\mu = \cos\theta$. The relativistic screened Rutherford (SR) DCS is given by

$$\sigma_{el}^{SR}(E,\mu) = \frac{(\tau+1)^2}{\tau^2(\tau+2)^2}\frac{C}{[1+2\eta(E)-\mu]^2}, \qquad (cm^2 sr^{-1}), \tag{3.16}$$

where the parameter C is a material constant given by

$$C = 2\pi r_0^2 Z^2 \mathcal{N}, \qquad (atoms\ cm^{-1}), \tag{3.17}$$

and the screening parameter [66] due to Molière is

$$\eta(E) = \frac{0.25Z^{2/3}}{(0.885\cdot 137)^2\tau(\tau+2)}\left[1.13 + 3.76\left(\frac{Z}{137}\right)^2\frac{(\tau+1)}{\tau(\tau+2)}\right], \tag{3.18}$$

which is an improvement over the screening term that appeared in Eq. (3.14).

The peakedness of the SR DCS is a function of both energy and the target material atomic number. Since the screening parameter drives the shape of the SR DCS, it is insightful to understand the dependence of the screening parameter on energy and atomic number which is given in Fig. 3.2. That is, as the screening parameter approaches zero, the SR DCS becomes highly forward peaked or anisotropic and nearly singular about unity. As the screening parameter grows larger, the SR DCS becomes isotropic. As seen in Fig. 3.2, the screening parameter is dependent on particle energy and the target material atomic number. Over a single decade in energy, the screening parameter varies by roughly an order of magnitude. For the same energy, over all materials, the screening parameter again varies a few orders of magnitude. The magnitude of screening parameter indicates the strength of the nuclear screening. Since the screening parameter is largest for high-Z materials and

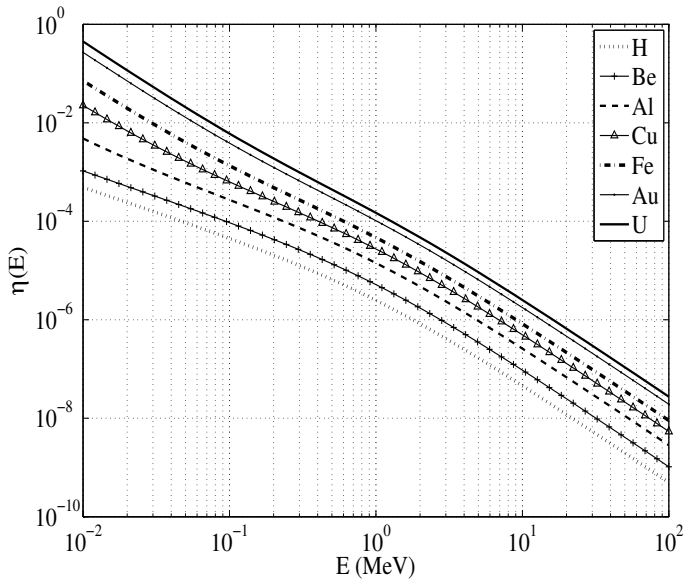

Figure 3.2: Screening parameter for various materials

lower energies, nuclear screening has the greatest impact in this regime. For higher energies and low-Z materials, the effect of nuclear screening is weak and the nucleus begins to appear bare to the incident electron.

The following figures demonstrate the impact of the screening parameter on the peakedness of the SR DCS. The SR DCS is most peaked for high-energy particles on low-Z targets as seen in Fig. 3.3a and effectively isotropic for low-energy particles on high-Z materials as seen in Fig. 3.3b. The screening parameter is a function of energy and target Z, so this implies that the peakedness of elastic scattering is generally driven by energy and target Z. This is made clear in the next section for the partial-wave (PW) DCS, which does not depend on a screening parameter but still demonstrates this same behavior.

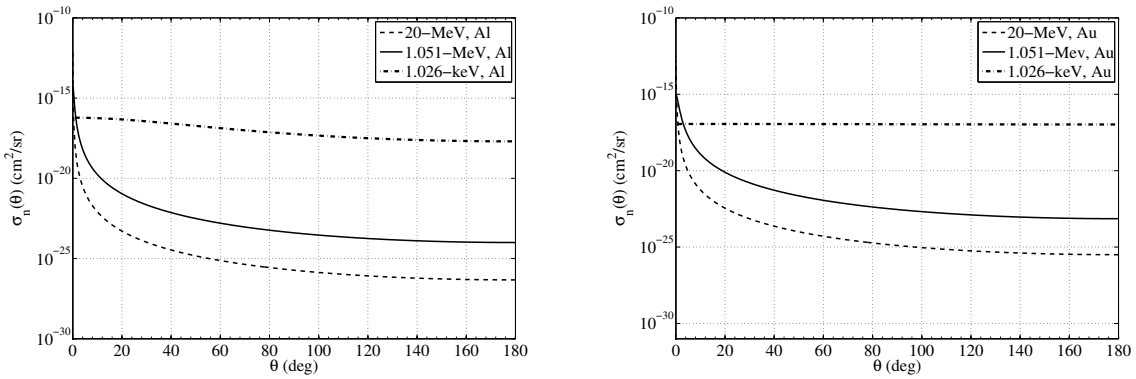

(a) Aluminum (b) Gold

Figure 3.3: Screened Rutherford (SR) DCS for elastic scattering of 1.026-keV, 1.051-MeV, and 20-MeV electrons by aluminum and gold nuclei.

3.2.4 Partial-wave DCS

In contrast to the time-independent Schrödinger equation, the Dirac equation is for relativistic waves. It describes all spin-1/2 particles and is consistent with both the principles of quantum mechanics and special relativity. For this reason, DCSs derived from the Dirac equation are intrinsically better representations of elastic scattering. Furthermore, the accuracy of the static-field approximation - used in previous sections to develop the screened Rutherford DCS - is limited by inelastic absorption and charge-polarization effects [18]. Inelastic absorption causes a reduction of the elastic DCS at intermediate and large angles that can be described by means of an approximate absorptive potential. Furthermore, as a result of charge-polarization effects, the charge distribution of the target is polarized by the electric field of the electron [18]. In turn, the electric field of the induced dipole acts back on the electron. This can be described approximately by means of a local correlation-polarization potential, which impacts the elastic DCS mostly at small angles. Thus, the effective interaction potential is described by an optical-model potential that includes the electrostatic potential, the exchange potential, the correlation-polarization potential,

and the imaginary absorptive potential, is given by

$$V(r) = V_{st}(r) + V_{ex}(r) + V_{cp}(r) - iW_{abs}(r). \tag{3.19}$$

The scattering of relativistic electrons by an interaction potential $V(r)$ with a finite range ($V(r) = 0,\ r > r_c$) is completely described by the scattering amplitude $f(\theta)$ and the spin-flip amplitude $g(\theta)$, which are solutions to the time-independent Dirac equation for a given interaction potential $V(r)$ [65]. That is,

$$\sigma_{el} = |f(\theta)|^2 + |g(\theta)|^2. \tag{3.20}$$

It can be shown that after some tedious manipulations (see ICRU 77 appendices [65] and references therein) that the scattering amplitude and the spin-flip amplitude have the following form

$$f(\theta) = \frac{1}{2ik}\sum_{\ell=0}^{\infty}\{(\ell+1)[\exp(2i\delta_{k=\ell-1}) - 1] + \ell[\exp(2i\delta_{k=\ell})]\}P_\ell(cos(\theta) \tag{3.21}$$

and

$$g(\theta) = \frac{1}{2ik}\sum_{\ell=0}^{\infty}[\exp(2i\delta_{k=\ell}) + \exp(2i\delta_{k=\ell-1}) - 1]P_\ell^1(cos(\theta), \tag{3.22}$$

where δ_k are the phase-shifts and determined from the asymptotic behavior of the radial Dirac equations. That is,

$$P_{Ek} \sim \sin\left(kr - \ell\frac{\pi}{e} + \delta_k\right) \tag{3.23}$$

where P_{Ek} is a radial function and satisfies the radial Dirac equation [65]. The point of being pedantic is to illustrate the need for a numerical calculation to determine the phase-shifts, the scattering amplitude, and the spin-flip amplitude. That is, there are no analytical representations of the phase-shifts, the scattering amplitude, and the spin-flip amplitude without applying an approximation (e.g. the Born Approximation), so they must be calculated numerically.

Though Eqs. (3.21) and (3.22) do not have an analytical form, which introduces additional considerations from the standpoint of working with DCS data, PW DCSs are the most accurate representation of elastic scattering available outweighing the difficulties associated with DCS data. The following PW DCSs and the DCS data used for this study were generated using the ELSEPA computer code [18]. The PW DCSs were generated using the following parameters:

- The Fermi nuclear charge distribution model
- The numerical Dirac-Fock electron distribution model
- The free atom model
- The Furness-McCarthy exchange potential
- The local-density approximation for correlation-polarization potential
- Measured dipole polarizability
- No absorption correction.

Examples of the PW DCS are presented in Fig. 3.4a and 3.4b. In Fig. 3.5, the PW DCS and the SR DCS are compared. There are distinct differences between the SR DCS and the PW DCS. The PW DCS are at least an order of magnitude more peaked and the tail of the higher energy PW DCSs tend to fall-off more rapidly. Furthermore, at low energies the PW DCS have distinct structure at large scattering angles resulting from absorption effects. In addition to differences in the behavior of the two DCSs, the moments also behave differently. Most importantly, the total cross-section associated with the PW DCS is larger, while the mean deflection cosine tends to be closer to unity.

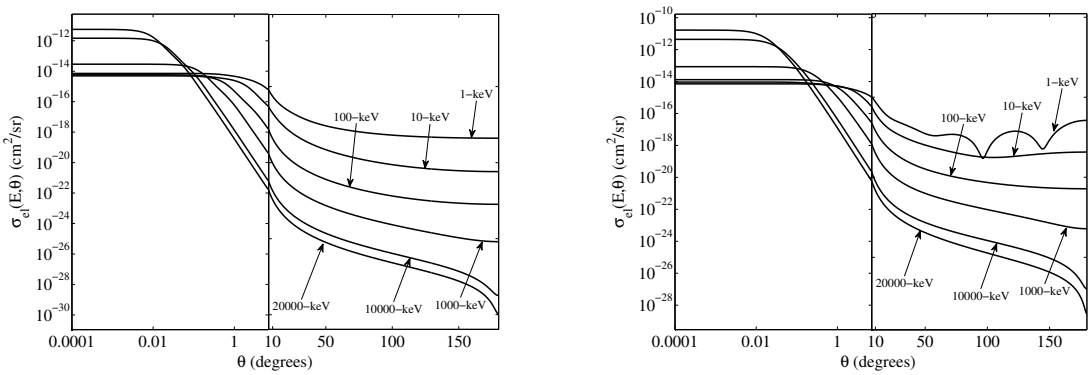

(a) Aluminum (b) Gold

Figure 3.4: Partial-wave differential cross-sections for the elastic scattering of 1-keV, 10-keV, 100-keV, 1000-keV, and 10000-keV electrons by aluminum and gold atoms.

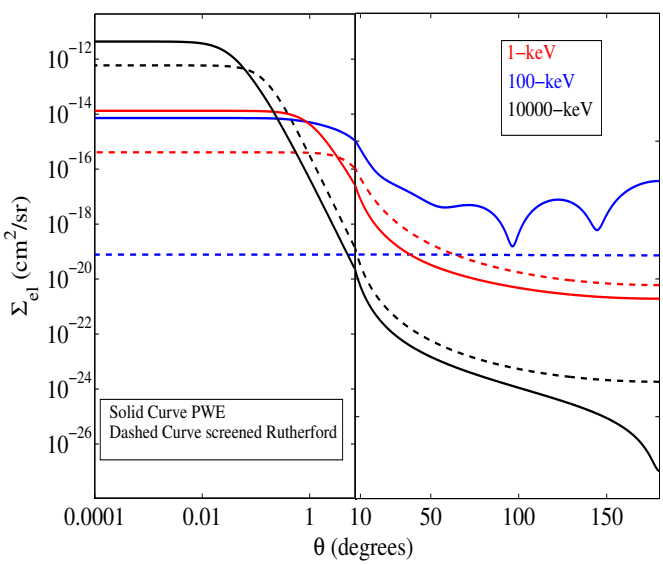

Figure 3.5: Comparison of the relativistic screened Rutherford and partial-wave differential cross-sections for elastic scattering of 1-keV, 100-keV, and 10000-keV electrons by gold atoms.

3.3 Inelastic Collisions with Atomic Electrons

Inelastic collisions with atomic electrons result in a transfer of energy from the incident electron to the atomic electron producing excitations or ionizations. Just as in the case of elastic scattering, there is a variety of inelastic DCSs ranging in accuracy and validity. The most basic form is the Rutherford inelastic DCS and typically improvements upon Rutherford all contain a Rutherford-like term. For example, the inelastic DCS used in this work, or the Möller DCS, introduced into the Rutherford cross-section the effects of quantum-mechanical exchange, and of relativity, by treating the problem of the collision between two free electrons, using the relativistic Dirac Theory of the electron [19]. Though Möller is an improvement over Rutherford, it is really only valid for energy transfers that are large compared to the mean ionization potential [67]. Therefore, some modifications to the Möller DCS are necessary for agreement with experimental benchmarks. Of course, advanced inelastic DCSs are utilized in codes like PENELOPE [27] that improve agreement with experiment, but for the purposes of this work the modified Möller DCS is sufficient.

3.3.1 Möller

The energy loss DCS for binary collisions of electrons with free electrons at rest, obtained from the Born approximation, is given by the Möller formula [27]. The Möller inelastic DCS in which the incident electron with energy E transfers the energy Q to the slower electron is given by

$$\sigma_{in}(E,Q) = \begin{cases} \frac{K}{\beta^2}\left[\frac{1}{Q^2} + \frac{1}{(E-Q)^2} + \frac{1}{(E+m_0c^2)} - \frac{m_0c^2(2E+m_0c^2)}{Q(E-Q)(E+m_0c^2)^2}\right] & : Q \in [Q_{min}, Q_{max}] \\ 0 & , \ otherwise, \end{cases} \tag{3.24}$$

where the lower bound, Q_{min}, is taken to be the mean ionization potential and the upper bound, $Q_{max} = E/2$. In Figs. 3.6a and 3.6b we present the Möller DCS for electrons of various energies scattered by aluminum and gold respectively. Like the elastic scattering DCS, the inelastic DCS is peaked about small changes in state or Q_{min}. As a function of incident particle energy, the inelastic DCS does not appear to change significantly in shape. In fact, the impact of the incident electron energy is subtle, as the inelastic DCS is inversely proportional to β^2 which varies slowly above 500-keV and is roughly unity, but grows large as $E \to Q_{min}$. Hence, the subtle peak at $\Sigma_{in}(E < 0.5MeV, Q_{min})$. Moreover, the Möller DCS does not differ appreciably from the Rutherford inelastic DCS except for relativistic energies and at $Q \sim Q_{max}$. The difference appears in the tail of the distribution making Möller slightly more peaked. As a function of Z, the Möller DCS becomes slightly less peaked. This can be seen by looking closely at the magnitude of the DCSs in Figs. 3.6a and 3.6b.

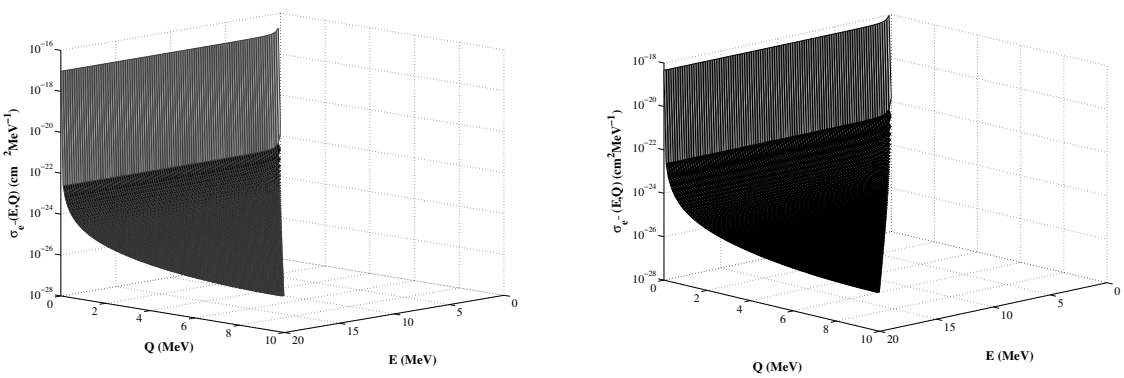

(a) Aluminum (b) Gold

Figure 3.6: Möller inelastic DCS for scattering electrons by aluminum and gold.

In this work, we correct the Möller DCS such that the first moment of Möller is

equal to the Berger-Seltzer formula [65]. That is,

$$\int_{Q_{min}}^{Q_{max}} dQ\ Q\Sigma_{in}(E,Q) = S_{BS}(E), \tag{3.25}$$

where

$$S_{BS}(E) = 2\pi r_0^2 m_e c^2 Z\mathcal{N}\frac{1}{\beta^2}\left[\ln\frac{2(\tau+1)}{(I/m_e c^2)} + F^-(\gamma,\gamma_{max}) - \delta\right] \tag{3.26}$$

and

$$F(\gamma,\gamma_{max}) = 1-\beta^2+\ln[(\gamma-\gamma_{max})]+\frac{\gamma}{\gamma-\gamma_{max}}+\frac{1}{\tau^2}\left[\frac{\gamma_{max}^2}{2}+2(\gamma+1)\ln\left(1-\frac{\gamma_{max}}{\gamma}\right)\right]. \tag{3.27}$$

The following list provides the definitions of the parameters required for the Berger-Seltzer formula:

	τ	=	$E/m_e c^2$	(unitless)
	γ	=	$\tau - 1$	(unitless)
Maximum Energy Transfer	γ_{max}	=	$\gamma/2$	(unitless)
Density Effect Correction See Sternheimer [68]	δ			(unitless)
Mean Ionization Energy See ICRU 37 [69]	I			(MeV)

3.4 Analog DCS Moments

In this section, analog DCS Moments that have a physical interpretation are described. In particular, the zeroth, first, and second moments of the elastic and inelastic analog DCS. These quantities are typically referred to as the total cross-section (zeroth), the mean scattering angle or energy-loss (first), and the mean-square scattering angle or energy-loss (second). In the remaining sections, the analog DCS moments are defined and the aforementioned physical quantities are developed. In addition, some attention is given to the the limitation of analytical DCSs like screened Rutherford and Möller.

3.4.1 Elastic DCS moments

Herein, we define Legendre moments of the elastic DCS as

$$\Sigma_{el,\ell} = 2\pi \int_{-1}^{1} P_l(\mu_0)\Sigma_{el}(E,\mu_0)d\mu_0, \tag{3.28}$$

and the momentum transfer moments as

$$G_\ell = \Sigma_{el,0} - \Sigma_{el,\ell}, \tag{3.29}$$

where $\Sigma_{el,0}$ is the total macroscopic elastic cross-section with units of cm^{-1} and defined as

$$\Sigma_{el,0} = 2\pi \int_{-1}^{1} \Sigma_{el}(E,\mu_0)d\mu_0. \tag{3.30}$$

The macroscopic elastic total cross section, presented in Fig. 3.7a, gives the probability of an elastic interaction occurring per unit distance and is extremely large for electrons. The microscopic total cross-section in barns is between 10^6-10^8. Contrast this to the total microscopic elastic cross section for neutrons that is typically between 10^2 to 10^4 barns for a wide range of materials and energies.

In Fig. 3.7a, one can see the impact of the approximations required to obtain the relativistic screened Rutherford DCS. Relativistic screened Rutherford is smaller in magnitude for all energies. As a function of increasing energy, both relativistic screened Rutherford and the partial-wave DCS monotonically decrease and eventually saturate. However, for decreasing energies, the partial-wave total cross-section is monotonically increasing, whereas relativistic screened Rutherford begins to fall-off for sufficiently low energies. This is a result of the validity of the Born approximation, which is valid for

$$\left(\frac{Z}{137\beta}\right)^2 << 1. \tag{3.31}$$

One can see the impact of Z on the validity of the Born approximation in Fig. 3.7a where the relativistic screened Rutherford total cross-section begins to diverge from

the partial-wave total-cross section nearby 100-keV as opposed roughly 10-keV for aluminum. The inverse of the macroscopic elastic total cross-section is the elastic mfp (cm) or

$$\lambda_{el} = \frac{1}{\Sigma_{el,0}}, \tag{3.32}$$

which is presented in Fig. 3.7b. The mfp provides a length scale over which a single collision occurs for the DCSs used in the simulation. For elastic scattering of electrons, the mfp is extremely small - on the order of microns for medium to intermediate energies.

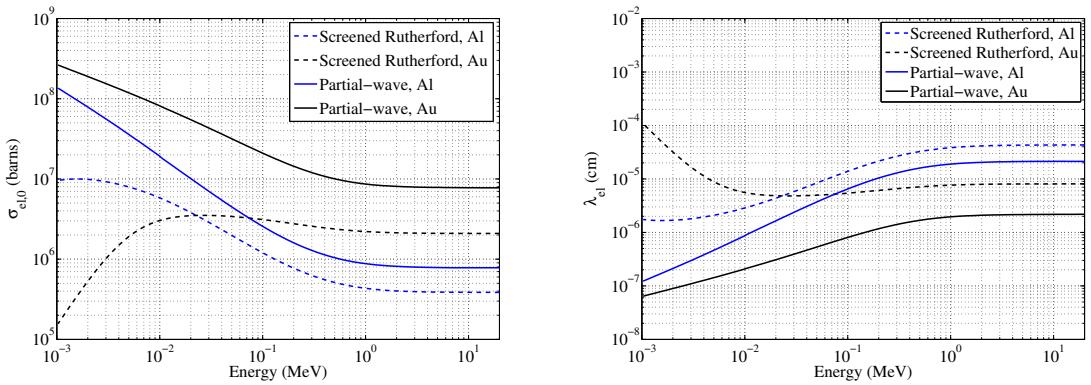

(a) Total Cross-Section (b) Mean Free Path

Figure 3.7: Screened Rutherford and partial-wave total cross-sections and mean free paths for elastic collisions with aluminum and gold nuclei.

The mean scattering angle or

$$\bar{\mu}_0 = \frac{\Sigma_{el,1}}{\Sigma_{el,0}}, \tag{3.33}$$

is related to the transport cross-section, or G_1, by

$$G_1 = \Sigma_{el,0} - \Sigma_{el,1} = \Sigma_{el,0}(1 - \bar{\mu}_0) \tag{3.34}$$

The transport cross-section is the inverse transport mfp (cm) or

$$\lambda_{tr} = \frac{1}{\Sigma_{el,1}}. \tag{3.35}$$

The transport mfp, presented in Fig. 3.8, provides a length scale over which an initially singular beam experiences significant spreading in space, angle, and energy. The ratio of the transport cross section to the total cross section is known and the scattering power of the medium. Under conditions of highly peaked scattering one can invoke the small angle approximation to further understand the significance of the transport cross-section. That is,

$$G_1 \approx 2\pi \int_0^{\pi} \frac{\theta_0^2}{2} \Sigma_{el}(E, \theta_0) \sin\theta_0 d\theta_0 = \langle \theta_0^2 \rangle, \tag{3.36}$$

where $\langle \theta_0^2 \rangle$ is the mean-square scattering angle and is related to the spreading of a beam. That is, the beam broadens with increasing $\langle \theta_0^2 \rangle$.

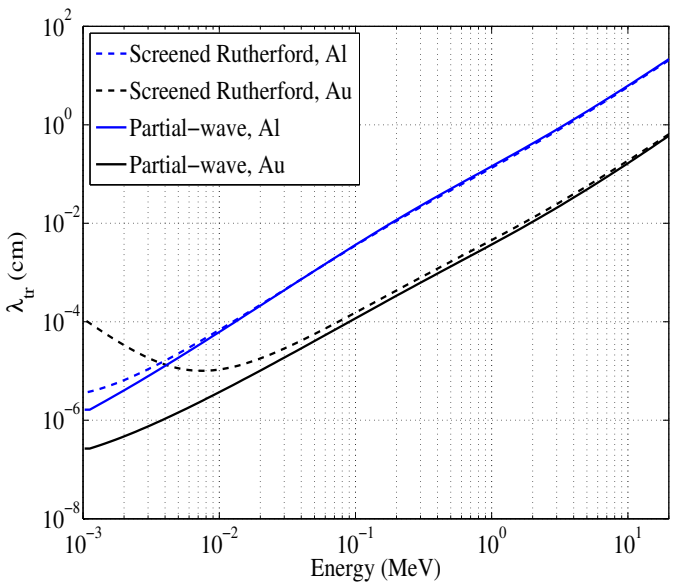

Figure 3.8: Screened Rutherford and partial-wave transport mean free paths for elastic collisions with aluminum and gold nuclei.

3.4.2 Inlastic DCS moments

Herein, we define energy-loss moments of the inelastic DCS as

$$Q_k = \int_{Q_{min}}^{Q_{max}} Q^k \Sigma_{in}(E, Q) dQ. \tag{3.37}$$

For $k = 0$, we have $Q_0 = \Sigma_{in,0}$, where $\Sigma_{in,0}$ is the total inelastic cross-section with units of cm^{-1} and defined as

$$\Sigma_{in,0} = \int_{Q_{min}}^{Q_{max}} \Sigma_{in}(E, Q) dQ. \tag{3.38}$$

In Fig. 3.9a the microscopic total cross-sections for aluminum and gold are presented. Again, the total cross-section begins to fall-off for sufficiently low energies in gold, which is characteristic of a limitation of the Born approximation used to obtain the Möller DCS. It is also of interest to note that the minimum and maximum values are roughly three orders of magnitude lower than the elastic DCS. Therefore, elastic scattering about 10^3 times more likely to occur than inelastic scattering.

The inverse of the inelastic total cross-section is the inelastic mfp (cm) or

$$\lambda_{in} = \frac{1}{\Sigma_{in,0}}, \tag{3.39}$$

which is presented in Fig. 3.9b. Again, this provides the mean distance to an inelastic collision and is on the order of mm.

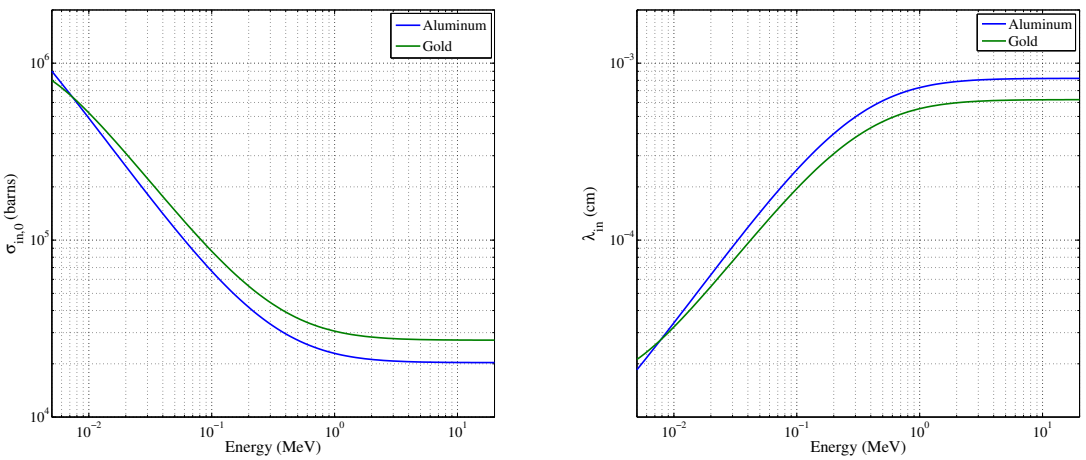

(a) Total Cross-Section (b) Mean Free Path

Figure 3.9: Möller total cross-section and mfp for inelastic collisions with aluminum and gold nuclei.

For $k = 1$, we have $Q_1 = S(E)$, where $S(E)$ is the stopping power with units of $MeVcm^{-1}$ and defined as

$$S(E) = \int_{Q_{min}}^{Q_{max}} Q\Sigma_{in}(E, Q)dQ. \tag{3.40}$$

The stopping power is the mean energy-loss per unit distance traveled. As previously noted, Eq. (3.41) does not result in stopping powers that agree with ICRU 37 [69] and is replaced with the Berger-Seltzer formula from Eq. (3.26). The Möller DCS is renormalized such that the first moment Q_1 is in agreement with the Berger-Seltzer formula. The differences in the two expressions are seen in Fig. 3.10, where Q_1 is roughly a factor of two lower than the more accurate Berger-Seltzer formula.

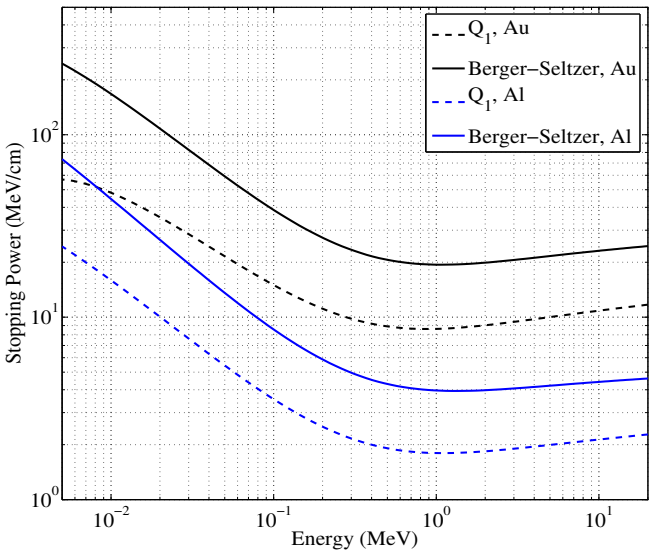

Figure 3.10: Stopping power from Eq. (3.41) and the Berger-Seltzer formula.

For $k = 2$, we have $Q_2 = T(E)$, where $T(E)$ is the straggling coefficient with units of MeV^2cm^{-1} and defined as

$$T(E) = \int_{Q_{min}}^{Q_{max}} Q^2 \Sigma_{in}(E, Q) dQ. \tag{3.41}$$

Energy straggling is the result of occasional inelastic collisions resulting in large energy-losses. In an energy-loss simulation for a thin slab where stopping power is applied in a CSD fashion, the resulting energy spectra will be singular and equal to the mean energy-loss. By including straggling, there will be a spread in energy about the mean energy-loss. The amount of spreading will depend on the strength of the energy straggling. Straggling impacts quantities like dose from electrons by smoothing out the Bragg peak.

Chapter 4

The Analog Problem

In this chapter, the challenges associated with the analog electron transport are expressed. That is, the challenges associated with solving the transport equation where the interaction physics are given by the single-scatter or analog DCSs described in Chapter 3. To understand the challenges it is necessary to describe the transport equation in some detail. To do so, a description of the independent variables associated with the transport equation, along with a discussion of the angular flux (that is, the solution) and quantities of interest that are derived from the angular flux are provided. Rather than deriving the transport equation, which can be found in numerous particle transport texts [11, 70], the transport equation of interest is written down and qualitative descriptions of the various terms that appear are provided. Furthermore, a summary of the Monte Carlo algorithm for electron transport is presented within the context of the Geant4 toolkit [3]. The chapter is concluded with example calculations corresponding to the aforementioned derived quantities using analog Monte Carlo, along with the computer time required to complete such calculations. The computational cost associated with analog Monte Carlo transport of electrons with moderate to high energies is the single-most important reason for developing efficient approximate methods.

4.1 Independent Variables

It is of interest to obtain solutions to the 3-D transport equation. The solution, or the angular flux, is the distribution of particles in a six-dimensional phase-space including position $\vec{r}$, energy E, and direction $\vec{\Omega}$, at some time t, where the position with respect to the origin in Cartesian coordinates is given by

$$\vec{r} = x\hat{i} + y\hat{j} + z\hat{k}. \tag{4.1}$$

A differential hexahedral volume, dV, is obtained by sweeping out an incremental amount in all directions about $\vec{r}$ and given by $dV = dxdydz$.

The direction, measured with respect to the polar angle, θ, and azimuthal angle, φ, is given by

$$\vec{\Omega} = \Omega_x\hat{i} + \Omega_y\hat{j} + \Omega_z\hat{k}, \tag{4.2}$$

where

$$\begin{aligned} \Omega_x &= (1 - \cos\theta)^{1/2}\cos\varphi \\ \Omega_z &= (1 - \cos\theta)^{1/2}\sin\varphi \\ \Omega_y &= \cos\theta. \end{aligned} \tag{4.3}$$

An incremental differential surface on the unit sphere, $d\Omega$, is swept out about $\vec{\Omega}$ and given by $d\Omega = d\mu d\varphi$, where $\mu = \cos\theta$ and $d\mu$ is an incremental displacement with respect to the polar angle, while $d\varphi$ is an incremental displacement with respect to the azimuthal angle.

4.2 The Angular Particle Density and Derived Quantities

The angular particle density describes a population of particles in the phase space of interest. The angular flux, or the solution to the transport equation, is related to the angular particle density. Numerous quantities of interest are derived from the angular flux. The angular particle density and various derived quantities are the subject of the following sections.

4.2.1 The angular particle density

The angular particle density is denoted as $N(\vec{r}, E, \vec{\Omega}, t)$, where $N(\vec{r}, E, \vec{\Omega}, t)dVdEd\Omega dt$ gives the number of particles in $dVdEd\Omega$ about $(\vec{r}, E, \vec{\Omega})$ at time t with units of $(cm^{-3}MeV^{-1})$. The quantity of interest, the angular flux, is related to the angular particle density by

$$\psi(\vec{r}, E, \vec{\Omega}, t) = vN(\vec{r}, E, \vec{\Omega}, t), \tag{4.4}$$

where v is the particle velocity. Therefore, the volume based interpretation of the angular flux, or $\psi(\vec{r}, E, \vec{\Omega}, t)dVdEd\Omega$, is the rate at which path length is generated by particles in $dVdEd\Omega$ about $(\vec{r}, E, \vec{\Omega})$ at time t with units of $(cm^{-2}MeV^{-1}s^{-1})$.

Many other derived quantities follow from the angular flux or the scalar flux which is given by

$$\phi(\vec{r}, E, t) = \int_{4\pi} d\Omega\psi(\vec{r}, E, \vec{\Omega}, t), \tag{4.5}$$

and is the zeroth angular moment of the angular flux. For example, quantities of interest presented in the results section include angular distributions, energy spectra, longitudinal and lateral distributions, dose or energy deposition, charge deposition,

and transmission and reflection fractions. Each of these quantities are defined in the following sections.

4.2.2 Derived quantities

It is uncommon to require the angular flux directly. Typically, quantities derived from the angular flux are of direct use. This includes quantities like angular distributions, energy spectra, longitudinal and lateral distributions, dose, charge deposition, and reflection and transmission fractions. These quantities are now described in greater detail and and in many cases, the result is a function p indicating that these distributions can be interpreted as probability distribution functions.

Angular distributions

Angular distributions at some position $\vec{r}$ are typically a function of the polar angle θ or $\mu = \cos\theta$, which requires integration of the angular flux over all azimuthal angles and energies or

$$p(\vec{r}, \mu) = \int_0^{2\pi} d\phi \int_0^{\infty} dE \psi(\vec{r}, E, \phi, \mu). \tag{4.6}$$

Though $p(\vec{r}, \mu)$ can be obtained at any position, it is common in electron transport to obtain reflected and transmitted angular distributions in thin slabs. For a 1-D slab of thickness L with the left face at the origin, the reflected and transmitted distributions are given by

$$p(0, \mu) = \int_0^{2\pi} d\phi \int_0^{\infty} dE \psi(0, E, \phi, \mu), \tag{4.7}$$

and

$$p(L, \mu) = \int_0^{2\pi} d\phi \int_0^{\infty} dE \psi(L, E, \phi, \mu) \tag{4.8}$$

respectively. Note that particles traveling in directions with $\mu > 0$ do not contribute to the reflected distribution, while particles traveling in directions with $\mu < 0$ do not contribute to the transmitted distribution.

Energy spectra

Energy spectra at some position $\vec{r}$ are a function of particle energy and an angular independent quantity that requires integration of the angular flux over all contributing angles. This quantity is effectively an energy dependent current, $J(\vec{r}, E)$, or

$$\begin{aligned} J(\vec{r}, E) = &\int_{\vec{\Omega}\cdot\hat{n}>0} d\Omega \int_{\partial R} dS \ (\vec{\Omega}\cdot\hat{n})\psi(\vec{r}, E, \phi, \mu) \\ &- \int_{\vec{\Omega}\cdot\hat{n}<0} d\Omega \int_{\partial R} dS \ |\vec{\Omega}\cdot\hat{n}|\psi(\vec{r}, E, \phi, \mu). \end{aligned} \tag{4.9}$$

Once again, it is common in electron transport to obtain reflected and transmitted energy spectra in thin slabs. In this case, the definition of an energy dependent partial current is necessary where particles flowing in positive directions $\vec{\Omega}\cdot\hat{n} > 0$ across a surface element ∂S contribute to the positive partial current

$$J^{+}(\vec{r}, E) = \int_{\vec{\Omega}\cdot\hat{n}>0} d\Omega \int_{\partial R} dS \ \vec{\Omega}\cdot\hat{n}\psi(\vec{r}, E, \phi, \mu), \tag{4.10}$$

and particles flowing in negative $\vec{\Omega}\cdot\hat{n} < 0$ directions across a surface element ∂S contribute to the negative partial current

$$J^{-}(\vec{r}, E) = \int_{\vec{\Omega}\cdot\hat{n}<0} d\Omega \int_{\partial R} dS \ |\vec{\Omega}\cdot\hat{n}|\psi(\vec{r}, E, \phi, \mu), \tag{4.11}$$

where $\hat{n}$ is a unit vector normal to the surface of flow. Therefore, in the 1-D slab described in section 4.2.2, the reflected energy spectrum is

$$p(0, E) = J^{-}(0, E), \tag{4.12}$$

and the transmitted energy spectrum is

$$p(L, E) = J^{+}(L, E). \tag{4.13}$$

In many cases, one is interested in energy-loss spectra as well which are given by

$$p(0, E_0 - E) = J^-(0, E_0 - E), \tag{4.14}$$

and

$$p(L, E_0 - E) = J^+(L, E_0 - E), \tag{4.15}$$

where E_0 is the initial energy of the particle.

Longitudinal and lateral distributions

Longitudinal and lateral distributions are closely related to Lewis theory. In fact, these distributions are obtained by solving an infinite medium transport equation for mono-energetic particles. The longitudinal distribution is

$$p(z, s) = \int_{-\infty}^{\infty} dx \int_{-\infty}^{\infty} dy \int_{4\pi} d\Omega \psi(x, y, z, s, \vec{\Omega}), \tag{4.16}$$

and gives the probability that a particle will be displaced a distance $\pm z$ along the axis of the initial direction of the particle given some pathlength s. The lateral distribution is

$$p(b, s) = \int_{-\infty}^{\infty} dz \int_{4\pi} d\Omega \psi(x, y, z, s, \vec{\Omega}), \tag{4.17}$$

where $b = \sqrt{x^2 + y^2}$ and gives the probability that a particle will be displaced laterally through a distance b orthogonal to the axis of the initial direction of the particle pathlength s. That is, the radial spread given some pathlength s.

Dose deposition

The dose gives the spatial distribution of the energy deposited per unit volume. It is obtained by integrating the product of the average energy lost per distance traveled,

$S(E)$, or the stopping power and the flux over all energies and angles or

$$D(\vec{r}) = \int_{4\pi} d\Omega \int_0^\infty dE\, S(E)\psi(\vec{r}, E, \vec{\Omega}) = \int_0^\infty dE\, S(E)\phi(\vec{r}, E), \quad (MeV/cm^3). \tag{4.18}$$

This quantity is of particular interest to nearly all applications of electron transport. Moreover, the dose is typically easier to resolve because it is only differential in space in contrast to some of the previous quantities that are also differential in angle or energy.

Charge deposition

Charge deposition is the spatial distribution of charge (positive or negative) produced by a particle slowing down through energies less than E_{min}. Similar to dose, charge deposition is related to the scalar flux or

$$C(\vec{r}) = \int_{E_{min}}^\infty dE' \int_0^{E_{min}} dE''\, \Sigma_{in}(E' \to E'')\phi(\vec{r}, E'), \quad (cm^{-3}), \tag{4.19}$$

where E_{min} is the energy below which particles are assumed deposited. Eq. (4.8) can be interpreted as a slowing down density. The inner integral gives the rate at which electrons with energies E' slow down past E_{min}. The outer integral then gives the total slowing down density for all electrons with energies $E' > E_{min}$.

Reflection and transmission fractions

Reflection and transmission fractions are typically thin-slab results and are a measure of the number of source particles that are not absorbed in the medium and either forward-scatter (transmission) or backscatter (reflection). For a 1-D slab (as described in section 4.2.2), the reflection fraction is the negative partial current evaluated at $x = 0$ or

$$J^-(0) = \int_0^\infty dE \int_{\vec{\Omega}\cdot\hat{n}<0} d\Omega \int_{\partial R} dS\, |\vec{\Omega} \cdot \hat{n}|\psi(0, E, \phi, \mu). \tag{4.20}$$

and the transmission fraction is the positive partial current evaluated at $x = L$ or

$$J^{+}(L) = \int_{0}^{\infty} dE \int_{\vec{\Omega}\cdot\hat{n}>0} d\Omega \int_{\partial R} dS\ \vec{\Omega}\cdot\hat{n}\psi(L, E, \phi, \mu) \tag{4.21}$$

4.3 The Electron Transport Equation

Given the definitions from section 4.2, the usual practice is to derive the transport equation by writing down an equation for the time rate of change in some incremental population of particles which is related to the rate of loss and the rate of gain. That is,

$$\frac{\partial}{\partial t} N(\vec{r}, E, \vec{\Omega}, t) = gains - losses. \tag{4.22}$$

Next, the angular particle density is related to the angular density, $\psi(\vec{r}, E, \vec{\Omega}, t) = vN(\vec{r}, E, \vec{\Omega}, t)$, and the contributions to gains and losses are obtained from first principles. Here, the transport equation for electrons is simply written down and each term is discussed as it relates to gains and losses. If necessary, the reader should refer to more complete derivations from the text [11, 70].

To begin, it is of interest to study the time-independent transport equation for electrons. In this equation, it is assumed that the solution is not changing as a function of time; therefore, particle losses are exactly balanced by particle gains and Eq. (4.22) becomes a balance equation or

$$\begin{aligned}
&\Omega\cdot\nabla\psi(\vec{r}, E, \vec{\Omega}) + \left[\Sigma_{el,0}(\vec{r}, E) + \Sigma_{in,0}(\vec{r}, E)\right]\psi(\vec{r}, E, \vec{\Omega}) \\
&= \int_{0}^{\infty} dE' \int_{4\pi} d\Omega' \left[\Sigma_{el}(\vec{r}, E'\to E, \vec{\Omega}'\cdot\vec{\Omega}) + \Sigma_{in}(\vec{r}, E'\to E, \vec{\Omega}'\cdot\vec{\Omega})\right]\psi(\vec{r}, E', \vec{\Omega}')
\end{aligned} \tag{4.23}$$

where the left hand side corresponds to losses from leakage and out-scatter and the right hand side corresponds to gains from in-scatter and secondary production. That

is, $\Omega \cdot \nabla\psi(\vec{r}, E, \vec{\Omega})dVdEd\Omega$ is the net leakage of particles with energies in dE about E and directions in $d\Omega$ about $\vec{\Omega}$ from dV. The out-scatter is a loss due to particles in $dVdEd\Omega$ about $(\vec{r}, E, \vec{\Omega})$ suffering an elastic or inelastic collision resulting in removal of the particles from the energy or angular phase-space. The elastic and inelastic in-scatter or $\int_0^\infty dE' \int_{4\pi} d\Omega' \big[\Sigma_{el}(\vec{r}, E' \to E, \vec{\Omega}' \cdot \vec{\Omega}) + \Sigma_{in}(\vec{r}, E' \to E, \vec{\Omega}' \cdot \vec{\Omega})\big]\psi(\vec{r}, E', \vec{\Omega}')$ is a gain from particles in $dVdE'd\Omega'$ about $(\vec{r}, E', \vec{\Omega}')$ scattering into $dVdEd\Omega$ about $(\vec{r}, E, \vec{\Omega})$. Finally, $Q_\delta(\vec{r}, E, \vec{\Omega})$ is a gain due to production of secondary electrons in $dVdEd\Omega$ about $(\vec{r}, E, \vec{\Omega})$.

It is customary to rewrite the transport equation in terms of the Boltzmann collision operator or

$$\Omega \cdot \nabla\psi(\vec{r}, E, \vec{\Omega}) = H^B\psi(\vec{r}, E, \vec{\Omega}) + Q_\delta(\vec{r}, E, \vec{\Omega}), \tag{4.24}$$

where the Boltzmann collision operator is defined as

$$\begin{aligned} H^B\psi(\vec{r}, E, \vec{\Omega}) = \int_0^\infty dE' \int_{4\pi} d\Omega' \big[&\Sigma_{el}(\vec{r}, E' \to E, \vec{\Omega}' \cdot \vec{\Omega}) \\ &+ \Sigma_{in}(\vec{r}, E' \to E, \vec{\Omega}' \cdot \vec{\Omega})\big]\psi(\vec{r}, E', \vec{\Omega}') - \Sigma_t(\vec{r}, E)\psi(\vec{r}, E, \vec{\Omega}), \end{aligned} \tag{4.25}$$

and $\Sigma_t(\vec{r}, E) = \Sigma_{el,0} + \Sigma_{in,0}$. Eq. (4.24) is subject to the following general boundary condition

$$\psi(\vec{r}, E, \phi, \mu) = \psi^b(\vec{r}, E, \phi, \mu), \ \vec{r} \in \partial V, \ \vec{\Omega}(\phi, \mu) \cdot \vec{n} < 0, \ 0 < E < \infty, \tag{4.26}$$

For electrons, elastic and inelastic scattering are treated separately as indicated in Eq. (4.25). Furthermore, it is assumed that elastic scattering occurs without energy loss and angular deflection from inelastic scattering is given by kinematics, so the collision operator can be expressed as

$$H^B\psi(\vec{r}, E, \vec{\Omega}) = H^B_{el}\psi(\vec{r}, E, \vec{\Omega}) + H^B_{in}\psi(\vec{r}, E, \vec{\Omega}), \tag{4.27}$$

where

$$H_{el}^{B}\psi(\vec{r},E,\vec{\Omega}) = \int_{4\pi} d\Omega' \Sigma_{el}(\vec{r},E,\vec{\Omega}'\cdot\vec{\Omega})\psi(\vec{r},E,\vec{\Omega}') - \Sigma_{el,0}(\vec{r},E)\psi(\vec{r},E,\vec{\Omega}) \quad (4.28)$$

and

$$\begin{aligned} H_{in}^{B}\psi(\vec{r},E,\vec{\Omega}) = &\int_{4\pi} d\Omega' \int_{0}^{\infty} dE' \Sigma_{in}(\vec{r},E'\rightarrow E)\delta[\vec{\Omega}' - f(E',Q)]\psi(\vec{r},E',\vec{\Omega}') \\ &- \Sigma_{in,0}(\vec{r},E)\psi(\vec{r},E,\vec{\Omega}), \end{aligned} \quad (4.29)$$

where the angle of the primary is

$$f(E,Q) = \sqrt{\frac{E-Q}{E}\frac{E+2m_ec^2}{E-Q+2m_ec^2}} \quad (4.30)$$

and the angle of the secondary is

$$g(E,Q) = \sqrt{\frac{Q}{E}\frac{E+2m_ec^2}{Q+2m_ec^2}}. \quad (4.31)$$

In the event that secondary production is neglected ($Q_\delta = 0$) and deflection of the primary from inelastic scattering is also considered negligible, Eq. (4.29) reduces to

$$H_{el}^{B}\psi(\vec{r},E,\vec{\Omega}) = \int_{0}^{\infty} dE' \Sigma_{in}(\vec{r},E'\rightarrow E)\psi(\vec{r},E',\vec{\Omega}) - \Sigma_{in,0}(\vec{r},E)\psi(\vec{r},E,\vec{\Omega}). \quad (4.32)$$

As previously mentioned, direct numerical solution of Eq. (4.24) is not realistic for most applications of interest because of the large total cross sections, $\Sigma_{el,0}$ and $\Sigma_{in,0}$, and DCSs, Σ_{el} and Σ_{in}, that are highly peaked about small deflections and energy losses. Because the computational effort is related to the number of collisions simulated per particle history and the outcome of the collision, simulation of Coulomb collisions are far more computationally intensive than the interactions characterizing neutral particles. Examples of analog electron transport calculations or solutions to Eq. (4.23), along with the associated computational cost, is the subject of the following section.

4.4 Analog Monte Carlo Calculations

When applying the Monte Carlo method to the transport equation, it is possible to obtain solutions by simulating the physical processes of particles without necessarily writing down or referring to the transport equation. Furthermore, a Monte Carlo solution does not include the fine detail that is characteristic of deterministic methods (that is, the angular flux) but instead provides information about certain specified quantities of interest (that is, derived quantities) [12]. Therefore, the Monte Carlo method might be described as an intuitive or physical approach to solving the transport equation through direct simulation of particle behavior, where the individual particle interactions can be considered a Markov process which are independent of their history.

Of course, one of the drawbacks of analog Monte Carlo is that the detailed physics may be computationally prohibitive as in the case of electrons. In this section, we demonstrate the computational cost associated with several analog Monte Carlo solutions to the transport equation. Before presenting any results, the analog Monte Carlo algorithm is summarized.

4.4.1 Analog Monte Carlo algorithm

What is generally required for an analog Monte Carlo calculation is a description of the geometrical boundaries, a description of the material properties in each region, and the differential and total cross-section for each material. In the algorithm described below, it is assumed that particles travel straight lines between collisions, particles suffer a collision per unit distance with probability Σ_t, the time during a collision can be neglected, and the particle transport being simulated is linear [12].

In general, a particle is tracked from "birth" until its "death," which starts by

sampling a particle from the source description. The source can be a boundary source, or boundary condition, and/or an internal source. Both boundary and internal sources can be functions of space, angle, and energy. Given a source particle, the distance to collision is sampled according to exponentially distributed collision sites. The particle is moved the distance to the next collision site in its current direction. Assuming the particle did not leave the system, the collision type and the collision outcome are sampled. This process is repeated until the particle is absorbed by the medium or the particle leaves the system.

As with all probabilistic quantities - the source function, the differential cross-section, the distance to collision, and so forth - they are determined by sampling (direct, rejection) a probability density function (PDF), which requires deriving a cumulative probability function (CDF). Details on direct and rejection sampling techniques are given in reference [12] and references therein.

The following is an outline of the analog Monte Carlo algorithm specifically for transporting electrons. The important steps are listed and some detail is given for the quantity sampled at each step along with other applicable considerations.

Analog Monte Carlo algorithm

1. Sample source particle
   - For monoenergetic pencil beams this simply requires initializing the particles position r_0, energy E_0, and direction $\vec{\Omega}_0$. For distributed sources one must obtain a CDF and apply inverse mapping. For example, for an isotropic point source the polar angle is determined by $\mu \leftarrow 2\xi_1 - 1$ and the azimuthal angle is determined by $\varphi \leftarrow 2\pi\xi_2$ where ξ_1 and ξ_2 are two different random numbers uniformly distributed between zero and one.
2. Sample distance to collision

- Distance to collision is generally given by $s \leftarrow -\ln(\xi)/\Sigma_t$, where Σ_t is the probability per unit distance that an elastic or inelastic collision will occur. Given the distance s and the current direction of the particle Ω_i, this must be compared with the distance to the next boundary d.
  - If $s < d$, the particle is moved to the collision site and algorithm continues with step 3.
  - If $s \geq d$ and the material on each side of the boundary is the same, the residual s and d are compared and the particle is moved to the collision site if the residual $s < d$ and algorithm continues with step 3.
  - If $s \geq d$ and the material on each side of the boundary is different, the particle is stopped at the boundary without colliding and restart at step 2.
  - If $s \geq d$ and the particle crosses a system boundary, the particle is killed, quantities of interest are tallied, and the algorithm restarts at step 1.

3. Sample collision type
   - The collision type is sampled from the point probability associated with each collision type. That is, the probability of the ith collision type is $p_i = \sigma_{i,0}/\sigma_t$, where $\sum_i p_i = 1$. As it relates to the analog problems studied herein, the two point probabilities for elastic and inelastic collisions are $p_{el} = \sigma_{el,0}/\sigma_t$ and $p_{in} = \sigma_{in,0}/\sigma_t$. To determine the collision type a random number is sampled and the following logic is applied:
     - If $\xi \leq p_{el}$, then an elastic collision occurred.
     - Otherwise, an inelastic collision occurred.

4. Sample collision outcome

   – Given the collision type, the appropriate DCS is sampled according to the necessary method (direct or rejection). For example, when sampling screened Rutherford the direct method used is $\mu_0 \leftarrow 1 - 2\eta\xi/(1.0 - \xi + \eta)$. When sampling from the partial-wave DCSs, methods for inverting discrete DCSs are used. Lastly, when sampling Möller a rejection method must be used because the Möller DCS cannot be inverted.

5. Update particle state

   – Given the collision outcome, the particles energy or direction is updated. In the event of an inelastic collision, some additional steps are required. That is,

     * If the sampled energy-loss is greater than the secondary production threshold, a secondary must be generated.

     * Otherwise, the energy-loss is assumed to be deposited locally and tallied if necessary.

6. Restart at step 1.

4.4.2 Tallies

In Monte Carlo calculations, quantities of interest are obtained through tallies. That is, counting events that contribute to some quantity being tracked. Each tally is related to the derived quantities from section 4.2, but it is typically easier to use an intuitive approach in obtaining expressions for tallies.

Angular distributions

The particle's polar angle is tallied when crossing a specified surface, when transmitted, reflected, or after reaching a maximum specified pathlength. Angular Distribution tallies are determined by summing up all contributions by each particle to some i^{th} angular bin. If the polar angle of the j^{th} particle is within the limits of the i^{th} bin, that bin is incremented by one. The expression for the angular distribution is

$$p(\theta_i) = \frac{1}{N\Delta\theta_i} \sum_j f(\theta_j), \tag{4.33}$$

where N is the number of source particles, $\Delta\theta_i = \theta_{i+1/2} - \theta_{i-1/2}$, $\theta_{i-1/2}$ and $\theta_{i+1/2}$ are the lower and upper limit of the i^{th} bin, and

$$f(\theta_j) = \begin{cases} 1 & : \theta_{i-1/2} \leq \theta_j < \theta_{i+1/2} \\ 0 & : otherwise. \end{cases} \tag{4.34}$$

Energy-loss spectra

The particle's energy-loss (Q=$E_0 - E$) is tallied when crossing a specified surface, when transmitted, reflected, or after reaching a maximum specified pathlength. Energy-loss spectra tallies are determined by summing up all contributions by each particle to some i^{th} energy-loss bin. If the energy-loss of the j^{th} particle is within the limits of the i^{th} bin, that bin is incremented by one. The expression for the energy-loss spectra is

$$p(E_i) = \frac{1}{N\Delta Q_i} \sum_j f(Q_j), \tag{4.35}$$

where N is the number of source particles, $\Delta Q_i = Q_{i+1/2} - Q_{i-1/2}$, $Q_{i-1/2}$ and $Q_{i+1/2}$ are the lower and upper limit of the i^{th} bin, and

$$f(Q_j) = \begin{cases} 1 & : Q_{i-1/2} \leq Q_j < Q_{i+1/2} \\ 0 & : otherwise. \end{cases} \tag{4.36}$$

Longitudinal and lateral distributions

The particle's longitudinal displacement (z/s) and lateral displacement (b/s, $b = \sqrt{x^2 + y^2}$) is tallied when a particle reaches a maximum specified path-length s. Longitudinal and lateral distribution tallies are determined by summing up all contributions by each particle to some i^{th} longitudinal or lateral displacement bin. The expression for the longitudinal distribution is

$$p\left(\frac{z_i}{s}\right) = \frac{1}{N\Delta(\frac{z_i}{s})} \sum_j f\left(\frac{z_j}{s}\right), \tag{4.37}$$

where N is the number of source particles, $\Delta z_i/s = \frac{z_{i+1/2}}{s} - \frac{z_{i-1/2}}{s}$, and

$$f\left(\frac{z_j}{s}\right) = \begin{cases} 1 & : \frac{z_{i-1/2}}{s} \leq \frac{z_j}{s} < \frac{z_{i+1/2}}{s} \\ 0 & : otherwise. \end{cases} \tag{4.38}$$

The expression for the lateral distribution is

$$p\left(\frac{b_i}{s}\right) = \frac{1}{N\Delta(\frac{b_i}{s})} \sum_j f\left(\frac{b_j}{s}\right), \tag{4.39}$$

where N is the number of source particles, $\Delta b_i/s = \frac{b_{i+1/2}}{s} - \frac{b_{i-1/2}}{s}$, and

$$f\left(\frac{b_j}{s}\right) = \begin{cases} 1 & : \frac{b_{i-1/2}}{s} \leq \frac{b_j}{s} < \frac{b_{i+1/2}}{s} \\ 0 & : otherwise. \end{cases} \tag{4.40}$$

Dose deposition

Dose tallies are determined by summing over all energy deposited in the i^{th} spatial cell, by the jth particle or

$$D(x_i, y_i, z_i) = \frac{1}{\rho_i V_i} \sum_j \frac{\Delta E_{i,j}}{N}, \tag{4.41}$$

where ρ_i is the density of the material in the i^{th} cell, V_i is the volume of the i^{th} cell, and $\Delta E_{i,j}$ is the energy deposited between x_i and x_{i+1}, y_i and y_{i+1}, and z_i and z_{i+1} by the j^{th} particle.

Charge deposition

Charge deposition is tallied for the i^{th} spatial bin when a particle slows down past some minimum energy (negative charge) and when a secondary is created (positive charge). The expression for charge deposition is

$$C(x_i, y_i, z_i) = \frac{R_0}{r_c N V_i} \sum_j f(c_j), \tag{4.42}$$

where N is the number of source particles, V_i is the volume of the i^{th} cell, R_0 is the CSDA range of the particle, r_c is the reflection factor given in the following section, c_j is -1 for charge deposition and 1 for secondary production, and

$$f(c_j) = \begin{cases} c_j & : \vec{r}_j \in V_i \\ 0 & : otherwise. \end{cases} \tag{4.43}$$

In other words, c_j is tallied in the i^{th} cell corresponding to where a charge was deposited ($c_j = -1$) or where a secondary was produced ($c_j = 1$). The factor r_c is used to normalize the charge deposition such that the total charge deposition (integration over all spatial dimensions) is unity.

Reflection and transmission fractions

Reflection and transmission fractions are typically calculated in thin slabs or semi infinite slabs when a particle exits through the left face (reflection) or through the right face (transmission). If a particle leaves the left face, the reflection tally is incremented by one, so after N source particles the reflection fraction is

$$r_c = \frac{1}{N} \sum_j f_r(x_j) \tag{4.44}$$

where

$$f_r(x_j) = \begin{cases} 1 & : x_j < 0 \\ 0 & : otherwise. \end{cases} \tag{4.45}$$

The transmission fraction is

$$t_c = \frac{1}{N} \sum_j f_t(x_j) \tag{4.46}$$

where

$$f_t(x_j) = \begin{cases} 1 & : x_j > L \\ 0 & : otherwise. \end{cases} \tag{4.47}$$

In this case, it is assumed that the left face of the slab is at $x = 0$ and the right face is at $x = L$ (that is, this is for a slab with thickness L).

4.4.3 Analog Monte Carlo calculations

In this section, several analog Monte Carlo calculations are presented to demonstrate the types of results of interest, along with the computational cost associated with these results. In most cases, the problem setup is a 1-D slab with a normally incident pencil beam on the left face and a vacuum boundary on the right face, as shown in Fig. 4.1. This is with exception of the longitudinal and lateral distributions that are obtained in an infinite medium.

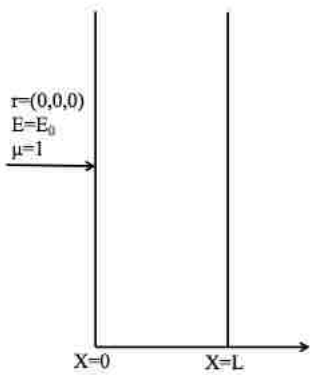

Figure 4.1: Problem schematic for analog calculation examples.

Table 4.1: Timing results for analog simulation of 10^6 1-MeV electrons normally incident on aluminum and gold slabs with varying thicknesses. The slab thicknesses presented in cm corresponds to aluminum slabs, while the gold slabs are roughly one-tenth the thickness of the aluminum slab. Note that the computer time scales roughly linearly for aluminum, while scaling non-linearly for gold.

Timing results for analog simulation		
Slab Thickness (mfp)	**Slab Thickness (cm)**	**CPU Time Al/Au (min)**
100	0.0019	6/7
300	0.0057	20/21
1000	0.019	72/100
3000	0.057	273/384

In Table 4.1, the computer times required for analog simulation of 10^6, 1-MeV electrons in aluminum and gold for varying slab thicknesses are presented. In general, the slab thickness in Table 4.1 are very small ($\sim mm - \mu m$), so this problem is not representative of the full spectrum of electron transport calculations. Even so, for this small sampling of calculations the computer times for the simulations with slab thicknesses $\sim mm$ are still on the order of one to six hours. This amount of computer time is impractical for routine calculations; especially, considering that these times are associated with just the transport of primary particles. That is, no secondaries were produced in these example calculations. Secondary production would only increase the amount of computer time required. The computer times associated with the aluminum slabs scale linearly. However, in gold, as the slab becomes thicker, inelastic collisions become more probable increasing the computer time. This is because as particles lose energy the mfp of the particle decreases and the particle suffers further collisions. Not to mention, inelastic collisions require a rejection technique that is more costly than direct sampling. In the following sections, several results associated with the computer times are provided to give a sense of typical results and how they behave.

Angular distributions

Reflected and transmitted angular distributions for 1-MeV electrons incident on 1-D aluminum and gold slabs with increasing thickness are presented in Figs. 4.2 and 4.3. In general, the angular distributions behave the same as a function of the target atomic number. However, in high-Z materials particles undergo larger-angle scattering because the DCS is less-peaked resulting in reflection distributions that are larger in magnitude and also transmission distributions that are less-peaked. In both aluminum and gold, the reflected angular distributions for slabs with thicknesses of 100 and 300 mfps are slightly anisotropic, but difficult to see because the slabs are so thin that most of the particles are transmitted before they can turn around. However, for the thicker slabs (1000 and 3000 mfps) the reflected angular distributions are mostly isotropic because the particles suffer numerous collisions before turning around; thus, spreading the distribution of angles significantly.

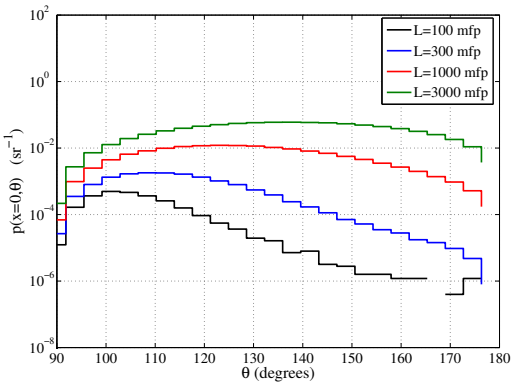

(a) Reflected Angular Distribution

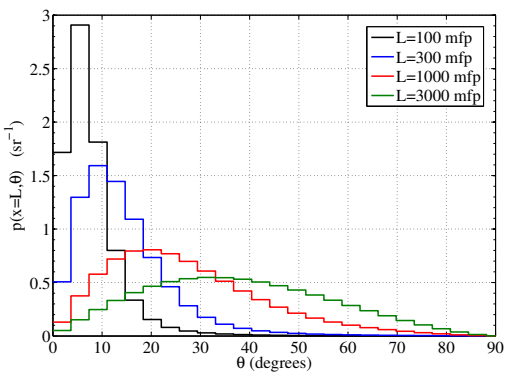

(b) Transmitted Angular Distribution

Figure 4.2: Reflected and transmitted angular distributions of 1000-keV electrons in aluminum slabs with thickness of 100, 300, 1000, and 3000 analog mfp.

The impact of elastic scattering is seen differently in the transmitted angular distributions because for thinner slabs particles undergo only enough collisions to slightly spread the initial singular state of the beam, while for thicker slabs particles

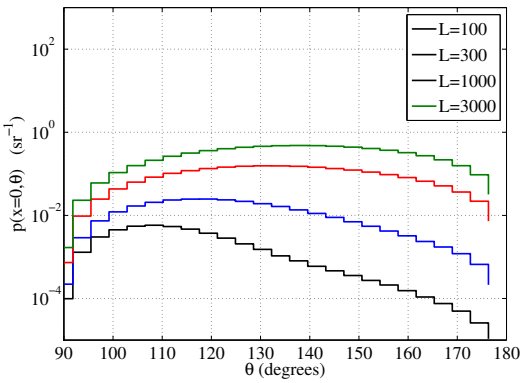

(a) Reflected Angular Distribution

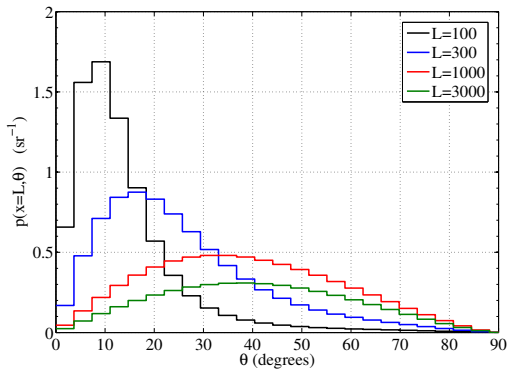

(b) Transmitted Angular Distribution

Figure 4.3: Reflected and transmitted angular distributions of 1000-keV electrons in gold slabs with thickness of 100, 300, 1000, and 3000 analog mfp.

suffer enough collisions that the beam is spread out significantly from its initial state resulting in a nearly isotropic distribution of angles.

Energy-loss spectra

Reflected and transmitted energy-loss spectra for 1-MeV electrons incident on 1-D aluminum and gold slabs with increasing thickness are presented in Figs. 4.4 and 4.5. Once again, the overall behavior of the reflected and transmitted energy-loss spectra is the roughly same as a function of the target atomic number. The exception being that more particles are reflected in gold and the magnitude of the reflected energy spectra are greater in gold, while the transmitted spectra are slightly lower in magnitude. As the thickness of the slab increases, particles suffer further inelastic collisions and the energy-loss spectra becomes smoother. This is true for both reflected and transmitted energy-spectra.

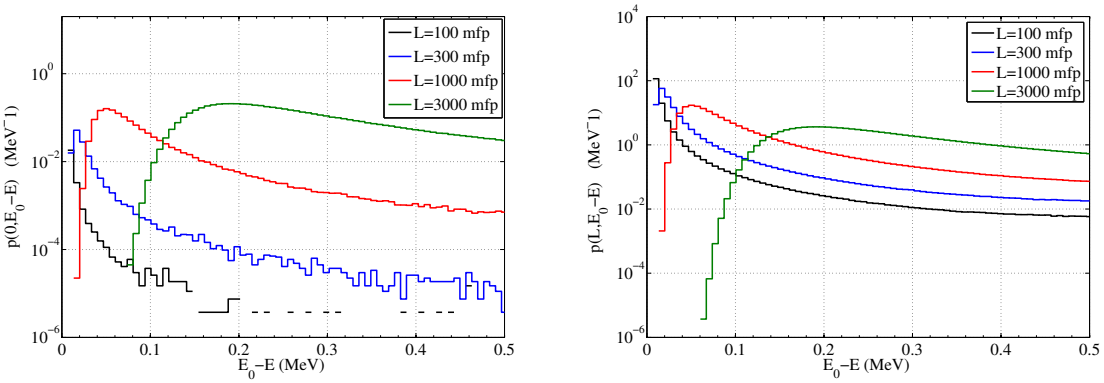

(a) Reflected Energy-Loss Spectra (b) Transmitted Energy-Loss Spectra

Figure 4.4: Reflected and transmitted energy-loss spectra for 1000-keV electrons in aluminum slabs with thickness of 100, 300, 1000, and 3000 analog mfp.

Longitudinal and lateral distributions

Longitudinal and lateral distributions for 1-MeV electrons in an infinite copper medium neglecting inelastic scattering are presented in Fig. 4.6. Longitudinal distributions give the displacement of the particle along the axis of the initial direction of the particle. This displacement is measured with respect to some maximum pathlength and is therefore between $-1 \leq z/s \leq 1$ for longitudinal distributions. As seen in Fig. 4.6a, for the thinnest slab (100 mfp) most particles stop between $0.95 < z/s \leq 1$ implying that after 100 collisions most particles are deflected incrementally from their initial direction. However, it is clearly possible for the occasional large angle scatter to result in particles traveling in directions opposite to their initial direction. As the slab thickens and particles suffer additional collisions, the longitudinal distribution smoothes out.

Lateral distributions give the displacement of the particle perpendicular to the axis of the initial direction of the particle. Again, this displacement is measured with respect to some maximum pathlength, but is between $0 \leq b/s \leq 1$ for lateral distributions because this is essentially a measure of the radius of a beam. In Fig. 4.6b

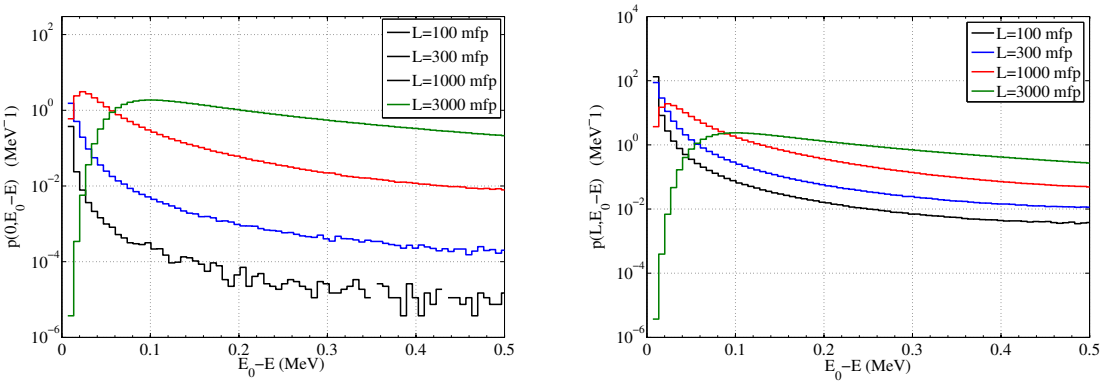

(a) Reflected Energy-Loss Spectra (b) Transmitted Energy-Loss Spectra

Figure 4.5: Reflected and transmitted energy spectra for 1000-keV electrons in gold slabs with thickness of 100, 300, 1000, and 3000 analog mfp.

the lateral distributions appear to be smoother than the longitudinal distributions.

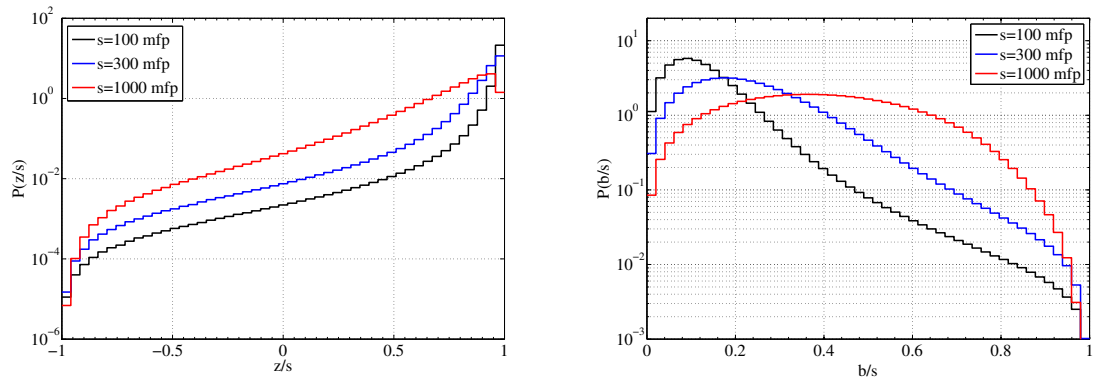

(a) Longitudinal Angular Distribution (b) Lateral Distribution

Figure 4.6: Longitudinal and lateral distributions of 1000-keV electrons in gold slabs with thickness of 100, 300, and 1000 analog mfp.

Dose deposition

Depth-dose profiles for 20-MeV electrons normally incident on 30 cm of water and 250-keV electrons normally incident on 0.008 cm of gold are presented in Fig. 4.7 In

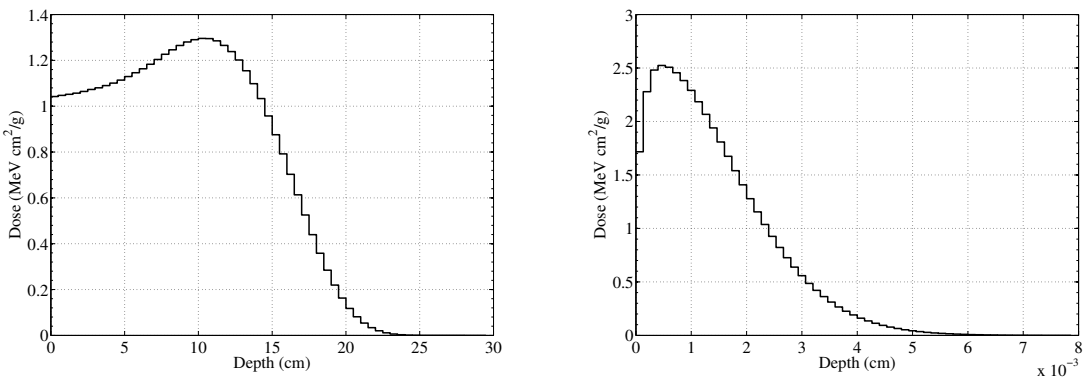

(a) 20000-keV electrons in water (b) 250-keV electrons in gold

Figure 4.7: Depth-dose profiles for 20000-keV electrons in water and 250-keV electrons in gold.

both Fig. 4.7a and Fig. 4.7b, the dose is a smooth function of position as opposed to depth-dose for protons and heavy ions containing a distinct Bragg peak. In Fig. 4.7a, the peak dose is roughly 10 cm into the slab because 20-MeV electrons mostly forward scatter at these energies; especially, in low-Z materials. In contrast, the peak dose in Fig. 4.7b is much closer to the source because the elastic scattering DCS is less anisotropic at 250-keV and backscattering is more pronounced in high-Z materials.

Charge deposition

Charge deposition profiles for 5-MeV and 10-MeV electrons normally incident on aluminum and gold slabs with thicknesses of $1.4r_0$ are presented in Fig. 4.8, where r_0 is the CSDA range. The impact of atomic number and particle energy is seen in Figs. 4.8a and 4.8b, where for low-Z materials secondaries produced near the source penetrate deeper into the slab and are less-likely to back-scatter and recombine in the regions where they were produced (that is, near $z/r_0 = 0$). For this reason, Fig. 4.8a is negative in the first several cells as opposed to Fig. 4.8b. The charge deposition

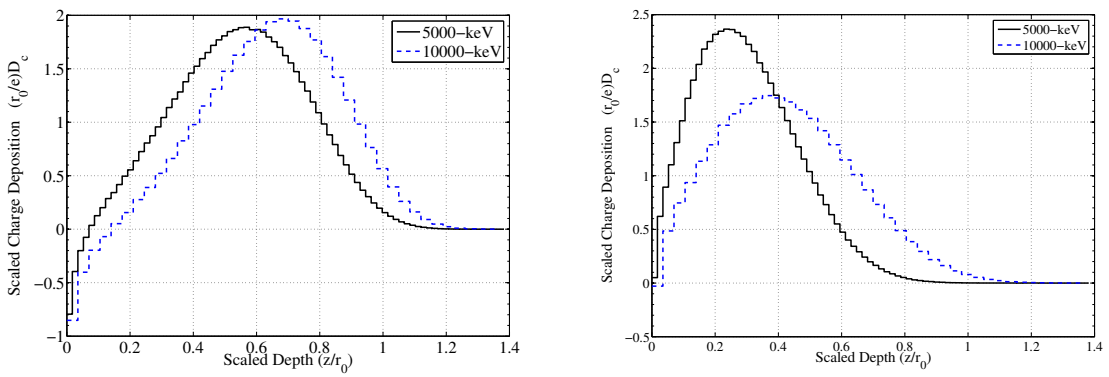

(a) Aluminum (b) Gold

Figure 4.8: Charge deposition for 5000-keV and 10000-keV electrons in aluminum and gold.

profile in Fig. 4.8b is only slightly negative for 10-MeV electrons. In general, with increasing source particle energy higher energy secondaries are produced carrying dose further into the slab. As a result, the peak charge deposition is shifted deeper into the slab.

Reflection and transmission fractions

Reflection and transmission fractions for 1-MeV electrons incident on 1-D aluminum and gold slabs with increasing thickness are presented in Table 4.2. As expected, nearly all of the electrons are transmitted in slabs with thicknesses of 100 to 300 mfps. However, with increasing thickness more particles are reflected; especially, in gold as particles are more likely to back-scatter. Clearly, reflection and transmission do not sum to one in all cases because some particles are absorbed in the slab.

CEASE telescope response function calculation

The Compact Environmental Anomaly Sensor (CEASE) was built as a space particle radiation environment monitoring and warning system [1]. In particular, CEASE monitors the radiation environment through measuring the energy spectra. In Fig. 4.9, the CEASE telescope is presented which is used to measure energy spectra. The major components of the CEASE telescope include the collimator and the front silicon detector (DFT) and the back silicon detector (DBT). Particles enter the telescope through the collimator and deposit energy in both DFT and DBT. The energy deposited in each detector is mapped to a channel determined according to the energy deposition matrix in Fig. 4.10.

CEASE does not measure energy spectra directly, but rather measures raw counts in response to electrons above ∼50-keV. To obtain energy spectra, one must relate the raw counts to the spectra through the response function in the following integral equation

$$C_i = \int_0^\infty R_i(E)\phi(E)dE, \tag{4.48}$$

where C_i is the count rate (counts/sec.) for the ith channel, $R_i(E)$ is the response of the ith channel to particles with energy E, and $\phi(E)$ is the energy spectra. The

Slab Thickness	**Material**	**Reflection**	**Transmission**
100 mfp	aluminum	0.0002±0.1	0.99979±0.00002
	gold	0.003±0.02	0.99715±0.00005
300 mfp	aluminum	0.0009±0.03	0.99964±0.00004
	gold	0.017±0.007	0.9825±0.0001
1000 mfp	aluminum	0.009±0.009	0.982±0.0001
	gold	0.138±0.002	0.855±0.004
3000 mfp	aluminum	0.041±0.005	0.701±0.001
	gold	0.370±0.001	0.470±0.001

Table 4.2: Reflection and transmission fractions with relative uncertainties for 1-MeV electrons normally incident on aluminum and gold slabs with thicknesses of 100, 300,1000, and 3000 mfps.

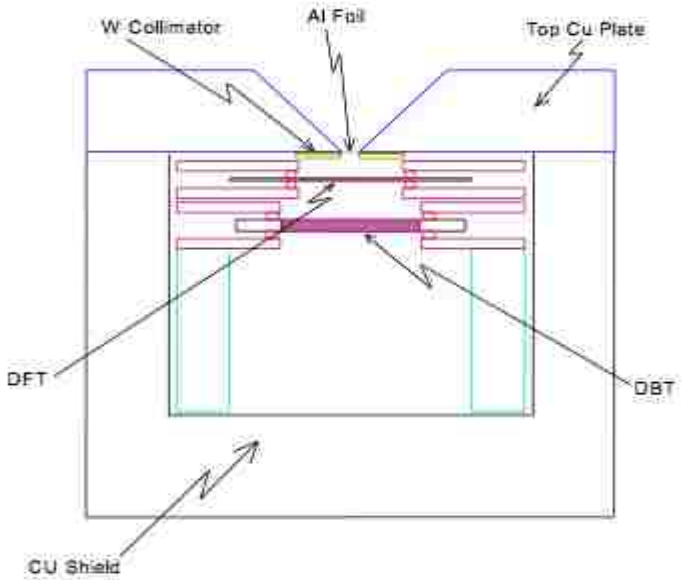

Figure 4.9: Schematic of the CEASE telescope used to measure energy spectra [1].

response function (cm^2sr),

$$R_i(E) = 2\pi \int_0^{\theta_{max}} A_i(E,\theta) \sin\theta d\theta, \tag{4.49}$$

is an integral of the effective area, $A_i(E,\theta)$, over all angles. The effective area is either measured in the laboratory or calculated using a particle transport code. That is,

$$A_i(E,\theta) = \frac{N_D^i(E,\theta,\varepsilon_{DFT},\varepsilon_{DBT})}{\rho_S} \cos\theta, \tag{4.50}$$

where $N_D^i(E,\theta,\varepsilon_{DFT},\varepsilon_{DBT})$ is the number of hits in the CEASE detector with energy ε_{DFT} deposited in the front detector and ε_{DBT} deposited in the back detector, $\rho_s = \frac{N_s}{A_s}$ is the source density, N_s is the total number of particles simulated, and A_S is the area of a disc source. Here, $N_D^i(E,\theta,\varepsilon_{DFT},\varepsilon_{DBT})$ is calculated using a Monte Carlo transport code and then some post-processing is used to carry out the integral in Eq. (4.49).

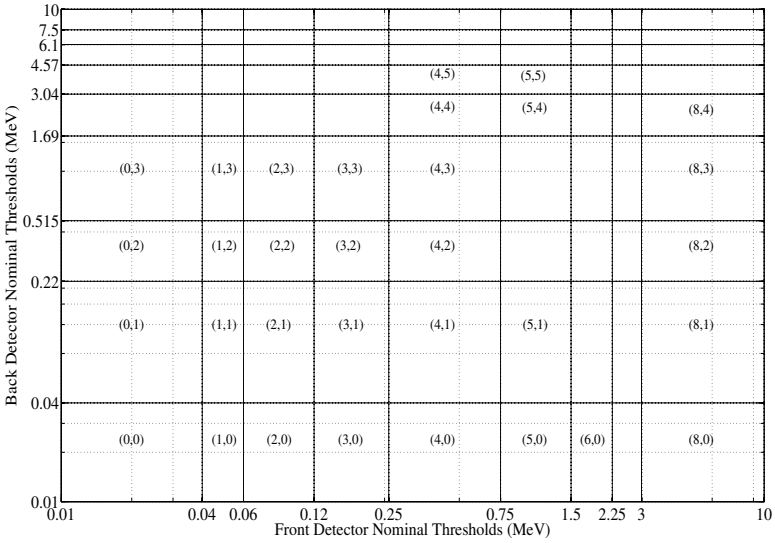

Figure 4.10: CEASE telescope energy threshold matrix with channel labels [1].

In this section, the total response due to N channels or

$$R(E) = 2\pi \sum_{i=1}^{N} \int_0^{\theta_{max}} A_i(E,\theta) \sin\theta d\theta, \tag{4.51}$$

is reported. To generate the total response, electrons with 62 different source energies at 19 different source angles were simulated. The energy deposition matrix for each source configuration was stored and processed. The result is given in Fig. 4.11. The total response indicates the energy range for which the detector is responsive. An ideal response is flat over all energies of interest. In Fig. 4.11, there is a lower energy bound below which detector response is negligible and an upper energy bound above which electrons fully penetrate the collimator and saturate the detector. To complete a response function calculation 1116 different simulations were run with 30000 source particles each. The total simulation time was 1380 processor-days. Of course, this was divided among hundreds of cores making the computational cost manageable.

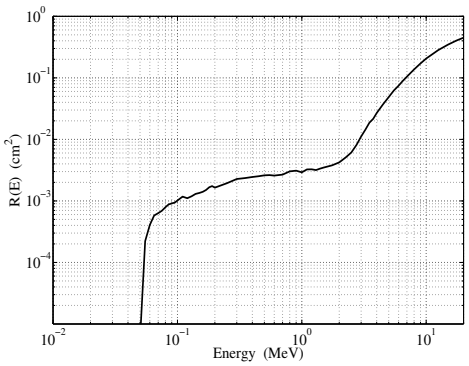

Figure 4.11: Response function generated using the partial-wave elastic DCS. Inelastic physics, positron physics, and photon physics are given by the default Geant4 physics with EM option 3.

Chapter 5

Differential Cross-Section Moments

In this chapter, the concept of a mathematical moment is developed. Given a general understanding of the information contained in a moment, the elastic and inelastic moments are again defined. With these definitions, the importance of moments within the context of electron transport is demonstrated. As previously discussed (see Chapter 3), it is possible to understand the importance of the lowest order moments through their physical interpretation. However, beyond low order moments it is difficult to make a physical connection; therefore, we must rely on mathematical interpretations where physical interpretations are not possible.

In mathematics, a moment is a specific quantitative measure of the shape of a set of points used in statistics. Moreover, one can reconstruct a distribution given the information contained in the moments of that distribution. Take for example the normal distribution or

$$f(x, \bar{\mu}, \sigma) = \frac{1}{\sigma\sqrt{2\pi}} e^{-\frac{(x-\bar{\mu})^2}{2\sigma^2}}, \tag{5.1}$$

where $\bar{\mu}$ is the mean and σ^2 is the variance as seen in Fig. 5.1. A normal distribution

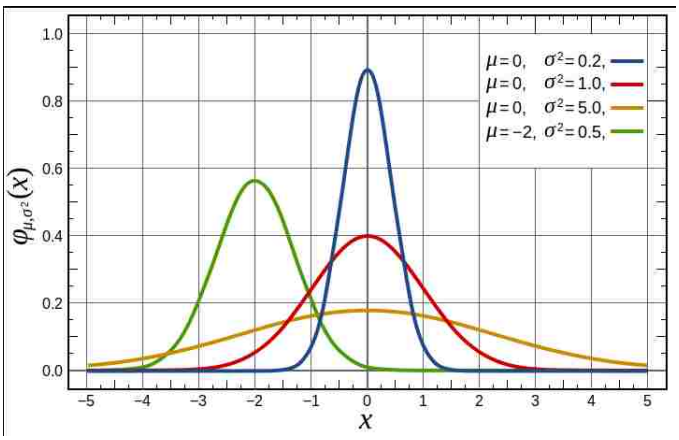

Figure 5.1: The normal distribution.

is completely specified by the mean, $\bar{\mu}$, and the variance, σ^2.

The role of moments is perhaps easier to understand in a mathematical context. It is then possible to extend these ideas to understanding the importance of moments of the analog DCS. To begin, the central moments, or moments of a probability distribution about the mean, are given by

$$\mu_n = \int_{-\infty}^{\infty} (x - \bar{\mu})^n f(x) dx. \tag{5.2}$$

Given the definition of the normal distribution and the central moments, the zeroth moment ($n = 0$) is defined. The zeroth moment gives the total area under a curve. By definition, all probability distributions are normalized such that the zeroth moment is unity. Therefore, the zeroth moment of the normal distribution is

$$\mu_0 = \int_{-\infty}^{\infty} \frac{1}{\sigma\sqrt{2\pi}} e^{-\frac{(x-\bar{\mu})^2}{2\sigma^2}} dx = 1. \tag{5.3}$$

In words, the zeroth moment is the probability that any possible outcome will occur and, therefore, must be one. The first central moment or the mean is given by

$$\mu_1 = \bar{\mu} = \int_{-\infty}^{\infty} (x - \bar{\mu}) \frac{1}{\sigma\sqrt{2\pi}} e^{-\frac{(x-\bar{\mu})^2}{2\sigma^2}} dx. \tag{5.4}$$

The mean provides the central tendency of a probability distribution and because the normal distribution is symmetric, the distribution is centered about the mean.

The second central moment or the variance is given by

$$\mu_2 = \sigma^2 = \int_{-\infty}^{\infty} (x - \bar{\mu})^2 \frac{1}{\sigma\sqrt{2\pi}} e^{-\frac{(x-\bar{\mu})^2}{2\sigma^2}} dx \tag{5.5}$$

and provides a measure of the width of the distribution. As described by Eq. (5.1), the normal distribution can be reconstructed with the mean and the variance or the first and second moments. The third central moment or the skewness is given by

$$\mu_3 = \int_{-\infty}^{\infty} (x - \bar{\mu})^3 \frac{1}{\sigma\sqrt{2\pi}} e^{-\frac{(x-\bar{\mu})^2}{2\sigma^2}} dx = 0, \tag{5.6}$$

and is, of course, zero because the normal distribution is symmetric. The forth central moment or the kurtosis is given by

$$\mu_4 = \int_{-\infty}^{\infty} (x - \bar{\mu})^4 \frac{1}{\sigma\sqrt{2\pi}} e^{-\frac{(x-\bar{\mu})^2}{2\sigma^2}} dx = 3\sigma^4, \tag{5.7}$$

and is a measure of whether a distribution is tall and skinny or short and squat. Higher-order moments, beyond kurtosis or the fourth central moment, are generally interpreted as estimations of further shape parameters used to capture a distribution. However, it is difficult to describe exactly how these higher order terms impact a distribution. That is not to say that these moments can simply be neglected or do not play an important role.

Observations similar to those made of moments of the normal distribution can be extended to electron transport and the physics associated with elastic and inelastic scattering. In general, the moments with clear physical interpretations include the zeroth, first, and second moments, which are referred to as the total cross-section (elastic and inelastic), the transport cross-section or the mean scattering angle (elastic), the stopping power or the mean energy-loss per unit distance (inelastic), the mean-square scattering angle (elastic), and energy straggling or the mean-square energy-loss (inelastic).

5.1 Elastic DCS Moments

Herein, we define Legendre moments of the elastic DCS as

$$\Sigma_{el,\ell} = 2\pi \int_{-1}^{1} P_l(\mu_0)\Sigma_{el}(E,\mu_0)d\mu_0, \tag{5.8}$$

and the momentum transfer moments as

$$G_\ell = 2\pi \int_{-1}^{1} \left[1 - P_l(\mu_0)\right] \Sigma_{el}(E,\mu_0)d\mu_0 = \Sigma_{el,0} - \Sigma_{el,\ell}, \tag{5.9}$$

which are given in Figs. 5.2a and 5.2b respectively for electrons with energies of 1-keV, 100-keV, and 10000-keV colliding with aluminum and gold nuclei. In general, the Legendre moments in Fig. 5.2a decrease with increasing order. For lower energies (the dash curve) the rate of decrease is more rapid than for the higher energies (the dash-dot curve). This behavior is a result of the shape of the elastic DCS. At higher energies, the DCS is highly peaked; therefore, the moments decay slowly. The slow decay of the moments implies that a staggering number of moments (perhaps hundreds of thousands) are required to reconstruct this distribution. Contrast this behavior with that of a delta function that requires an infinite number of terms for reconstruction. That is to say, these distributions are nearly singular like a delta function. At lower energies, the DCS is less peaked; therefore, the moments decay rapidly. An alternative interpretation of the behavior of the moments is given by the momentum transfer moments in Fig. (5.2b). The momentum transfer moments are the difference between the zeroth moment and the ℓ^{th} moment. For 10000-keV electrons in aluminum and gold this difference is very small for the low order moments; especially, when compared to the zeroth moment (about 10^8 to 10^9 barns). For this reason, one can also conclude that many of these moments contribute significantly when reconstructing, for example, the Goudsmit-Saunderson distribution [32, 33] (up to 240 momentum transfer moments are typically used). The Goudsmit-Saunderson distribution is discussed in the following section.

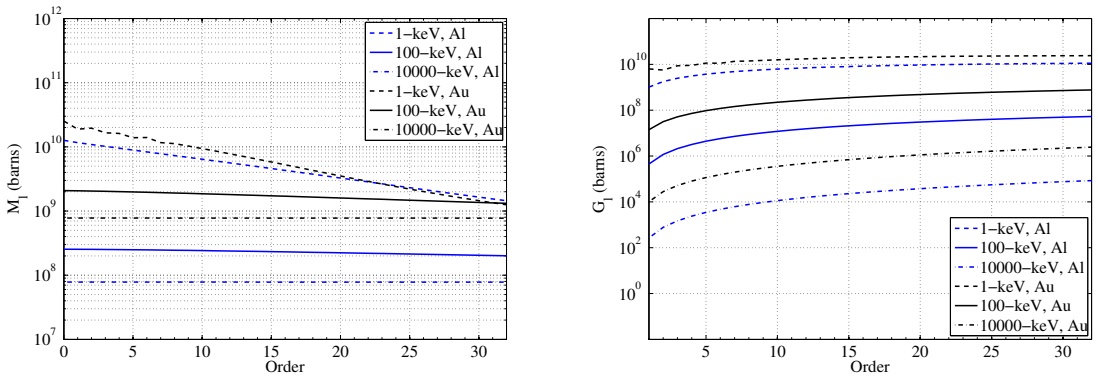

(a) Legendre Moments

(b) Momentum Transfer Moments

Figure 5.2: Legendre moments and momentum transfer moments of the Partial-wave differential cross-section for elastic collisions with aluminum and gold nuclei..

5.2 Inlastic DCS Moments

Herein, we define energy-loss moments of the inelastic DCS as

$$Q_k = \int_{Q_{min}}^{Q_{max}} Q^k \Sigma_{in}(E, Q) dQ. \tag{5.10}$$

The first seven energy-loss moments are given in Fig. 5.3 as a function of energy. At lower energies, the moments appear to decay; however, energy-loss moments are asymptotic. That is, beyond a specific order for all energies, the moments begin to grow without bound, which is clear in Fig. 5.3 at higher energies where the higher-order moments begin to grow larger than the lower order moments. This implies that for higher energies the higher-order moments are more important than for lower energies. In fact, for energies greater than roughly 7-MeV, the straggling coefficient Q_2 is as large as the stopping power Q_1, which would imply that these processes contribute equally at these energies. In other words, at higher energies particles suffer numerous collisions resulting in small energy losses, which can be described by the continuous slowing down approximation through the stopping power. However, occasional large energy losses do occur that contribute significantly to the solution.

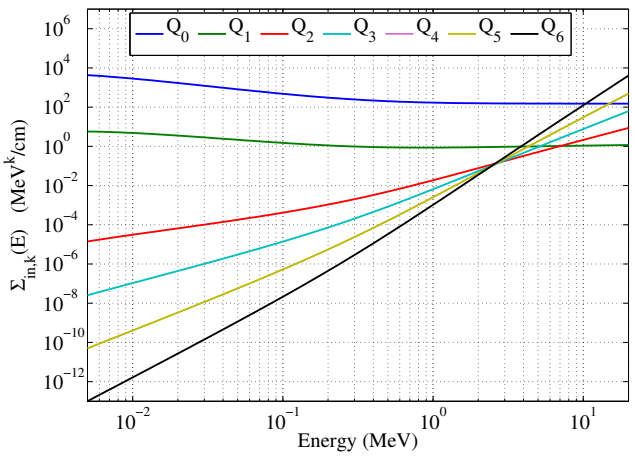

Figure 5.3: Energy-loss moments of the Möller differential cross-section for inelastic collisions with aluminum and gold atomic electrons.

5.3 Goudsmit-Saunderson Distribution

To illustrate the role of the momentum transfer moments and by extension the Legendre moments, we turn to a pathlength solution to an infinite medium transport equation where particles only undergo elastic scattering. That is,

$$\frac{\partial}{\partial s}\psi(s,\mu) = 2\pi \int_{-1}^{1} \Sigma_{el}(E,\mu_0)\psi(s,\mu')d\mu_0 - \Sigma_{el,0}(E)\psi(s,\mu), \tag{5.11}$$

with

$$\psi(0,\mu) = \frac{\delta[\mu-\mu^*]}{2\pi} \tag{5.12}$$

Eq. 5.11 is solved in a typical fashion by expanding the solution ψ in terms of Legendre polynomials

$$\psi(s,\mu) = \sum_{\ell=0}^{\infty} \frac{2\ell+1}{4\pi}\varphi_\ell(s)P_\ell(\mu), \tag{5.13}$$

where $P_\ell(\mu)$ is a Legendre polynomial of order ℓ and

$$\varphi_\ell(s) = 2\pi \int_{-1}^{1} P_\ell(\mu)\psi(s,\mu)d\mu. \tag{5.14}$$

The DCS is also expanded in terms of Legendre polynomials

$$\Sigma_{el}(E,\mu_0) = \sum_{\ell=0}^{\infty} \frac{2\ell+1}{4\pi} \Sigma_{el,\ell}(E) P_\ell(\mu_0), \tag{5.15}$$

and $\Sigma_{el,\ell}$ is given by Eq. (5.8). After substituting these expansions and some algebra, the following result is obtained

$$\psi(s,\mu) = F_{GS}(s,\mu) = \sum_{\ell=0}^{\infty} \frac{2\ell+1}{4\pi} e^{-sG_\ell} P_\ell(\mu) P_\ell(\mu^*). \tag{5.16}$$

Though Eq. (5.16) is limited in applicability, it is a clear illustration of the role played by the analog DCS moments in electron transport. The solution, which depends on s, μ, and ℓ, is constructed directly by the moments. The number of moments required to construct the distribution depends on the product sG_ℓ. For short pathlengths and highly peaked scattering, a large number of moments are required because the product sG_ℓ is small. As the pathlength grows longer making sG_ℓ larger, less terms are required. For highly-peaked scattering, sG_ℓ is small regardless of the size of the pathlength because the momentum-transfer moments are very small, so a large number of terms are required. For nearly isotropic scattering, the momentum-transfer moments are larger and sG_ℓ becomes large after a few terms. The pathlength dependence is connected to the momentum-transfer moments in the sense that the solution or the angular distribution is more peaked for short pathlengths because the particles are not deflected significantly from their initial direction (this is illustrated in Fig. 5.4) and therefore requires a larger number of momentum transfer moments to resolve the distribution (unless scattering is nearly isotropic). However, for sufficiently long pathlengths fewer momentum transfer moments may be necessary.

5.4 Lewis Theory

An even stronger link between analog DCS moments and solutions to the transport equation is a result due to Lewis [43]. Lewis showed that space-angle moments of the

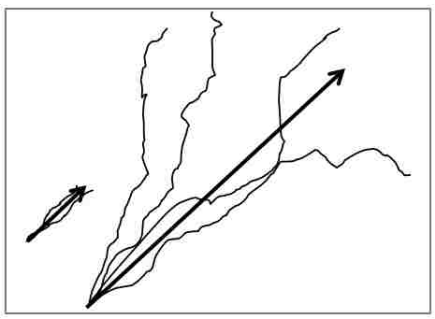

Figure 5.4: Hypothetical paths traveled by electrons.

solution only depend on momentum transfer moments of the analog DCS. In other words, Lewis theory is a statement of equivalence between preservation of space-angle moments of the solution and Legendre moments of the analog DCS. Here this result is derived in 1-D to illustrate the relationship between space-angle moments of solutions to the transport equation and Legendre moments of the analog DCS for elastic scattering.

We begin by writing down an infinite homogeneous medium transport equation in 1-D, planar geometry for mono-energetic electrons or

$$\frac{\partial}{\partial s}\psi(s,z,\mu)+\mu\frac{\partial}{\partial z}\psi(z,z,\mu)=2\pi\int_{-1}^{1}\Sigma_{el}(E,\mu_0)\psi(s,z,\mu')d\mu_0-\Sigma_{el,0}(E)\psi(s,z,\mu), \tag{5.17}$$

with the following initial condition

$$\psi(0,z,\mu)=\delta(z)\frac{\delta(\mu-1)}{2\pi} \tag{5.18}$$

We then define spatial moments of the solution as

$$\varphi_n=\int_{-\infty}^{\infty}dz\ z^n\psi(s,z,\mu). \tag{5.19}$$

If we take z^n moments of Eq. 5.17, we have

$$\frac{\partial}{\partial s}\varphi_n(s,\mu)-\mu\varphi_{n-1}(s,\mu)=2\pi\int_{-1}^{1}\Sigma_{el}(E,\mu_0)\varphi_n(s,\mu)d\mu_0-\Sigma_{el,0}(E)\varphi_n(s,\mu), \tag{5.20}$$

with

$$\varphi_n(0,\mu) = \delta_{n0}\frac{\delta(\mu-1)}{2\pi}. \tag{5.21}$$

We now define mixed spatial and Legendre moments of the solution as

$$\varphi_{mn} = 2\pi\int_{-1}^{1} d\mu \int_{-\infty}^{\infty} dz\ z^n P_m(\mu)\psi(s,z,\mu), \tag{5.22}$$

expand the elastic DCS

$$\Sigma_{el}(E,\mu_0) = \sum_{\ell=0}^{\infty}\frac{2\ell+1}{4\pi}\Sigma_{el,\ell}P_\ell(\mu')P_\ell(\mu), \tag{5.23}$$

and take Legendre moments of Eq. (5.20) which gives

$$\frac{\partial}{\partial s}\varphi_{nm}(s) + \Sigma_{el,0}(E)\varphi_{nm}(s,\mu) = \Sigma_{el,\ell}\varphi_{nm}(s) + 2\pi\int_{-1}^{1}\mu P_m(\mu)\varphi_{n-1}(s,\mu). \tag{5.24}$$

Rearranging Eq. (5.24) and using properties of Legendre polynomials to expand $\mu P_m(\mu)$ gives

$$\frac{\partial}{\partial s}\varphi_{nm}(s) + G_m\varphi_{nm}(s,\mu) = n\left[\frac{m}{2m+1}\varphi_{n-1,m-1}(s) + \frac{m+1}{2m+1}\varphi_{n-1,m+1}(s)\right], \tag{5.25}$$

for $n, m = 0, 1, 2, ...$, where $\phi_{nm}(0) = \delta_{n0}$. The general solution to Eq. (5.25) is

$$\varphi_{mn}(S) = \delta_{n0}e^{-sG_m} + n\int_0^s ds' e^{-G_m(s-s')}\left[\frac{m}{2m+1}\varphi_{n-1,m-1}(s') + \frac{m+1}{2m+1}\varphi_{n-1,m+1}(s')\right]. \tag{5.26}$$

One cannot obtain a solution to Eq. (5.17) given the Lewis moments. One can show that the mixed spatial and Legendre moments of the solution, which can be related to space-angle moments of the solution, only depend on G_m. This relationship is the important result from Lewis theory. To do so, we begin by setting $n = 0$ which gives

$$\varphi_{m0}(S) = e^{-sG_m}. \tag{5.27}$$

This is the result from the Goudsmit-Saunderson section and shows that Legendre moments of the solution depend only on G_m and s. By setting $n = 1$ we have

$$\varphi_{mn}(S) = \int_0^s ds' e^{-G_m(s-s')} \left[\frac{m}{2m+1} e^{-s'G_{m-1}} + \frac{m+1}{2m+1} e^{-s'G_{m+1}} \right], \tag{5.28}$$

which depends only on G_{m-1}, G_m, G_{m+1}, and s. By induction, ϕ_{nm} must depend on G_{n+m},...,G_{n-m}, and s. It is easy to show that the mixed spatial and Legendre moments φ_{nm} are related to space-angle moments of the solution Φ_{nm}, which are given by

$$\Phi_{mn} = 2\pi \int_{-1}^{1} d\mu \int_{-\infty}^{\infty} dz \; z^n \mu^m(\mu) \psi(s, z, \mu), \tag{5.29}$$

Therefore, what we have shown is that space-angle moments of the solution depend on momentum transfer moments of the DCS.

The significance of this result is understood by considering two different transport equations: the analog transport equation which gives the exact solution and an approximate transport equation that gives an approximate solution with respect to the exact analog solution. The analog transport equation has a DCS $\Sigma_{el}(\mu)$, momentum transfer moments G_m, and space angle moments Φ_{nm}, while the approximate transport equation has a DCS $\tilde{\Sigma}_{el}(\mu)$, momentum transfer moments $\tilde{G}_m$, and space angle moments $\tilde{\Phi}_{nm}$. If the analog and approximate DCS are related such that $G_m = \tilde{G}_m$ for $m = 1, 2, ..., M$ and $G_m \neq \tilde{G}_m$ for $m > M$, then it is also true that $\Phi_{nm} = \tilde{\Phi}_{nm}$ for $n + m = M$. Therefore, Lewis theory provides a strong connection between preservation of momentum transfer moments and accuracy of an approximation.

In addition, a Lewis-like theory was shown for energy straggling [44], where the equation for energy loss of a beam of charged particles traversing a target medium is given by

$$\frac{\partial}{\partial s}\psi(s, E) = \int_0^{\infty} \Sigma_{in}(E' \to E)\psi(s, E')dE' - \Sigma_{in,0}(E)\psi(s, E), \; 0 < s < T \tag{5.30}$$

with initial condition

$$\psi(0, E) = \delta[E_0 - E]. \tag{5.31}$$

In Eq. (5.30), s is the distance travelled by a particle, E is the particle energy, $\psi(s, E)$ is the solution or the energy spectrum, and Σ_{in} and $\Sigma_{in,0}$ are the DCS and total cross-section respectively. Similar to obtaining the result from Lewis theory, we define energy moments of the solution as

$$I_k(s) = \int_0^\infty E^k \psi(s, E) dE, \tag{5.32}$$

and then relate these moments to the energy-loss moments from Eq. (3.38). The resulting theorem states that if the energy-loss moments from Eq. (3.38) for the analog and approximate problem satisfy $Q_k = \tilde{Q}_k$ for $k = 1, 2, ..., K$ for some finite K then $\tilde{\psi}(S, E)$ is an N^{th}-order moment-preserving approximation to $\psi(s, E)$ in the sense that

$$\int_0^\infty E^k [\psi(s, E) - \tilde{\psi}(s, E)] dE = 0, \ n = 1, 2, ..., N \tag{5.33}$$

where $\tilde{\psi}(s, E)$ is the approximate solution with an approximate DCS $\tilde{\Sigma}_{el}(E' \to E)$.

5.5 Eigenvalues of the Elastic Collision Operator

Eigenvalues have a wide variety of applications. In the context of operators, eigenvalues can be used to characterize or understand the properties of an operator. For elastic collision operator, one finds that the eigenvalues are bounded, therefore, the operator is stable. Moreover, it of interest to develop approximate operators and one can get a sense of the accuracy of an approximate operator by comparing the eigenvalues of the approximation to the eigenvalues of true operator. That said, the eigenvalues of the elastic collision operator are related to the moments of the elastic

DCS. Therefore, in a completely different context, yet again we see the necessity of moment-preservation. To be clear, we derive an expression for the eigenvalues of the elastic collision operator given by

$$H_{el}\psi = 2\pi \int_{-1}^{1} d\mu' \Sigma_{el}(E, \mu_0)\psi(E, \mu') - \Sigma_{el,0}(E)\psi(E, \mu) = \lambda\psi(E, \mu). \tag{5.34}$$

We begin by defining Legendre moments of the solution as

$$\varphi_\ell(E) = 2\pi \int_{-1}^{1} d\mu P_\ell(\mu)\psi(E, \mu), \tag{5.35}$$

and expand the DCS in term of Legendre polynomials

$$\Sigma_{el}(E, \mu_0) = \sum_{\ell=0}^{\infty} \frac{2\ell + 1}{4\pi} \Sigma_{el,\ell} P_\ell(\mu')P_\ell(\mu). \tag{5.36}$$

Now, Eq. (5.36) is substituted into Eq. (5.34) and the left-hand side is rearranged such that Eq. (5.35) can be substituted or

$$\lambda\psi(E, \mu) = \sum_{\ell=0}^{\infty} \frac{2\ell + 1}{2} \Sigma_{el,\ell} P_\ell(\mu) \int_{-1}^{1} d\mu' P_\ell\psi(E, \mu') - \Sigma_{el,0}(E)\psi(E, \mu). \tag{5.37}$$

We then apply orthogonality

$$2\pi \int_{-1}^{1} d\mu P_m(\mu) \left[\lambda\psi(E, \mu) = \sum_{\ell=0}^{\infty} \frac{2\ell + 1}{2} \Sigma_{el,\ell} P_\ell(\mu)\varphi_\ell(E) - \Sigma_{el,0}(E)\psi(E, \mu) \right], \tag{5.38}$$

and obtain

$$\lambda_m \varphi_m(E) = -\left[\Sigma_{el,0}(E) - \Sigma_{el,m}(E)\right] \varphi_m(E), \tag{5.39}$$

In Eq. (5.39),

$$\lambda_m = -\left[\Sigma_{el,0}(E) - \Sigma_{el,m}(E)\right] \tag{5.40}$$

are the eigenvalues and equal to the momentum-transfer moments defined by Eq. (5.9) (presented in Fig. 5.2b) and $\varphi_m(E)$ are the associated eigenfunctions. Now if one were to obtain an approximation to Eq. (5.34), a comparison of the eigenvalues of the approximate and exact operator provides a measure the accuracy of the

approximation. Moreover, if one were to simply approximate the DCS and, in turn, the operator, then one must ensure that the approximate DCS preserves as many moments of the analog DCS as reasonably possible. That said, the accuracy of the approximate operator is difficult to measure irrespective of the problem to which the operator is applied. That is, when calculating dose in thick targets, one can expect to reasonably approximate the elastic collision operator with an operator that only preserves a relatively small number of eigenvalues. However, calculating differential distributions in angle in thin targets may require preservation of a large number of eigenvalues.

A similar analysis for the inelastic collision operator is not possible because it is not possible to determine the eigenvalues of this operator. However, the Lewis-theory for energy straggling is sufficient to suggest that an accurate approximate inelastic operator consists of a moment-preserving scattering kernel.

Chapter 6

The Condensed History Method

In this chapter, the condensed history (CH) method for electron transport is reviewed. This includes an introduction to the CH method, an outline of the CH class I and class II algorithms and the limitations associated with these schemes.

Berger describes CH as an alternative approach to direct simulation of Coulomb scattering, in which the diffusion process is imitated by letting the particles carry out an (artificially constructed) random walk, each step of which takes into account the combined effect of many collisions [2]. This artificially constructed random walk is typically referred to as a *step* and on the order of hundreds of analog mfps making the calculation more efficient. However, by extending the distances between collisions to a step-size, the analog DCS is no longer valid. Therefore, one typically replaces the DCSs with the corresponding multiple scattering and energy-loss straggling theories that are solutions to transport equations requiring severe restrictions necessary for analytical treatment. That is, without making simplifying assumptions it would be impossible to obtain a useful solution to the transport equation. Use of multiple scattering and energy-loss straggling distributions rather than a DCS, in effect, requires an operator split procedure [39], where one is now approximating the solution

to the transport equation.

As a result of applying multiple scattering and energy-loss straggling distributions and the operator split procedure, CH suffers from inherent limitations. In particular, these limitations are due to application of multiple scattering and energy-loss straggling distributions outside of the conditions for which multiple scattering and energy-loss straggling theory is valid and a deterministic error resulting from the operator split procedure necessary to utilize multiple scattering theory. These limitations are a result of some or all of the following assumptions required for analytical treatment:

- infinite medium;
- negligible energy-loss;
- negligible angular deflection;
- small-angle approximation;
- no spatial correlation.

Some specific examples of commonly used multiple scattering and energy-loss straggling theory and the associated limitations are now provided.

First, multiple scattering theories due to Molière [66] and Goudsmit-Saunderson [32, 33] are discussed. The Molière distribution is typically found in CH algorithms where multiple-scattering distributions are required for randomly sampled steps. The form of the Molière distribution, a universal function of a scaled angular variable, makes it ideal for such CH algorithms. However, the small-angle approximation is required to obtain the Molière distribution and is limited to deflections of no more than about 20 degrees. In addition, spin and relativistic effects are not taken into account and the distribution is restricted to at least roughly 100 elastic collisions, which

can be difficult to satisfy with the CH algorithm [71]. The Goudsmit-Saunderson distribution is more complicated for sampling purposes, but it is not restricted by the small-angle approximation and in theory, it is not restricted to steps of at least roughly 100 elastic collisions[1]. Also, the Goudsmit-Saunderson distribution can be applied to any DCS for which moments up to an arbitrary order can be generated. However, this all comes at a price because the Goudsmit-Saunderson distribution must be stored for predetermined steps because it is impractical to apply to randomly sampled steps. Ultimately, this results in a significantly different CH algorithm from the CH algorithm associated with the Molière distribution. Regardless of the type of multiple-scattering distribution, the distributions are only valid for an infinite medium and though one can account for energy dependence through the CSDA, this solution does not provide any information about the distribution of energies after a step. Therefore, the multiple-scattering distributions are limited to angular information for particles with steps s in an infinite medium where energy-loss is, at most, accounted for in a CSD fashion. Furthermore, space-angle correlations are not directly accounted for in multiple-scattering distributions, so when a particle is forced to travel a distance s in a straight path some error in the longitudinal and lateral displacement is incurred.

Another example includes the Landau distribution for multiple excitations and ionizations [34] or energy-loss straggling. The Landau distribution, accounts for the energy lost after traveling a distance s. However, Landau theory takes into account only the mean value, but not the higher moments, of the cross section for small energy transfers [71]. The Blunck-Leisegang correction [72] takes into account the correct second moment and consists of convoluting the Landau distribution with a Gaussian distribution with a zero mean value and with the appropriate variance [71]. Even then, the "appropriate" variance is not necessarily a straightforward quantity

[1]In practice, the numerics required to generate the Goudsmit-Saunderson distribution struggle with sufficiently small steps [42]

and there are various procedures for estimating it. As a result of the condition for the applicability of Landau theory, the step-size is required to be longer than desirable for the sampling of the multiple elastic scattering distributions. In addition, by extending the distance traveled by an electron, secondary production is no longer sampled directly and must be accounted on an average basis. As an alternative to Landau theory, it is possible to separate inelastic collisions into "soft" collisions (with large impact parameters[2] and small momentum transfers and energy losses) and "hard" collisions (with small impact parameters and large momentum transfers and energy losses). Typically, an energy cut-off is selected below which collisions are considered soft and the CSDA is applied. Above the cut-off collisions are considered hard and an inelastic DCS is used to sample energy loss and subsequent secondary production. With this treatment, secondary production is captured exactly and random sampling of steps is possible.

Given the multiple-scattering and energy-loss straggling theories, which are approximate, CH combines the necessary theories into one coherent scheme. The multiple-scattering and energy-loss straggling distributions are typically smoother and less peaked than the analog DCS. This feature combined with the fact that a step is typically hundreds of analog mfps leads to a more efficient calculation. Different combinations of different multiple-scattering and energy-loss straggling distributions results in different CH schemes. There are two major schemes, class I and class II, and the major distinction between the two is whether particles move fixed, deterministic steps or randomly sampled steps. An example of the class I CH scheme is the ITS code system [73], where particles move a fixed step-size and elastic and inelastic collisions are given by the Goudsmit-Saunderson and Landau distributions respectively. An example of the class II CH scheme is the EGS code system, where the step-size is chosen as the minimum of the distance in the current

[2]The impact parameter characterizes the "closeness" of the collision. Closer collisions with small impact parameters are more catastrophic.

direction to the nearest boundary, the exponentially distributed distance associated with sampling distance to hard collisions, and the maximum step-size for which the multiple-scattering theory is valid. In EGS, elastic collisions are given by the Molière distribution and inelastic collisions separated into soft and hard collisions. Regardless of the CH scheme, the application of multiple-scattering and energy-loss straggling theory results in limitations that impact the accuracy of the CH method. In particular, the accuracy of CH is step-size dependent even when applied to an infinite medium problem [39]. Moreover, when applying multiple-scattering theory in a heterogenous media, additional error is introduced at material interfaces because multiple-scattering distributions are typically valid for an infinite medium. In both class I and class II CH schemes, it is possible to mitigate the impact of the aforementioned limitations by introducing algorithms that determine the optimal step-sizes or perform tedious studies for the same purpose.

In the remaining sections, the CH algorithm is discussed and the class I and class II schemes are outlined. Given an understanding of the CH algorithm, the aforementioned limitations are discussed in greater detail along with a demonstration of the typical approaches for mitigating these limitations.

6.1 The Condensed History Algorithm

In this section, the class I and class II condensed history schemes are discussed. In particular, the class I scheme discussed is based on the ITS algorithm, while the class II scheme discussed is based on the Geant4 algorithm. The descriptions of the algorithms are intended to emphasize the differences between the two schemes and are not necessarily perfect descriptions. To fully understand the two different algorithms, one should refer to the manuals and the source code (where possible) for both code systems [73, 3].

6.1.1 Complete grouping, class I

Class I CH algorithms have the oldest history of the different schemes and date back to the original ETRAN code system [16]. One might argue that the distinguishing feature of class I algorithms is the treatment of secondaries, or perhaps, fixed step-sizes resulting from use of the Goudsmit-Saunderson distribution[3]. Regardless, the resulting algorithm is the same. That is, if one decides to use the Goudsmit-Saunderson distribution for fixed step-sizes, a mixed approach for energy-loss straggling is no longer appropriate. Therefore, Landau theory is used and secondaries are treated on an average basis. Alternatively, one could decide to use Landau theory and as a result, would be forced to handle secondary production accordingly making use of fixed step-sizes and the Goudsmit-Saunderson distribution a natural choice. That said, class I algorithms move electrons fixed distances over which the electron is assumed to lose a constant fraction of energy (typically about 8%). An energy grid is established for corresponding to this fractional energy loss and step-sizes consistent with the energy grid are determined. Multiple-scattering and energy-loss straggling distributions are also pre-computed and stored for the previously mentioned energy grid. Once the pre-processing is completed electrons are transported according to the design of the algorithm specific to the code system. The remainder of this section presents an overview of an ITS-like algorithm.

To begin, the data for the simulation must be prepared. For electrons, this includes generating multiple-scattering and energy-loss straggling distributions for an energy grid determined by the maximum particle energy and the cut-off energy. The energy grid is determined by the following expression

$$E_k = E_{k-1} 2^{-1/J}, \tag{6.1}$$

where J is typically set to 8. Now, steps are generated for the $K-1$ energy-losses,

[3]There are codes that now use Goudsmit-Saunderson for randomy sampled step-sizes [**?**].

or $\Delta E_k = E_k - E_{k-1}$. The Landau distribution is evaluated at each of the k energy grid points along with the Goudsmit-Saunderson distribution where some effort is made to account for the changing energy over the step. The steps are sub-divided into m sub-steps. This is, of course, executed for all materials. Given the necessary data, the transport begins.

First, energy-straggling is determined for the entire step. Once the energy loss for the step is determined it is applied in a CSD manner divided evenly among the sub-steps in the step [74]. The electron is moved the distance of a sub-step and at this point, angular deflection is sampled from the Goudsmit-Saunderson distribution and secondaries are sampled. Secondaries are sampled based on the mean number expected to be produced above the cut-off energy over the sub-step distance. The mean number expected is determined by integrating the Möller DCS over the range above the cut-off energy and dividing the sub-step by this quantity. The energies of the secondaries are also sampled from the Möller DCS above the cut-off. Given the mean expected secondary production and their energies, the locations of the secondaries are sampled randomly along the sub-step. It is important to note that the energy lost by the primary electron is accounted for at the beginning of the step. When secondaries are produced negative energy deposition is tallied to account for the removal of energy in the form of a secondary. Though negative energy deposition is non-physical, energy balance is achieved over many histories. bremsstrahlung photons are also produced over a sub-step and sampled from the Poisson distribution. However, the energy of the primary electron is reduced by the energy of the bremsstrahlung photons produced along the sub-step because photon production is not accounted for in the energy-loss straggling. The process of moving a particle over a sub-step is repeated until the particle reaches the end of the step. At this point, the energy-loss straggling distribution is again sampled and all of the processes at the sub-step level are repeated.

The process of transporting the electron is interrupted when a material boundary is encountered. This is a complication for the algorithm because the sub-step must be truncated at the boundary and the multiple scattering distributions are predetermined for fixed steps. Therefore, a modified multiple-scattering distribution, or the Jordan-Mack correction, is applied [41]. This distribution takes the form of a Gaussian to account for small-angle scatter plus a Poisson to account for large-angle scatter. The distribution is applied over the truncated sub-step. Secondary production and bremsstrahlung photons are determined as usual for the truncated step. However, the energy-loss straggling that was calculated for the entire step must now be corrected for the abbreviated step. This is done by re-sampling the Landau distribution for the abbreviated step.

Once the particle leaves the problem volume or slows down through the minimum energy, the particle is killed and a new history begins.

6.1.2 Mixed procedures, class II

Class II CH algorithms are more modern than class I and according to Salvat [14], intrinsically more accurate than class I algorithms. The class II algorithm under consideration in this section is the one associated with the Geant4 default electromagnetic physics. Significant detail is provided because this CH algorithm is compared to the Moment-Preserving method in Chapter 9. The Geant4 CH method is a combination of a multiple elastic scattering model and an hybrid inelastic model. The multiple-scattering model is based on Lewis' multiple-scattering theory and uses model functions to determine the angular and spatial distributions after a step. The functions have been chosen in such a way as to give the same moments of the (angular and spatial) distributions as the Lewis theory [75]. The hybrid inelastic model is based on the Berger-Seltzer stopping power formula for soft collisions and the Möller

DCS for hard collisions. A secondary production threshold is selected for each material. Below the threshold, collisions are considered soft, and above the threshold, collisions are considered hard.

Precomputed data is not required by class II algorithms, which is the first major distinction between class I and class II schemes. This is because the distance to collision is determined as the minimum of the distance in the current direction to the nearest boundary, the exponentially distributed distance associated with sampling distance to hard collisions, and the maximum step-size for which the multiple-scattering theory is valid. The Geant4 algorithm begins by determining distance to collision, s, and then comparing that with the distance to the nearest geometrical boundary and taking the shortest of the two. The physics step length, or s, must be transformed into a geometric step length before the comparison. This transformation is called the inverse pathlength correction. The reason this must occur is because the step length associated with the physics is path traveled in an infinite medium and typically longer than the geometrical step length, which is the shortest distance between the starting point and the ending point associated with a path. If the step is short enough the transformation is given by

$$\langle z \rangle = \lambda_{tr} \left[1 - \exp\left(-\frac{s}{\lambda_{tr}} \right) \right]. \tag{6.2}$$

If the step is longer, energy-loss must be accounted for and the transformation becomes

$$\langle z \rangle = \frac{a}{\alpha \left(1 + \frac{1}{\alpha \lambda_{tr,0}} \right)} \left[1 - (1 - \alpha s)^{1 + \frac{1}{\alpha \lambda_{tr,0}}} \right], \tag{6.3}$$

where $\alpha = \frac{\lambda_{tr,0} - \lambda_{tr,1}}{s \lambda_{tr,0}}$ and $\lambda_{tr,0}$ and $\lambda_{tr,1}$ are the transport mfps at the beginning and the end of a step. Given the relationship between z and s, the pathlength correction is applied and compared to the geometric step length. After the step length is selected, the particle is moved to the next location and the associated geometric step length is transformed back to the physics step length so that the multiple-scattering

distribution and energy-loss distribution can be evaluated. The scattering angle is sampled from what is referred to as a "model" function that has the following form

$$g(\mu) = p[qg_1(\mu) + (1-q)g_2(\mu)] + (1-p)g_3(\mu), \tag{6.4}$$

where

$$\begin{aligned} g_1(\mu) &= C_1 \exp\left(-a(1-\mu)\right), \qquad \mu_{cut} \leq \mu \leq 1, & (6.5)\\ g_2(\mu) &= \frac{C_2}{(b-mu)^d}, \qquad -1 \leq \mu \leq \mu_{cut}, & (6.6)\\ g_3(\mu) &= C_3, \qquad -1 \leq \mu \leq 1, & (6.7) \end{aligned}$$

C_1, C_2, and C_3 are normalization constants, and a, b, d, p, q, and μ_{cut} are model parameters. The model parameters are determined such that $g(\mu)$ and its first derivative are continuous at $\mu = \mu_{cut}$. Another constraint is that the mean value of $g(\mu)$ must give the mean value from theory. The parameter a is chosen such that

$$a = \frac{0.5}{1-\cos\theta_0}, \tag{6.8}$$

where θ_0 is chosen according to the modified Highland-Lynch-Dahl formula. The parameter μ_{cut} is chosen as

$$\mu_{cut} = 1 - \frac{3}{a} \tag{6.9}$$

and the parameter d is

$$d = 2.40 - 0.027Z^{2/3}. \tag{6.10}$$

With the scattering distribution completely determined, the scattering angle can be sampled. After the scattering angle is sampled, a lateral correction is made according to

$$\langle x\Omega_x + y\Omega_y \rangle = \frac{2\lambda_{tr}}{3}\left[1 - \frac{\kappa}{\kappa-1}e^{-\tau} + \frac{1}{\kappa-1}e^{-\kappa s}\right], \tag{6.11}$$

where $\tau = s/\lambda_{tr}$ and $\kappa = \lambda_{tr}G_2$ and G_2 is the second momentum transfer moment. Eq. (6.11) gives the correlation strength between final lateral position and the final direction.

Energy-loss resulting from soft collisions is applied along each step according to the Berger-Seltzer formula for energy transfers between the mean ionization energy and the secondary production threshold. After the mean energy-loss is computed over the step, the energy-loss fluctuations are added to account for the stochastic nature of the continuous energy-loss process. Energy-loss resulting from hard collisions are applied randomly as a discrete process and sampled from the Möller DCS. See Chapter 3 for both the Berger-Seltzer formula and the Möller DCS.

Both step-size limitations and boundary crossing algorithms are used to control error in the Geant4 CH method. Step-size limitations originate from both the elastic and inelastic physics. For example, continuous energy-loss, or application of the Berger-Seltzer formula, imposes a limit on the step-size because of the energy dependence of the cross-sections. It is generally assumed that the cross-sections, or rather the Berger-Seltzer formula, is constant over a step. That is, energy-loss over a step is small enough to neglect variation in the stopping power. For sufficiently long steps, this assumption is violated and that is why step limitations are imposed. The default step limitation for continuous energy-loss limits the step such that the range of the particle cannot decrease more than 20% over a step. In addition, the computation of the mean energy loss, ΔE, over a step is given by

$$\Delta E = S(E_0)s, \tag{6.12}$$

where $S(E_0)$ is the stopping power evaluated at the energy of the particle at the beginning of the step and s is the step-length. To use Eq. (6.12), $\Delta E < \xi E_0$, where ξ is the linear-loss-limit parameter defaulting to $\xi = 0.01$. If this energy loss limit is exceeded, the following expression is used

$$\Delta E = E_0 - f_T(r_0 - s), \tag{6.13}$$

where f_T is inverse range that gives the kinetic energy of a particle as the function of some distance and $r_0 - s$ is the range of a electron with energy E_0 less the step-length. Eq. (6.14), is presumably more accurate for larger energy losses.

The multiple-scattering step limitations are also considered. The first step limitation is used to prevent steps leaving or entering a volume from taking too large of steps and is given by

$$s < \mathcal{F}_r max(R(E), \lambda_{tr}), \tag{6.14}$$

where the step is limited to no longer than a fraction, $\mathcal{F}_r = 0.2$, of the maximum of the range of the particle with energy E or the transport mfp. This limitation improves the angular distribution leaving a volume and backscattering for electrons entering a volume. In addition, a minimum step limit is also imposed according to

$$s > max(\lambda_{el}, \lambda_{tr}/25) \tag{6.15}$$

to prevent small, unphysical steps from being taken. To prevent particles from crossing a volume without colliding, the following limitation is imposed

$$s < \frac{d_{geom}}{\mathcal{F}_g}, \tag{6.16}$$

where d_{geom} is the distance to the boundary and $\mathcal{F}_g = 2.5$ forces the particle to have at least two collisions in a volume.

In addition to the step limitations, the Geant4 CH algorithm also requires a boundary crossing algorithm. The algorithm prevents the last step in a volume from being too large. In fact, the last step in a volume is limited to an analog mfp and the scattering is sampled according to an analog DCS, so the Geant4 CH essentially switches over to analog Monte Carlo near boundaries. The boundary cross algorithm is a combination of the analog model and an algorithm for sensing how close a particle is to a boundary. The key parameter for latter algorithm is referred to as *skin*. If $skin < 0$ the boundary crossing algorithm is not active, or analog Monte Carlo is

not activated. If $skin > 0$, analog Monte Carlo is activated in boundary layers with thicknesses of $skin \cdot \lambda_{el}$. The scattering at the end of these small steps are single or plural and no pathlength corrections are made.

Chapter 7

The Moment-Preserving Method

The Moment-Preserving (MP) method employs the experience gained from development of various charged particle transport solution methods. Like the condensed history method, Lewis theory is a critical component of the MP method. In addition, the MP method incorporates insights from work on the Fokker-Planck equation, the Boltzmann Fokker-Planck equation, and generalized Fokker-Planck theory. Ultimately, the MP method is characterized by several key features that are a consolidation of many important discoveries drawn from both condensed history and various reduced order physics models. These key features are:

- Physically sound - physics reflect analog process;
- Mathematically robust - preserves the correct transport mechanics;
- Computationally efficient - longer mfps and less peaked DCSs;
- Systematic - accuracy limits to analog;
- Versatile - physics refinement without fundamental algorithmic modification;
- Simple - implementation and maintenance cost are reduced.

In the MP method, a reduced order physics (ROP) transport equation is formed by replacing the analog DCSs in Eqs. (4.28) and (4.29) with ROP DCSs, $\tilde{\Sigma}$. That is,

$$\tilde{H}_{el}^{B}\psi(\vec{r},E,\vec{\Omega}) = \int_{4\pi} d\Omega' \tilde{\Sigma}_{el}(\vec{r},E,\vec{\Omega}'\cdot\vec{\Omega})\psi(\vec{r},E,\vec{\Omega}') - \tilde{\Sigma}_{el,0}(\vec{r},E)\psi(\vec{r},E,\vec{\Omega}) \quad (7.1)$$

and

$$\tilde{H}_{in}^{B}\psi(\vec{r},E,\vec{\Omega}) = \int_{0}^{\infty} dE' \tilde{\Sigma}_{in}(\vec{r},E'\rightarrow E)\psi(\vec{r},E',\vec{\Omega}) - \tilde{\Sigma}_{in,0}(\vec{r},E)\psi(\vec{r},E,\vec{\Omega}). \quad (7.2)$$

Although simply replacing the analog DCS with an ROP DCS may seem trivial or even arbitrary, there is no absence of rigor in this method. Particularly, much consideration is given to the form and properties of the ROP DCSs. The ROP DCSs are constructed such that they are smoother or less-peaked functions of deflection angle and energy loss and have significantly longer mfps than the analog DCSs. Thus, the ROP collision operators in Eqs. (7.1) and (7.2) have better properties than the analog collision operators, especially, from an efficiency standpoint.

Beyond efficiency, there are additional properties of the ROP collision operators that set this method apart from other approximate methods. For example, one of the unique characteristics of this method is that the integral form of the Boltzmann collision operators are maintained. Therefore, the description of the underlying transport mechanics is not lost, specifically, the correct Markovian feature of exponentially distributed collision sites [60]. Therefore, special algorithms for handling material and vacuum interfaces are not required.

Moreover, exact treatment of collisions as Markov processes and less-peaked DCSs with longer mfps make it practical to simulate transport with a single-event method. Implementation of single-event methods are very straightforward compared to other methods like CH that are considerably more complicated. In fact, Monte Carlo codes with pre-existing single-event algorithms do not require any retrofitting when implementing the MP method, since this method treats electrons like neutral particles.

The MP method is efficient and implementation is straightforward, but there has been no mention of accuracy. This method must not only be competitive with, and potentially superior to CH with regard to efficiency and simplicity, but accuracy as well, and in many cases it is. Unlike CH, which introduces inherent and irreducible limits on accuracy as a result of the underlying theory, accuracy is systematically controllable. This is largely a result of the moment-preserving strategies that are central to this approach. The moment-preserving strategy is motivated by Lewis theory [43, 44], where Lewis proved that one can relate space-angle moments of the angular flux to momentum-transfer moments of the elastic scattering DCS. In addition, the eigenvalues of the elastic collision operator are directly dependent on the momentum-transfer moments. For these reasons, it is prudent to construct an ROP DCS that preserves moments of the analog DCS.

Given the relationship between the ROP DCS and the analog DCS moments, the following moment-preserving constraints are a natural choice when constructing an ROP DCS. If the analog elastic scattering moments are given by

$$\Sigma_{el,\ell} = 2\pi \int_{-1}^{1} P_\ell(\mu)\Sigma_{el}(\mu)d\mu, \tag{7.3}$$

the moment preserving constraint is

$$\Sigma_{el,\ell} = \tilde{\Sigma}_{el,\ell}, \quad \ell = 1, 2, ...L \tag{7.4}$$

and the higher order moments are functions of the lower order moments

$$\Sigma_{el,\ell} = f(\Sigma_{el,1}, \Sigma_{el,2}, ..., \Sigma_{el,L}), \quad \ell > L. \tag{7.5}$$

For inelastic scattering the moments are given by

$$\Sigma_{in,j} = \int_{Q_{min}}^{Q_{max}} Q^j \Sigma_{in}(Q)dQ. \tag{7.6}$$

The moment preserving constraint is similar and given by

$$\Sigma_{in,j} = \tilde{\Sigma}_{in,j}, \quad j = 1, 2, ...J. \tag{7.7}$$

Again, the higher order moments are functions of the lower order moments

$$\Sigma_{in,j} = f(\Sigma_{in,1}, \Sigma_{in,2}, ..., \Sigma_{in,J}), \quad j > J. \tag{7.8}$$

By constructing an ROP DCS that preserves moments of the analog DCS, one can systematically control the accuracy of the ROP DCS models. That is, improvements in accuracy are achieved by simply preserving more moments of the analog DCS. In addition, the higher order moments are functions of the exact lower order moments, so the higher order moments are good approximations rather than being neglected as is the case for other ROP models like Fokker-Planck.

The following sections present the two ROP DCS models that are used in this paper. Given the discrete ROP DCS model, we present a corresponding derivation of the ROP transport model for a discrete elastic and inelastic ROP DCS to emphasize the difference in the ROP transport model and the analog model. The details of the ROP DCS construction process for each model are presented. Finally, we provide analysis of the efficiency and accuracy of the method.

7.1 ROP DCS models

In this section, we present two forms of the elastic and inelastic ROP DCSs that are demonstrated herein: the discrete DCS and the hybrid DCS. The discrete DCS is a superposition of discrete points and weights. One of the benefits of the discrete DCS is the simple form of the DCS. The discrete DCS is simple to sample and requires significantly less memory requirements than DCS data because only a few points and weights are required for most problems of interest. The accuracy and efficiency of the discrete DCS are especially promising when calculating integral quantities like dose [60]. We define the discrete DCS for elastic scattering as

$$\tilde{\Sigma}_{el}(\vec{r}, E, \mu_0) = \sum_{n=1}^{N} \frac{\alpha_n(E)}{2\pi} \delta[\mu_0 - \zeta_n], \tag{7.9}$$

and for inelastic scattering as

$$\tilde{\Sigma}_{in}(\vec{r}, E, Q) = \sum_{n=1}^{N} \beta_n(E)\delta[Q - \gamma_n]. \tag{7.10}$$

The one drawback of the discrete DCS is the presence of discrete artifacts [63, 76], especially, if the discrete DCS is used when calculating differential quantities in thin slabs. However, discrete artifacts can be mitigated by use of the hybrid DCS, while still achieving efficiency gains.

The hybrid DCS is a superposition of both discrete points and weights and a smooth function represented by an analog DCS. In previous work [64], the smooth component was represented by the SR DCS over $[-1, 1]$. The screening parameter was artificially selected such that the smooth component was less peaked near one. Moments of the smooth component are then subtracted from the analog DCS moments and this difference is then used to generate the discrete scattering angles. In this work, a slightly different representation was chosen where the tail is represented exactly by the analog model up to some cut-off point, μ_0^*. Beyond the cut-off point or for $\mu_0 \in [\mu_0^*, 1]$ a discrete representation is used. The resulting hybrid DCS is:

$$\tilde{\Sigma}_{el}(\vec{r}, E, \mu_0) = \Sigma_{el}^{S}(E, \mu_0) + \sum_{n=1}^{N} \frac{\alpha_n(E)}{2\pi}\delta[\mu_0 - \zeta_n], \tag{7.11}$$

where $\Sigma_{el}^{S}(E, \mu_0)$ is an analog DCS for $\mu_0 \in [-1, \mu_0^*)$ and otherwise zero. The cut-off, μ_0^*, is typically chosen to be near the peak or unity to gain the benefit of the properties of the discrete DCS, while capturing the large-angle scattering exactly by the analog DCS. For inelastic scattering, the cut-off, Q^*, is selected near the peak or near Q_{min} for the aforementioned reasons.

From an implementation standpoint, there is little difference between the discrete and hybrid DCS. It requires the ability to sample hard collisions from the analog DCS and soft collisions from the discrete DCS. The only difference in generating the

discrete DCS versus the hybrid DCS is that the moments are now defined over a sub-interval corresponding to the peak.

Given the form of the ROP DCSs, a derivation of the ROP collision operators that comprise the ROP transport equation is presented.

7.2 Derivation of the ROP Collision Operators

The ROP DCS is constructed such that the singular contribution to inscatter and outscatter cancel (similar to the FP operator [49]). Ultimately, the purpose of constructing such a DCS is that the resulting ROP transport equation can be solved accurately and efficiently using single-scatter models. To be clear, a derivation of the elastic and inelastic ROP collision operators is presented. A derivation of both operators is presented because there is a subtle difference between the two that deserves some attention. For the sake of simplicity, the discrete DCS is used, but the same ideas carry over to any ROP DCS.

The starting point is the elastic collision operator. Substitution of Eq. (7.9) into Eq. (4.28) gives

$$\tilde{H}_{el}^{B} = \int_{4\pi} d\vec{\Omega}' \sum_{n=1}^{N+1} \frac{\alpha_n(E)}{2\pi} \delta[\mu_0 - \zeta_n] \psi(\vec{r}, E, \vec{\Omega}') - \left(\sum_{n=1}^{N+1} \alpha_n(E) \right) \psi(\vec{r}, E, \vec{\Omega}). \quad (7.12)$$

It is required that the discrete point $\zeta_{N+1} = 1$. Now, this point is intentionally separated from the remaining N points and weights in the inscatter and outscatter terms. That is,

$$\begin{aligned} \tilde{H}_{el}^{B} = & \int_{4\pi} d\vec{\Omega}' \sum_{n=1}^{N} \frac{\alpha_n(E)}{2\pi} \delta[\mu_0 - \zeta_n] \psi(\vec{r}, E, \vec{\Omega}') - \left(\sum_{n=1}^{N} \alpha_n(E) \right) \psi(\vec{r}, E, \vec{\Omega}) \\ & + \int_{4\pi} d\vec{\Omega}' \frac{\alpha_{N+1}(E)}{2\pi} \delta[\mu_0 - \zeta_{N+1}] \psi(\vec{r}, E, \vec{\Omega}') - \alpha_{N+1} \psi(\vec{r}, E, \vec{\Omega}). \end{aligned} \quad (7.13)$$

If it can be shown that the last two terms in Eq. (7.13) indeed cancel, the resulting ROP transport equation will have an elastic scattering kernel that is significantly less peaked with reduced total cross section because α_{N+1} no longer contributes to the total cross section. To do so, one must first expand the delta function in terms of Legendre polynomials or

$$\int_{4\pi} d\vec{\Omega}' \frac{\alpha_{N+1}(E)}{2\pi} \delta[\mu_0 - \zeta_{N+1}] \psi(\vec{r}, E, \vec{\Omega}') = \frac{\alpha_{N+1}(E)}{2\pi} \int_{4\pi} d\vec{\Omega}' \sum_{\ell=0}^{\infty} \frac{2\ell+1}{2} P_\ell(\mu_0) P_\ell(1) \psi(\vec{r}, E, \vec{\Omega}'), \tag{7.14}$$

Through use of the addition theorem for spherical harmonics, or

$$P_\ell(\mu_0) = P_\ell(\vec{\Omega}' \cdot \vec{\Omega}) = \frac{4\pi}{2\ell+1} \sum_{m=-\ell}^{\ell} Y^*_{\ell m}(\vec{\Omega}') Y_{\ell m}(\vec{\Omega}) \tag{7.15}$$

and noting that $P_\ell(1) = 1$, Eq. (7.22) becomes

$$\alpha_{N+1}(E) \int_{4\pi} d\vec{\Omega}' \sum_{\ell=0}^{\infty} \frac{2\ell+1}{4\pi} P_\ell(\mu_0) P_\ell(1) \psi(\vec{r}, E, \vec{\Omega}') =$$

$$\alpha_{N+1}(E) \int_{4\pi} d\vec{\Omega}' \sum_{\ell=0}^{\infty} \frac{2\ell+1}{4\pi} \frac{4\pi}{2\ell+1} \sum_{m=-\ell}^{\ell} Y^*_{\ell m}(\vec{\Omega}') Y_{\ell m}(\vec{\Omega}) \psi(\vec{r}, E, \vec{\Omega}'). \tag{7.16}$$

Next, Eq. 7.16 is reorganized and the following definitions

$$\psi(\vec{r}, E, \vec{\Omega}) = \sum_{\ell=0}^{\infty} \sum_{m=-\ell}^{\ell} \psi_{\ell m} Y_{\ell m}(\vec{\Omega}), \tag{7.17}$$

and

$$\psi_{lm} = \int_{4\pi} d\vec{\Omega}' Y^*_{\ell m}(\vec{\Omega}) \psi(\vec{r}, E, \vec{\Omega}), \tag{7.18}$$

are applied which gives

$$\begin{aligned} \alpha_{N+1}(E) \sum_{\ell=0}^{\infty} \sum_{m=-\ell}^{\ell} Y_{\ell m}(\vec{\Omega}) \int_{4\pi} d\vec{\Omega}' Y^*_{\ell m}(\vec{\Omega}') \psi(\vec{r}, E, \vec{\Omega}') &= \alpha_{N+1}(E) \sum_{\ell=0}^{\infty} \sum_{m=-\ell}^{\ell} \psi_{\ell m} Y_{\ell m}(\vec{\Omega}) \\ &= \alpha_{N+1}(E) \psi(\vec{r}, E, \vec{\Omega}). \end{aligned} \tag{7.19}$$

This term clearly cancels with the last term in Eq. (7.13). However, the same is not true for the inelastic collision operator, which is now shown.

The derivation of the inelastic ROP collision operator is easier to follow after a change of variables change variables from Q to $(E' - E)$. This gives

$$\tilde{\Sigma}_{in}(\vec{r}, E' \to E) = \sum_{n=1}^{N} \beta_n(E)\delta[(E' - E) - \gamma_n]. \tag{7.20}$$

Again, Eq. (7.20) is substituted into Eq. (4.29) and the argument of the delta function is rewritten as $E' - (E + \gamma_n)$ which gives

$$\tilde{H}_{in}^{B} = \int_0^\infty dE' \sum_{n=1}^{N+1} \beta_n(E)\delta[E' - (E + \gamma_n)]\psi(\vec{r}, E, \vec{\Omega}) - \left(\sum_{n=1}^{N+1} \beta_n(E)\right)\psi(\vec{r}, E, \vec{\Omega}). \tag{7.21}$$

Now, the singular component or the $N + 1$ term is separated from the inscatter and the outscatter, the inelastic ROP collision operator becomes

$$\begin{aligned}\tilde{H}_{el}^{B} = &\int_0^\infty dE' \sum_{n=1}^{N} \beta_n(E)\delta[E' - (E + \gamma_n)]\psi(\vec{r}, E, \vec{\Omega}) - \left(\sum_{n=1}^{N} \beta_n(E)\right)\psi(\vec{r}, E, \vec{\Omega}) \\ &+ \int_0^\infty dE' \beta_{N+1}(E)\delta[E' - (E + \gamma_{N+1})]\psi(\vec{r}, E, \vec{\Omega}) - \beta_{N+1}(E)\psi(\vec{r}, E, \vec{\Omega}).\end{aligned} \tag{7.22}$$

Carrying out the integration over the $N + 1$ term results in the following singular contributions to inscatter and outscatter

$$\gamma_{N+1}(E)\psi(\vec{r}, E + \chi_{N+1}, \vec{\Omega}) - \gamma_{N+1}(E)\psi(\vec{r}, E, \vec{\Omega})) \neq 0. \tag{7.23}$$

The terms in Eq. (7.23) do not cancel, unless $\chi_{N+1} = 0$. Typically, the singular component of the inelastic DCS and the lower bound of the inscatter or energy-loss moments is chosen as the mean ionization potential. Therefore, $\chi_{N+1} = I_{MeV}$, where I_{MeV} is the mean ionization potential in MeV. So, if $\psi(\vec{r}, E + \chi_{N+1}, \vec{\Omega})$ is expanded about E as a Taylor series, one can get a sense of the error introduced by choosing

$\chi_{N+1} = I_{MeV}$. That is,

$$\begin{aligned}
&\gamma_{N+1}(E)\psi(\vec{r}, E+\chi_{N+1}, \vec{\Omega}) - \gamma_{N+1}(E)\psi(\vec{r}, E, \vec{\Omega})) \\
&= \sum_{j=1}^{\infty} \frac{\chi_{N+1}^{j}}{j!} \frac{\partial^{j}}{\partial E^{j}} [\gamma_{N+1}(E)\psi(\vec{r}, E, \vec{\Omega})] + \gamma_{N+1}(E)\psi(\vec{r}, E, \vec{\Omega}) - \gamma_{N+1}(E)\psi(\vec{r}, E, \vec{\Omega}) \\
&= \sum_{j=1}^{\infty} \frac{\chi_{N+1}^{j}}{j!} \frac{\partial^{j}}{\partial E^{j}} [\gamma_{N+1}(E)\psi(\vec{r}, E, \vec{\Omega})]. \qquad (7.24)
\end{aligned}$$

So, to first order, the error introduced by assuming that $\chi_{N+1} = 0$ is proportional to I_{MeV} which is $<< 1$. Therefore, this assumption introduces manageable error.

7.3 Generation of the Discrete and Hybrid Differential Cross-Sections

The procedure for constructing both the discrete and hybrid DCS from analog DCS moments is described. The form of the moment preservation constraints in Eqs. (7.4) and (7.7) is unstable to direct numerical inversion, so another approach similar to generation of Radau quadrature is taken [77]. First, the discussion in the beginning of Chapter 7 is expanded. Initially, attention is given to the discrete elastic DCS and then the discussion is extended to the discrete inelastic DCS and the hybrid DCS.

It is of interest to obtain a DCS that satisfies the moment constraint in Eq. (7.4). Given the discrete elastic DCS in Eq. (7.9), a system of equations for N points and weights (in total $2N$ unknowns) is formed. Substitution of Eq. (7.9) into

the right-hand-side of Eq. (7.4) results in the following system of equations:

$$\begin{aligned}
\Sigma_{el,\ell} &= \tilde{\Sigma}_{el,\ell} \\
&= 2\pi \int_{-1}^{1} P_\ell(\mu)\tilde{\Sigma}_{el}(E,\mu_0) \\
&= \sum_{n=1}^{N} \alpha_n(E) \int_{-1}^{1} P_\ell(\mu_0)\delta[\mu_0 - \zeta_n] \\
&= \sum_{n=1}^{N} \alpha_n(E) P_\ell(\zeta_n). \qquad (7.25)
\end{aligned}$$

A total of $L = 2N$ equations are necessary because there are $2N$ unknowns,. That is,

$$\begin{aligned}
\Sigma_{el,1} &= \alpha_1(E)P_1(\zeta_1) + \alpha_2(E)P_1(\zeta_2) + ... + \alpha_{2N}(E)P_1(\zeta_{2N}) \\
\Sigma_{el,2} &= \alpha_1(E)P_2(\zeta_1) + \alpha_2(E)P_2(\zeta_2) + ... + \alpha_{2N}(E)P_2(\zeta_{2N}) \\
&\vdots \\
\Sigma_{el,2N} &= \alpha_1(E)P_{2N}(\zeta_1) + \alpha_2(E)P_{2N}(\zeta_2) + ... + \alpha_{2N}(E)P_{2N}(\zeta_{2N}). \qquad (7.26)
\end{aligned}$$

The system formed in Eq. (7.26) emphasizes the requirement that ζ_n and α_n are obtained such that Legendre moments of the analog DCS are preserved. The system is then recast into one encountered when generating Gauss-Radau Quadrature for a non-classical weight function [78, 79]. That is,

$$\Sigma_{el,\ell} = \sum_{n=1}^{N} \alpha_n(E)P_\ell(\zeta_n) + \alpha_{N+1}(E)P_\ell(\zeta_{N+1} = 1), \qquad (7.27)$$

which is a Gauss-Radau Quadrature system for a non-classical weight function, where in this case, the weight function is the analog DCS. Note that an additional unknown, α_{N+1}, is added in Eq. (7.27) and multiplied by $P_\ell(\zeta_{N+1} = 1)$. This is indicative of Radau quadrature and an expression for determining α_{N+1} is given below. A Radau approach is selected rather than standard Gauss quadrature because Radau

ensures that one point will correspond to the peaked component of the DCS (that is, $\zeta_{N+1} = 1$). Once the discrete points and weights are obtained, the peaked component is eliminated, thus, reducing the total cross section after renormalizing the discrete DCS. This is equivalent to satisfying the moment preservation constraints given in Eqs. (7.4) and (7.7).

To obtain the points and weights, coefficients of monic Legendre polynomials (α_j and β_j) are mapped to the coefficients of polynomials orthogonal to the analog DCS (a_j and b_j). The algorithm for this mapping is referred to as the modified Chebyshev algorithm (MCA) [79] and requires $2N-1$ moments of the analog DCS and $2N-2$ coefficients of monic Legendre polynomials. Given a successful mapping and the resulting coefficients, a_j and b_j, the Golub and Welsch algorithm [80] is used to obtain the eigenvalues of the Jacobi matrix. The Jacobi matrix is a tridiagonal matrix where the diagonal is set to a_i and the off-diagonals are set to $\sqrt{b_i}$. The eigenvalues of the Jacobi matrix are the points and the first entry of each corresponding eigenvector squared are the weights. That is, $\zeta_n = \lambda_n(J)$ and $\alpha_n = (V_{n,1})^2$, where V is a eigenvector matrix. The application of the Golub and Welsch algorithm to the aforementioned Jacobi matrix will result in Gauss Quadrature and must be modified according to Golub [78] for Radau quadrature. Therefore, the Jacobi matrix is modified such that

$$J_{N+1} = \begin{bmatrix} J_N & b_N \vec{e}_N \\ b_N \vec{e}_N^T & a_{N+1} \end{bmatrix}, \tag{7.28}$$

where

$$a_{N+1} = 1 - b_N \frac{p_{N-1}(b)}{p_N(b)}. \tag{7.29}$$

Application of the Golub and Welsch algorithm to Eq. (7.28) will result in $N+1$ points and $N+1$ weights normalized to unity. To obtain the final discrete DCS, the $N+1$ point and weight is eliminated and the remaining weights are then scaled by

the analog total cross section or $\Sigma_{el,0}$. The total cross section for the discrete DCS is then

$$\tilde{\Sigma}_{el,0}(\vec{r}, E) = \sum_{n=1}^{N} \alpha_n(E), \tag{7.30}$$

which does not include the $N+1$ weight. The total cross section in Eq. (7.30) is significantly reduced depending on the order of the discrete DCS, the particle energy, and the target material, thus, extending the mfp. This completes the process of generating a discrete elastic DCS.

The process of generating a discrete inelastic DCS is similar. To use the same quadrature tools, the inelastic DCS must be mapped to an elastic DCS since the bounds on the elastic DCS are ideal for these tools (that is, $[-1, 1]$). Given a mapping, the moments of the inelastic DCS are related to Legendre moments of an ROP elastic DCS. Points on $(-1, 1]$ are generated with corresponding weights and then mapped back to $[0, Q_{max})$[1]. The mapping is

$$Q(\mu) = \frac{Q_{max}}{2}(1 - \mu) \tag{7.31}$$

and the resulting relationship between the moments is

$$\hat{\Sigma}_{el,\ell} = \sum_{j=0}^{\ell} c_j^{\ell} \frac{(-1)^j}{j!} \left(\frac{2}{Q_{max}}\right)^j Q_j(\Sigma_{in}), \tag{7.32}$$

where

$$c_j^{\ell} = \frac{1}{2^j j!} \prod_{i=0}^{j-1} [l(l-1) - i(i-1)]. \tag{7.33}$$

This summarizes the process of generating the discrete elastic and inelastic DCS. Many of the same ideas carry over to generation of the discrete component of the hybrid DCS.

[1]Note that the interval $(-1, 1]$ and $[0, Q_{max})$ only includes one endpoint. When generating Gaussian quadrature points are always generated on the interval $(-1, 1)$. When generating Radau or Lobatto one can include a one or both endpoints respectively. Here the endpoint $\mu = 1$ is included, but not $\mu = -1$. Therefore, the resulting points are on $(-1, 1]$ and the interval after the mapping is $[0, Q_{max})$.

To generate the discrete points and weights for the hybrid DCS a cut-off value is selected. It should be selected such that additional accuracy is gained while still maintaining efficient runtimes. Although, this is problem dependent and mostly a heuristic exercise.

Given a cut-off, the following moments are used to generate the discrete points and weights:

$$\Sigma_{el,\ell}^{D} = 2\pi \int_{\mu_0^*}^{1} P_\ell(\mu) f(\mu) d\mu \tag{7.34}$$

and

$$\Sigma_{in,j}^{D} = \int_{Q_{min}}^{Q^*} Q^j f(Q) dQ. \tag{7.35}$$

In both cases, to use the DCS generation tools, the moments must be mapped to the appropriate domain $[-1, 1]$ just as for the discrete inelastic DCS. For the inelastic hybrid DCS the mapping does not change significantly from Eqs. (7.31) and (7.32) and is

$$Q(\mu) = \frac{1}{2} Q^*(1 - \mu), \tag{7.36}$$

where μ is on $[-1, 1]$ and Q is on $[0, Q_{cut}]$. Given this mapping, the moments are related by

$$\hat{\Sigma}_{el,\ell} = \sum_{j=0}^{\ell} c_j^\ell \frac{(-1)^j}{j!} \left(\frac{2}{Q^* - Q_{min}} \right)^j \sum_{k=0}^{j} \binom{j}{k} (-Q_{min})^{j-k} Q_k^D(\Sigma_{in}), \tag{7.37}$$

where c_j^ℓ is given by Eq. (7.33).

The map for the hybrid elastic DCS is given by

$$\mu'(\mu) = \frac{\mu^* - 1}{2}(1 - \mu) + 1, \tag{7.38}$$

where μ is on $[-1, 1]$ and μ' is on $[\mu_{cut}, 1]$. Given this mapping, the moments are related by

$$\hat{\Sigma}_{el,\ell} = \sum_{n=0}^{\ell} c_n^\ell \frac{(-1)^n}{n!} \left(\frac{2}{1 - \mu^*} \right)^n \sum_{k=0}^{n} b_k^n M_k^D, \tag{7.39}$$

where b_k^n is

$$b_k^n = \int_{-1}^{1} P_k(\mu)(1-\mu)^n d\mu = \sum_{m=0} c_m^k \frac{(-1)^m}{m!} \frac{2^{n+m+1}}{n+m+1} \tag{7.40}$$

and the coefficient c_m^k or c_n^ℓ is given in Eq. (7.33).

To further demonstrate how the hybrid DCS is generated, a brief summary of the algorithm is written down.

1. Select a cut-off value.
2. Calculate moments given by Eqs. (7.34) and (7.35).
3. Map moments to ROP elastic DCS on $(-1, 1]$ using Eqs. (7.37) or (7.39).
4. Map resulting points and weights back to proper space using Eqs. (7.36) or (7.38).
5. Renormalize or remove point and weight associated with $\mu_0 = 1$ and $Q = 0$.

7.4 Properties of the ROP Collision Operators and Differential Cross-Sections

The notion of an approximation is to simplify a model that is difficult to use with another model that is nearly the same, but easier to use. In doing so, some information is lost in exchange for the approximate model. In the MP method, information or accuracy is lost when approximating the analog DCS. However, the loss in accuracy resulting from the moment-preserving approach is in many cases negligible, while remaining efficient. As it is, one cannot always gain orders of magnitude in efficiency while maintaining analog level accuracy. Nonetheless, it is possible to optimize such that in some cases significant efficiency gains are accompanied by negligible losses

in accuracy. To better understand the relationship between accuracy and efficiency, properties of the ROP collision operators and DCSs are discussed along with the associated impact on efficiency and accuracy.

7.4.1 Efficiency: impact of the regularization process

As discussed in section 7.3, the process of generating discrete points and weights is completed when the point at $\mu_0 = 1$ and the corresponding weight is eliminated (or $Q_{min} = 0$ for inelastic scattering) and the total cross section is renormalized. We refer to this step as the regularization process, which yields a less-peaked DCS with a corresponding total cross section that is reduced by the magnitude of the weight that was eliminated. The impact of the regularization process on the total cross section is seen in Figs. 7.1 and 7.2. As a function of increasing energy, the elastic and inelastic DCSs become more peaked (see sections 3.2 and 3.3). The impact of the regularization process depends on the peakedness of the DCS, so for higher energies the ROP total cross section is reduced more than for lower energies. Depending on the collision type, target nuclei, and the particle energy, an ROP mfp is one to four orders of magnitude longer than the analog mfp. Regardless of the collision type and target nuclei, all of the ROP DCSs approach analog level efficiency for sufficiently low energies. However, the same is true for CH methods at lower energies. At these energies, efficiency gains are not necessarily significant enough to justify the loss of accuracy when making the approximation. Therefore, analog Monte Carlo is typically used below a low energy threshold where efficiency gains are negligible. This threshold is problem dependent and also depends on the approximation, but it is clear in Figs. 7.1 and 7.2 that below roughly 100-keV the ROP total cross-section approaches the analog total cross-section. Although, it should be noted that the following figure correspond to the screened Rutherford DCS, which is less-peaks for a given energy than the partial-wave DCS. One should expect the ratio of the

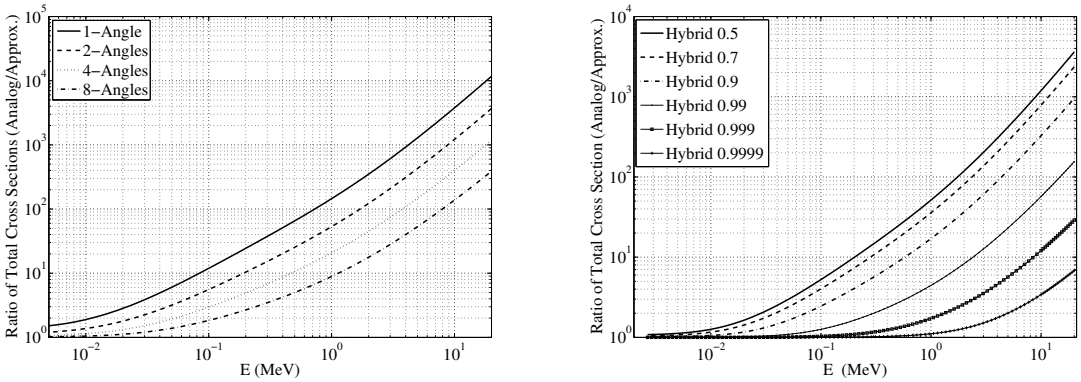

(a) Discrete (b) Hybrid

Figure 7.1: Comparison of total cross section of screened Rutherford DCS with several discrete and hybrid DCSs when colliding with gold nuclei.

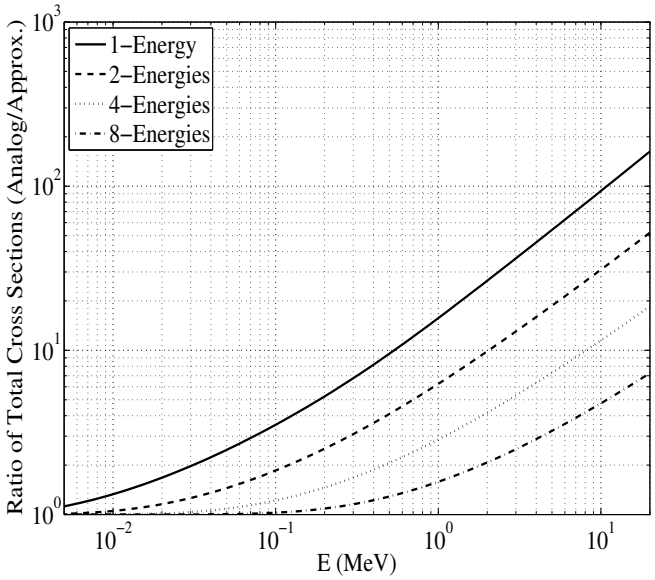

Figure 7.2: Comparison of total cross section of Moller DCS with several discrete DCSs when colliding with gold nuclei.

partial-wave DCS to a corresponding ROP total cross-section to be even greater.

Beyond efficiency gains, the regularization process impacts the peakedness of the the ROP DCSs. As a result, scattering events are not dominated by small deflections and small energy losses, which also improves efficiency. Take, for example, the four-point discrete DCSs for elastic scattering in Fig. 7.3a (the weights are normalized such that the largest weight is one). The discrete DCS only varies by roughly four orders of magnitude as opposed to 15 to 30 orders of magnitude for the analog DCS in Fig. 3.5a. This is a dramatic reduction in the peakedness of the elastic DCS. The inelastic analog DCS is less peaked so the regularization process is not quite as significant. Regardless, there is still a reduction in the peakedness by two to three orders of magnitude as seen in Fig. 7.3b.

At high energies where analog Monte Carlo is impractical, longer mfps result in significant efficiency gains over analog Monte Carlo. In addition, the ROP DCSs are significantly less peaked than the analog DCSs. However, efficiency gains are only meaningful if sufficient levels of accuracy are maintained. This is the subject of the

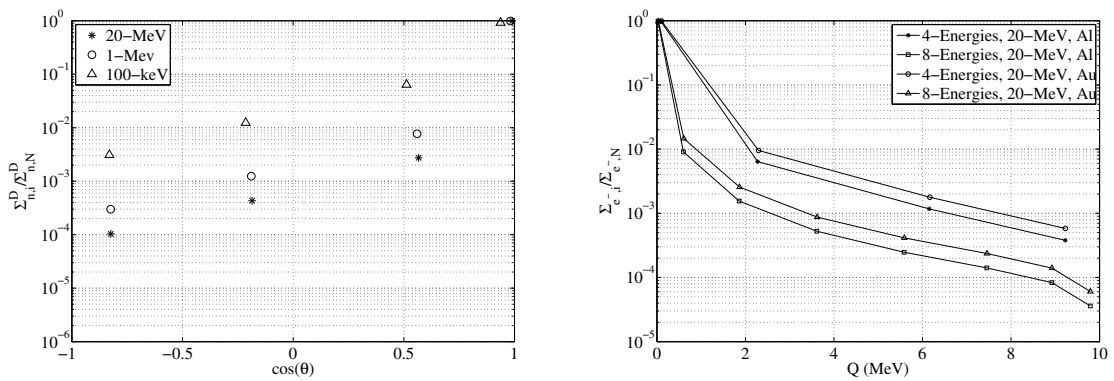

(a) Elastic (b) Inelastic

Figure 7.3: Impact of regularization process on reduced order physics DCSs for elastic and in elastic scattering reduces DCS variation from 10 to 30 orders of magnitude to 3 to 5 orders of magnitude. In (a) four-point discrete DCS for elastic scattering of 100-keV, 1-MeV, and 20-MeV electrons by aluminum are shown and in (b) four-point and eight-point discrete DCS for inelastic scattering of 20-MeV electrons by aluminum and gold are shown.

following section.

7.4.2 Accuracy: analog and ROP collision operator eigenvalues

It is difficult to draw any conclusions on the accuracy of this method without presenting results. However, we know heuristically that electron transport problems require physics models that preserve the first few moments of both the analog elastic and inelastic DCS. That is, the most important physics are captured by the transport cross section, stopping power, and straggling as discussed in section 5. The eigenvalues of the Boltzmann elastic collision operator (analog and approximate) are given by

$$\lambda_l(H_{el}^B) = -\left[\Sigma_{el,0} - \Sigma_{el,\ell}\right]. \tag{7.41}$$

Specifically, the analog eigenvalues are

$$\lambda_l(H_{el}^B) = 2\pi \int_{-1}^{1} P_\ell(\mu_0)\Sigma_{el}(E,\mu_0)d\mu - \Sigma_{el,0}, \tag{7.42}$$

the discrete eigenvalues are

$$\lambda_l(\tilde{H}_{el}^B) = \sum_{n=1}^{N} \alpha_n(E)\left[P_\ell(\zeta_n) - 1\right], \tag{7.43}$$

and the hybrid eigenvalues are

$$\lambda_l(\tilde{H}_{el}^B) = \sum_{n=1}^{N} \alpha_n(E)\left[P_\ell(\zeta_n) - 1\right] + 2\pi \int_{-1}^{\mu^*} P_\ell(\mu)\Sigma_{el}^S(E,\mu)d\mu. - \Sigma_{el,0}^S. \tag{7.44}$$

An accurate ROP collision operator will at least preserve the first few moments of the analog DCS and, in turn, eigenvalues of the elastic operator. In many cases, preservation of moments beyond the first few will improve accuracy making a generalized moment-preserving approach ideal because accuracy can be adjusted as the

problem demands it. For the sake of clarifying the remaining discussion, ROP collision operators with the first four to eight eigenvalues in agreement with the analog collision operator typically provide superb accuracy for integral quantities like dose in 1-D.

As a measure of accuracy the eigenvalues of the various ROP collision operators are compared with the eigenvalues of the analog collision operator. In Fig. 7.4, the relative error in the eigenvalues of various elastic ROP collision operators are given for 1-MeV electrons colliding with gold nuclei. For the discrete DCSs, the eigenvalues, $\lambda_1, ..., \lambda_{2N}$, are in excellent agreement with the analog eigenvalues. There is a distinct jump in the relative error at λ_{2N+1} where the higer-order eigenvalues are approximated in terms of the lower order eigenvalues. As discussed in previous sections, this result is expected and follows from the form of the discrete DCS and the moment-preservation constraint. Furthermore, the relative error in the higher-order eigenvalues for the discrete DCSs grows non-linearly.

Expectations for the accuracy of the hybrid DCS are not as clear. In fact, one can only expect perfect agreement with $\lambda_1, ..., \lambda_{2N}$, as was the case for the discrete DCS. For example, only λ_1 and λ_2 are exact in the event a single-point is selected to represent the peak. As it is, the hybrid DCS is more effective at approximating the higher order moments because the exact representation of the tail results in improved accuracy of higher order moments as seen in Fig. 7.4. In addition, the relative error in the higher-order moments grows linearly for the hybrid DCSs. In Fig. 7.4, the hybrid DCSs have a single discrete point near one. As the cut-off approaches one, the hybrid DCS becomes more accurate and the higher-order eigenvalues are better approximated. Although the level of accuracy associated with the hybrid DCS with $\mu_0^* = 0.999$ may not be necessary, it demonstrates a favorable property of this method. That is, the ROP DCS models can systematically limit to the analog DCS.

This analysis is only appropriate for the elastic collision operator, because one

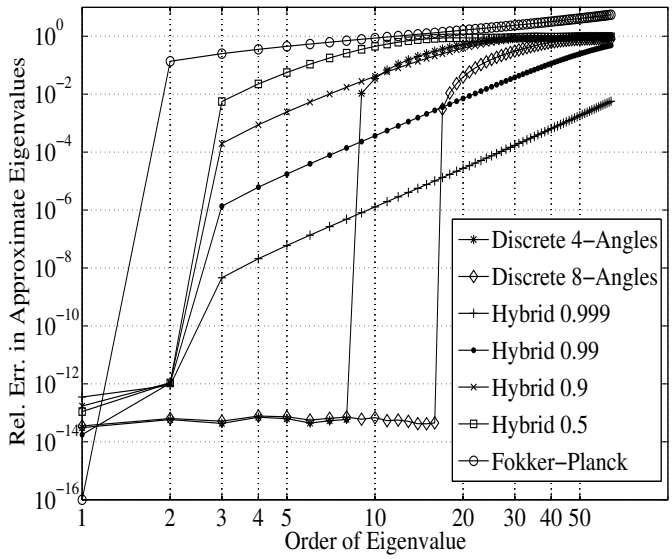

Figure 7.4: Comparison of eigenvalues of various approximations of the elastic collision operator for 1-MeV electrons colliding with gold.

cannot obtain eigenvalues of the inelastic operator. However, eigenvalues are closely related to the moments of the DCS, so one can assume that preservation of more moments will result in a more accurate inelastic ROP collision operator. Moreover, we know from Lewis theory that preservation of moments of the DCS is equivalent to preservation of moments of the solution. Therefore, we will not present any inelastic moment results since it was shown in previous sections that the ROP DCS are formed such that moments are preserved exactly up to some finite order.

Chapter 8

The Geant4 Toolkit

Geant4 is a C++ object-oriented simulation toolkit. The toolkit provides a diverse, wide-ranging, yet cohesive set of software components which can be employed in a variety of settings. These range from simple one-off studies of basic phenomena and geometries to full-scale detector simulations for experiments at the Large Hadron Collider and other facilities [3]. Geant4 utilizes advanced software engineering techniques to maximize functionality, modularity, extensibility, and openness based on the Booch methodology. Geant4 is modular and flexible, and the implementation of the physics is transparent and open to the user such that the user can understand and customize, or extend, the various classes available in the toolkit. The key domains of Monte Carlo simulation that subsequently led to class categories within the framework of the Geant4 toolkit include:

- geometry and materials,
- interaction physics,
- tracking management,
- digitization and hit management,

- event and track management,
- visualization and visualization framework,
- user interface.

The following sections discuss how users interact with the toolkit, whether as a typical user building applications against the toolkit or as an advanced user interested in toolkit development. The implementation of the Moment-Preserving method within Geant4 toolkit is detailed including a discussion of the physics classes, the cross-section construction classes, and the data libraries along with the Geant4 data processing classes that were utilized.

8.1 Developing with the Geant4 toolkit: Application Developers and Toolkit Developers

There are two types of Geant4 developers or users: those that develop simulation applications for research purposes requiring the development of the mandatory user classes specific to the users needs and the building of said application against the toolkit; and those that develop the toolkit itself (toolkit developers are typically application developers as well). These two types of developers interact with the toolkit differently.

Application developers do not necessarily need to know the details and the complexities of the entire toolkit. Application developers are typically interested in solving some specific radiation transport problem for which they have a varying knowledge of the geometry and materials, the source characteristics (that is, energy, angular, and spatial dependence), and the necessary physics models. Geant4 provides the abstract interface for eight user classes, but the concrete implementation,

instantiation and registration of these classes are mandatory for only three of the eight classes. In other words, Geant4 application developers are required to create a user specific implementation of the methods specified by the mandatory classes.

These three mandatory classes are *G4VUserDetectorConstruction, G4VUserPhysicsList,* and *G4VUserPrimaryGeneratorAction*, and describe the geometry and materials, the physics models to be used, and the particle source, respectively. These classes in addition to a main are all that application developers are required to implement. However, additional user classes are available that can be used to complete a wide variety of tasks including setting problem parameters, extracting information, modifying the state of the particle, printing results, and so on. These user classes include *G4UserRunAction, G4UserEventAction, G4UserStackingAction, G4UserTrackingAction,* and *G4UserSteppingAction* and are all associated with a "unit of simulation." That is, the *Run, Event, Stack, Track,* and *Step*. The *Run* is the largest unit of simulation and is a sequence of *Events*. An *Event* includes a source particle and all of the secondary particles produced by the source particle which are all classified as *Tracks*. A *Track* contains all of the information about a particle from its birth to its death (primary or secondary). The *Stack* manages the *Tracks* and can be used to prioritize or kill *Tracks*. The smallest unit of simulation where physics processes are applied is the *Step*. With the eight user classes, application developers can accomplish a great deal by only implementing any number of the optional user classes. However, possibilities for ambitious Geant4 users are seemingly limitless with sufficient time and knowledge of the toolkit.

On the other hand, toolkit developers are typically interested in adding classes relevant to any of the aforementioned class categories to enhance the toolkit. This does not necessarily require any of the development that was just discussed; however, toolkit developers are typically application developers as well. In efforts to implement the Moment-Preserving method, both types of development were undertaken. The

various aspects of the Moment-Preserving method development are discussed in the following section.

8.2 The Moment-Preserving Method Classes

Reduced order physics DCS models are central to the Moment-Preserving method and therefore, the majority of the development effort is in generating, storing, and accessing the ROP DCSs. Geant4 considers all physical interactions as processes, requiring implementation of the *G4VEmProcess* class, and the details of each process is captured by the model.This is accomplished through implementation of the *G4VEmModel* class, which is the primary source of development for the Moment-Preserving method (assuming the ROP DCS are available in the form of a DCS data library). The reason that the majority of the development occurs at the level of implementing the *G4VEmModel* class is because this is where the ROP DCS are stored by means of reading-in the data and storing in Geant4 data classes, and this is where the ROP DCSs are accessed when looking-up the total cross-section and sampling the DCS.

The other major component of development was creation of the ROP DCS construction classes. These were initially developed and interpreted as stand-alone DCS objects, in that upon construction of the ROP model class the ROP DCS is constructed for every material using the ROP DCS construction classes. This required that the ROP DCSs were constructed during runtime, which can be relatively CPU intensive (at most one minute). Further into the development of this method, with a better understanding of the toolkit, the ROP DCS construction classes were used to create a library of ROP DCS models making the ROP model classes more compact and easy to integrate into the toolkit.

The remaining sections provide detail on the associated physics process and model

classes, the cross-section construction classes, and the cross-section library and data processing tools. In addition, coding examples are provided when possible.

8.2.1 Physics processes

Physics processes for discrete and hybrid DCSs were implemented and include:

- *G4DiscreteElasticProcess*
- *G4HybridSoftElasticProcess*
- *G4HybridHardElasticProcess*
- *G4DiscreteInelasticProcess*
- *G4HybridSoftInelasticProcess*
- *G4HybridHardInelasticProcess*

The physics process is relatively simple because use is made of many of the virtual functions in *G4VEmProcess*. For example, *G4VEmProcess* contains a function for calling the physics model at the end of a step to sample a collision outcome. A user can override a virtual function, but only if it is necessary. Therefore, code duplication is reduced (this is a C++ concept and not specific to Geant4) and the resulting process class is very simple. The only functions that required implementation include a function that initializes the process class (this consists of constructing the associated physics model and setting a few data members) and a function that determines the applicable particles.

8.2.2 Physics models

Physics models for discrete and hybrid DCSs were implemented and include:

- *G4DiscreteElasticModel*
- *G4HybridSoftElasticModel*
- *G4HybridHardElasticModel*
- *G4DiscreteInelasticModel*
- *G4HybridSoftInelasticModel*
- *G4HybridHardInelasticModel*

Three important functions are included in the physics model class: an initialization function where the cross-section data is constructed or read in; a function for obtaining the total cross-section; and a function for sampling the DCS. In developing the Moment-Preserving method, there were two versions of the associated physics classes. The early version was designed to be included locally. That is, in application development the source files specific to the application are stored in some user working directory. Here, the user develops the mandatory classes and any additional classes required. It is possible to bring in new physics locally by storing the classes in this working directory. This approach was used during the early testing phases and the ROP cross-sections were constructed at runtime. For example, in the following lines of code, the *crossSection* vector is populated with pointers to *GBFPAngularDeflection* objects (see section 8.2.3 for detail on the *GBFPAngularDeflection* cross-section class). Each object corresponds to a different element from which the problem materials are composed, so the *crossSection* vector will have a length equivalent to the number of elements required by the problem. The drawback of this approach is that the *GBFPAngularDeflection* objects are constructed at runtime and this adds to the total time for the run. In addition, the Geant4 data classes make it very straightforward to access data for an element with atomic number Z. Here, additional functionality must be added to access the correct position

in the *crossSection* vector, which is not ideal for integration of the models into the toolkit.

```
// loop through all materials or couples
for (int i=0; i<numOfCouples; i++)
{
   // get a list of the each element in current material
   matEle = theCoupleTable->GetMaterialCutsCouple(i)->
                GetMaterial()->GetElementVector();
   // loop through each element
   for (int j=0; j<theCoupleTable->GetMaterialCutsCouple(i)->
                   GetMaterial()->GetNumberOfElements(); j++)
   {
      crossSection.push_back(new
          GBFPAngularDeflection(numPoints,evec,(*matEle)[j],theModel));
   }

}
```

During later stages of development, a more effective approach was identified where the ROP DCS library (see section 8.2.4) is constructed and the necessary data is read in at runtime. Not only does this cut down on runtime, but the pre-existing Geant4 data tools were utilized reducing development overhead and easing integration of the models into the toolkit. The code required to utilize the Geant4 data classes is left to the appendices (see appendix **??**) and section 8.2.5 describes the use the Geant4 data classes in greater detail.

There are two functions remaining for the physics model discussion, a function for obtaining the ROP total cross-section and a function for sampling the ROP DCS. These functions are essentially the same regardless of how the ROP cross-section data

is handled (constructed at runtime or read in from DCS data library). Obtaining the total cross-section is trivial and requires a table look-up as a function of energy. Given a particle energy, the upper and lower energy indices are determined using a binary search algorithm such that $E_k \leq E < E_{k+1}$. Then total cross-section is interpolated by using a linear weighting on log-log scale, or $\Sigma_{el,0} = \Sigma_{el,0}(E_k)\pi_k + \Sigma_{el,0}(E_{k+1})\pi_{k+1}$. The weights are given by

$$\begin{aligned} \pi_k &= \frac{\ln E_{k+1} - \ln E}{\ln E_{k+1} - \ln E_k}, \\ \pi_{k+1} &= \frac{\ln E - \ln E_k}{\ln E_{k+1} - \ln E_k}. \end{aligned} \tag{8.1}$$

The function for sampling the DCS requires two steps. First, the energy index of the data is determined using the previously discussed binary search; however, the linear interpolation is accomplished through random sampling using the weights from Eq. (8.1). That is, a random number, r, is sampled between zero and one, and if $r \leq \pi_k$ the DCS data for energy E_k is used; otherwise, the DCS data for energy E_{k+1} is used. This is possible because the weights can be considered as point probabilities and they sum to unity. Given the energy index for the DCS data, and of course, the material index which is assumed to be known, the discrete cumulative distribution function (CDF) can be accessed and used to sample the DCS. This is done by sampling another random number, r, and then searching the CDF until a bin is determined such that $F_j < r \leq F_{j+1}$ is satisfied. The form of the discrete CDF can be taken advantage of because it is known that for a CDF with J discrete values F_J corresponds to the most probable bin, so the CDF search is done in reverse as seen in the following code example. Here, m and k are known and are the material index and the energy index respectively. This loop cycles through the CDF values for the (m, k) data and locates the bin for the quantity sampled. Once the angular or energy-loss bin is determined, the jth deflection cosine or energy-loss for (m, k) material and energy is retrieved and the state of the particle is updated accordingly.

It should be noted that the largest typical discrete DCS is no more than eight points and weights, so sampling the discrete DCS is rapid.

```
for (G4int j=numPoints-1;j>0;j--)
{
    if ( (r>=crossSection[m]->GetCDF(k,j-1))
    {
        G4double cosTheta = crossSection[m]->GetPoint(k,p);
        break;
    }
}
```

At this point, no mention was made of the hybrid cross-section. As seen in the list of models, the hybrid cross-section is composed of two models: one for soft collisions and one for hard collisions. The soft collisions are given by the discrete cross section and all of the previous discussion carries over. The hard collisions are given by the analog DCS. For the partial-wave elastic DCS much of the previous discussion also carries over. However, for the Möller inelastic DCS, an analytical expression is used to obtain the total cross-section and a rejection technique is used to sample the DCS.

This summarizes the physics model classes required for this work. The remaining sections provide additional detail on the classes used for generating the ROP DCSs, the structure of the ROP DCS data library, and the Geant4 data classes required to process the data library.

8.2.3 Cross-section construction

All ROP DCS classes inherit from the *GBFPCrossSection*[1] base class. The *GBFPCrossSection* base class contains data members and functions required to generate an ROP DCS. The data members include vectors for storing ROP DCS points and weights, CDFs, and total cross-sections, along with vectors associated with the quadrature functions like coefficients of Legendre polynomials and Gauss-Legendre quadrature points and weights. The critical functions include the function for the modified Chebyshev algorithm and the function for obtaining Radau quadrature which includes a matrix eigenvalue solver (see Chapter 7 for details). The ROP DCSs are generated when constructing either a *GBFPAngularDeflection* or a *GBFPMollerEnergyLoss* object. The *GBFPAngularDeflection* or *GBFPMollerEnergyLoss* classes have data members and functions specific to elastic and inelastic DCSs respectively. Here, an outline of the algorithm for generating a discrete DCS is provided with some coding examples.

When a *GBFPAngularDeflection* object is created,

```
GBFPAngularDeflection* crossSection
       = new GBFPAngularDeflection(numPoints,evec,(*matEle)[j],theModel);
```

data members are initialized. For example, the vectors *points*, *CDF*, and *Sigmat* are sized appropriately and set to zero.

```
points.resize(energyGrid.size()); CDF.resize(energyGrid.size());
Sigmat.resize(energyGrid.size()); int N = numberOfPoints;
for (int i = 0; i < energyGrid.size(); i++){
    points[i].resize(N,0.0); CDF[i].resize(N,0.0);}
```

[1]The significance of GBFP is from the previous naming of the method; that is, the Generalized Boltzmann Fokker-Planck method [60].

In addition, vectors for the coefficients for Legendre polynomials are populated and local or temporary vectors for storing the coefficients of the polynomials orthogonal with respect to the analog DCS are initialized along with vectors for temporarily storing points and weights.

```
vector<double> alpha = GetALeg(); // coefficient of Legendre polynomials
vector<double> beta = GetBLeg(); // coefficient of Legendre polynomials
// Temp vectors for coefficient of special polynomials (aa,bb)
// and points and weights (x,w)
vector<double> aa(N,0.0), bb(N,0.0), x(N,0.0), w(N,0.0);
```

Once the necessary data members are initialized, a loop over all energies is executed, where the ROP DCSs for the current material are generated for each energy. Below, the associated code is provided for generating a discrete elastic DCS based on the screened Rutherford analog DCS. For a given energy, the parameters defining the screened Rutherford DCS are determined. That is, the screening parameter and the material constant (*eta* and *CC*). Now that the analog DCS is completely described, moments of the DCS are generated using an adaptive quadrature technique. The modified Chebyshev algorithm (MCA) requires monic moments, so the moments are then renormalized. These moments, along with the coefficients of monic Legendre polynomials (that is, *Ml*, *alpha*, and *beta*) are passed to the MCA. The MCA then returns the coefficients of polynomials that are orthogonal with respect the screened Rutherford DCS. These coefficients (*aa* and *bb*) are passed to the *Radau* function where a tridiagonal matrix is setup and the discrete points and weights are determined from this matrix (that is, the Jacobi matrix). The points and weights returned by the *Radau* function, must be regularized. The *Regularize* function removes the $N + 1$ point and weight, and then multiplies the remaining points and weights by the total cross section, *Ml[0]* because the weights passed to *Regularize* sum to unity.

Prior to storing the DCS data, testing is completed to ensure meaningful data. The discrete points are stored as the weights are summed. The sum of the weights are then stored in the total cross-section vector and a CDF is generated and stored as well. All of the temporary vectors are cleared and reset to zero. The process then continues for the next energy. The cross-section generation classes are provided in appendix **??**.

```
for (int i=0; i<E.size(); i++){
    G4double eta  =
        model->CalculateScreeningParameter(E[i], 0.51099891, ele->GetZ());
    G4double CC   =
        model->CalculateMaterialConstant(E[i], 0.51099891, ele->GetZ());
    SetAngularDeflectionMomentsWithAdaptiveQuadrature(E[i],CC,eta,Ml);
    Monic(Ml);
    orthog(Ml,alpha,beta,aa,bb);
    Radau(aa,bb,x,w);
    Regularize(x,w,Ml[0]);
    // Testing of points and weights removed for compactness
    // in coding example
    sum = 0.;
    for (int j=0; j<x.size(); j++){
        SetPoint(i,j,x[j]); sum += w[j]; SetCDF(i,j,sum);}
    SetSigt(i,sum);
    for (int j=0; j<x.size(); j++){SetCDF(i,j,GetCDF(i,j)/sum);}
        //normalizing CDF
    aa.clear(), bb.clear(), x.clear(), w.clear(), Ml.clear();
    aa.resize(N,0.0), bb.resize(N,0.0), x.resize(N,0.0), w.resize(N,0.0),
        Ml.resize(2*N,0.0);}
```

8.2.4 Cross section library

An ROP cross-section library was generated for the screened Rutherford DCS and the partial-wave DCS for 1, 2, 4, and 8 points and weights. The libraries are formatted such that the Geant4 data classes could be used (see section 8.2.5). For each material and number of points and weights, there are two data files: one for the total cross-section and one for the CDF. The files are named accordingly. For example, for a 2-angle discrete DCS based on the partial-wave DCS for aluminum the two files are named *gbfp_pwe_tcs_13_2.dat* and *gbfp_pwe_cdf_13_2.dat*, where the first number is the atomic number and the second number is the number of points and weights. The total cross-section file has the following format

```
20 0.00102648 123 123
0.00102648 1.895310594263357e-15
0.00111939 1.895310594263357e-15
0.00122070 1.735008462388171e-15
...
18.3401000 3.231888773330259e-21
19.1521000 3.014865567609761e-21
20.0000000 2.812460738247908e-21
```

The first row indicates that maximum energy, the minimum energy, and the length of each column. The first column is the particle energy and the second column is the total cross section in mm^2. The CDF file has the following format

```
0.1253630590705352 -0.5474023266341548
1.0000000000000000  0.7102211565388719
0.1253630590705352 -0.5474023266341548
1.0000000000000000  0.7102211565388719
0.1176158475868398 -0.5376566009643416
1.0000000000000000  0.7163622043775827
...
0.0013006768714632 -0.0091294921937126
1.0000000000000000  0.9732752885064547
0.0012783923557266 -0.0076636446407933
1.0000000000000000  0.9735167107563724
0.0012560788028267 -0.0060866632871608
1.0000000000000000  0.9737602097136864
```

The first column is the value of the CDF for some discrete angle and because this is a 2-angle data file, every two values corresponds to one energy. The second column is the discrete angle associated with the CDF.

The next section discusses the Geant4 data classes required and the how the data files are processed.

8.2.5 Data processing

There are two primary Geant4 data classes utilized in processing and storing the ROP DCS data: *G4ElementData* and *G4PhysicsVector*. *G4ElementData* is a very powerful class that stores data for a particular element and then only requires the atomic number to retrieve the data. Upon construction, the *G4ElementData* object requires the atomic number and the data in the form of a pointer to a *G4PhysicsVector* object, so the *G4ElementData* class is really a container of *G4PhysicsVector* objects. The

data is actually stored in the *G4PhysicsVector* object, which is also a very powerful class because as long as the data is properly formatted, one must simply pass the *G4PhysicsVector* object a stream of the data.

As an example, the process of reading total cross-section data is provided, where *tcs* is a pointer to a G4ElementData object. First, in the initialize function of the *G4DiscreteElasticModel*, the materials and their constituents are processed. The atomic number of the current element is determined and a check is performed to determine if the data already exist. If it does not exist, *ReadData* is called with the material Z and the path to the data.

```
for(G4int i=0; i<numOfCouples; ++i){
    const G4Material* material =
        theCoupleTable->GetMaterialCutsCouple(i)->GetMaterial();
    const G4ElementVector* theElementVector = material->GetElementVector();
    G4int nelm = material->GetNumberOfElements();
    // loop through all elements
    // if data for element does not exist process it
    for (G4int j=0; j<nelm; ++j){
        G4int Z = (G4int)(*theElementVector)[j]->GetZ();
        else if(Z > maxZ){ Z = maxZ; }
        if(!tcs->GetElementData(Z)) { ReadData(Z, path); } } }
```

The following code provides an example of what occurs inside *ReadData* specifically for processing the total cross-section data. First, a stream is opened for the total cross-section data determined by the path to the data file. A temporary pointer to a *G4PhysicsVector* object is constructed. Then the *Retrieve* function is used to read in the data for the current stream. Once the data is read in, the pointer to the *G4PhysicsVector* object containing the data is passed to the G4ElementData object,

tcs, using the *InitialiseForElement* function. At this point, the total cross-section data for the current element is processed.

```
std::ifstream in(tcsPath, std::ifstream::binary|std::ifstream::in);
// Create a temporary G4PhysicsVector object pointer
G4PhysicsVector* tempData = new G4PhysicsVector(false,true,false);
// Use retrieve to read in the total cross section (tcs) data
tempData->Retrieve(in,true);
// pass this data to the tcs object and initialise for current element
tcs->InitialiseForElement(Z,tempData);
in.close();
```

Another powerful feature of the G4ElementData class is the simplicity in accessing the data. For example, to obtain the total cross-section for an electron with energy E in an element with atomic number Z, one uses the $GetValueForElement$ function.

```
tcs->GetValueForElement(Z,E);
```

Chapter 9

Results

In this chapter, a wide array of results that capture the key features of the Moment-Preserving (MP) method are presented. In particular, the key features of this method demonstrated are:

- systematic accuracy,
- efficient,
- mathematically robust,
- versatile,
- simple.

The results section begins by demonstrating the first feature of the MP method through calculation of highly differential quantities like angular distributions and energy spectra. In these calculations, the MP method is tested under the strictest possible conditions (that is, high-energy mono-energetic pencil beams normally incident on thin slabs). Under these conditions, analog or single-scatter models are

typically required. However, it is shown that both transmitted and reflected angular distributions and energy-loss spectra can be resolved through use of the hybrid DCS. Though the emphasis of this section is the demonstration of the systematic nature of the MP method, efficiency gains of at least five times analog efficiencies were demonstrated while maintaining analog level accuracy in very thin slabs. Under these extreme conditions where the hybrid model is successful, the discrete model tends to result in artifacts. However, it is possible to utilize the discrete model in thicker slabs where the benefit of efficiency gains is significantly improved. Following the angular distribution and energy spectrum results, longitudinal and lateral distributions are presented where the first two features of the method are again demonstrated on this different, but important quantity.

Given a clear understanding of the systematic feature of this method, results for less extreme problem conditions are presented to show that for more practical applications the MP method is not just accurate, but also very efficient. That is, we show that for 1-D and 2-D dose calculations the MP method achieves analog level accuracy while improving efficiency up to three orders of magnitude over analog efficiencies. We show that this is true for low-Z and high-Z materials, for molecules like water or bone, and multi-region problems. Furthermore, it is shown that material interfaces in multi-region problems do not introduce additional error at interfaces as does the condensed history method. This is because the MP method is a transport-based approximation and the benefit of this type of approach is that no additional algorithm is required to handle material interfaces.

Prior to this work, no effort had been made to validate the MP method through comparison with experimental benchmarks. Therefore, several results are presented in efforts to begin this validation process. Specifically, results from the MP method are compared to the experimentally determined energy deposition profiles (that is, the Lockwood data [81]). Similar calculations are made with the Geant4 default elec-

tromagnetic physics option 3, so that accuracy and efficiencies for the MP method can be compared to the Geant4 physics. In addition, we compare charge deposition results generated using MP method with experimentally determined charge depositions (that is, the Tabata data [82]). A key concept to point out in comparing with experimental results is that if an analog model exists that is in acceptable agreement with an experimental benchmark and moments of this analog model are readily available, one can generate reduced order physics DCSs based on the aforementioned analog model and show similar levels of agreement while significantly improving efficient. In this sense, the versatility and simplicity of the method is demonstrated. That is, to improve agreement through use of a different analog model algorithmic changes are not required; one must simply obtain moments of some preferable analog model, generate an ROP DCS library for this analog model, and run the calculation.

Finally, for completeness the MP method is applied to a space weather application to show that this method is not just effective for theoretical calculations. In particular, the total response function is generated for the CEASE detector telescope using an analog model, a discrete model, and the default Geant4 electromagnetic physics with option 3.

In all comparisons, the analog benchmark is obtained by using an analog elastic DCS and an analog inelastic DCS (with exception of the validation section). The analog benchmark is numerical rather than experimental, so to some degree it is idealized. This type of benchmarking is required to illustrate how accuracy is achieved through preservation of the analog DCS moments. In the following sections, accuracy and efficiency is measured with respect to the analog benchmark.

9.1 Angular Distributions and Energy Spectra

In this section, the accuracy of the MP method is tested under conditions that are often times impractical to simulate without the use of an analog model. That is, the transport of a mono-energetic pencil beam of electrons with energies above several hundred keV in thin slabs. Of particular interest is the calculation of reflected and transmitted angular distributions and energy spectra in slabs with varying thicknesses down to 100 analog elastic mfps ($\sim$ 1 to 100 μm). It is shown that under these conditions the MP method is effective at resolving angular distributions and energy spectra through the use of suitable reduced order physics (ROP) DCSs. Under these extreme conditions, a hybrid DCS is, in most cases, required to resolve these distributions. While it is possible to resolve highly peaked distributions with analog level accuracy using the MP method, this is typically accompanied by losses in efficiency. Nonetheless, the ability to systematically control accuracy such that one can predict angular distributions and energy spectra for highly-peaked scattering in thin slabs is a strong feature of this method.

While it is true that one cannot expect to realize significant efficiency gains with analog level accuracy under the aforementioned conditions, in more realistic settings (that is, thicker regions) it is possible to relax the ROP models such that both analog level accuracy and significant efficiency gains are achieved. Relaxation of the ROP models is possible in thicker slabs because the initial pencil beam experiences more spreading in space, angle, and energy in thicker slabs. This is simply an effect of the number of collisions sustained by an electron while traversing a medium. In thicker slabs, electrons suffer more collisions; thus, causing additional spreading of the initial state of the beam. With additional spreading of the beam, less information in the form of analog DCS moments is required to resolve angular distributions and energy spectra. Therefore, the ROP DCS can be relaxed or models preserving fewer moments can be utilized.

In the following two sections, the impact of the size of the slab on the accuracy of the MP method is demonstrated. Both discrete and hybrid models are tested for angular distribution and energy spectrum calculations in low-Z and high-Z slabs with varying thicknesses. The thickness of the slab is measured with respect to the analog elastic mfp corresponding to the source particle energy and the target material. Results for slabs with thicknesses of 100, 300, 1000, and 3000 analog elastic mfps are presented (in the remaining discussion mfp implies analog elastic mfp). In Fig. 9.1, problem setup is described.

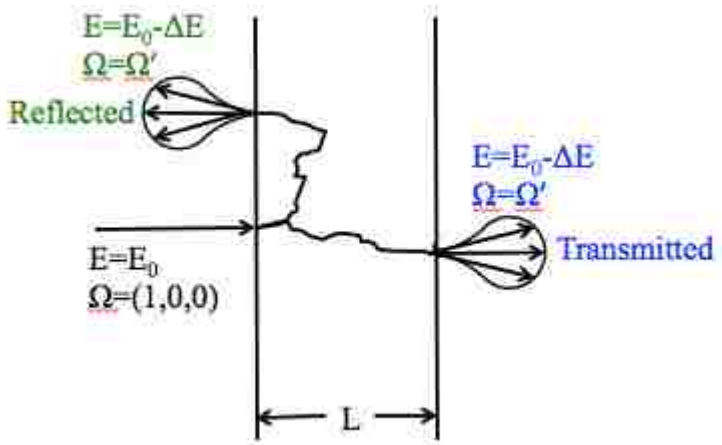

Figure 9.1: Problem setup for calculation of angular distributions and energy spectra.

9.1.1 Angular distributions

Reflected and transmitted angular distributions are presented below for one-dimensional slabs composed of aluminum or gold with thicknesses of 100, 300, 1000, and 3000 mfps (that is, $L = 100\lambda_{el},\ 300\lambda_{el},\ 1000\lambda_{el},\ 3000\lambda_{el}$). The source is positioned at $x = 0$ with a direction of $\vec{\Omega} = (1, 0, 0)$. A total of 4×10^7 source particles are simulated when calculating the angular distributions. The analog benchmark is a solution to the aforementioned problem using analog Monte Carlo, where elastic scattering is

given by the partial-wave DCS and inelastic scattering is given by the Möller DCS. Uncertainties associated with these results are within 1% in most bins, such that one can state conclusively that good agreement exists between the ROP models and the analog benchmark.

First, the most challenging problem is presented. That is, calculation of transmitted angular distributions for 10000-keV electrons incident on an aluminum or gold slab 100 mfps thick. In Figs. 9.2a and 9.2b, transmitted angular distributions in aluminum and gold computed using the discrete and hybrid DCSs are compared to the analog benchmark. There are a few features to note in Fig. 9.2. The peakedness of this distribution is extreme and varies about three orders of magnitude over only 10 degrees. This level of peakedness is difficult to resolve with a discrete elastic DCS and results in the discrete artifacts seen clearly in the Figs. 9.2a and 9.2b. The difficulty in resolving highly peaked distributions using the discrete DCS results from the form of the DCS. That is, electrons can only scatter through N discrete angles determined by the order of the DCS. Therefore, the N discrete angles are favored in the angular distribution because in thin slabs electrons do not suffer enough collisions such that various combinations of scattering events smooth out the artifacts. However, through use of the hybrid model the discrete artifacts are mitigated and the only noticeable differences in the hybrid model solution and the analog benchmark are in the tail where the differences in the solutions are statistically insignificant. In Fig. 9.2c, the impact of target atomic number is shown, where for increasing Z the distribution is less-peaked. However, the impact of the atomic number on the peakedness of the scattering is not significant enough to dramatically improve the discrete results in thin slabs for 10000-keV electrons.

Even in aluminum slabs with thicknesses of 3000 mfps for 10000-keV electrons, the discrete DCS results in artifacts as seen in Fig. 9.3a. This is an indication of the extreme peakedness of the scattering at higher energies and in this regime a hybrid

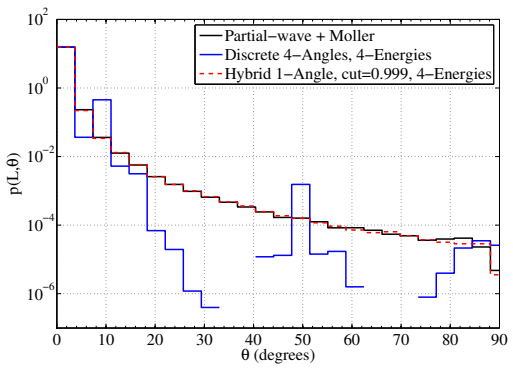

(a) Aluminum

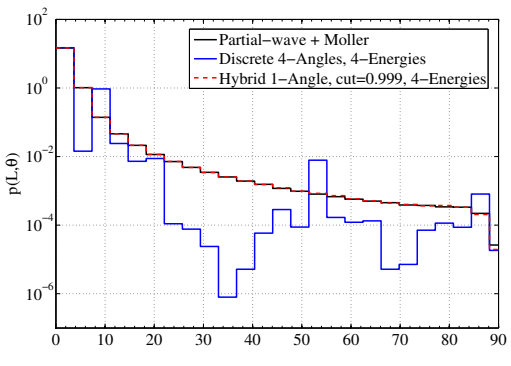

(b) Gold

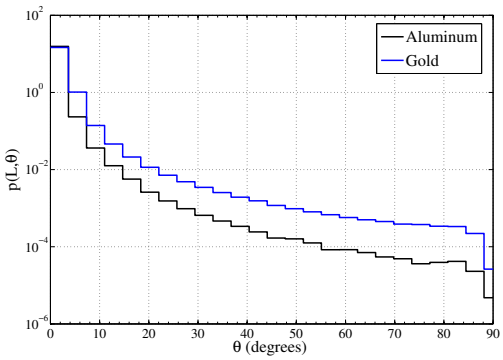

(c) Analog Benchmark

Figure 9.2: Transmitted angular distributions for 10000-keV electrons on 100 mfp thick aluminum (a) and gold (b) slabs calculated using the analog model (solid black), a purely discrete model with 4-angles and 4-energies (solid blue), and a hybrid elastic model with a single angle and $\mu^* = 0.999$ and a discrete inelastic model with 4-energies (dashed red). The analog benchmarks (c) are in black for aluminum and blue for gold.

DCS is required to resolve the transmitted angular distribution unless additional angles are used. However, it is clear by Figs. 9.3a and 9.3b that in thicker slabs where particles undergo thousands of collisions that the discrete artifacts are greatly reduced. Furthermore, the impact of the atomic number is seen in Fig. 9.3b, where the discrete artifacts are less pronounced in the gold slab because scattering of electrons by high-Z materials is less peaked. Nonetheless, it is always possible to utilize a hybrid model to resolve angular distributions overwhelmed by discrete artifacts.

In thicker slabs, it is possible to relax the cut-off to $\mu^* = 0.99$ for the hybrid model improving the efficiency of the calculation while remaining accurate.

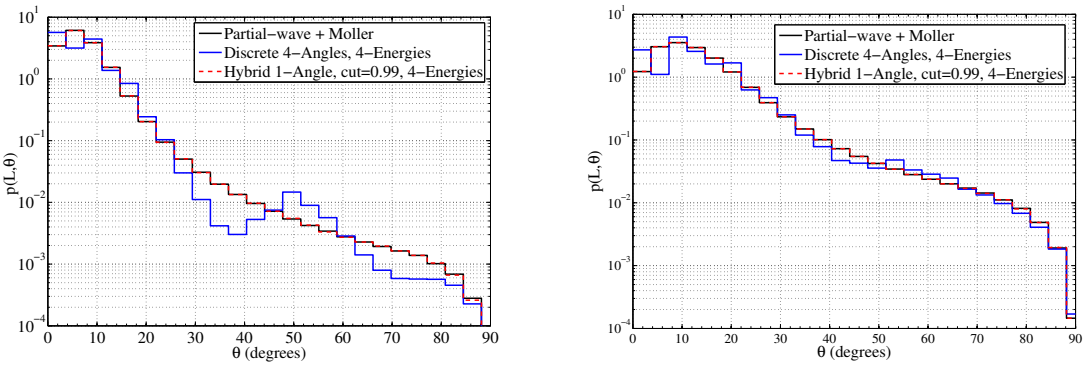

(a) Aluminum

(b) Gold

Figure 9.3: Transmitted angular distributions for 10000-keV electrons on 3000 mfp thick aluminum (a) and gold (b) slabs calculated using the analog model (solid black), a purely discrete model with 4-angles and 4-energies (solid blue), and a hybrid elastic model with a single angle and $\mu^* = 0.999$ and a discrete inelastic model with 4-energies (dashed red).

The results in Figs. 9.2 and 9.3 indicate that it is possible to resolve angular distributions in highly-peaked scattering regimes by systematically increasing the accuracy of the ROP DCS through preservation of additional moments. Of course, increasing accuracy will reduce the efficiency of the calculation, but under these conditions (highly-peaked scattering in thin slabs) analog Monte Carlo efficiencies are typically manageable, so efficiency gains of two to five times faster than analog Monte Carlo is considered a significant improvement. As was pointed out, the emphasis of this section was not to necessarily demonstrate orders of magnitude efficiency gains, but rather to show that the ROP models limit to analog level accuracy even under extreme conditions. That said, it is of interest to maximize efficiency gains whenever possible. Therefore, the following results provide a sense of the accuracies associated with a less-extreme scattering regime. Efficiency results are presented later in section 9.1.3 and indicate that it is possible to resolve angular distributions efficiently (up

to two orders of magnitude more efficient than analog) and accurately; especially, in less-extreme scattering regimes.

The following figures present transmitted angular distributions in a less-peaked scattering regime. That is, 1000-keV electrons incident on gold slabs with varying thicknesses. As noted, the peakedness of the scattering is a function of particle energy and the target atomic number. With decreased particle energy and increased atomic number, the peakedness is reduced. Nonetheless, even for 1000-keV electrons on gold the problem is still extremely anisotropic with respect to neutral particle scattering. In Fig. 9.4, the impact of slab thickness and in turn, the effectiveness of the discrete model is demonstrated. In Figs. 9.4a and 9.4b, discrete artifacts are present for slabs 100 and 300 mfps thick, but the hybrid model is in good agreement in these cases. However, in Figs. 9.4c and 9.4d, discrete models with at most 4-angles are sufficient when resolving the transmitted angular distribution. In fact, in Fig. 9.4d the discrete artifacts resulting from a single-angle discrete model are almost negligible and though there is not perfect agreement the general behavior of the transmitted angular distribution is captured.

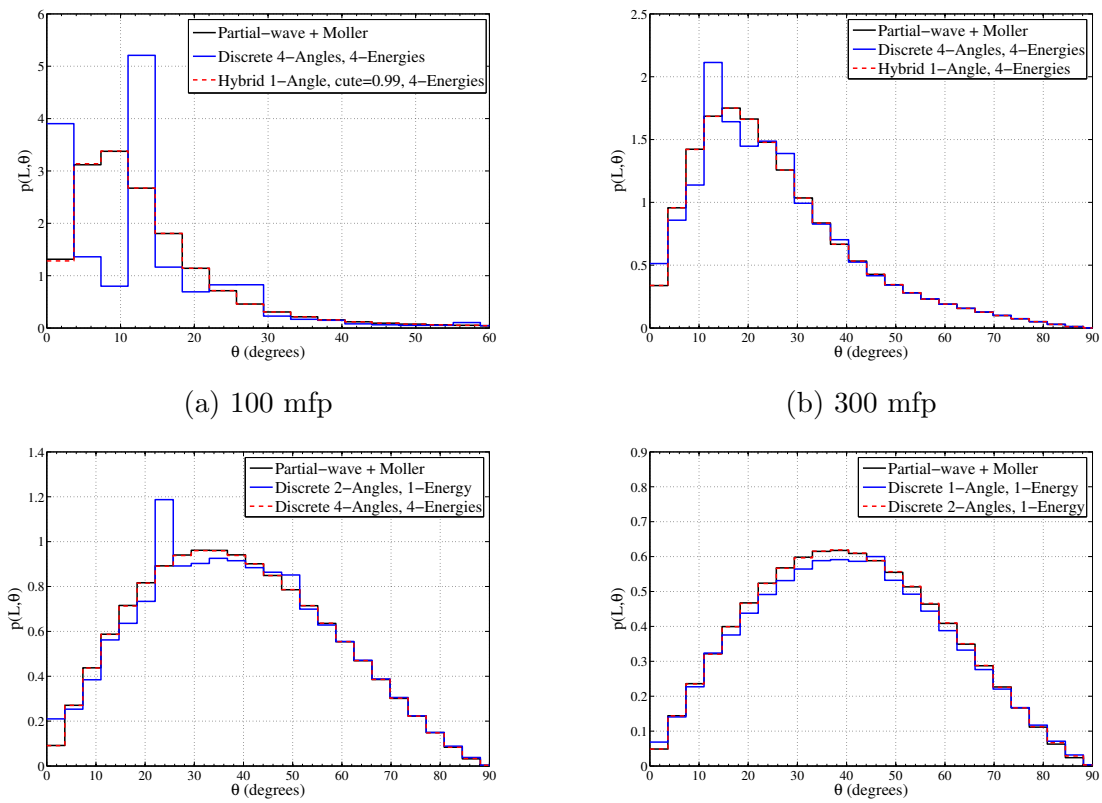

(a) 100 mfp

(b) 300 mfp

(c) 1000 mfp

(d) 3000 mfp

Figure 9.4: Impact of slab thickness on the transmitted angular distribution for 1000-keV electrons on gold. Various discrete and hybrid models are compared to the analog benchmark for gold slabs 100, 300, 1000, and 3000 mfps thick.

We now present reflected angular distributions for 1000-keV and 10000-keV electrons on aluminum or gold slabs with thicknesses of 100, 300, 1000, and 3000 mfps. In Fig. 9.5 reflected angular distributions for 10000-keV electrons on gold are presented. First, note the distributions in Fig. 9.5 are significantly reduced in magnitude relative to the transmitted angular distributions for 10000-keV electrons. For highly-peaked scattering, a very small fraction of particles are reflected. Slab thickness has

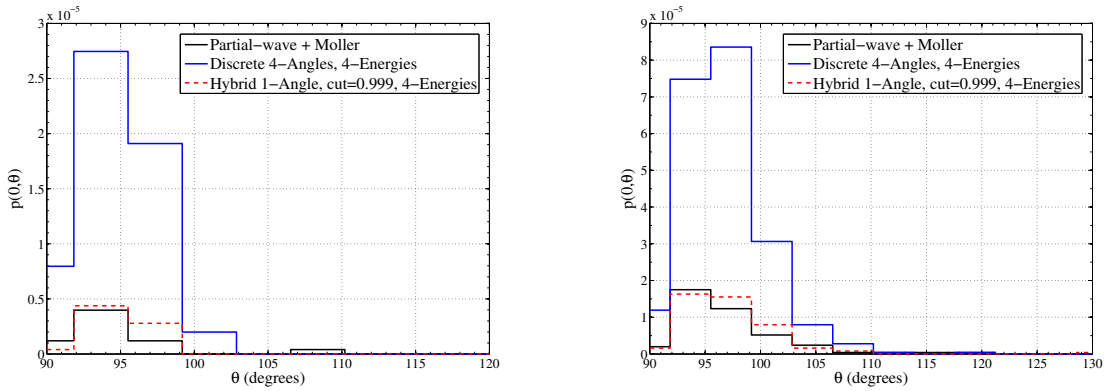

(a) 100 mfp

(b) 300 mfp

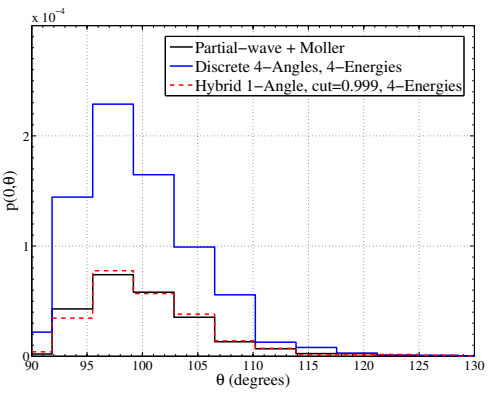

(c) 1000 mfp

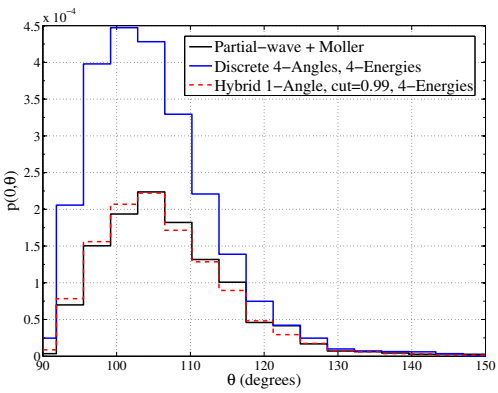

(d) 3000 mfp

Figure 9.5: Impact of slab thickness on the reflected angular distribution for 10000-keV electrons on aluminum. Various discrete and hybrid models are compared to the analog benchmark for aluminum slabs 100, 300, 1000, and 3000 mfps thick.

a similar impact on reflected distributions as for transmitted distributions. That is, with increasing slab thickness electrons suffer more collisions before being reflected, spreading the distributions in angle. In general, the discrete model tends to have the correct behavior; however, the distribution is roughly two to five times greater in magnitude. Once again, the hybrid model can be used in all cases. The disagreement between the analog benchmark and the hybrid models is statistical because very few particles are reflected.

In Fig. 9.6 angular distributions for 1000-keV electrons incident on gold slabs with thicknesses of 100, 300, 1000, and 3000 mfps are presented. For lower energies in high-Z materials the scattering is less-peaked and the ROP model can be relaxed under these conditions. Specifically, reflected angular distributions generated using the discrete model are not overwhelmed by artifacts as seen in Fig. 9.6. For slabs of sufficient thickness, a hybrid model is not required and the more efficient discrete model can be utilized. For slabs that are 3000 mfps thick (Fig. 9.6d), a single-angle, single-energy discrete model provides noteworthy agreement.

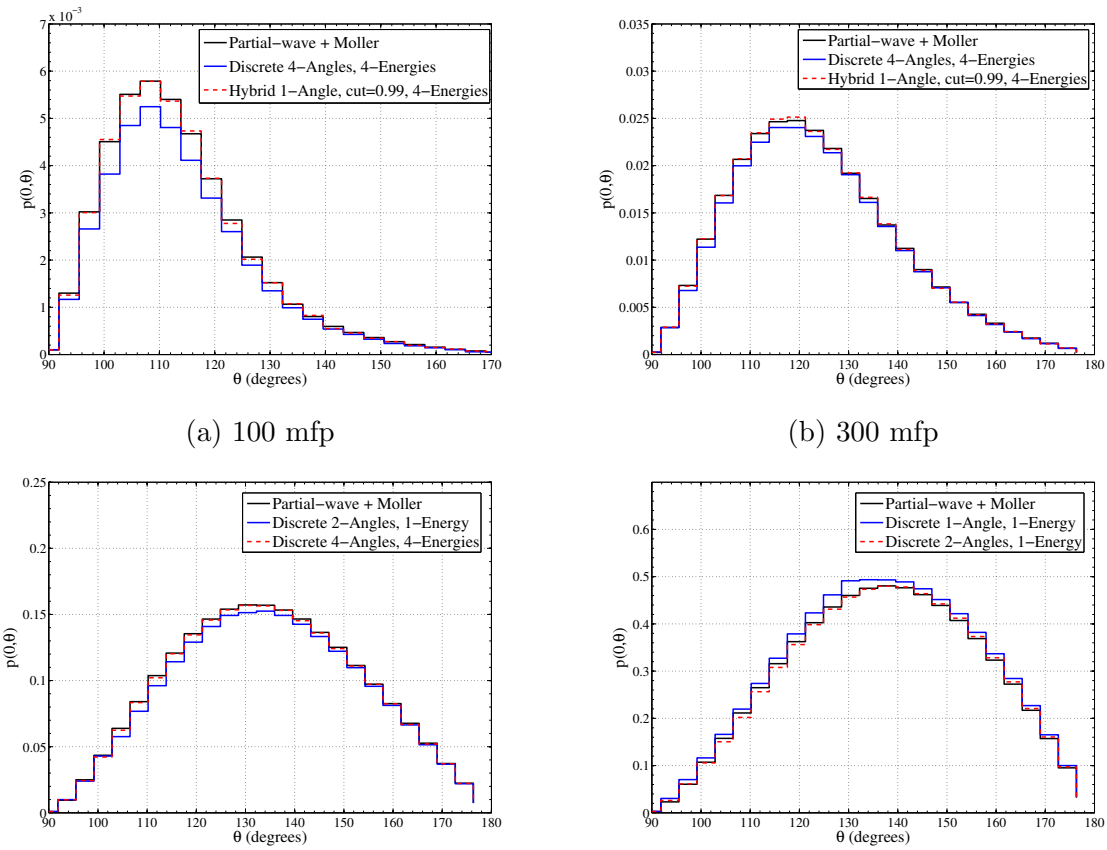

(a) 100 mfp

(b) 300 mfp

(c) 1000 mfp

(d) 3000 mfp

Figure 9.6: Impact of slab thickness on the reflected angular distribution for 1000-keV electrons on gold. Various discrete and hybrid models are compared to the analog benchmark for gold slabs 100, 300, 1000, and 3000 mfps thick.

9.1.2 Energy spectra

Next, reflected and transmitted energy spectra are examined. The simulation characteristics, including slab thickness, material types, and the number of source particles, are the same as described in the previous section. Discrete inelastic DCS models are not presented because a sufficient number of inelastic collisions do not occur in thin slabs overwhelming the spectra with discrete artifacts. Therefore, the focus is on two different hybrid inelastic DCS models. The hybrid models include DCSs with $Q^* = 10\text{-}keV$ and one or two discrete energies. In each of the following results, elastic scattering is modeled by a discrete four-angle DCS. Again, the most challenging problem, 10000-keV electrons on aluminum slabs, is considered first. In Fig. 9.8, transmitted energy-loss spectra are presented for aluminum slabs with thicknesses of 100, 300, 1000, and 3000 mfps. As seen in Fig. 9.7, it is possible to resolve the transmitted energy-loss spectra with a sufficiently accurate hybrid inelastic model. For 10000-keV electrons on aluminum, a two-energy hybrid model is required. However, for 1000-keV electrons on gold, it is possible to relax the inelastic model to a single energy with the same cut-off. In Fig. 9.8, results for 1000-keV electrons on gold are presented. Under these conditions, inelastic scattering is also less-peaked and the hybrid model can be relaxed. However, a discrete representation is still not sufficient.

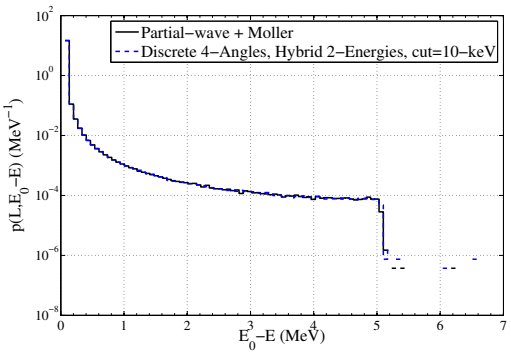

(a) 100 mfp

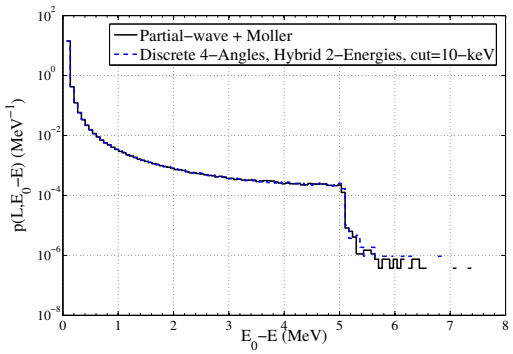

(b) 300 mfp

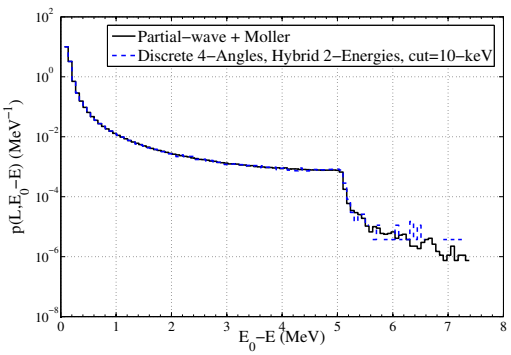

(c) 1000 mfp

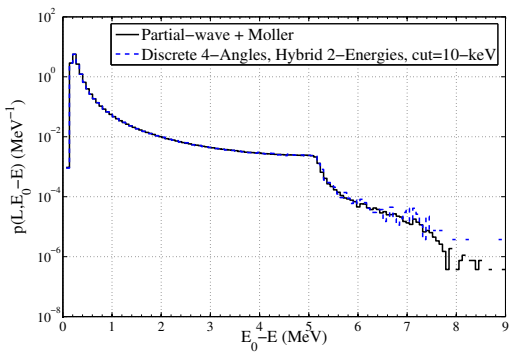

(d) 3000 mfp

Figure 9.7: Impact of slab thickness on the transmitted energy-loss spectra for 10000-keV electrons on aluminum slabs 100, 300, 1000, and 3000 mfps thick.

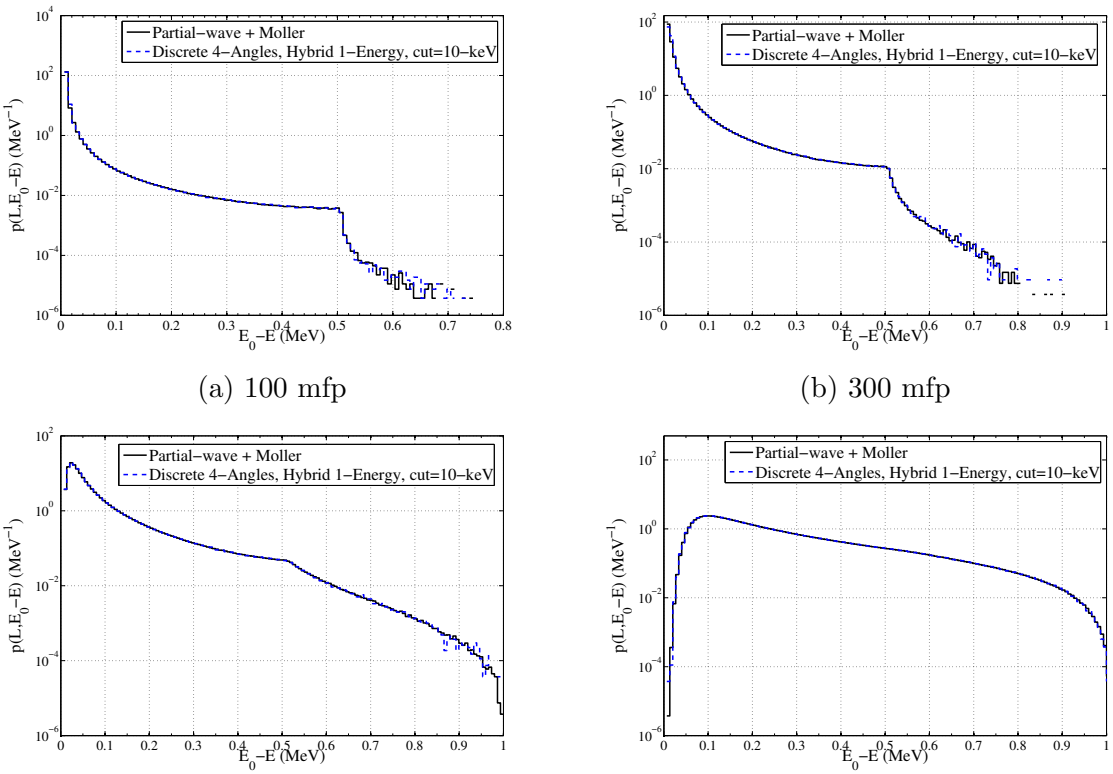

(a) 100 mfp

(b) 300 mfp

(c) 1000 mfp

(d) 3000 mfp

Figure 9.8: Impact of slab thickness on the transmitted energy-loss spectra for 1000-keV electrons on gold slabs 100, 300, 1000, and 3000 mfps thick.

Reflected energy-loss spectra for 10000-keV and 1000-keV electrons on gold are presented next. Reflected energy-loss spectra for 10000-keV electrons on aluminum are not presented because the reflected electrons experience almost no inelastic collisions. This is true even for gold as seen in Figs. 9.9a and 9.9b for slabs that are 100 and 300 analog mfps thick, where the distributions are nearly singular about zero energy-loss. That said, the hybrid model also predicts this nearly singular behavior. For thicker slabs, 1000 and 3000 analog mfps, the reflected energy-loss spectra spreads out more. Here, the hybrid model is in good agreement in the statistically significant regions of the spectra (that is, the peaked region of the spectra).

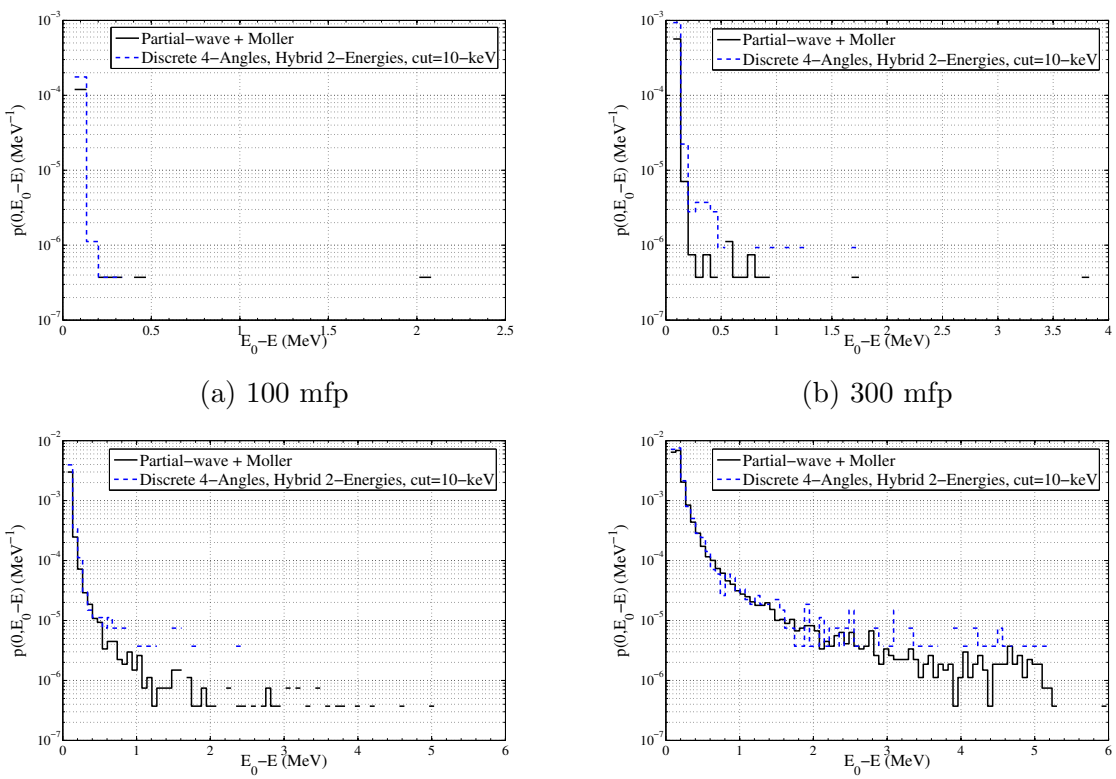

(a) 100 mfp

(b) 300 mfp

(c) 1000 mfp

(d) 3000 mfp

Figure 9.9: Impact of slab thickness on the reflected energy-loss spectra for 10000-keV electrons on gold slabs 100, 300, 1000, and 3000 mfps thick.

In Fig. 9.10, reflected energy-loss spectra are presented for 1000-keV electrons on gold. Once again, in this less-peaked regime the spectra are not nearly as singular and a relaxed, single-energy hybrid model can be utilized.

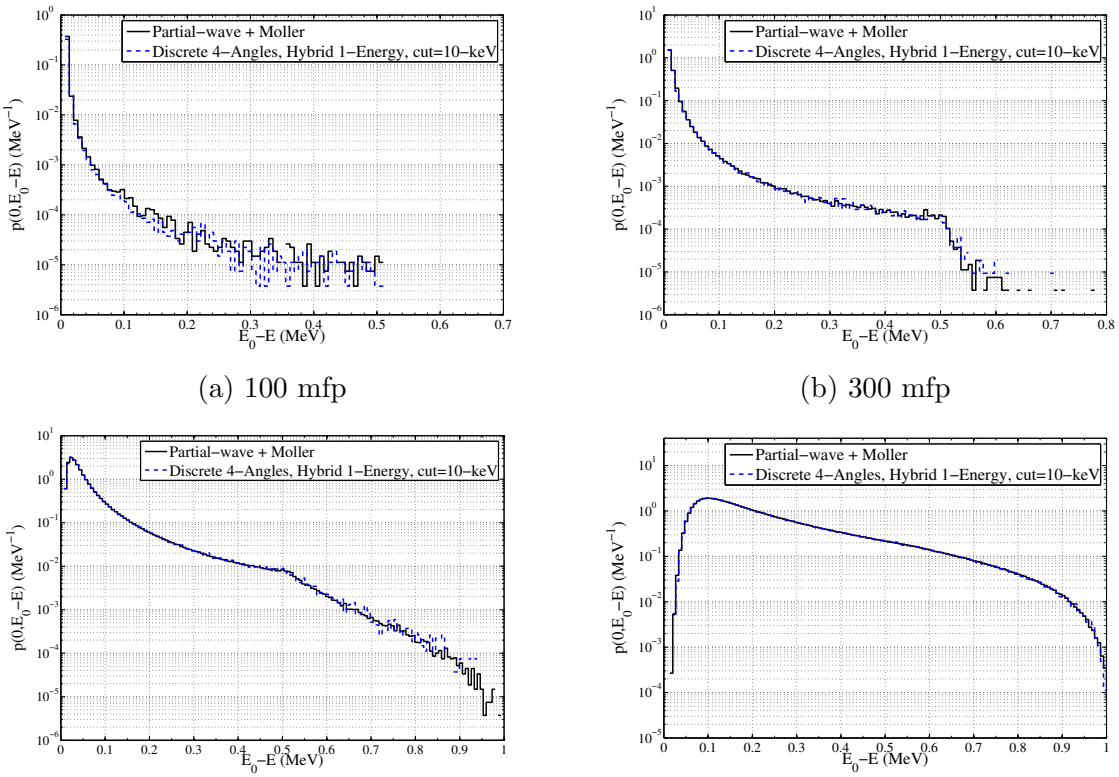

(a) 100 mfp

(b) 300 mfp

(c) 1000 mfp

(d) 3000 mfp

Figure 9.10: Impact of slab thickness on the reflected energy-loss spectra for 1000-keV gold slabs 100, 300, 1000, and 3000 mfps thick.

9.1.3 Efficiencies for thin slab problems

In this section, efficiency results for the previously discussed thin slab problems are presented in Tables 9.1 and 9.2 for 1000-keV and 10000-keV on aluminum or gold slabs of various thicknesses respectively. In general, efficiency gains depend on the slab thickness, the target atomic number, and the energy of the particle. The dependence of efficiency on target atomic number and energy was noted in Chapter 7 and presented in Figs. 7.1 and 7.2. However, the dependence on the problem geometry, or the slab thickness in particular, is captured in the following tables. The greatest efficiencies are realized in thicker slabs where particles undergo more collisions. In thin slabs (100 and 300 analog mfps), efficiency gains range from 5 to 60 times faster than analog Monte Carlo. Whereas for thicker slabs, efficiency gains range from one to three orders of magnitude faster than analog Monte Carlo.

In previous sections, it was mentioned that there is a trade-off between accuracy and efficiency. This will be clarified in remainder of this discussion. First, remember that under the most extreme conditions (10000-keV electrons on 100 to 300 mfps of aluminum) hybrid models were required to resolve angular distributions and energy spectra. The efficiency gains associated with these models, under these conditions range from 15-47 times the efficiency of an analog Monte Carlo calculation. What would take a day now requires only an hour without sacrificing accuracy. Now, note that it was possible to resolve angular distributions for 1000-keV electrons on gold slabs with thicknesses of 1000 and 3000 mfps using various discrete models. Under these conditions, efficiency gains of 150-500 times the efficiency of an analog Monte Carlo calculation are realized without sacrificing accuracy. In this case, what would take a day takes less than ten minutes.

Table 9.1: Efficiency gains for various ROP DCSs when simulating 1000-keV and 10000-keV electrons incident on aluminum slabs 100, 300, 1000, and 3000 mfps thick.

		Reduce Order Physics Model				
Slab-width (mfps)	Particle Energy	1-Angle 1-Energy	4-Angles 1-Energies	4-Angles 4-Energies	1-Angle $\mu^* = 0.99$ 4-Energies	4-Angles 1-Energy $Q^* = 10\text{-}keV$
100	1000-keV	21.003	17.829	15.295	4.8543	10.221
	10000-keV	22.034	21.951	20.729	15.796	12.956
300	1000-keV	55.862	42.782	32.539	15.688	21.566
	10000-keV	60.086	61.626	55.159	47.856	27.176
1000	1000-keV	173.72	63.216	55.952	11.345	40.848
	10000-keV	200.40	170.12	145.16	86.197	84.930
3000	1000-keV	475.48	178.07	108.84	20.762	75.594
	10000-keV	609.86	555.76	360.40	113.76	71.241

Table 9.2: Efficiency gains for various ROP DCSs when simulating 1000-keV and 10000-keV electrons incident on gold slabs 100, 300, 1000, and 3000 mfps thick.

		Reduce Order Physics Model				
Slab-width (mfps)	Particle Energy	1-Angle 1-Energy	4-Angles 1-Energies	4-Angles 4-Energies	1-Angle $\mu^* = 0.99$ 4-Energies	4-Angles 1-Energy $Q^* = 10\text{-}keV$
100	1000-keV	20.211	16.183	15.049	7.6928	12.279
	10000-keV	18.713	20.255	19.429	17.257	19.977
300	1000-keV	60.548	36.899	33.331	10.377	26.222
	10000-keV	61.954	56.729	54.230	86.197	45.301
1000	1000-keV	173.72	63.216	55.952	17.954	29.534
	10000-keV	200.40	170.12	145.16	89.322	39.129
3000	1000-keV	564.75	133.90	121.69	22.994	90.900
	10000-keV	1174.5	860.55	591.36	255.05	254.25

In section 9.1, it was shown that for a given ROP DCS model, the accuracy of the result depends on the peakedness of the distribution being resolved. The peakedness of the distribution, in turn, depends on the slab thickness and the regime of scattering which is a function of particle energy and target atomic number. Regardless, an ROP DCS can be made to preserve additional moments of the analog DCS; thus, refining the model and achieving analog level accuracy under very extreme simulation conditions. While it is not possible to achieve several orders of magnitude efficiency gains under these conditions, the ROP models were at least five times faster than analog Monte Carlo and up to 45 times faster in some cases. Under more relaxed conditions, up to three orders of magnitude efficiency gains were achieved. Regardless, accuracy and efficiency suitable for a wide variety of problems can be realized by adjusting the ROP DCSs.

9.2 Longitudinal and Lateral Distributions

At this point, it is clear that accuracy and efficiency is problem dependent. Nonetheless, it is possible to refine the ROP DCS such that sufficient levels of accuracy and efficiency are realized. In this section, a few additional results are presented that overlap with the previous section in the sense that problems corresponding to scattering regimes ranging from extreme peakedness to less-extreme peakedness are tested. Here, results in connection with Lewis theory are presented to demonstrate the moment-preserving property of this method, while again demonstrating the accuracy of this method is systematically controllable.

In particular, longitudinal and lateral distributions for 100-keV, 1000-keV, and 10000-keV electrons after traveling a distance of 100, 300, 1000, and 3000 mfps in an infinite medium of copper are presented (similar to Benedito et al. [83]). In these problems, energy-loss is not considered. The longitudinal and lateral distributions

are generated using the analog Monte Carlo method where elastic scattering is given by the partial-wave DCS. These distributions are referred to as the analog benchmark and are compared with several solutions generated using discrete and hybrid models. In all of the results presented in this section, 4×10^7 electrons were simulated for each model and uncertainties associated with the majority of the results are within 1%; especially, in the highly probable regions. However, in regions where the distribution is small with respect to the maximum value (for example, in the tails of the distributions), the results are statistically insignificant.

In Fig. 9.11, a diagram of the problem simulated is presented. The electron starts at $s = 0$ with an initial direction and travels until reaching a distance of $s = s_{max}$. At this point, the electrons longitudinal displacement, or the projection of the path traveled onto the initial trajectory, and lateral displacement, or the orthogonal projection of the pathlength, is tallied. Although it is not clear from Fig. 9.11, it is possible for an electron to turn around and travel in directions opposite to the initial direction. In these cases, it is possible for the electron to have a negative longitudinal displacement. The same is not true for lateral displacement because the lateral displacement is a measure of radius and therefore, non-negative.

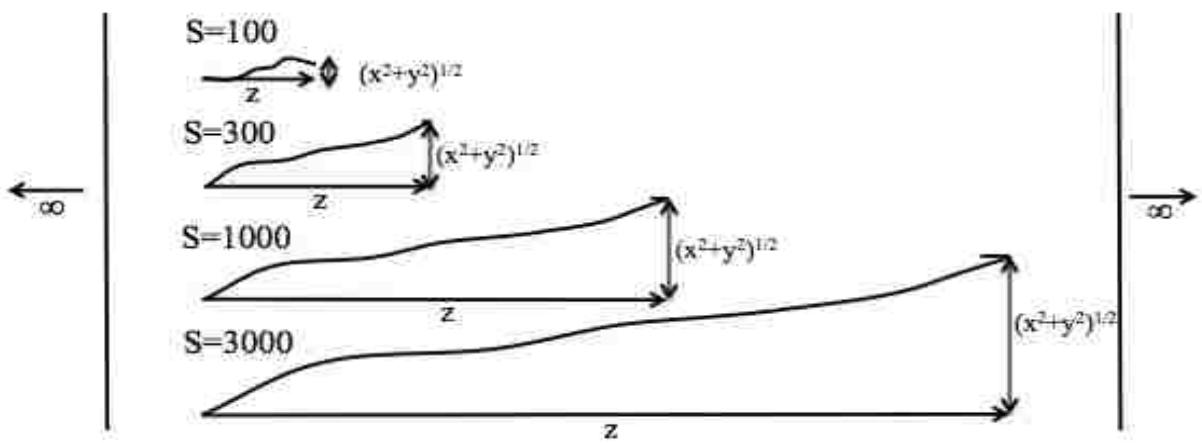

Figure 9.11: Problem setup for longitudinal and lateral distribution calculations.

In addition to the longitudinal and lateral distributions, a few Lewis moments are compared including $\langle z \rangle$ and $\langle x^2 + y^2 \rangle$ or

$$\langle z \rangle = \int_{4\pi} d\Omega \int_{-\infty}^{\infty} dx \int_{-\infty}^{\infty} dy \int_{-\infty}^{\infty} dz \; z\psi(x, y, z, s, \vec{\Omega}), \tag{9.1}$$

and

$$\langle x^2 + y^2 \rangle = \int_{4\pi} d\Omega \int_{-\infty}^{\infty} dx \int_{-\infty}^{\infty} dy \int_{-\infty}^{\infty} dz \; (x^2 + y^2)\psi(x, y, z, s, \vec{\Omega}). \tag{9.2}$$

Here, the Monte Carlo method is used to carry out the integrals in Eqs. (9.1) and (9.2), by simulating the particle transport and tallying the longitudinal and lateral displacement after traveling 100, 300, 1000, or 3000 analog mfps. These results are presented in the following tables for each energy. As predicted by Lewis theory and seen in Table 9.3, models preserving at least $\Sigma_{el,1}$ will preserve $\langle z \rangle$. Therefore, even the very efficient single-angle model will have the correct average longitudinal displacement. Once again as predicted by Lewis theory and seen in Table 9.4, models preserving at least $\Sigma_{el,1}$ and $\Sigma_{el,2}$ will preserve $\langle x^2 + y^2 \rangle$. Therefore, the single-angle model that preserves $\Sigma_{el,1}$ and $\Sigma_{el,2}$ will have the correct average lateral displacement as well. Models preserving additional moments are not presented in Tables 9.3 and 9.4 because these results are redundant. Preservation of average longitudinal and lateral displacement are important to electron transport methods and in many cases these methods seek to preserve at least average longitudinal and lateral displacement. One of the major distinctions between condensed history and the MP method is that typically in condensed history the underlying multiple scattering theory is only setup to preserve $\Sigma_{el,1}$ and $\Sigma_{el,2}$, while the MP method can preserve an arbitrary number of Legendre moments guaranteeing preservation of higher-order Lewis moments. Not to mention, the most simple, efficient ROP model associated with the MP method preserves at least the average longitudinal and lateral distances.

Table 9.3: Average longitudinal displacement, $\langle z \rangle$, for 100-keV, 1000-keV, and 10000-keV electrons in copper after traveling a distance of 100, 300, 1000, and 3000 mfps.

Pathlength (mfps)	Particle Energy (keV)	$\langle z \rangle$ Analog	$\langle z \rangle$ 1-Angle	Rel. Unc.
100	100	0.8432	0.8433	0.00006
	1000	0.986664	0.986667	0.00001
	10000	0.999643	0.999644	0.000001
300	100	0.61815	0.61820	0.0002
	1000	0.96069	0.96070	0.00004
	10000	0.998931	0.998932	0.000005
1000	100	0.2761	0.2763	0.001
	1000	0.87673	0.87680	0.0001
	10000	0.996449	0.996448	0.00001
3000	100	0.09493	0.09497	0.006
	1000	0.6861	0.6863	0.0007
	10000	0.989399	0.989387	0.00005

Table 9.4: Average lateral displacement, $\langle x^2+y^2 \rangle$, for 100-keV, 1000-keV, and 10000-keV electrons in copper after traveling a distance of 100, 300, 1000, and 3000 mfps.

		$\langle x^2+y^2 \rangle$ Physics Model		
Pathlength (mfps)	Particle Energy (keV)	Analog	1-Angle	Rel. Unc.
100	100	0.154457	0.154456	0.0003
	1000	0.016420	0.016415	0.0008
	10000	0.000455	0.000454	0.003
300	100	0.26942	0.26944	0.0004
	1000	0.04683	0.04682	0.0009
	10000	0.001365	0.001364	0.004
1000	100	0.2365	0.2366	0.0007
	1000	0.1315	0.1314	0.001
	10000	0.0045244	0.0045245	0.0009
3000	100	0.11012	0.11016	0.002
	1000	0.2532	0.2531	0.001
	10000	0.01338	0.01339	0.004

Although preservation of $\Sigma_{el,1}$ and $\Sigma_{el,2}$ guarantees preservation of $\langle z \rangle$ and $\langle x^2 + y^2 \rangle$, resolving the longitudinal and lateral distributions $\big(p(z,s)$ and $p(b,s)\big)$ respectively (see section 4.2) requires preservation of additional moments. Similar to results from the previous section, discrete artifacts impact the shape of the longitudinal and lateral distributions. The impact of the artifacts is again dependent on the peakedness of the scattering and the number of collisions suffered by the electrons before tallying their displacement.

In Figs. 9.12-9.17, longitudinal and lateral distributions for 10000-keV down to 100-keV electrons in an infinite copper medium are presented. Each figure contains four results corresponding to gradually increasing pathlengths of 100, 300, 1000, and 3000 mfps. Again, the most challenging problem, or longitudinal and lateral distributions for 10000-keV electrons in copper, is presented first in Figs. 9.12 and 9.13. In all cases, the hybrid DCS utilized is in excellent agreement with the analog benchmark. For shorter pathlengths, both discrete models oscillate about the analog benchmark. The oscillations are an effect resulting from the discreteness of the DCS model where electrons tend to travel in preferential directions. Even for pathlengths of 1000 analog mfps, the 16-angle discrete model still oscillates subtly about the analog benchmark, but does not for pathlengths of 3000 analog mfps.

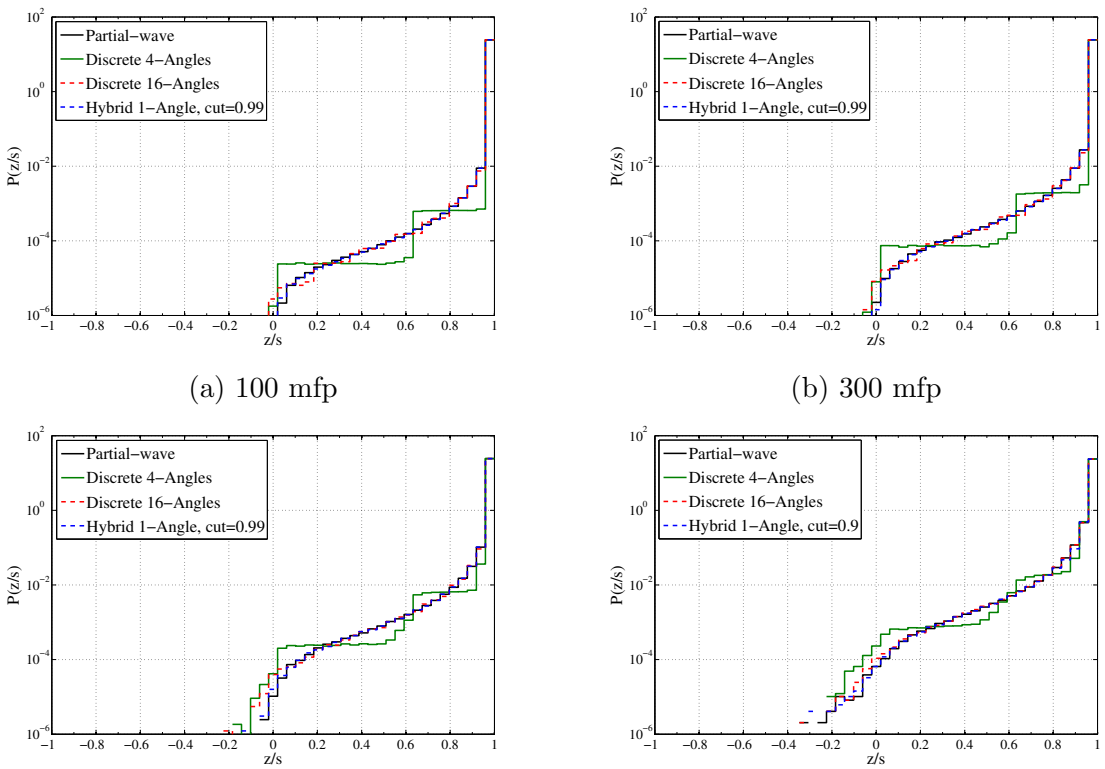

(a) 100 mfp

(b) 300 mfp

(c) 1000 mfp

(d) 3000 mfp

Figure 9.12: Comparison of longitudinal distributions for 10000-keV electrons after traveling a distance of 100, 300, 1000, and 3000 analog elastic mfps in copper.

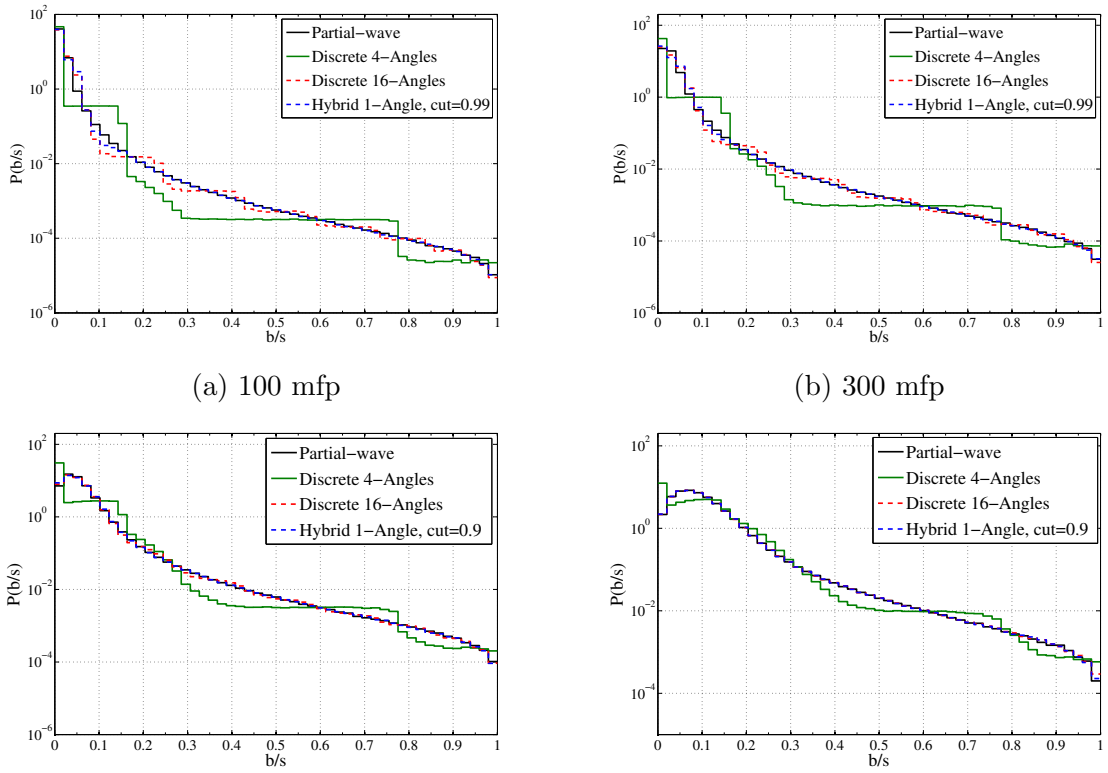

(a) 100 mfp

(b) 300 mfp

(c) 1000 mfp

(d) 3000 mfp

Figure 9.13: Comparison of lateral distributions for 10000-keV electrons after traveling a distance of 100, 300, 1000, and 3000 analog elastic mfps in copper.

As the energy of the particle decreases, the effectiveness of relaxed models (that is, models preserving fewer moments) is improved. For example, longitudinal and lateral distributions for 1000-keV electrons in copper are presented first in Figs. 9.14 and 9.15. In all cases, the hybrid DCS utilized is in excellent agreement with the analog benchmark and was relaxed from a cut-off of 0.99 down to a cut-off of 0.9 for pathlengths of 100 and 300 analog mfps and down to a cut-off of 0.5 for pathengths of 1000 and 3000 analog mfps. Moreover, discrete artifacts are not nearly as significant for 1000-keV electrons with exception of longitudinal and lateral distributions for pathlengths of 100 and 300 analog mfps. In fact, a 4-angle discrete model is sufficient for resolving longitudinal and lateral distributions for pathlengths of 1000 and 3000

analog mfps.

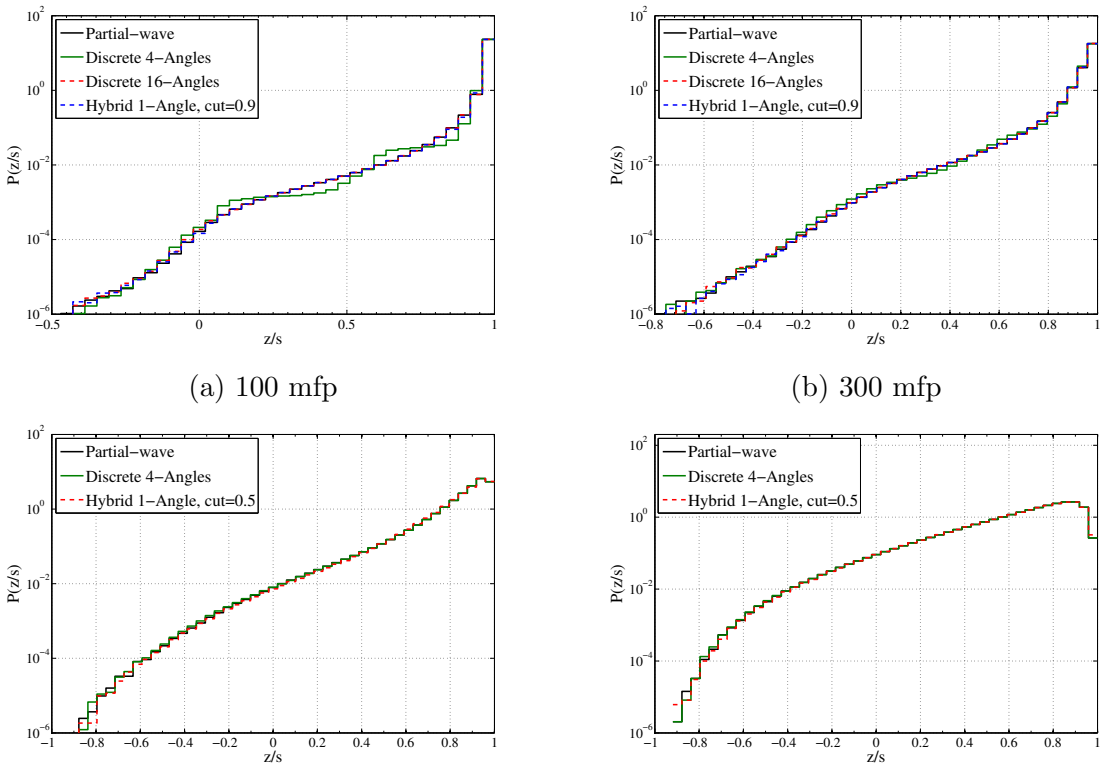

(a) 100 mfp

(b) 300 mfp

(c) 1000 mfp

(d) 3000 mfp

Figure 9.14: Comparison of longitudinal distributions for 1000-keV electrons after traveling a distance of 100, 300, 1000, and 3000 analog elastic mfps in copper.

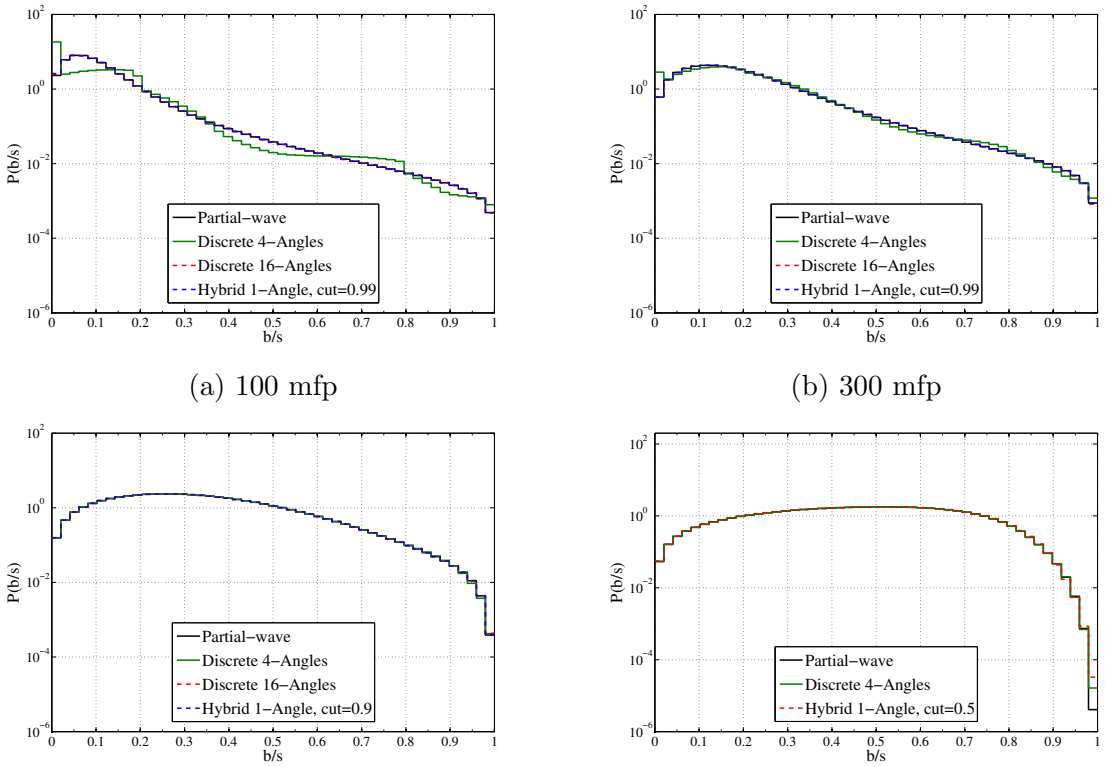

(a) 100 mfp

(b) 300 mfp

(c) 1000 mfp

(d) 3000 mfp

Figure 9.15: Comparison of lateral distributions for 1000-keV electrons after traveling a distance of 100, 300, 1000, and 3000 analog elastic mfps in copper.

Finally for 100-keV electrons, the most relaxed models tested are sufficient for pathlengths down to 100 analog mfps as seen in Figs. 9.16 and 9.17. Although single-angle results were not presented, a single-angle model is reasonably accurate for 100-keV electrons for pathlengths of 100 analog mfps and greater.

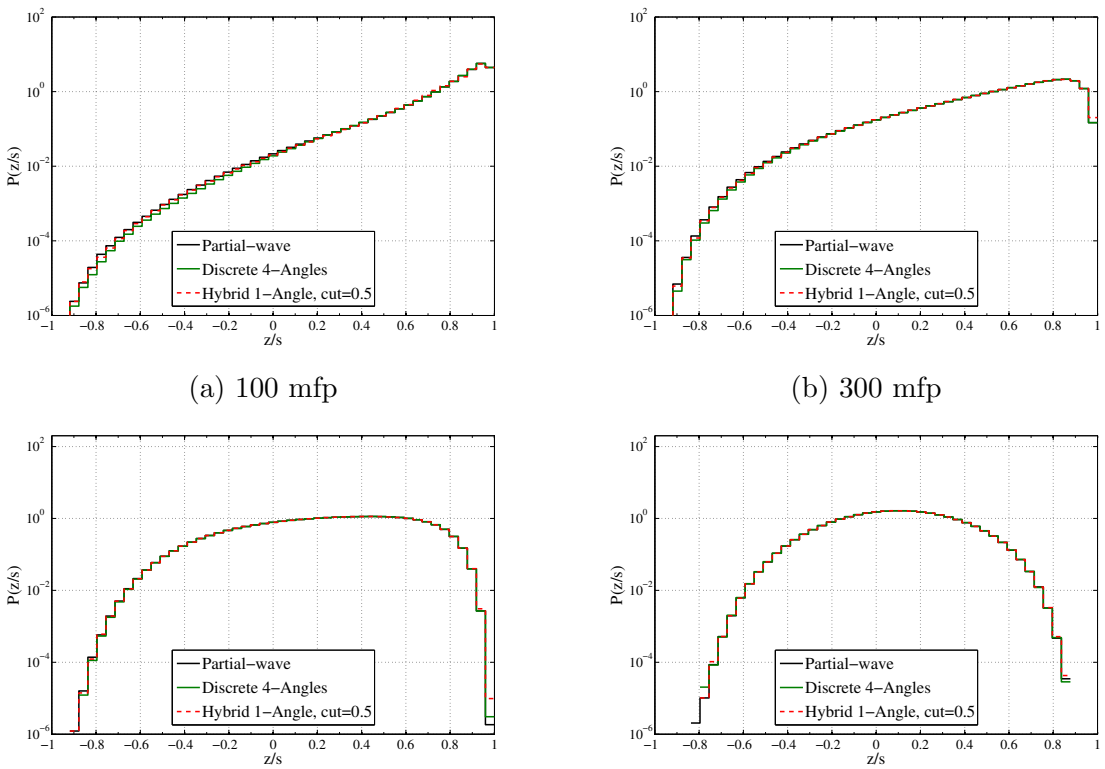

(a) 100 mfp

(b) 300 mfp

(c) 1000 mfp

(d) 3000 mfp

Figure 9.16: Comparison of longitudinal distributions for 100-keV electrons after traveling a distance of 100, 300, 1000, and 3000 analog elastic mfps in copper.

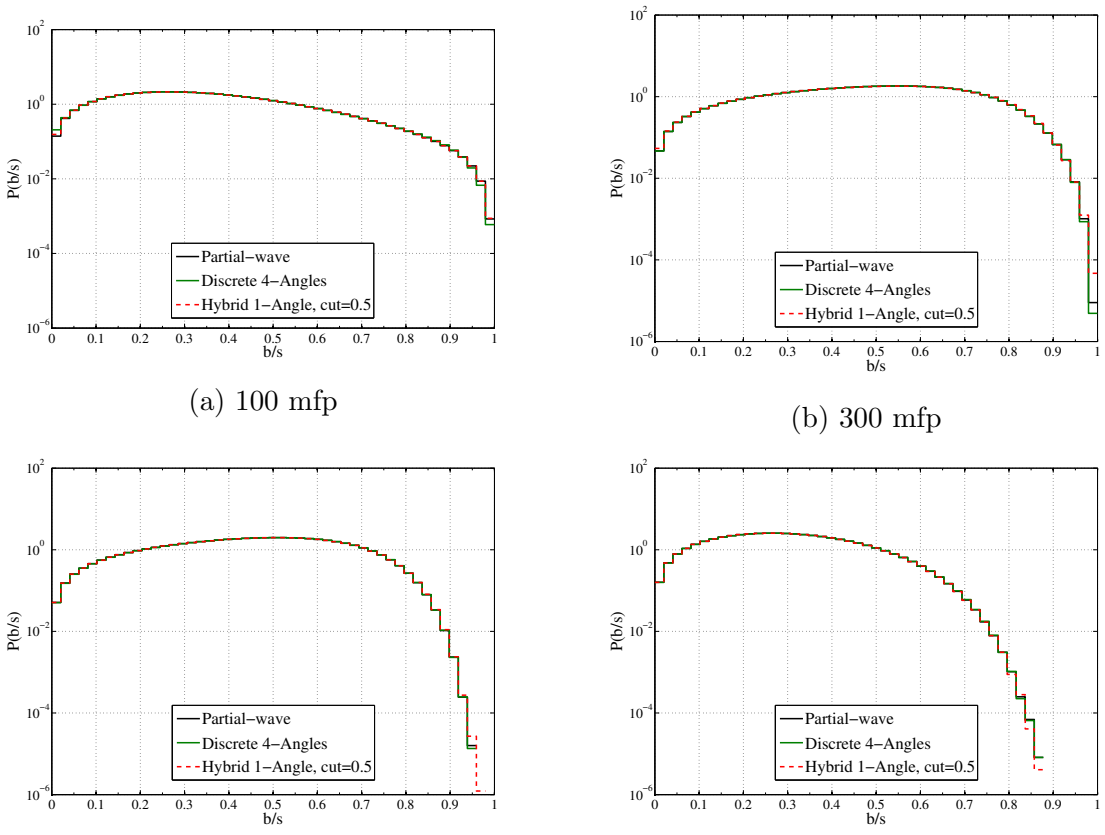

(a) 100 mfp

(b) 300 mfp

(c) 1000 mfp

(d) 3000 mfp

Figure 9.17: Comparison of lateral distributions for 100-keV electrons after traveling a distance of 100, 300, 1000, and 3000 analog elastic mfps in copper.

In this section, longitudinal and lateral results were presented to demonstrate the effectiveness of the MP method when calculating quantities that are critical to most CH methods and electron transport methods in general. It was shown that the average longitudinal and lateral displacement (typically used in CH pathlength correction algorithms) is in exact agreement with analog results for a single-angle (two moment-preserving) model. In other words, no additional pathlength correction algorithm is required in the MP method because the ROP DCS are constructed such that the Lewis moments are inherently preserved. In addition, longitudinal and lateral distributions for 100-keV (less-peaked scattering) to 10000-keV (highly-peaked

scattering) were generated using various ROP models. Depending on the problem at hand, ROP models requiring preservation of only a few moments were required for agreement with the analog benchmark. When necessary, additional moments were preserved to achieve analog level accuracy, but there was never a problem too extreme that the MP method failed to resolve the longitudinal or lateral distributions.

9.3 1-D and 2-D Dose Calculations

In this section, 1-D and 2-D dose results are presented. The dose results were generated using the partial-wave elastic scattering DCS and the Möller inelastic scattering model for the analog benchmark and the ROP DCSs were, in turn, constructed from these DCSs. Secondary production was not considered for this section. The following results show that the MP method can be used to calculate dose accurately in both relatively isotropic and highly peaked regimes regardless of the form of the analog model used to construct the ROP DCS. That is, accurate models can be constructed from both analytical DCS and tabulated DCS data. In this dissertation the emphasis is on tabulated elastic DCS data, as applications of the MP method to analytical DCSs has been demonstrated in the past [60, 61]. Efficiency gains improve significantly with increasing source energies without sacrificing accuracy. The trade-off between accuracy and efficiency, where it exist, ultimately depends on the application and the level of accuracy required by the user.

9.3.1 One-dimensional depth-dose profiles

Transversely integrated depth-dose profiles and relative differences are presented for 250-keV electrons in gold and 20000-keV electrons in water. In Fig. 9.18a, the results are nearly indistinguishable from the benchmark. However, Fig. 9.18b shows

disagreements that would otherwise be indistinguishable. In this simulation, disagreement is attributed to both the elastic and inelastic scattering models. Additional angles or use of the hybrid DCS smooths out the overestimation in the first cell. Adding another energy point to the discrete inelastic model smooths out the oscillation that begins near the peak dose. Though some refinement was necessary, only small adjustments were required to reduce the relative differences to within 1%.

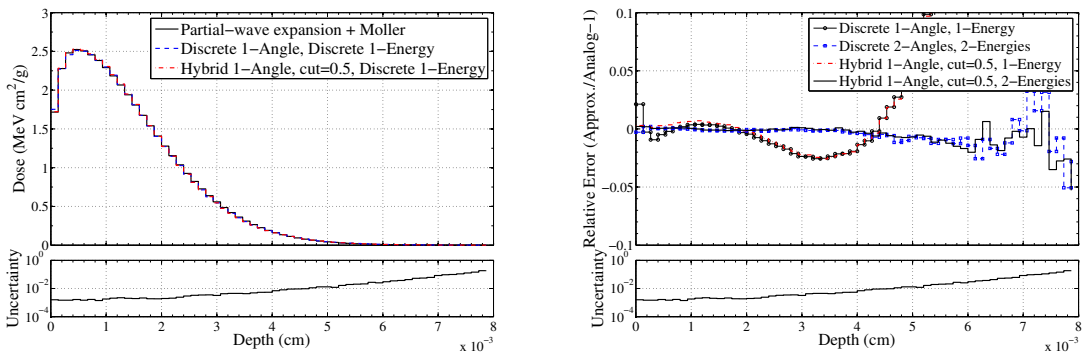

(a) Depth-dose profile

(b) Relative error

Figure 9.18: Comparison of depth-dose profiles (a) from 250-keV electrons on gold with discrete and hybrid elastic scattering and discrete inelastic models. The relative error in dose (b) from 250-keV electrons on gold calculated using discrete and hybrid elastic scattering models and discrete inelastic models. The relative error is measured with respect to the numerical benchmark generated using the partial-wave expansion elastic DCS and the Möller inelastic scattering models. The associated statistical uncertainty is included below each plot.

Efficiency gains are presented in Tables 9.5 and 9.6. For 250-keV electrons in gold efficiencies range from about 3 to 50 times faster than analog depending on the accuracy of the ROP DCS used. For 20000-keV electrons, in gold efficiencies range from about 70 to 1800 times faster than analog, while achieving accuracies nearly the same as those presented in Fig. 9.18b.

Table 9.5: Efficiency gains for various discrete DCSs when calculating dose due to a beam of electrons with energies of 250-keV, 1000-keV, and 20000-keV incident on a gold slab.

	ROP Model				
Particle Energy	1-Angle 1-Energy	2-Angles 1-Energy	2-Angles 2-Energies	4-Angles 1-Energy	4-Angles 4-Energies
250-keV	50.843	23.112	22.960	10.879	10.990
1000-keV	163.62	72.155	71.199	31.292	31.261
20000-keV	1793.6	967.01	883.47	416.00	378.52

Table 9.6: Efficiency gains for various hybrid DCSs when calculating dose due to a beam of electrons with energies of 250-keV, 1000-keV, and 20000-keV incident on a gold slab.

	ROP Model		
Particle Energy	$\mu_{cut} = 0.5$ 1-Angle 2-Energies	$\mu_{cut} = 0.9$ 1-Angle 2-Energies	$\mu_{cut} = 0.99$ 1-Energy 2-Energies
250-keV	17.929 18.490	7.5518 7.4511	2.5423 2.5341
1000-keV	58.737 60.332	19.882 21.725	6.2259 6.1956
20000-keV	915.00 843.63	306.25 301.63	69.465 68.203

In Fig. 9.19a, the results are distinguishable from the benchmark at 20000-keV because the relaxed approximations do not capture large angle scatter or large energy losses. Once again, small refinements to the elastic and inelastic ROP scattering models improves the accuracy of the results. As seen in Fig. 9.19b, model refinement through preservation of additional moments reduces the relative differences to <1%. Efficiency gains for the 20000-keV water simulation range from about 110 to 1600. However, accuracies within 1% were achieved with models that were 650 to 700 times more efficient than analog. Additional efficiency gains are presented in Tables 9.7 and 9.8.

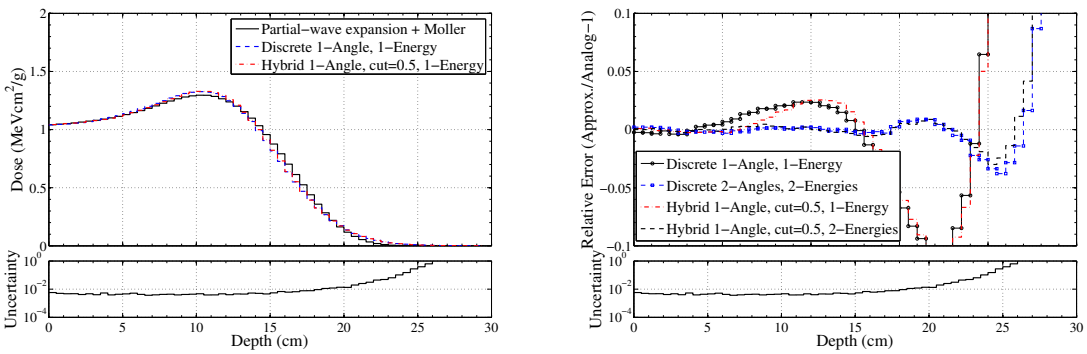

(a) Depth-dose profile

(b) Relative error

Figure 9.19: Comparison of depth-dose profiles (a) from 20000-keV electrons on water with discrete and hybrid elastic scattering and discrete inelastic models. The relative error in dose (b) from 20000-keV electrons on water calculated using discrete and hybrid elastic scattering models and discrete inelastic models. The relative error is measured with respect to the numerical benchmark generated using the partial-wave expansion elastic DCS and the Möller inelastic scattering models. The associated statistical uncertainty is included below each plot.

Table 9.7: Speed-up factors for various discrete DCSs when calculating dose due to a beam of electrons with energies of 250-keV, 1000-keV, and 20000-keV incident on a water slab.

	ROP Model				
Particle Energy	1-Angle 1-Energy	2-Angles 1-Energy	2-Angles 2-Energies	4-Angles 1-Energy	4-Angles 4-Energies
250-keV	54.199	30.066	24.115	14.945	11.246
1000-keV	147.31	82.849	60.842	39.284	26.781
20000-keV	1606.6	1121.6	709.04	612.26	292.89

Table 9.8: Efficiency gains for various hybrid DCSs when calculating dose due to a beam of electrons with energies of 250-keV, 1000-keV, and 20000-keV incident on a water slab.

	ROP Model		
Particle Energy	$\mu_{cut} = 0.5$ 1-Angle 2-Energies	$\mu_{cut} = 0.9$ 1-Angle 2-Energies	$\mu_{cut} = 0.99$ 1-Energy 2-Energies
250-keV	26.038 19.603	10.944 9.4577	3.4617 3.2682
1000-keV	74.289 52.097	29.799 24.925	8.0258 7.4572
20000-keV	1078.5 646.91	500.96 380.35	118.02 109.18

In addition to the single-material depth-dose profiles, an interface problem is presented. In this problem a 150-keV pencil beam of electrons is normally incident on a gold-aluminum slab. The first 0.0004 cm of the slab is gold and the remainder of the slab is aluminum. In Fig. 9.20, the depth-dose profiles for the analog benchmark and a single-angle, single-energy discrete model are presented along with the relative error in several discrete models. The interface occurs between the 4^{th} and 5^{th} cells; however, there is no distinguishable error in Fig. 9.20b resulting from the interface. As previously noted, the MP method preserves transport mechanics allowing for exponentially distributed collision sites. Clearly, boundary crossings are a non-issue for this method and no additional algorithms are required to handle boundary crossings.

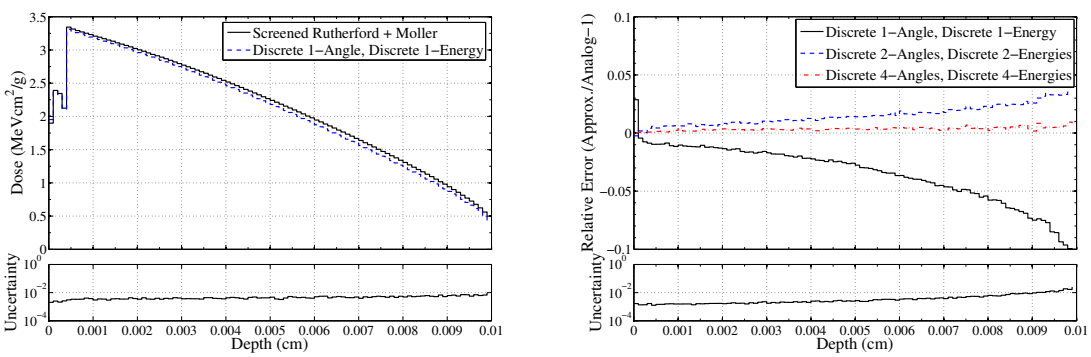

(a) Depth-dose profile

(b) Relative error

Figure 9.20: Comparison of depth-dose profiles (a) from 150-keV electrons on a gold-aluminum slab with discrete elastic scattering and discrete inelastic models. The relative error in dose (b) from 150-keV electrons on a gold-aluminum slab calculated using discrete and hybrid elastic scattering models and discrete inelastic models. The relative error is measured with respect to the numerical benchmark generated using the partial-wave expansion elastic DCS and the Möller inelastic scattering models. The associated statistical uncertainty is included below each plot.

9.3.2 Two-dimensional dose deposition

As indicated by the transversely integrated dose results in the previous section, this method provides excellent accuracy and efficiency when radial spreading is not considered. However, in this section we present two-dimensional dose deposition results that include the impact of radially spreading. At lower energies this method is more effective at capturing radial spreading. We begin the two-dimensional dose deposition results by presenting the low energy simulation. The geometry setup for this simulation is presented in Fig. 9.21a. For the 150-keV simulation 10^9 histories were completed. In Fig. 9.21b, the analog benchmark for the 150-keV simulation is presented. A significant portion of the dose is deposited along the beamline close to the source. In the gold region the dose is deposited more rapidly than in the silicon region where it is apparent that the dose diffuses slower.

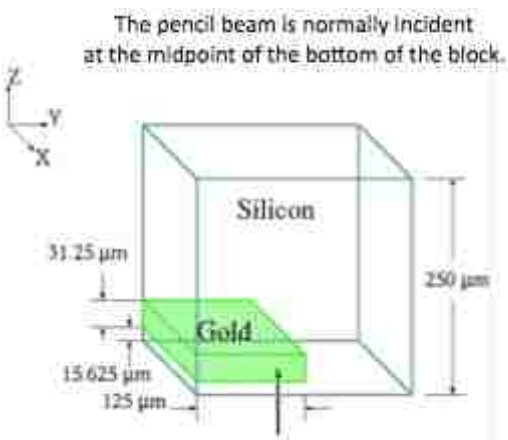

(a) Problem setup

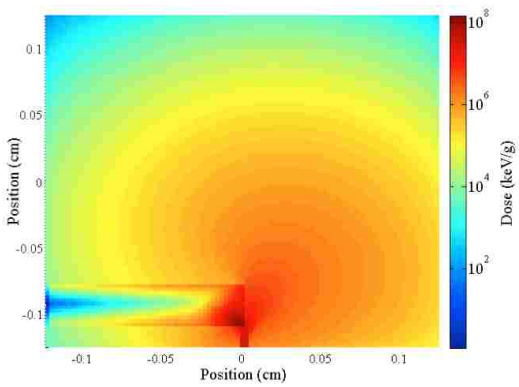

(b) Analog Benchmark

Figure 9.21: Problem setup for 150-keV electrons incident on 250-μm by 250-μm Si cube with gold region and analog benchmark. The benchmark was generated using the partial-wave expansion elastic DCS and the Möller inelastic scattering models.

In Fig. 9.22, relative differences for discrete models are presented to demonstrate the impact of adjusting the number of discrete angles and energies, and in turn, the number of moments preserved. In Figs. 9.22a and 9.22b, low-order moment-preserving models are presented. Discrete artifacts are very distinct in in Fig. 9.22a for the single-angle, single-energy model. By increasing the number of discrete angles in both Figs. 9.22b and 9.22c, the discrete artifacts are mitigated without requiring the hybrid model. However, there are still some significant differences in the dose in some regions resulting from the single-energy model seen in Figs. 9.22b and 9.22c. By including additional energies, the relative error in all regions is significantly reduced as seen in Fig. 9.22d. Notice that along the gold-silicon interface near the beam, the agreement is within 1%, with exception of the single-angle model where the solution is overwhelmed with discrete artifacts.

Another artifact to point out is the over/under estimation of the dose in the first two cells next to the source. This error persists as the models are refined, but it is actually an artifact of the source type and source location. That is, the source is a pencil beam that is singular in space and it is directed at the tally cell boundary between. In the next 2-D result, the source is no longer singular in space and the artifact is no longer present.

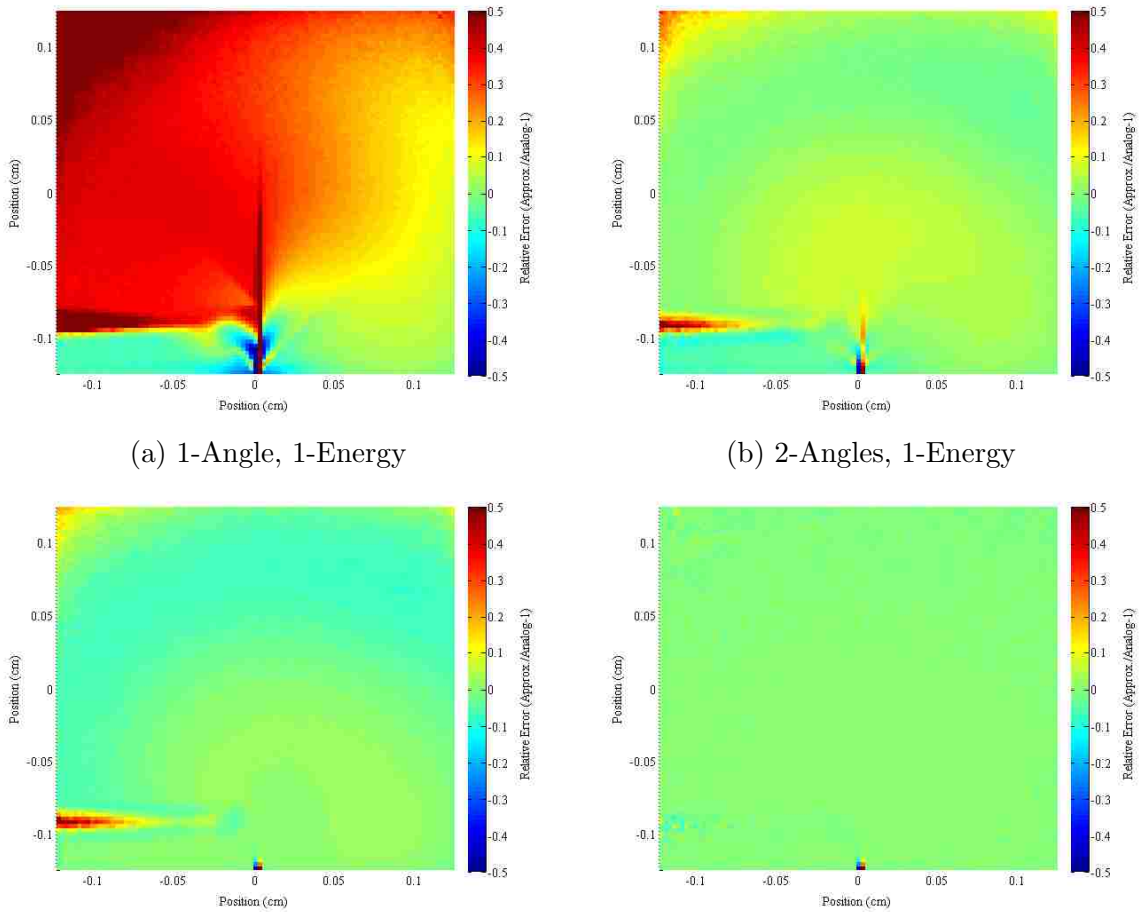

(a) 1-Angle, 1-Energy

(b) 2-Angles, 1-Energy

(c) 4-Angles, 1-Energy

(d) 4-Angles, 4-Energies

Figure 9.22: The relative error in dose from 150-keV electrons in a 250-μm by 250-μm Si/Au cube calculated using a discrete (a) single-angle and single-energy model, (b) two-angle and single-energy model, (c) four-angle and single-energy model, and (d) four-angle and four-energy model. The relative error is measured with respect to the numerical benchmark generated using the partial-wave expansion elastic DCS and the Möller inelastic scattering models.

Table 9.9: Speed-up factors for various discrete DCSs when calculating dose from 150-keV electrons in a 250-μm by 250-μm Si/Au cube.

	ROP Model				
Particle Energy	1-Angle 1-Energy	2-Angles 1-Energy	2-Angles 2-Energies	4-Angles 1-Energy	4-Angles 4-Energies
150-keV	51.4	29.3	29.2	15.5	15.5

In Fig. 9.23a, the two-dimensional problem setup is given along with the analog benchmark in Fig. 9.23b. In this simulation, a beam of 10000-keV electrons are transported with radius of 0.02 cm is normally incident on a water cube with a small bone region. The analog benchmark is in logscale and provides a sense of where most of the dose is deposited. That is, a significant portion of the dose is deposited along the beamline within fractions of a cm to the left and right of the origin. The electrons with these energies penetrates deeply into the medium as seen in Fig. 9.23b.

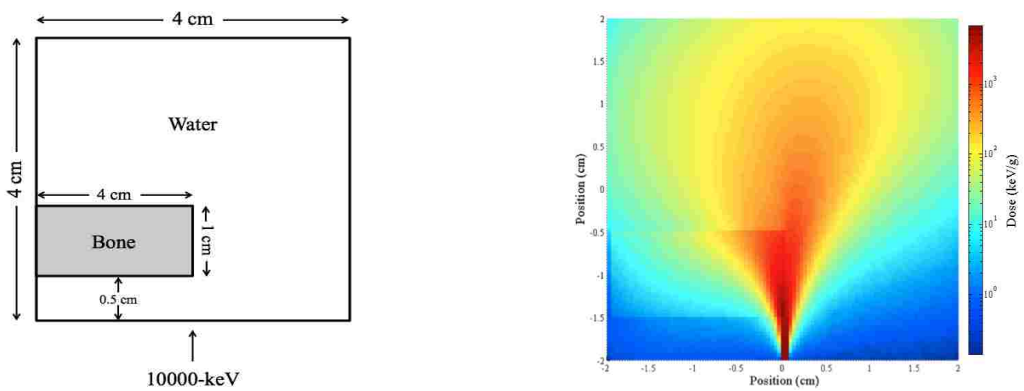

(a) Problem Setup (b) Analog Benchmark

Figure 9.23: The problem setup (a) and analog benchmark (b) for 10000-keV electrons on a 4-cm by 4-cm water/bone cube. The benchmark was generated using the partial-wave elastic DCS and the Möller inelastic DCS models.

The following figure presents relative error results corresponding two discrete ROP DCS models. In Fig. 9.24a, the relative error in the four-angle, four-energy discrete DCS models with respect to the analog benchmark is presented. Discrete

artifacts can be seen clearly in Fig. 9.24a. However, by refining the model through preservation of additional moments with the addition of four more discrete angles, discrete artifacts aremitigated and backscatter is captured more accurately as seen in the relative error result in Fig. 9.24b. In both the four-angle and eight-angle results, no interface effects are present. It should be noted that in the backscatter is not significant at 10000-keV and some of the error in the lower left and right corners is statistical in nature.

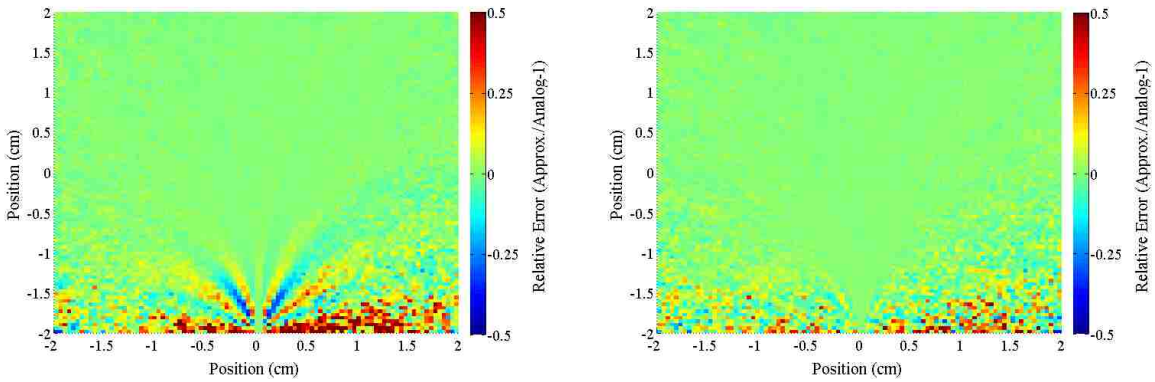

(a) 4-Angles, 4-Energies

(b) 8-Angles, 4-Energies

Figure 9.24: The relative error in dose from 10000-keV electrons on a 4-*cm* by 4-*cm* water/bone cube calculated using a (a) four-angle discrete elastic DCS model and four-energy discrete inelastic DCS model and a (b) eight-angle discrete elastic DCS model and four-energy discrete inelastic DCS model. The relative error is measured with respect to the analog benchmark generated using the partial-wave expansion elastic DCS and the Möller inelastic scattering models.

In Fig. 9.25, the relative error between the analog benchmark and two hybrid models are presented. In Fig. 9.25a, a hybrid model with $\mu^* = 0.9$ shows very subtle discrete artifacts, but otherwise is in good agreement. In Fig. 9.25b, a hybrid model with $\mu^* = 0.99$ does not suffer from any discrete artifacts and the only disagreement is in the lower left and right corners where again the error is statistical in nature.

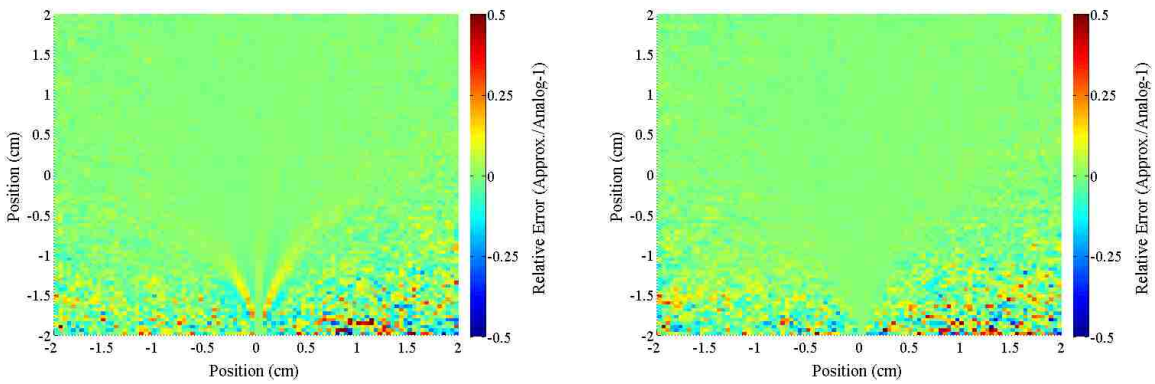

(a) Hybrid $\mu^* = 0.9$, 4-Energies (b) Hybrid $\mu^* = 0.99$, 4-Energies

Figure 9.25: The relative error in dose from 10000-keV electrons in a 4-*cm* by 4-*cm* Water/Bone cube calculated using a (a) single-angle hybrid elastic DCS model with $\mu^* = 0.9$ and four-energy discrete inelastic DCS model and a (b) single-angle hybrid elastic DCS model with $\mu^* = 0.99$ elastic DCS model and four-energy discrete inelastic DCS model. The relative error is measured with respect to the analog benchmark generated using the partial-wave expansion elastic DCS and the Möller inelastic scattering models.

In adding more discrete angles, or through use of the hybrid model, we demonstrated an approach to mitigate discrete artifacts through controlling the accuracy of the ROP DCS models. The only drawback to applying a more accurate ROP DCS model is the loss of efficiency as presented in Table 9.10. Here, the 4-angle model is the most efficient as expected. Inclusion of additional discrete angles or use of the hybrid model reduces the efficiency gain from roughly 120 to between 47 and 94.

As previously noted, it is possible to optimize such that significant reduction in efficiency is not incurred by applying higher-order models in regions nearby the

Table 9.10: Speed-up factors for various discrete DCSs when calculating dose from 10000-keV electrons incident on a 4-*cm* by 4-*cm* water cube with small bone region.

	ROP Model			
Particle Energy	4-Angles 4-Energies	8-Angles 4-Energies	1-Angle $\mu^* = 0.9$ 4-Energies	1-Angle $\mu^* = 0.99$ 4-Energies
10000-keV	120.7	85.6	93.9	47.0

source where the solution remains highly peaked and splaying lower-order models in regions where the solution is less-peaked. The following results present region dependent elastic ROP DCSs.

In Fig. 9.26, the schematic for a region dependent discrete elastic model is presented along with the associated relative error from such an approach. As seen in Fig. 9.26a, default 4-angle, 4-energy discrete model is applied to all regions. The default is then deactivated in the region bounded by the red dashed line and an 8-angle, 4-energy discrete model is applied in this region. The associated relative error is given in 9.26b. The relative error in Fig. **??**b is nearly indistinguishable from the relative error in Fig. 9.24b where an 8-angle discrete model is applied everywhere. The resulting gain in efficiency is 106 times faster than the analog simulation as opposed to 86 when applying an 8-angle model to all regions.

In Fig. 9.27, the schematic for another region dependent discrete elastic model is presented along with the associated relative error from such an approach. Again, in this problem a 4-energy discrete inelastic model is used in all regions. As seen in Fig. 9.27a, an 8-angle model is applied in the region where the peak dose occurs and a single-angle model is applied in all other regions. The associated relative error is given in 9.27b and is a modest improvement over the relative error in 9.26b as the backscatter is captured more accurately. Again, the relative error in Fig. 9.27b is nearly indistinguishable from the relative error in Fig. 9.24b where an 8-

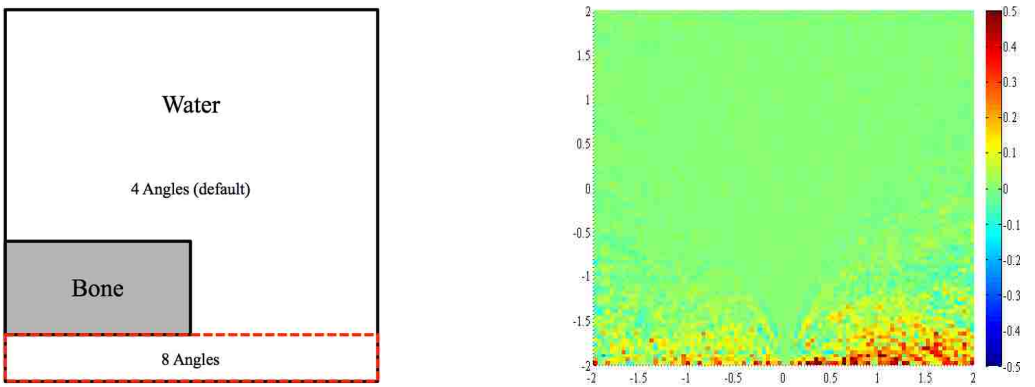

(a) Region dependent ROP DCSs (b) Relative error

Figure 9.26: The schematic of region dependent ROP DCS (a) and the relative error (b) in dose from 10000-keV electrons on a 4-*cm* by 4-*cm* water/bone cube calculated using the region dependent ROP DCS 8-angles applied near the source and 4-angles applied in all other regions. A 4-energy discrete inelastic model is used throughout. The benchmark was generated using the partial-wave elastic DCS and the Möller inelastic DCS models.

angle discrete model is applied everywhere. The resulting gain in efficiency is 97 times faster than the analog simulation and is reduced slightly from 106, which was efficiency gain associated with the previous region dependent models, but accuracy was improved.

Ultimately, a region dependent application of the ROP DCS models is simply an exercise in demonstrating that accuracy and efficiency can be optimized. In practice, a more suitable approach would be to develop an algorithm that determines the optimal DCS model as the electron is transported. At this point, it is unclear what metric should is ideal for determining the optimal ROP DCS model because the parameter space is large. The following problem is illustrates this point.

For problems with singular boundary conditions like the previous problem, it is clear that high-order models are necessary nearby the source and low-order models can be used away from the source as the solution becomes less peaked. However, the same is not necessarily true for distributed sources. For example, in the following

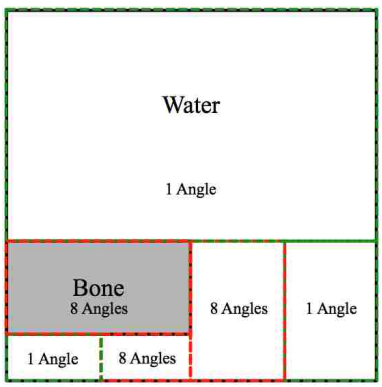

(a) Region dependent ROP DCSs

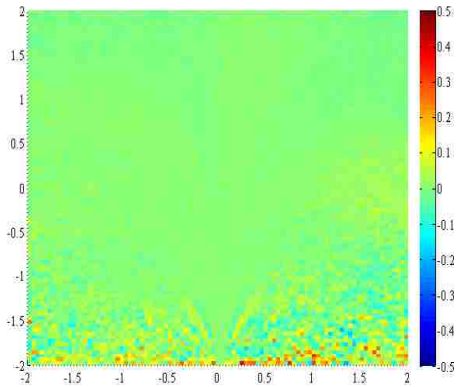

(b) Relative error

Figure 9.27: The schematic of region dependent ROP DCS (a) and the relative error (b) in dose from 10000-keV electrons on a4-*cm* by 4-*cm* water/bone cube calculated using the region dependent ROP DCS with 8-angles applied in the peak dose region and 1-angle applied in all other regions. A 4-energy discrete inelastic model is used throughout. The benchmark was generated using the partial-wave elastic DCS and the Möller inelastic DCS models.

problem an isotropic point source of 2500-keV electrons in a gold cube 1 cm on each face is simulated. The problem setup and analog benchmark is given in Fig. 9.28. As seen in Fig. 9.28b, the dose is deposited uniformly about the point source located at the origin. It is also of interest to point out that most of the dose is deposited nearby the source.

As seen in Fig. 9.29, relatively low-order models can used to estimate the dose due to distributed sources. The most efficient model tested, single-angle, single-energy, is about 400 times more efficient than the analog simulation and the associated relative error is presented in Fig. 9.29a. By adding another discrete energy the relative error improves as seen in Fig. 9.29b, but the efficiency decrease to about 300 times faster than the analog simulation. Finally, the most accurate model tested, 2-angles, 2-energies, is presented in Fig. 9.29c. This model provides good agreement, while remaing roughly 180 times more efficient than the analog simulation. Here we showed that accuracy and efficiency is impacted by the source configuration. Again,

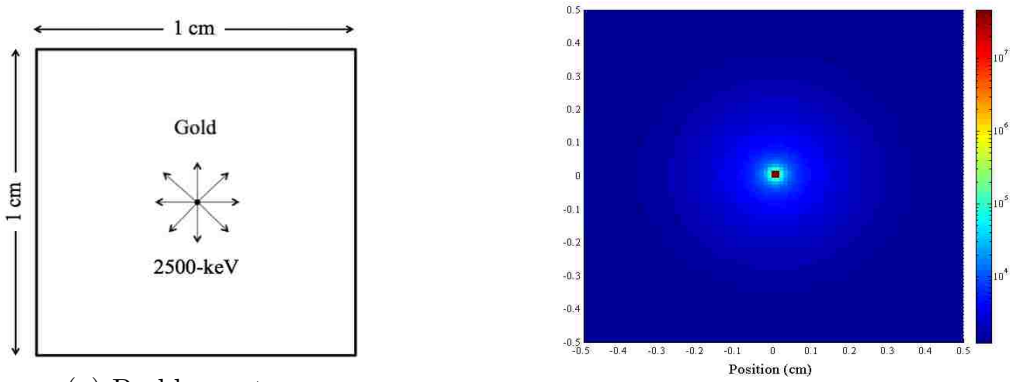

(a) Problem setup

(b) Absolute dose

Figure 9.28: The problem setup for an isotropic point source located at the origin of a 1-*cm* by 1-*cm* by 1-*cm* gold cube (a) and the analog benchmark (b) generated using the partial-wave elastic DCS and the Möller inelastic DCS models.

region dependent models could be applied in this setting for optimization, but more importantly an adaptive cross-section algorithm that incorporates source information and solution information for given problem would improve the MP method.

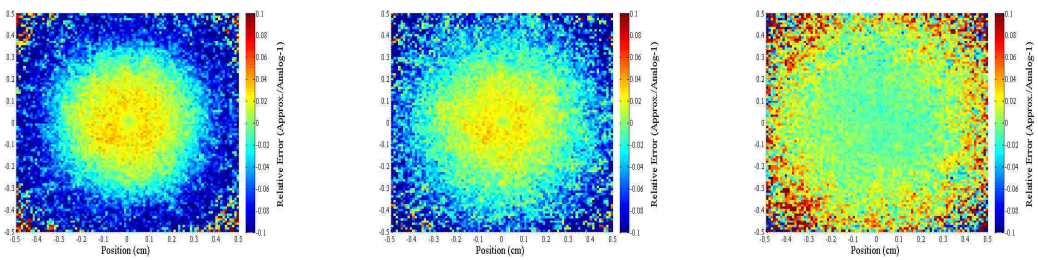

(a) 1-Angle, 1-Energy (b) 1-Angle, 2-Energies (c) 2-Angles, 2-Energies

Figure 9.29: The relative error in dose from 2500-keV electrons in a 1-*cm* by 1-*cm* by 1-*cm* gold cube calculated using (a) a single-angle, single-energy discrete model, (b) a single-angle, two-energy discrete model, and (c) a two-angle, two-energy discrete model. The relative error is measured with respect to the analog benchmark generated using the partial-wave elastic DCS and the Möller inelastic DCSmodels.

9.4 Comparison with Experiment

In this section, an initial validation of the Moment-Preservation method is presented. Given the nature of the method, the key is to first obtain analog elastic and inelastic DCSs that are in good agreement with the experimental benchmarks of interest. Therefore, the following results are really a validation of the analog DCS models used herein. Initial validation results indicate that the renormalized Möller DCS (see Chapter 3) does not give good agreement with the Lockwood energy deposition data [81]. Use of the Geant4 G4eIonization class in place of the renomarlized Möller DCS improved agreement. However, when comparing with the Tabata charge deposition data [82], differences between the renormalized Möller DCS and the G4eIonization class were negligible. Until further development of the analog inelastic model is completed, use is made of the G4eIonization class (see Chapter 8) for the validation test under consideration in this section to be consistent. Once again, the analog elastic DCS models used are the partial-wave elastic DCSs generated using the ELSEPA code. The first validation test includes comparisons to depth-dose profiles referred to as the Lockwood data [81]. Next, comparisons to charge deposition experiments due to Tabata [82] are presented. In addition to the Lockwood and Tabata data, numerous experimental benchmarks are available for validation test [84, 85, 86, 87, 88, 89, 90, 91]. However, further validation of the MP method remains as future work.

9.4.1 Energy deposition profiles

One of the most common electron transport results in basic research is energy deposition, where an accurate description of particle transport is required for different energies in various materials. Below, energy deposition profiles and total energy deposition calculations are compared with experimental results from Lockwood et al.

[81]. The Lockwood data was produced by Sandia National Laboratories using a sophisticated calorimetric technique for measuring absolute, high-resolution electron energy deposition profiles in a wide range of materials. The uncertainty of the data is estimated to be from 1.0% to 2.0%.

The comparisons cover low-Z and high-Z materials including carbon, aluminum, molybdenum, and tantalum for pencil beam sources with energies of 500-keV and 1000-keV and angles of incidence of 0° and 60°. In each simulation, 10^5 source particles were transported and the energy deposition profiles are normalized to the mean CSDA range and the depth variable is in terms of a fraction of the mean CSDA range. The primary objective of this comparison is to validate the ROP models that are the subject of this dissertation, but also to demonstrate how well these models perform with respect to the current state-of-art physics models available to Geant4 users. Both accuracy and efficiency results are presented, contrasting the MP method and the default Geant4 electromagnetic physics.

Simulations were completed for three different models where the treatment of elastic scattering varies between each model. These models include an analog elastic scattering model given by the partial-wave DCS, a discrete single-angle DCS, and the geant4 elastic multiple scattering model referred to as the Urban model or the G4UrbanMscModel96 class. Each of the models tested used the same inelastic scattering model and bremsstrahlung model along with the same physics for transporting photons and positrons. The settings associated with the aforementioned physics are in accordance with the Geant4 standard electromagnetic physics list option 3, which was found to give the best agreement with the Lockwood data [92] and enforces the strictest multiple scattering step limitation [93] (this is only relevant to the Urban model). In addition, the maximum step-size was set to 0.01 mm for carbon and aluminum and 0.001 mm for molybdenum and tantalum when using the Urban model (step limits are not required for the analog model or the discrete model).

In general, the energy deposition profiles calculated using the analog model, the ROP model, and the geant4 CH model exhibit behavior similar to the experimental results. The Geant4 physics tends to estimate values higher than the discrete model in the peak energy deposition region, while the discrete model tends to estimate higher values in the tails of the energy deposition profile (see Figs. 9.31-9.36). This is true for both normal incidence and 60° off-normal incidence. The total energy deposition tends to be nearly the same for both the MP method and the Geant4 physics models. For normally incident electrons, the agreement between all models and the experimentally determined total energy deposition is roughly 1-3% relative difference for all materials and energies with exception of 1000-keV electrons on tantalum which is between roughly 4-5% (see Table 9.11). For off-normal incidence, the agreement between all models and the experimentally determined total energy deposition is roughly 2-4% relative difference (see Table 9.12) for all materials and energies with exception of 1000-keV electrons on molybdenum which is between roughly 6-7%. While this level of agreement is generally acceptable, it is of interest to develop an analog inelastic model that improves overall agreement to within a few percent relative error.

The timing results are presented in Tables 9.13 and 9.15. For normal incidence, efficiency gains are roughly the same for the MP method and the Geant4 physics. However, for off-normal incidence, the MP method is in all cases a factor of two times faster than the Geant4 physics.

For energy deposition calculations, neither the MP method or the Geant4 physics overwhelmingly outperform the other. However, the MP method was more efficient for the off-normal incidence simulations. In addition, if an analog model is developed that provides better agreement with experiment, the same level of agreement would be anticipated for the MP method. Therefore, it is important to identify an ideal analog inelastic model as the partial-wave DCSs are assumed to be most accurate

representation of elastic scattering and do not contribute to any disagreement found herein.

Furthermore, no multi-region problems were validated in this section. It is known that material interfaces are problematic for condensed history methods and there are reported discrepancies between the Geant4 physics and the Lockwood data for material interfaces [92]. Validation of the MP method for energy deposition in slabs with material interfaces remains as future work, but it has been shown in the past that the MP method does not suffer from boundary crossing limitations [60, 61, 62] (see section 9.3). Therefore, no significant interface discrepancies are anticipated.

Table 9.11: Total energy deposition comparison for 500-keV and 1000-keV electrons normally incident on aluminum, molybdenum, and tantalum semi-infinite slabs.

Energy (keV)	**Material Type**	**Model Type**	**Total Energy (keV)**	**Relative Error**
500	aluminum	Analog	472.921	-0.013
		Discrete 1-Angle	471.169	-0.016
		G4EmStandard	468.550	-0.022
1000	aluminum	Analog	958.381	-0.012
		Discrete 1-Angle	954.665	-0.016
		G4EmStandard	953.089	-0.017
500	molybdenum	Analog	383.612	0.028
		Discrete 1-Angle	381.167	0.022
		G4EmStandard	376.032	0.008
1000	molybdenum	Analog	801.527	0.029
		Discrete 1-Angle	795.534	0.021
		G4EmStandard	791.940	0.017
500	tantalum	Analog	323.144	0.023
		Discrete 1-Angle	316.823	0.003
		G4EmStandard	321.674	0.018
1000	tantalum	Analog	681.921	0.052
		Discrete 1-Angle	675.622	0.043
		G4EmStandard	678.301	0.047

Table 9.12: Total energy deposition for 60 degrees off-normal incidence electrons on semi-infinite slabs of aluminum, molybdenum, and tantalum.

Energy (keV)	**Material Type**	**Model Type**	**Total Energy (keV)**	**Relative Error**
500	aluminum	Analog	380.501	-0.027
		Discrete 1-Angle	379.573	-0.029
		G4EmStandard	375.752	-0.038
500	molybdenum	Analog	282.940	0.040
		Discrete 1-Angle	279.703	0.028
		G4EmStandard	277.925	0.022
1000	molybdenum	Analog	597.557	0.073
		Discrete 1-Angle	593.249	0.065
		G4EmStandard	591.644	0.062
500	tantalum	Analog	230.202	0.014
		Discrete 1-Angle	226.327	-0.003
		G4EmStandard	232.331	0.023
1000	tantalum	Analog	493.342	0.045
		Discrete 1-Angle	489.207	0.036
		G4EmStandard	495.368	0.050

Table 9.13: Timing results for energy deposition calculations for 500-keV and 1000-keV electrons normally incident on carbon, aluminum, molybdenum, and tantalum semi-infinite slabs.

Energy (keV)	**Material Type**	**Model Type**	**CPU time (mins.)**	**Efficiency Gains**
1000	carbon	Analog	75	1
		Discrete 1-Angle	3	25
		G4EmStandard	3	25
500	aluminum	Analog	41	1
		Discrete 1-Angle	3	14
		G4EmStandard	2	21
1000	aluminum	Analog	74	1
		Discrete 1-Angle	4	19
		G4EmStandard	3	25
500	molybdenum	Analog	100	1
		Discrete 1-Angle	2	50
		G4EmStandard	2	50
1000	molybdenum	Analog	151	1
		Discrete 1-Angle	3	50
		G4EmStandard	5	30
500	tantalum	Analog	90	1
		Discrete 1-Angle	2	45
		G4EmStandard	1	90
1000	tantalum	Analog	134	1
		Discrete 1-Angle	3	45
		G4EmStandard	3	45

Table 9.14: Timing results for dose calculations for 60 degrees off-normal incidence electrons on semi-infinite slabs of aluminum, molybdenum, and tantalum.

Energy (keV)	**Material Type**	**Model Type**	**CPU time (mins.)**	**Efficiency Gains**
500	aluminum	Analog	60	1
		Discrete 1-Angle	2	30
		G4EmStandard	5	12
500	molybdenum	Analog	71	1
		Discrete 1-Angle	1	71
		G4EmStandard	2	35
1000	molybdenum	Analog	115	1
		Discrete 1-Angle	2	58
		G4EmStandard	4	29
500	tantalum	Analog	61	1
		Discrete 1-Angle	1	61
		G4EmStandard	2	30
1000	tantalum	Analog	103	1
		Discrete 1-Angle	1	103
		G4EmStandard	2	52

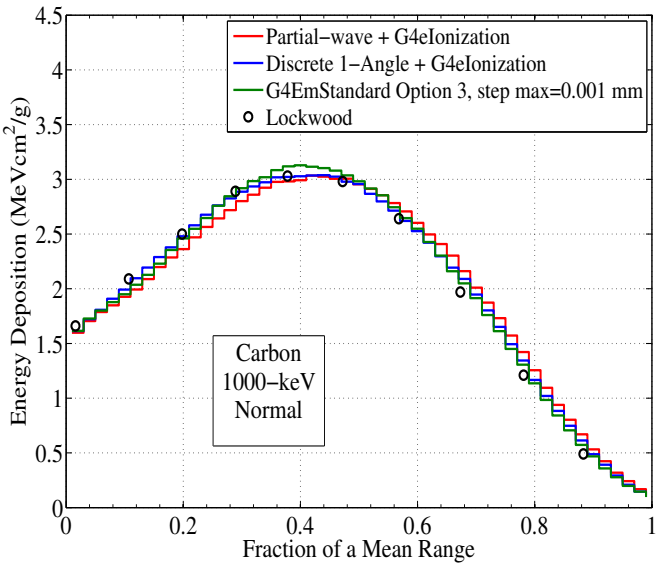

Figure 9.30: Comparison with Lockwood data for 1000-keV electrons normally on carbon slab.

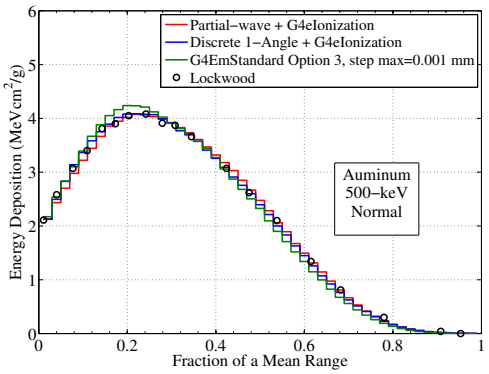

(a) 500-keV

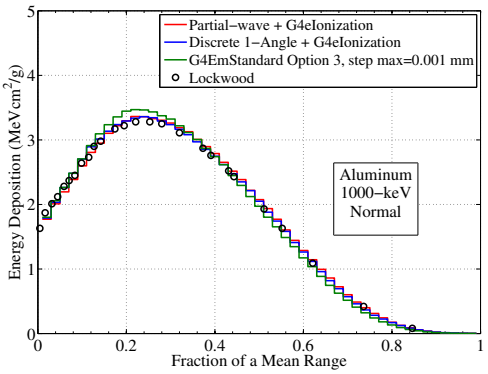

(b) 1000-keV

Figure 9.31: Comparison with Lockwood data for 500-keV and 1000-keV electrons normally incident on aluminum slab.

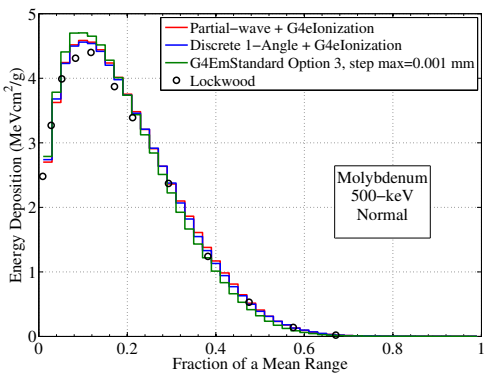

(a) 500-keV

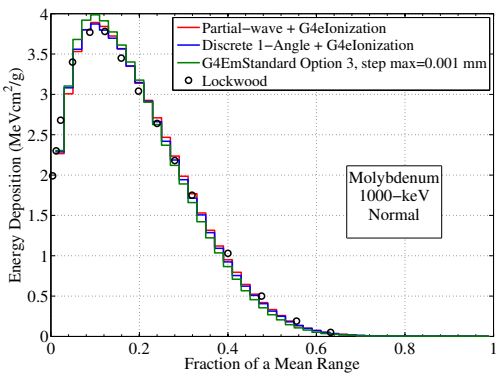

(b) 1000-keV

Figure 9.32: Comparison with Lockwood data for 500-keV and 1000-keV electrons normally incident on molybdenum slab.

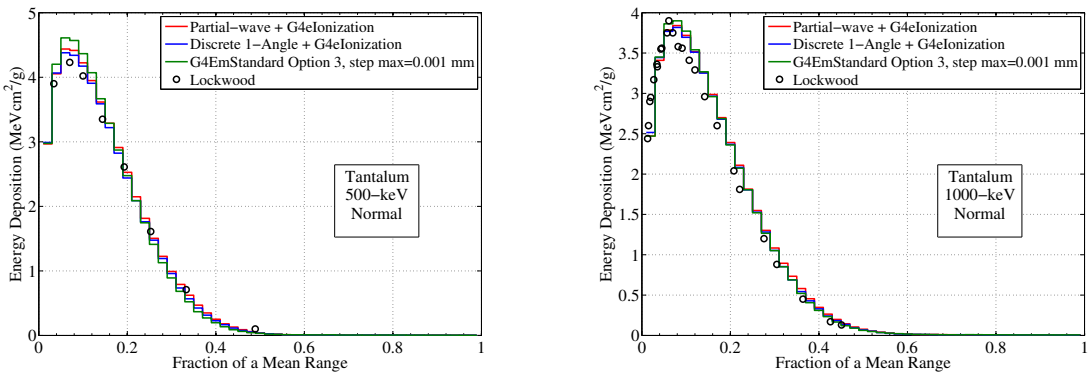

(a) 500-keV (b) 1000-keV

Figure 9.33: Comparison with Lockwood data for 500-keV and 1000-keV electrons normally incident on tantalum slab.

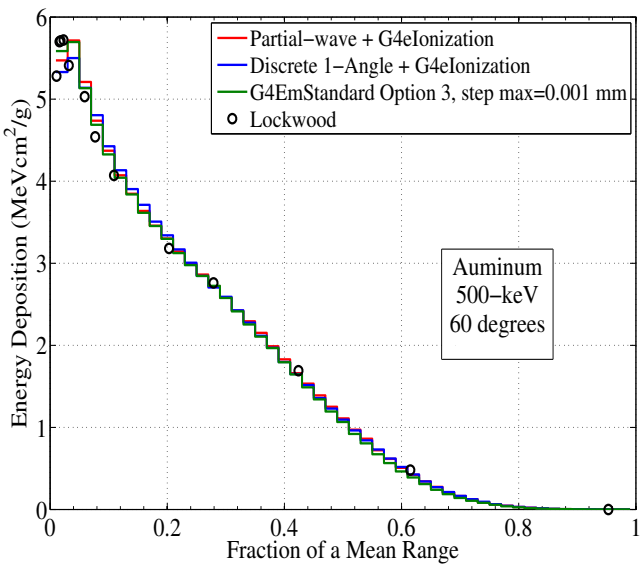

Figure 9.34: Comparison with Lockwood data for 500-keV electrons with 60 degrees off-normal incidence on aluminum slab.

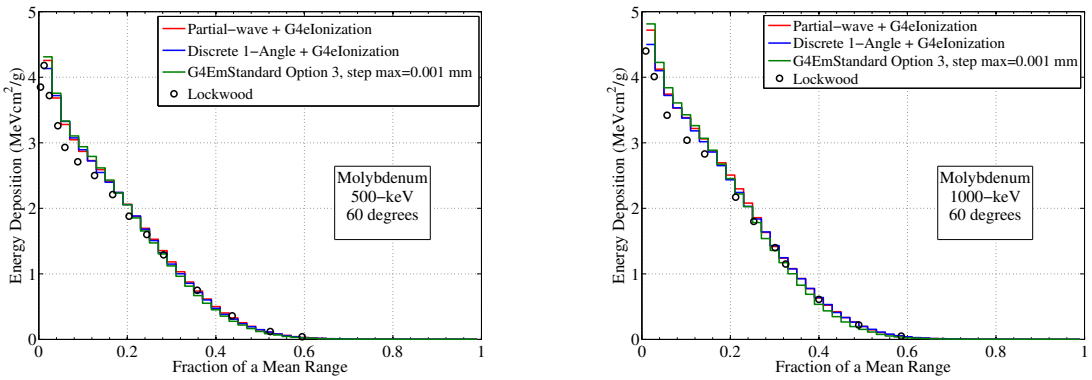

(a) 500-keV (b) 1000-keV

Figure 9.35: Comparison with Lockwood data for 500-keV and 1000-keV electrons with 60 degrees off-normal incidence on molybdenum slab.

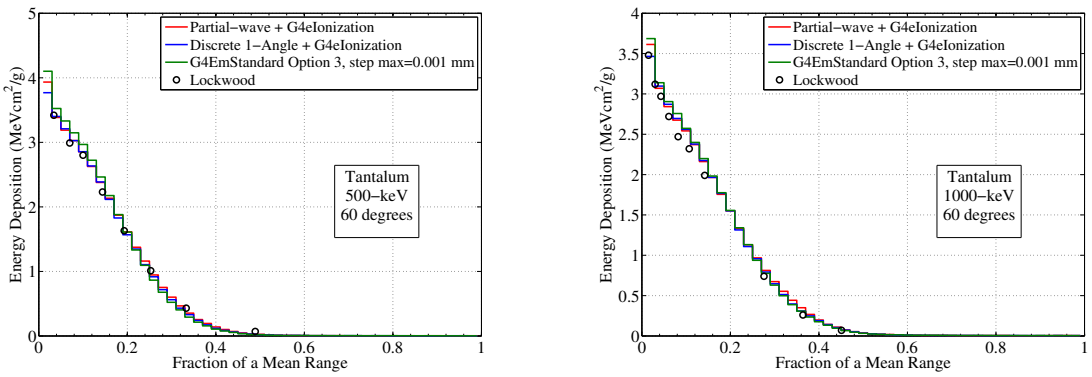

(a) 500-keV (b) 1000-keV

Figure 9.36: Comparison with Lockwood data for 500-keV and 1000-keV electrons with 60 degrees off-normal incidence on tantalum slab.

9.4.2 Charge deposition

Another important electron transport result is charge deposition. Charge deposition is important to understanding charge buildup in nonconductive materials. Below, charge-deposition profiles are compared with experimental results from Tabata et al. [82]. Among the published experimental results of charge deposition distributions, those of Tabata et al. [84] cover the widest regions of absorber atomic number (from 4 to 79) and incident-electron energy (from 4.09 to 23.5 MeV) [82].

Calculations of charge deposition distributions were performed for normally incident electron pencil beams with energies of 5000-keV, 10000-keV, and 20000-keV on aluminum and gold targets of thickness $2.5r_0$, where r_0 is the CSDA range. A total of 2.4×10^5 source particles were simulated. The target regions were divided into 80 sub-regions for scoring (scoring regions are not physical boundaries) for 5000-keV source particles and 40 sub-regions for 10000-keV and 20000-keV source particles. Particles are tracked down to 250-keV.

Figs. 9.37-9.42, present comparisons of charge-deposition and dose distributions generated using the partial-wave elastic DCS or a discrete DCS with the default Geant4 inelastic physics for electrons and the default Geant4 physics for positrons and photons. The charge-deposition distributions are compared with experimental results from Tabata et al. [82]. In general the correct behavior of the charge-deposition distribution is captured for all energies and materials tested. In aluminum, agreement with the experimental benchmark is satisfactory with exception of a slight shift in the distribution. In gold, agreement with the experimental benchmark is again satisfactory with exception of the 5000-keV results where the charge deposition is overestimated. Notice that the analog solution and the discrete solution are in excellent agreement. Again, the conclusion is that an analog model that gives good agreement should be identified and it is assumed that the ROP models will

provide similar levels of agreement. Further investigation is required to understand the disagreements seen below (in particular, 5000-keV electrons on gold).

The dose results in Figs. 9.37-9.42, do show good agreement in gold but do not in aluminum. This result was not anticipated considering the level of agreement in the previous section and suggest that future validations should be avoided until this disagreement can be identified. Possible sources of the disagreement includes the increased presence of bremsstrahlung radiation at higher energies, an inconsistency between the Geant4 physics implementation and discrete model, or a coding error. Regardless, future work will include the use of an inelastic ROP model based on an improved inelastic DCS, so that reliance on the Geant4 physics is reduced.

Table 9.15: Timing results for charge deposition calculations for 5000-keV, 10000-keV, and 20000-keV electrons normally incident on aluminum and gold semi-infinite slabs.

Energy (keV)	**Material Type**	**Model Type**	**CPU time (mins.)**	**Efficiency Gains**
5000	aluminum	Analog	1.6	1
		Discrete 4-Angles	0.009	178
		Discrete 8-Angles	0.02	80
10000	aluminum	Analog	2.7	1
		Discrete 4-Angles	0.01	270
		Discrete 8-Angles	0.03	90
20000	aluminum	Analog	5.8	1
		Discrete 4-Angles	0.02	290
		Discrete 8-Angles	0.05	116
5000	gold	Analog	2.3	1
		Discrete 4-Angles	0.03	77
		Discrete 8-Angles	0.06	38
10000	gold	Analog	4.3	1
		Discrete 4-Angles	0.06	72
		Discrete 8-Angles	0.11	43
20000	gold	Analog	13.8	1
		Discrete 4-Angles	0.2	69
		Discrete 8-Angles	0.3	46

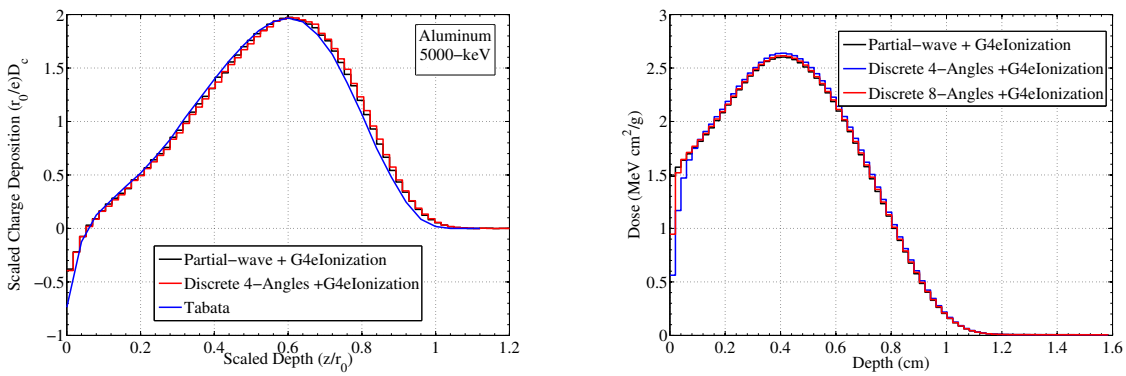

(a) Charge Deposition (b) Dose

Figure 9.37: Comparison with Tabata data for 5000-keV electrons normally incident on an aluminum slab.

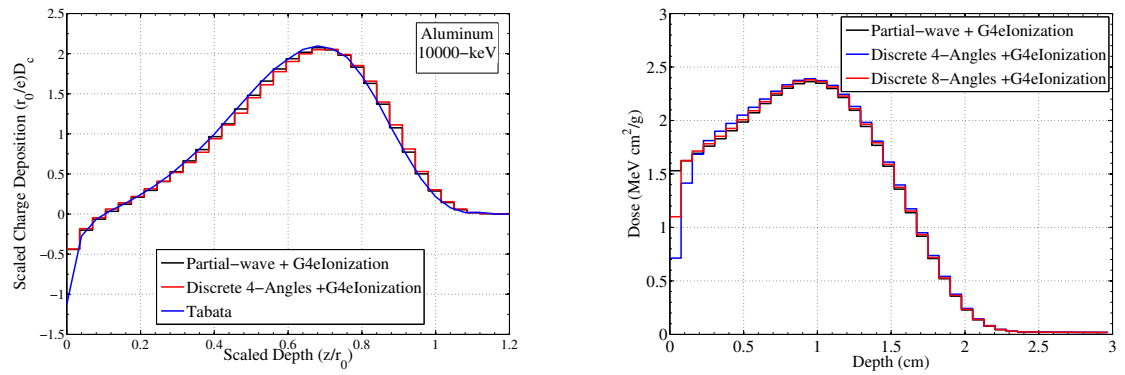

(a) Charge Deposition (b) Dose

Figure 9.38: Comparison with Tabata data for 10000-keV electrons normally incident on an aluminum slab.

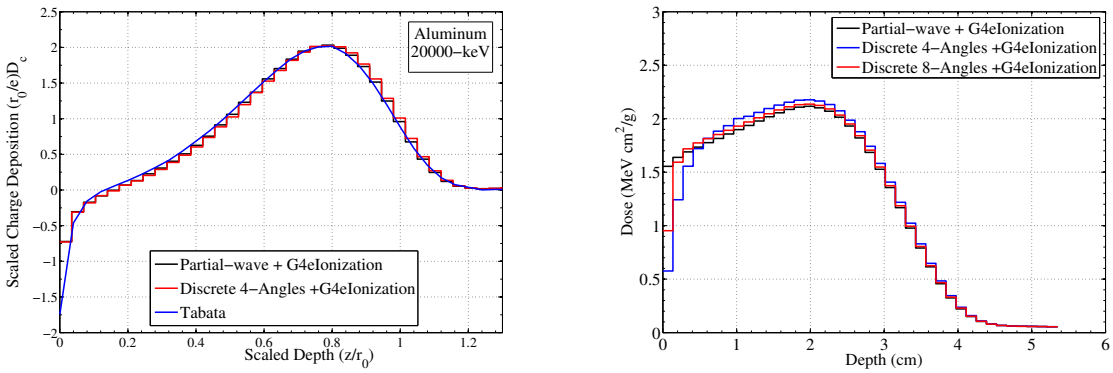

(a) Charge Deposition (b) Dose

Figure 9.39: Comparison with Tabata data for 20000-keV electrons normally incident on an aluminum slab.

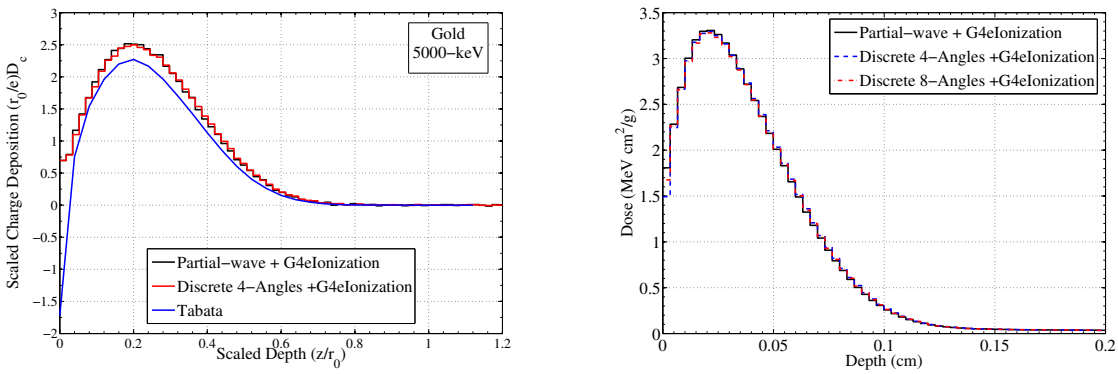

(a) Charge Deposition (b) Dose

Figure 9.40: Comparison with Tabata data for 5000-keV electrons normally incident on a gold slab.

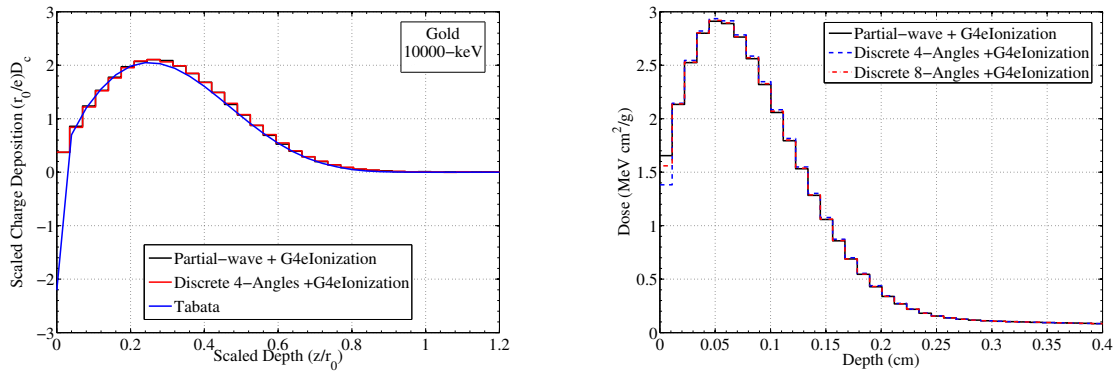

(a) Charge Deposition (b) Dose

Figure 9.41: Comparison with Tabata data for 10000-keV electrons normally incident on a gold slab.

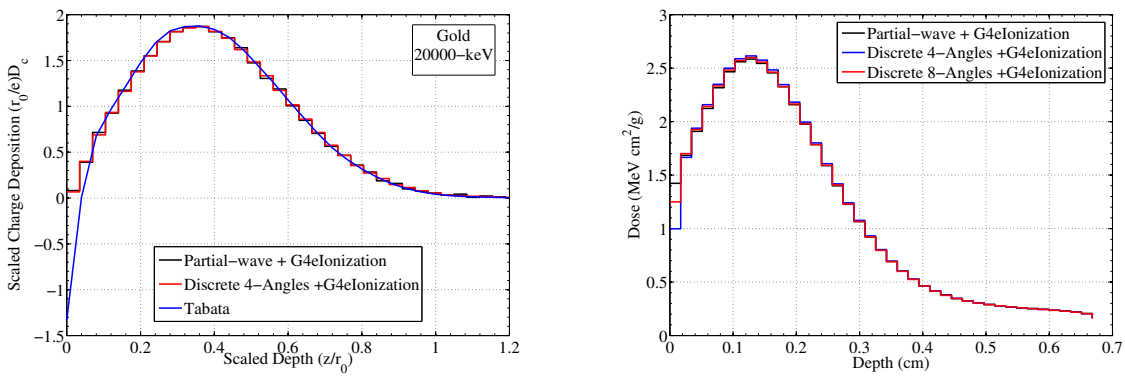

(a) Charge Deposition (b) Dose

Figure 9.42: Comparison with Tabata data for 20000-keV electrons normally incident on a gold slab.

9.5 CEASE Response Function Calculation

Given the experimental validation and the associated level of confidence in the accuracy of the analog DCS models and the ROP DCSs constructed from such models, the CEASE response function calculation is revisited. Here, it is shown that the response function can be generated with an efficient ROP DCS model while remaining accurate. For this calculation, three models were tested each with the same positron, photon, and electron inelastic physics. What varies for each of the models is the elastic scattering physics. An analog model given by the partial-wave elastic DCS is tested and a single-angle discrete model based on the partial-wave elastic DCS is compared. In addition, the response function is also calculated using the default Geant4 electromagnetic physics option 3. In Fig. 9.43, response functions generated using each different model are compared. The analog and the discrete model are in excellent agreement, while the Geant4 physics (that is, class II CH with out a user applied step limitation) shows significant disagreement at higher energies. Assuming the analog model is the most accurate, the Geant4 physics tends to under predict the detector response at higher energies. This could be an effect of the collimator, as it is known that the Geant4 physics, without step limitation, tends to overestimate energy deposition in high-Z materials. Therefore, it is possible that electrons do not fully penetrate the collimator because they lose too much energy in the tungsten collimator (see Fig. 9.44 for an example of trajectories penetrating the collimator).

The efficiency gains associated with the discrete DCS are outstanding. To complete an analog simulation of 1116 runs for 18 source angles and 62 source energies with 1000 source particles each, it requires roughly 46 days, while for the discrete model it only takes roughly five days. That is an order of magnitude efficiency gain. The CH runs were roughly 10 times faster than the discrete model or 0.5 days.

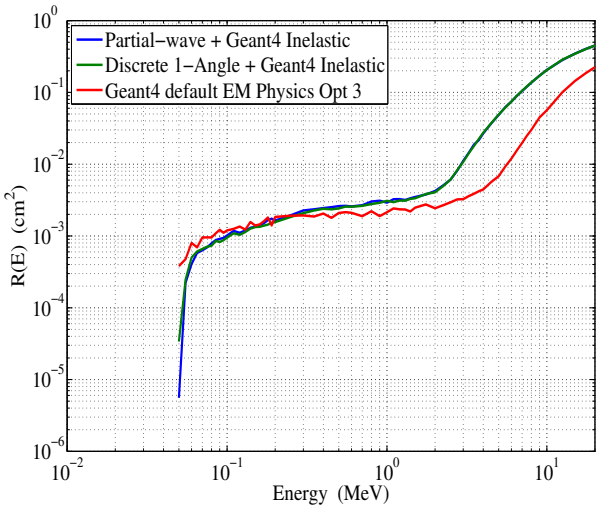

Figure 9.43: Comparison of response functions generated using the partial-wave elastic DCS, the discrete model, the default Geant4 physics with EM option 3. All inelastic physics, positron physics, and photon physics are the same and given by the default Geant4 physics with EM option 3.

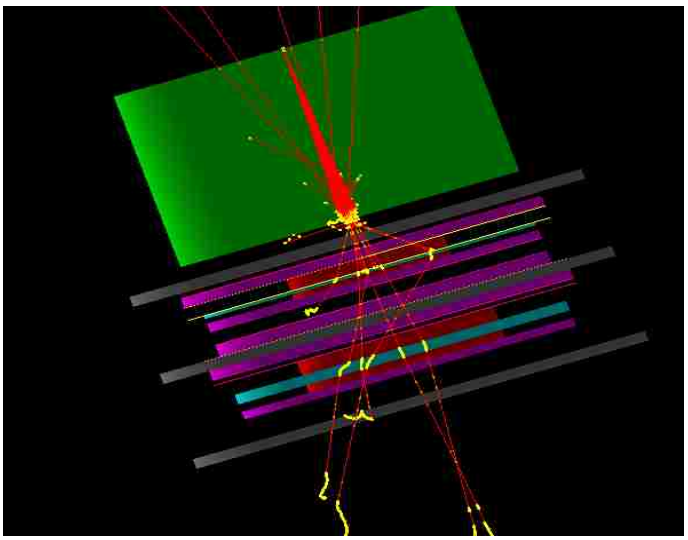

Figure 9.44: Electrons traversing the CEASE telescope. Collimator is in green and electron tracks are in red.

Chapter 10

Conclusions and Future Work

In this chapter, the dissertation is concluded by restating the objectives of this work, discussing what was required to satisfy the objectives, and discussing to what level the objectives were achieved. In addition, future work is organized into several subjects and a research pathway is considered for each subject.

10.1 Conclusions

It is of interest to develop an alternative to the CH method that is free of the limitations inherent to CH. The subject of this dissertation, or the Moment-Preserving method, is such an alternative and therefore, the accuracy and efficiency of this method must be demonstrated and contrasted (to some degree) with the CH method. To do so, the theoretical development of the method was discussed in great detail, emphasizing how elements of accuracy and efficiency are inherent to the method, while also providing an exhaustive numerical demonstration including validation of the method.

Through theoretical development, it was shown that in the Moment-Preserving

method a reduced order physics (ROP) transport equation is formed by replacing the analog DCS with ROP DCSs that are less-peaked with longer mfps. By doing so, solution to the ROP transport equation using a single-event Monte Carlo method is computationally efficient with respect to analog Monte Carlo. To simply replace the analog DCSs with another more ideal DCS requires a process for constructing such a DCS that guarantees accurate results. This is achieved by applying a theory ubiquitous in electrons transport methods, or Lewis theory, that relates moments of the analog DCS to moments of the solution. By recognizing the importance of Lewis theory, a process was developed for constructing ROP DCSs by applying a moment-preservation constraint, where both elastic and inelastic ROP DCSs are constructed such that they preserve some finite number of moments of the analog DCS exactly and higher-order moments are approximated in terms of the lower-order moments. The resulting ROP DCSs preserve key physical moments like the mean scattering cosine, the transport cross-section, the stopping power, and the straggling coefficient, along with any other user specified higher-order moments. Furthermore, by constructing the ROP DCSs such that one point is required to coincide with the nearly-singular point of the analog DCS, the method takes advantage of a convenient cancellation of in-scatter and out-scatter due to these nearly-singular points about zero changes-in-state resulting in a reduction of the total cross-section. Between the moment preserving constraint and the cancellation of the nearly-singular points, moment-preserving ROP DCSs that are less-peaked with a longer mfp (up to four orders of magnitude longer than the analog mfp) can be generated and accurate solutions to the corresponding ROP transport equation can be obtained efficiently. These findings, though satisfactory, only partially satisfy the objective of the dissertation which is to develop and demonstrate an alternative for electron transport.

To completely satisfy the objectives, a numerical demonstration of the Moment-Preserving method was presented. The results associated with the numerical demonstration, served to extend and modernize the significant body of work completed by

Franke and Prinja in 2005 [60]. By extending their study, several key features of this method were addressed including: systematically controllable accuracy, efficiency, mathematical robustness, versatility through the independence of the method from the form of the analog DCS, flexibility of the method through usage of both the discrete and hybrid DCS, and simplicity easing implementation in transport codes. The accuracy and efficiency of the method was demonstrated through calculation of both differential and integral quantities in both highly-peaked scattering regimes and less-peaked scattering regimes for a wide variety of target materials and source energies. Results including reflected and transmitted angular distributions and energy-loss spectra in thin slabs, longitudinal and lateral distributions in infinite media, dose deposition in 1-D and 2-D slabs, and charge deposition were presented. For the theoretical problems where the method is compared to an analog benchmark, analog level accuracies were achieved with efficiency gains up to three orders of magnitude greater than analog level efficiencies. For the validation results, the accuracies and efficiencies were similar to the default Geant4 electromagnetic physics with a factor of two improvement in efficiency for off-normal incidence source problems. Although the Moment-Preserving method was not a dramatic improvement over the default Geant4 electromagnetic physics, this was a first attempt at validating the method and much work remains in identifying an analog DCS model for inelastic scattering. Improvements in accuracy beyond what was reported herein are anticipated with such an inelastic DCS model. As it stands, the Moment-Preserving is a suitable alternative; however, with these improvements one can expect that the Moment-Preserving method will provide a clear advantage over the default Geant4 electromagnetic physics.

In its current state with regards to accuracy and efficiency, the Moment-Preserving method is a strong alternative to CH methods. Under conditions where CH methods and the Moment-Preserving method provide identical levels of accuracy and efficiency, the Moment-Preserving method has the added advantage of versatility and

simplicity. That is, no changes to the source code or the algorithm are required to make significant changes to the underlying physics. The moment-preserving algorithms are completely independent of the form of the analog DCS that ultimately drives the accuracy of this method. Therefore, if an improved elastic or inelastic DCS is developed, one must simply generate an ROP DCS library corresponding to the improved models. In addition, initial implementation of the Moment-Preserving method is straightforward; especially, in transport codes with pre-existing single-scatter algorithms. As a result of the mathematical robustness of the method, no additional algorithms are required beyond what is typically used for a single-scatter algorithm that uses tabulated DCS data. The algorithm simply requires methods for table look-ups to obtain the total-cross section, methods for sampling DCS data without interpolation, and methods for processing the ROP DCS. In Geant4, this required utilization of the existing data classes and base classes for physics models and processes. Any maintenance associated with Moment-Preserving method would be a result of changes to the base classes from which the Moment-Preserving method physics inherit.

Given the accuracy, efficiency, mathematical robustness, versatility, flexibility, and simplicity of the Moment-Preserving method, this method provides a clear alternative to the prevailing electron transport method - Condensed History. This work establishes a modern basis from which further testing of this method will be completed. This is the subject of the final section.

10.2 Future Work

Although a significant demonstration of this method was completed, further testing and demonstration remains. Furthermore, there are other areas of work related to this method that have not yet been investigated. This includes an adaptive cross-

section selection algorithm, extension of the method to protons and heavy ions, implementation with variance reduction techniques, and countless applications. Lastly, extension of the Moment-Preserving method for use deterministic transport codes is an area of research where only Fokker-Planck and improved Fokker-Planck schemes like Boltzmann Fokker-Planck and generalized Fokker-Planck methods have been tested. Detail on each of these topics is provide below.

10.2.1 Identification of an analog model

Prior to any further work on the Moment-Preserving method, it is of interest to identify and benchmark an analog model. As demonstrated in this work, use of the partial-wave DCS with both renormalized Möller and the Geant4 default inelastic model requires improvement. Presumably, the disagreement in the validation results is attributed to the inelastic model because the partial-wave elastic DCSs are the most accurate description of elastic scattering available. Therefore, what remains is identification of an inelastic DCS model that improves agreement with experiment. At this point, a few inelastic models have been identified including the evaluated electron data library (EEDL) or the Livermore data [20], and the PENELOPE inelastic physics that simulates inelastic collisions on the basis of a generalized oscillator strength model [27, 94], and a modified Möller DCS [71]. What remains is implementation and testing of the aforementioned models along with a study of the application the moment-preserving algorithms to these inelastic models.

10.2.2 Validation

Given an analog model that provides reasonable agreement with experimental benchmarks, it is of interest to complete a more thorough validation of the Moment-Preserving method including further studies of energy deposition and charge depo-

sition, along with reflection, transmission, and absorption studies, and other studies like the Fano cavity test and an external beam radiotherapy test. The following sections provide specific details on the potential validation studies along with references to experimental benchmarks.

Energy deposition

In addition to the energy deposition validation test [81] completed herein, further energy deposition experimental benchmarks remain. For example, several multiple-material configurations from Lockwood et al. [81] remain unstudied which are presented in Figs. 10.1 and 10.2. In addition, Tabata et al. provided an energy-deposition comparison [85] with several experiments for source energies ranging between 2-MeV up to 20-MeV as seen in Figs. 10.3 and 10.4. It would be insightful to extend the scope of the validation test beyond single-material configurations and to energies as high as 20-MeV for low-Z and high-Z materials.

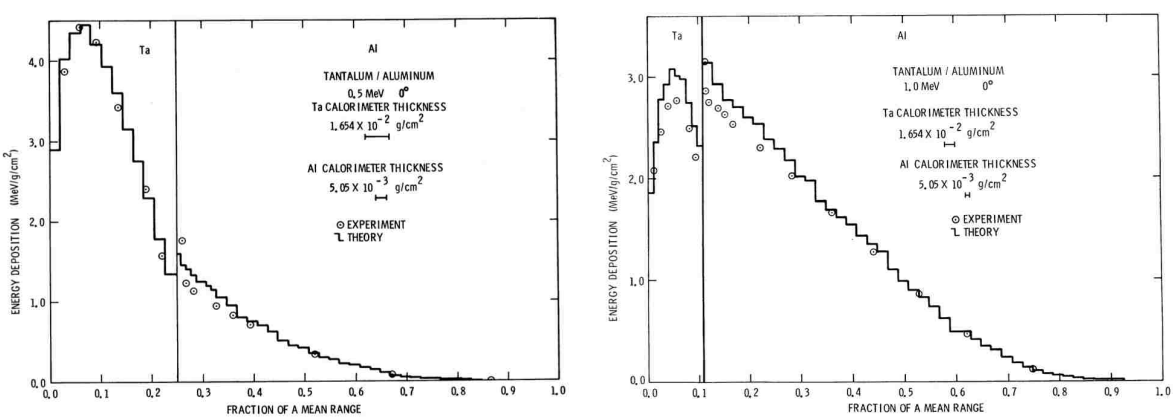

(a) 500-keV (b) 1000-keV

Figure 10.1: Comparison of experimental and theoretical energy deposition profiles in a tantalum/aluminum configuration for 500 and 1000-keV electrons normally incident (fig. ref. [81]).

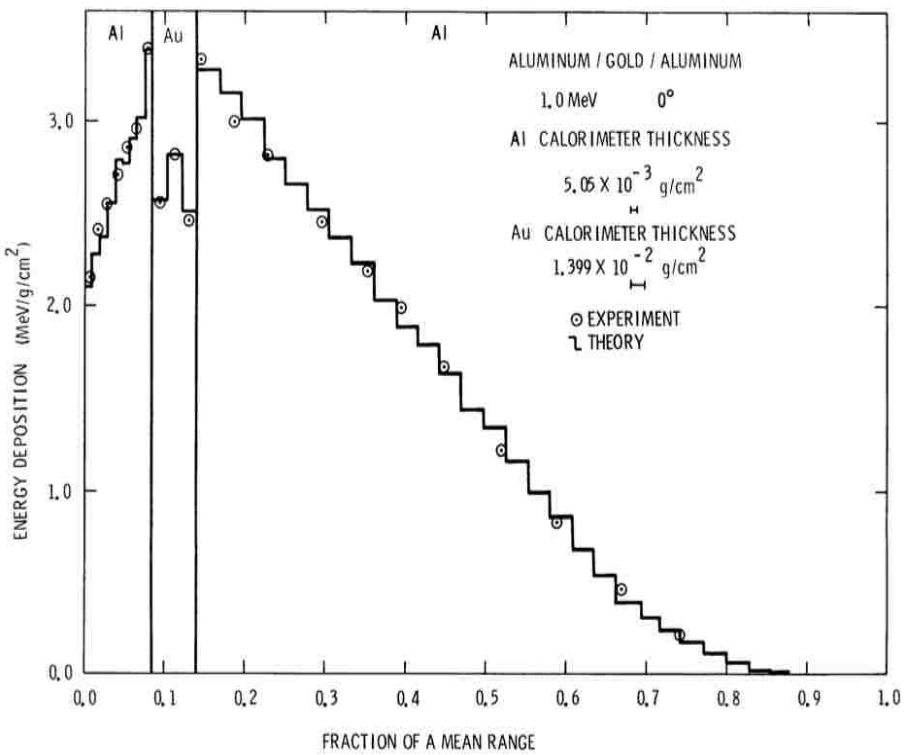

Figure 10.2: Comparison of experimental and theoretical energy deposition profiles in an aluminum/gold/aluminum configuration for 1000-keV electrons normally incident (fig. ref. [81]).

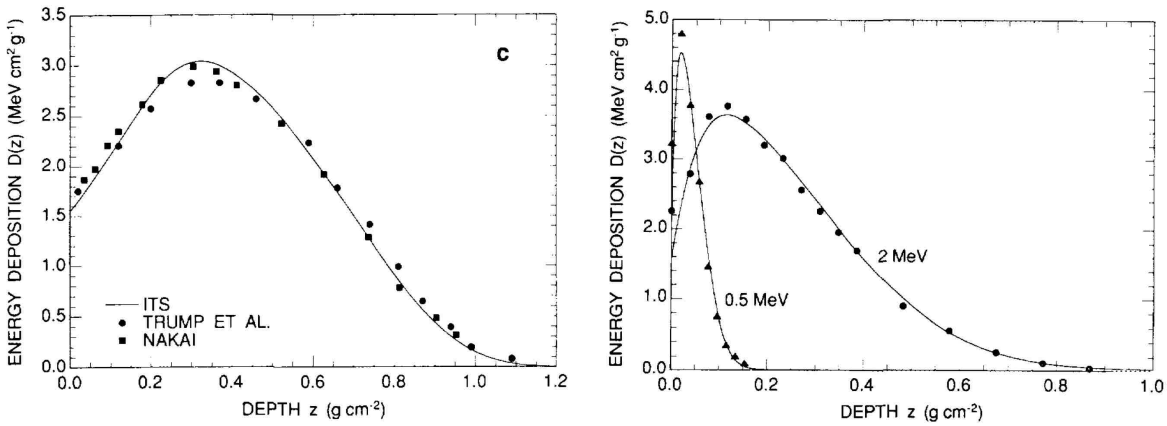

(a) Aluminum (b) Gold

Figure 10.3: (a) Energy-deposition distributions of 2-MeV electrons in aluminum. Line, ITS/TIGER; circles experiment by Trump et al. [95]; squares experiment by Nakai et al. [96] (fig. ref. [85]). (b) Energy-deposition distributions of 2-MeV electrons in gold. Line, ITS/TIGER; circles experiment by Aiginger and Gonauser [97] (fig. ref. [85]).

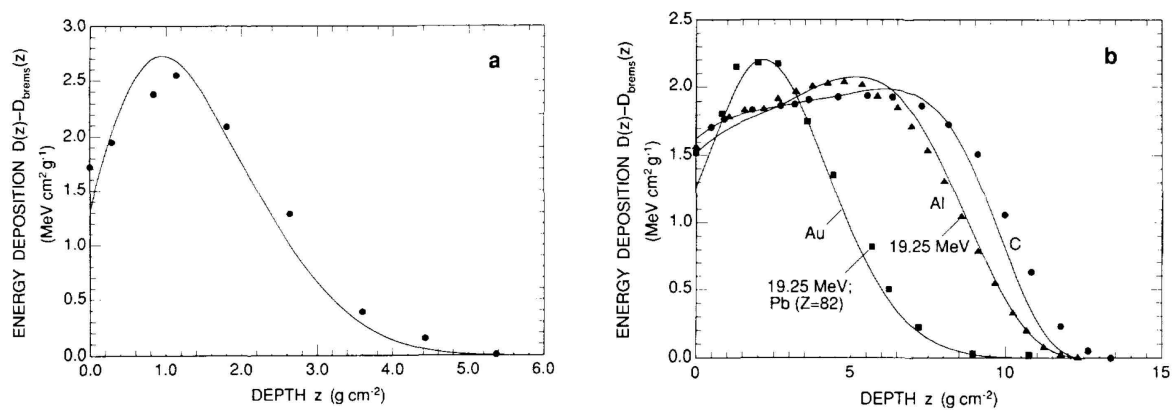

(a) 10-MeV (b) 20-MeV

Figure 10.4: Energy deposition in (a) lead for 10-MeV electrons and in (b) carbon, aluminum, and gold for 20-MeV electrons. Line, ITS/TIGER; symbols, experiment by Harder [98] (fig. ref. [85]).

Charge deposition

The charge deposition results presented in this work only included aluminum and gold target materials. For the sake of completeness, the Moment-Preserving method should be validated for lower-Z (like beryllium) and mid-Z (like copper and silver, see Fig. 10.5) targets. Tabata et al. [82] included experimental charge deposition results for a wide range of targets.

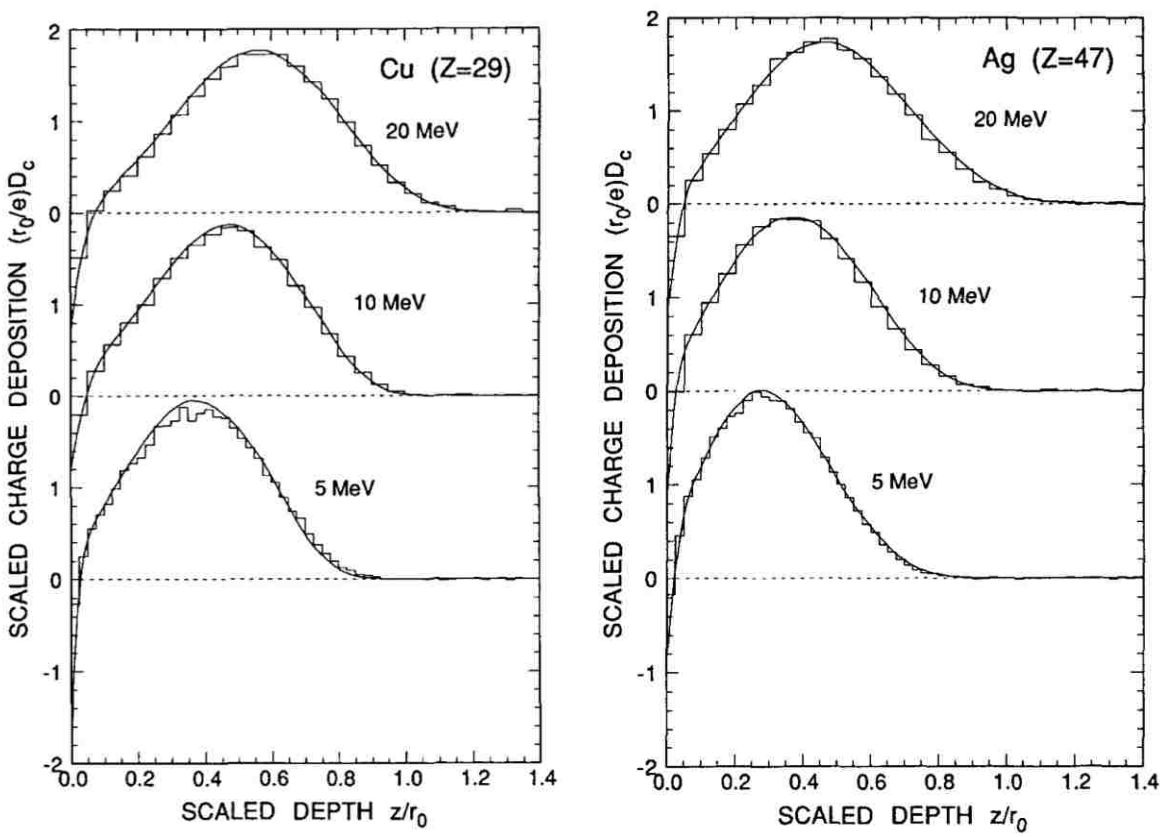

(a) Copper

(b) Silver

Figure 10.5: Charge-depostion distributions by 5, 10, and 20 MeV electrons incident on copper and silver. Historgrams, ITS Monte Carlo results; curves, experimental results obtained by the interpolation of data.

Reflection, transmission, and absorption

At this point, no reflection, transmission, or absorption fraction validation studies have been completed. The Moment-Preserving method has been shown to give good agreement with an analog benchmark when calculating reflection, transmission, or absorption fractions, but there were no efforts to compare with experimental benchmarks. That said, assuming an analog DCS model is identified that provides acceptable agreement with experiment, there is no reason to believe that the Moment-Preserving method will not provide similar agreement. There is a variety of reflection, transmission, or absorption fraction experiments due to Bishop, Darlington, Lockwood, Nubert, and Ebert [99, 87, 100, 101, 102]. The following figures provide examples of quantities of interest from a few of these studies.

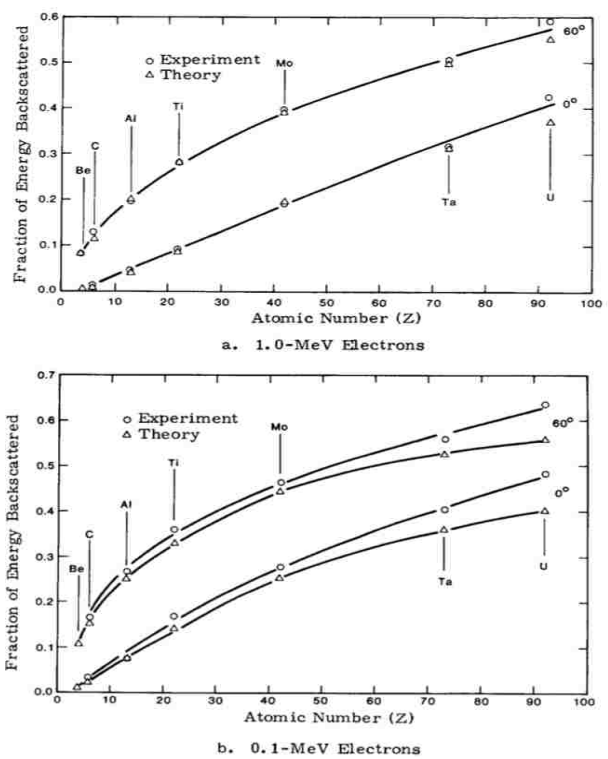

Figure 10.6: Comparison of experimental and theoretical energy backscatter for electrons incident at 0° and 60° as a function of target atomic number (fig. ref. [100].)

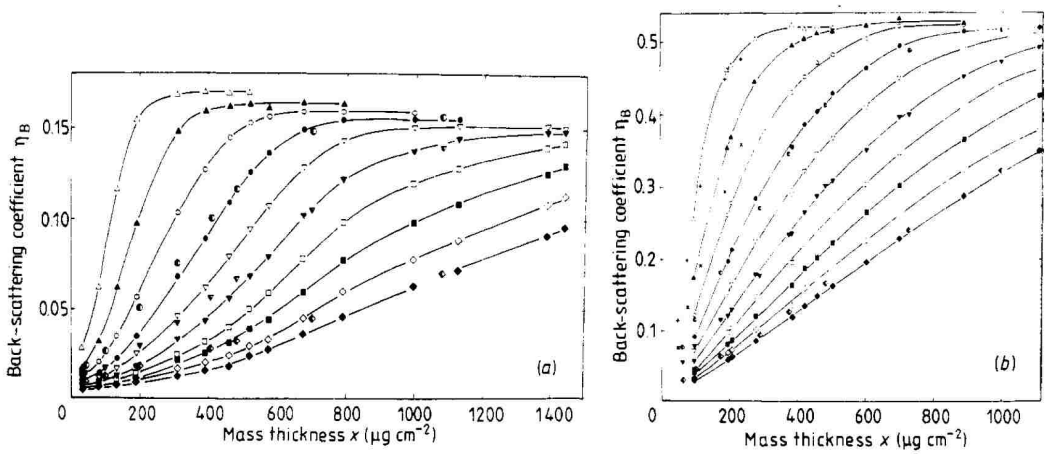

Figure 10.7: Back-scattering coefficient as a function of the mass thickness of aluminum films and gold films for different energies normally incident electrons (fig. ref. [101]).

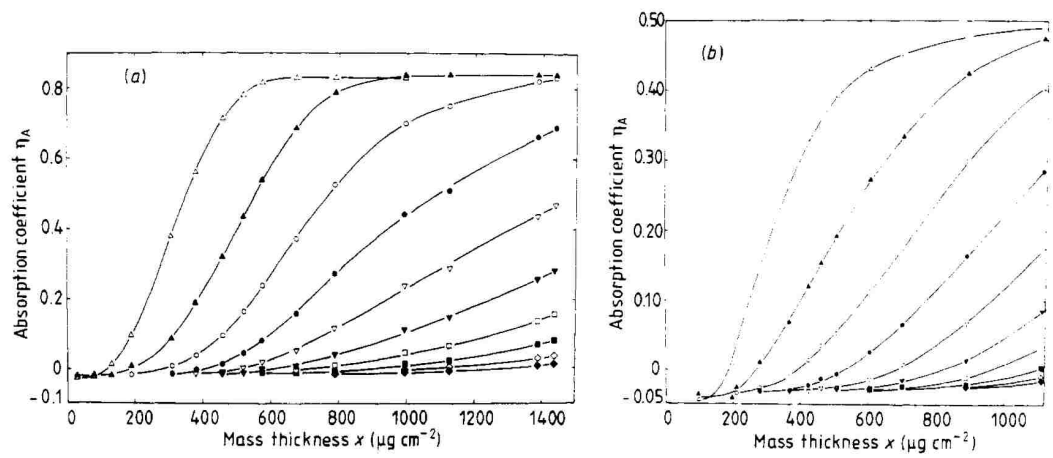

Figure 10.8: Absorption coefficient as a function of the mass thickness of aluminum films and gold films for different energies normally incident electrons (fig. ref. [101]).

Fano cavity test

One of the most stringent tests for the electron transport and boundary crossing algorithms in any condensed history Monte Carlo code is the simulation of an air cavity as a representation of an ionization chamber [91]. The Fano cavity test (see Fig. 10.9) is an ionization chamber test under idealized conditions such that use can be made of the Fano Theorem [30]. That is, under charged particle equilibrium in an infinite medium, the charged particle fluence will not be altered by density variations from point to point. Under these conditions, a condensed history method should agree with theoretical prediction regardless of the step-size. Ultimately, the Fano cavity test is used to test the different mechanisms involved in CH electron transport including step limitation, energy-loss fluctuation, and multiple scattering. At this point, it is unclear whether or not the Fano cavity test is applicable to the Moment-Preserving method. However, if the test is applicable it would present an interesting comparison because the Moment-Preserving method is not step-size dependent and does not require boundary crossing algorithms.

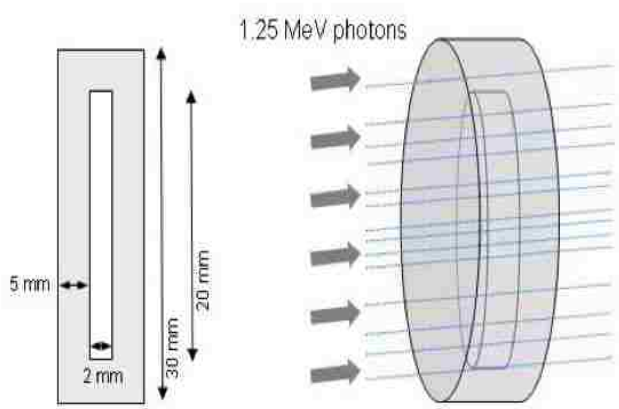

Figure 10.9: Fano cavity test schematic (fig. ref. [90]).

External beam radiotherapy

The last suggestion for a validation test is a comparison to the experimental results due to Ross et al. [103] similar to work by Faddegon et al. [89]. With increased availability of Monte Carlo methods for planning electron beams, there is an increased interest in modulated electron radiotherapy. It is imperative to determine the accuracy of various Monte Carlo methods for fluence and dose calculation in emerging electron therapy treatments [89]. The accuracy of the calculated fluence distribution may not be as accurate as calculated dose distributions. Electron therapy is generally done using scattered electron beams and the accuracy of calculated dose distributions is typically not as sensitive to scattered beam effects. However, calculated fluence distributions may not be as accurate as calculated dose distributions because fluence is sensitive to scattered beam effects. Therefore, it is important to make efforts to validate electron transport codes against accurate measurements of fluence. Ross et al. [103] completed such an experiment that allows a more accurate assessment of fluence calculations. The experimental setup is presented in Fig. 10.10a, and results from an accuracy test of EGSnrc, Geant4, and PENELOPE [89] are presented in Fig. 10.10b.

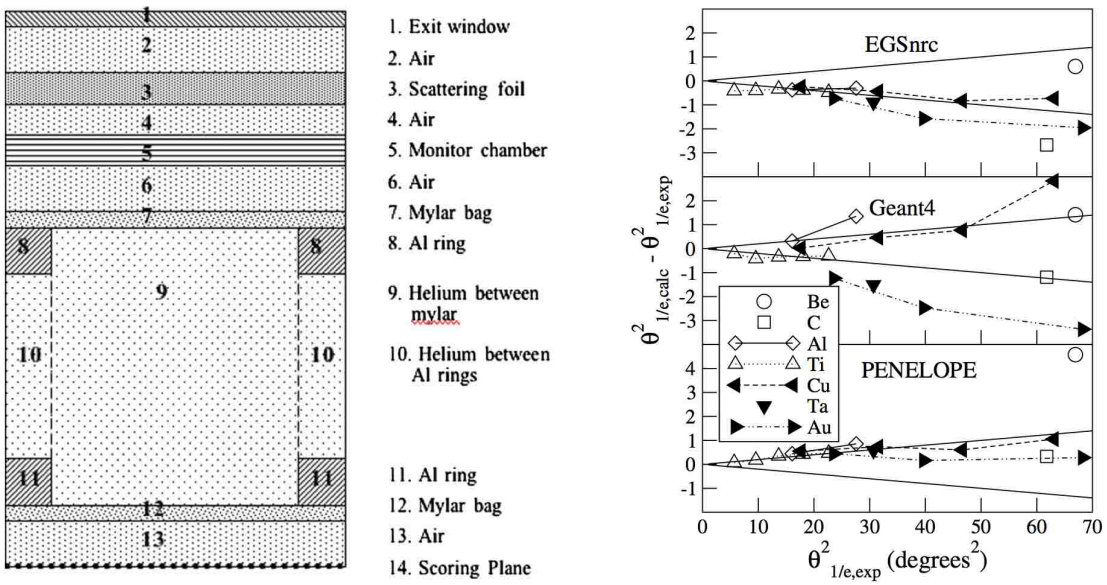

(a) Experimental Setup

(b) Characteristic Angle Comparison

Figure 10.10: (a) Experimental geometry, as simulated. Drawing is not to scale. Positions of the different components are listed below. (b) Difference of the calculated and measured square characteristic angle, 13 MeV beam. EGSnrc top panel, Geant4 center panel and PENELOPE bottom panel. The triangular area bounded by a solid straight line is 1% experimental uncertainty (fig. ref. [89]).

10.2.3 Adaptive cross-section selection

In section 9.3.2, 2-D dose deposition results were presented where the impact of radial spreading is seen in the form of discrete artifacts. The discrete artifacts are mitigated in one of two ways. That is, by adding more discrete angles to the discrete elastic DCS or through use of the hybrid DCS with a sufficient cut, the discrete artifacts are no longer present. As a result, the efficiency of the calculation is reduced because more accurate representation of elastic scattering is required.

It is likely that the more accurate models are not necessary throughout the entire calculation. For example, one could assign an ROP DCS to regions of the problem where higher accuracy is required (for example, nearby the source) and relax the ROP DCS in regions where lower levels of accuracy are sufficient. The selection of the ROP DCS for each region will depend on how much information, in the form of analog DCS moments, should be propagated from the source to the various regions of the problem. Although interesting, this process would be tedious and is problem dependent.

Alternatively, one could use an adaptive cross-section selection algorithm for determining the ideal DCS given the initial and current state of the particle. The metric for determining what cross-section is required is the key subject of the development of an adaptive cross-section selection algorithm. For example, the number of collisions suffered by the particle or the fraction of the transport mfp travelled could be used. In addition, spatial information like longitudinal or lateral displacement with respect to the source could be a viable metric. If such an algorithm is developed, users would not be required to select the DCS and can rely on the adaptive cross-section selection algorithm for optimization of accuracy and efficiency.

10.2.4 Protons and heavy ions

Currently, the Moment-Preserving method has only been applied to electrons. Extension of the method to positrons is trivial and simply requires the necessary analog DCSs. However, extension to protons and heavy ions has not yet been studied. This will require identification of an elastic and inelastic DCS like those given by Janni or Evans [104, 19] or for a generic ion there is a DCS suggested by Boschini et al. [105].

Given a DCS model, the moment-preserving algorithms should be tested to determine if they are effective for protons and heavy ions where the peaked-ness of the scattering is even more extreme. It is possible that the numerics could break down; although, some testing has been completed where the screening parameter for the screened Rutherford elastic DCS was driven to machine precision and the moment-preserving algorithms still produced ROP DCS that passed all tests for determining if a viable ROP DCS was generated. One last complexity, that is converting from center-of-mass to the lab frame when using ROP DCSs for protons and heavy ions, must be addressed.

Lastly, the algorithms for generating ROP DCSs and the Geant4 physics models will remain unchanged for protons and heavy ions, which makes extension of the Moment-Preserving method to additional particles straightforward.

10.2.5 Variance reduction

Variance reduction techniques are used to reduce the number of source particles; in turn, the efficiency of a Monte Carlo calculation is improved. There are a variety of variance reduction techniques and all of these techniques require that the physics models do not change throughout the calculation. For this reason, variance reduc-

tion techniques can be used in conjunction with the Moment-Preserving method because one can select a single elastic and inelastic ROP model for use throughout the calculation.

No testing has been completed on this subject with respect to the Moment-Preserving method. Geant4 supports some variance reduction tools like importance sampling (or geometrical splitting and Russian roulette) and the weight window technique, so testing of variance reduction techniques in conjunction with the Moment-Preserving method will not require further code development.

10.2.6 Deterministic methods

Various deterministic methods based on Fokker-Planck, Boltzmann Fokker-Planck, and generalized Fokker-Planck have been implemented. However, each of these methods rely on Fokker-Planck when regularizing the singular component of the elastic DCS. Therefore, only the transport cross section is preserved. Deterministic methods based on the Moment-Preserving method have yet been tested. It is unclear what kernel decomposition will be required, but it is likely that a discrete or hybrid model will not be appropriate in deterministic settings because of the discrete representation. However, it is possible to construct ROP models where the singular component is regularized with a "smoothing" function. That is, one can use an approach similar to the hybrid DCS, where the tail is represented by the analog DCS and a moment-preserving smoothing function is applied over the peaked region of the DCS.

References

[1] Brautigam, et al., Compact environmental anomaly sensor (CEASE): Response functions, Tech. Rep. AFRL-VS-HA-TR-2006-1030, Air Force Research Laboratories (March 2006).

[2] M. J. Berger, Monte Carlo calculation of the penetration and diffusion of fast charged particles, in: Methods in Computational Physics, Vol. 1 of Statistical Physics, Advances in Research and Applications, Academic Press, 1963, pp. 135–215.

[3] S. Agostinelli, et al., Geant4—a simulation toolkit, NIMA 506 (2003) 250–303.

[4] L. Evans, P. Bryant, LHC machine, Jinst 3.

[5] V. N. Ivanchenko, et al., Geant4 electromagnetic physics for LHC upgrade, J. Phys.: Conf. Ser. (2014) 022015.

[6] T. Aso, et al., A geant4 based simulation for proton therapy, Computing in High Energy Physics.

[7] H. Paganetti, et al., Clinical implementation of full Monte Carlo dose calculation in proton beam therapy, Phys. Med. Biol. 53 (2008) 4825–4853.

[8] D. Brautigam, Compact environmental anomaly sensor (CEASE): Geometric factors, Tech. Rep. AFRL-RV-HA-TR-2008-1129, Air Force Research Laboratories (2008).

[9] M. Y. Kim, J. W. Wilson, F. A. Cucinotta, Description of transport codes for space radiation shielding, Health Phys. 103 (2012) 621–639.

[10] E. R. Parkinson, Monte Carlo analysis of the EMP response of a random-lay cable, IEEE Trans. Nucl. Sci. NS-29 (1982) 1920–1923.

[11] G. I. Bell, S. Glasstone, Nuclear Reactor Theory, Van Nostrand Reinhold Inc., New York, 1970.

[12] L. Carter, E. Cashwell, Particle transport simulation with the Monte Carlo method, Tech. Rep. TID 36607, Technical Information Division (1975).

[13] B. G. Carlson, Solution of the tranport equation by S_n approximations, Tech. Rep. LA 1891, Los Alamos Scientific Laboratory (1955).

[14] F. Salvat, J. M. Fernández-Varea, S. Segui, Analog electron physics. interaction cross-sections, in: Advanced Monte Carlo for Radiation Physics, Particle Transport Simulation, 2001.

[15] A. K. Prinja, Statement of work, Tech. Rep. BAA-RV-10-01, Air Force Research Laboratories (2011).

[16] S. M. Seltzer, An overview of ETRAN Monte Carlo methods, in: T. M. Jenkins, W. R. Nelson, A. Rindi (Eds.), Monte Carlo Transport of Electrons and Photons, Vol. 38 of Ettore Majorana International Science, Physical Sciences, Plenum Press, 1988, pp. 153–181.

[17] G. Wentzel, Z. Phys. 40 (1927) 590.

[18] F. Salvat, A. Jablonski, C. J. Powell, ELSEPA—Dirac partial-wave calculation of elastic scattering of electrons and positrons by atoms, positive ions and molecules, Comp. Phys. Comm. 165 (2005) 157–190.

[19] R. Evans, The Atomic Nucleus, tenth printing Edition, McGraw-Hill, New York, 1955.

[20] S. T. Perkins, D. E. Cullen, S. M. Seltzer, Tables and graphs of electron-interaction cross-sections from 10 eV to 100 GeV derived from the LLNL evaluated electron data library (EEDL), Z=1-100, Tech. Rep. UCRL-50400, University of California Radiation Laboratories (1997).

[21] MacCallum, Bull. Am. Phys. Soc. 5 (1960) 379.

[22] J. M. Fernández-Varea, D. Liljequist, R. Räty, F. Salvat, Monte Carlo simulation of 0.1-100 keV electron and positron transport in solids using optical data and partial wave methods, Nucl. Instr. Meth. B 108 (1996) 35–50.

[23] G. H. III, Recent developments in low-energy electron/photon transport for mcnp6, Progress in Nuclear Science and Technology, International Conference on Radiation Shielding and 17^{th} Topical Meeting of the Radiation Protection and Shielding Division of ANS, Nara, Japan, 2012.

[24] Ivanchenko, et al., Recent improvements in geant4 electronmagnetic physics modeling, Progress in Nucl. Sci. Tech. 2 (2011) 898–903.

[25] A. Bielajew, F. Salvat, Improved electron transport mechanics in the PENELOPE Monte-Carlo model, Nucl. Instr. Meth. B 173 (2001) 332–343.

[26] W. R. Nelson, H. Hirayama, D. W. O. Rogers, The EGS4 Code System, Stanford Linear Accelerator Center, SLAC–265 (1985).

[27] F. Salvat, J. M. Fernández-Varea, J. Sempau, PENELOPE-2011: A Code System for Monte Carlo Simulation of Electron and Photon Transport, Universitat de Barcelona (July 2011).

[28] W. Bothe, Handbuch der Physik 22 (1933) 1.

[29] B. Rossi, High Energy Particles, Prentice-Hall, Englewood Cliffs, New Jersey, 1952.

[30] U. Fano, Degredation and range straggling of high-energy radiations, Phys. Rev. 92 (1953) 328.

[31] R. D. Birkhoff, Handbuch der Physik 34 (1958) 53.

[32] S. Goudsmit, J. L. Saunderson, Multiple scattering of electrons, Phys. Rev. 57 (1940) 24–29.

[33] S. Goudsmit, J. L. Saunderson, Multiple scattering of electrons. ii, Phys. Rev. 58 (1940) 36–42.

[34] L. Landau, On the energy loss of fast particles by ionization, J. Phys. 8 (1944) 201.

[35] P. V. Vavilov, Ionization losses of high-energy heavy particles, Sov. Phys. JETP 5 (4) (1957) 920–923.

[36] D. W. O. Rogers, A. F. Bielajew, A comparison of EGS and ETRAN, in: T. M. Jenkins, W. R. Nelson, A. Rindi (Eds.), Monte Carlo Transport of Electrons and Photons, Vol. 38 of Ettore Majorana International Science, Physical Sciences, Plenum Press, 1988, pp. 323–342.

[37] S. M. Seltzer, M. J. Berger, Transmission and reflection of electrons by foils, Nucl. Instr. Meth. 119 (1974) 157.

[38] D. W. O. Rogers, Low energy electron transport with egs, Nucl. Instr. Meth. A A227 (1984) 535.

[39] E. W. Larsen, Generalized Fokker-Planck approximations of particle transport with highly forward-peaked scattering, Ann. Nucl. Energy 19 (1992) 701–714.

[40] A. Bielajew, D. D. O. Rogers, PRESTA: The parameter reduced electron-step transport algorithm for electron Monte Carlo transport, Nucl. Instr. Meth. B 18 (1986) 165–181.

[41] D. Jensen, Monte Carlo calculation of electron multiple scattering in thin foils, Ph.D. thesis, Naval Postgraduate School (1988).

[42] R. L. Keith, R. P. Kensek, Order-of-convergence study of a condensed-histroy algorithm implementation, in: International Conference on Mathematics, Computational Methods and Reactor Physics 2009, American Nuclear Society, Saratoga Springs, New York, 2009, on CD-ROM.

[43] H. W. Lewis, Multiple scattering in an infinite medium, Phys. Rev. 78 (1950) 526–529.

[44] A. K. Prinja, Lewis theory for energy straggling in thin layers, Nucl. Instr. Meth. B 330 (2014) 99–102.

[45] G. C. Pomraning, The Fokker-Planck operator as an asymptotic limit, Math. Mod. Meth. Appl. Sci. 2 (1992) 21–36.

[46] C. Borgers, E. Larsen, Fokker-Planck approximation of monoenergetic transport processes, Trans. Am. Nucl. Soc. 71 (1994) 235–236.

[47] P. A. Haldy, J. Ligou, A multigroup formalism to solve the Fokker-Planck equation characterizing charged particl transport, Nucl. Sci. Eng. 74 (1980) 178–184.

[48] T. M. Tran, J. Ligou, An accurate numerical method to solve the linear Fokker-Planck equation characterizing charged particle transport, Nucl. Sci. Eng. 79 (269-277).

[49] J. E. Morel, Fokker-Planck calculations using standard discrete ordinates transport codes, Nucl. Sci. Eng. 79 (1981) 340–356.

[50] J. E. Morel, An improved Fokker-Planck angular differencing scheme, Nucl. Sci. Eng. 89 (1985) 131–136.

[51] J. Ligou, Fusion reaction product transport in inertially confined plasmas, in: Proc. ANS-ENS Int. Topl. Mtg, Advances in Mathematical Methods for the Solution of Nuclear Engineering Problems, Fachinformationszentrum Energie,Physik, Mathematik GmbH, Karlsruhe, West Germany, 1981.

[52] K. Przybylski, J. Ligou, Numerical analysis of the Boltzmann equation including Fokker-Planck terms, Nucl. Sci. Eng. 81 (1981) 92–109.

[53] M. Caro, J. Ligou, Treatment of scattering anisotropy of neutrons through the Boltzmann-Fokker-Planck equation, Nucl. Sci. Eng. 83 (1983) 242–252.

[54] M. Landesman, J. E. Morel, Angular Fokker-Planck decomposition and representation techniques, Nucl. Sci. Eng. 103 (1989) 1–11.

[55] D. P. Sloan, A new multigroup Monte Carlo scattering algorithm for neutral and charged-particle Boltzmann and Fokker-Planck calculations, Tech. Rep. SAND83-7094, Sandia National Laboratories (1983).

[56] J. E. Morel, L. J. Lorence, Jr., R. P. Kensek, J. A. Hableib, D. P. Sloan, A hybrid multigroup/continuous-energy Monte Carlo method for solving the Boltzmann-Fokker-Planck equation, Nucl. Sci. Eng. 124 (1996) 369–389.

[57] G. C. Pomraning, Higher order Fokker-Planck operators, Nucl. Sci. Eng. 124 (1996) 390–397.

[58] A. K. Prinja, G. Pomraning, A generalized Fokker-Planck model for transport of collimated beams, Nucl. Sci. Eng. 137 (2001) 227–235.

[59] C. L. Leakas, E. W. Larsen, Generalized Fokker-Planck approximations of particle transport with highly forward-peaked scattering, Nucl. Sci. Eng. 137 (2001) 236–250.

[60] B. C. Franke, A. K. Prinja, Monte Carlo electron dose calculations using discrete scattering angles and discrete energy losses, Nucl. Sci Eng. 149 (2005) 1–22.

[61] D. Dixon, A. K. Prinja, B. C. Franke, Geant4 implementation of a novel single-event Monte Carlo method for electron dose calculations, Trans. Am. Nucl. Soc.

[62] D. Dixon, A. K. Prinja, B. C. Franke, Application of the generalized Boltzmann Fokker-Planck method to electron partial-wave expansion elastic scattering differential cross sections within the geant4 toolkit, in: RPSD 2014, Radiation Protection and Shileding Division of the ANS, Knoxville, Tennessee, 2014.

[63] B. C. Franke, A. K. Prinja, R. P. Kensek, L. J. Lorence, Discrete scattering-angle model for electron pencil beam transport, Trans. Am. Nucl. Soc. 86 (2002) 206–208.

[64] B. C. Franke, A. K. Prinja, R. P. Kensek, L. J. Lorence, Ray effect mitigation for electron transport with discrete scattering-angles, Trans. Am. Nucl. Soc. 87 (2002) 133–135.

[65] ICRU Report No. 77, Elastic scattering of electrons and positrons, Journal of ICRU 7.

[66] G. Molière, Theori der streuung schneller geladener teilchen i: Einzelstreuung am abgeschirmten coulomb-field, Z. Naturforsch. 2a (1947) 133.

[67] Overview of physical interaction models for photon and electron transport used in Monte Carlo codes, Metrologia 46 (2009) S112–S138.

[68] R. M. Sternheimer, Phys. Rev. (1971) 3681.

[69] ICRU Report No. 37, Stopping powers for electrons and positrons, Journal of ICRU.

[70] A. K. Prinja, E. W. Larsen, Handbook of Nuclear Engineering, Springer, 2010, Ch. Principles of Neutron Transport.

[71] M. J. Berger, R. Wang, Multiple-scattering angular deflectionsand energy-loss straggling, in: T. M. Jenkins, W. R. Nelson, A. Rindi (Eds.), Monte Carlo Transport of Electrons and Photons, Vol. 38 of Ettore Majorana International Science, Physical Sciences, Plenum Press, 1988, pp. 21–56.

[72] O. Blunck, S. Leisegang, Zum energieverlustschneller elektronen in dünnen schichten, Z. Phys. 128 (1950) 500.

[73] J. A. Halbleib, R. P. Kensek, T. A. Mehlhorn, G. D. Valdez, S. M. Seltzer, M. J. Berger, ITS Version 3.0: The Integrated TIGER Series of Coupled Elctron/ Photon Monte Carlo Transport Codes, Sandia National Laboratories, SAND91–1634 (1992).

[74] B. C. Franke, Private communication (November 2014).

[75] L. Urbán, A model for multiple scattering in geant4, Tech. rep., CERN (2006).

[76] L. Harding, Monte Carlo simulatinos of electron and positron energy-loss straggling, Master's thesis, University of New Mexico (2006).

[77] W. Gautschi, Numerical Analysis, second ed. Edition, Birkhauser, New York, 2012.

[78] G. H. Golub, Some modified matrix eigenvalue problems, SIAM Rev. 15 (2) (1973) 318–334.

[79] G. H. Golub, J. H. Welsch, Questions of numerical condition related to orthogonal polynomials, Studies in Numerical Analysis 24 (1984) 140–177.

[80] G. H. Golub, J. H. Welsch, Caculation of Gauss quadrature rules, Math. Comp. 23 (106) (1969) 221–230.

[81] G. J. Lockwood, L. E. Ruggles, G. H. Miller, J. A. Halbleib, Calorimetric measurement of electron energy deposition in extended media– theory vs experiment, Tech. Rep. SAND79-0414, SNL (1987).

[82] T. Tabata, P. Andreo, K. Shinoda, R. Ito, Depth profiles of charge deposition by electrons in elemental absorbers: Monte Carlo results, experimental benchmarks and derived parameters, Nucl. Instr. Meth. B 95 (1995) 289–299.

[83] E. Benedito, J. M. Fernández-Varea, F. Salvat, Mixed simulation of the multiple elastic scattering of electrons and positrons using partial-wave differential cross-sections, Nucl. Instr. Meth. B 174 (2001) 91–110.

[84] T. Tabata, R. Ito, S. Okabe, Y. Foujita, Charge distribution produced by 4- to 24-MeV electrons in elemental materials, Phys. Rev. B 3 (3) (1971) 572–583.

[85] T. Tabata, P. Andreo, R. Ito, Energy-deposition distributions in materials irradiated by plane-parallel electron beams with energies between 0.1 and 100 MeV, Atomic Data and Nuclear Data Tables 56 (1994) 105–131.

[86] T. Tabata, P. Andreo, K. Shinoda, R. Ito, Range distributions and projected ranges of 0.1 to 100-MeV electrons in elemental absorbers, Nucl. Instr. Meth. B 108 (1996) 11–17.

[87] E. H. Darlington, Backscattering of 10-100 keV electrons from thick targets, J. Phys. D: Appl. Phys. 8 (1975) 85–93.

[88] P. Libby, G. Hughes III, J. Goorley, Electron transmission and backscatter verification calculations using mcnp5, Tech. Rep. LA-UR-03-5751, LANL (2003).

[89] B. A. Faddegon, et al., Accuracy of EGSnrc, Geant4, and PENELOPE Monte Carlo systems for simulation of electron scattering in external beam radiotherapy, Phys. Med. Biol. 54 (2009) 6151–6163.

[90] S. Elles, V. N. Ivanchenko, M. Maire, L. Urbán, Geant4 and fano cavity test: where are we?, J. Phys.: Conf. Ser. 102 (012009).

[91] E. Poon, J. Seuntjens, F. Verhaegen, Consistency test of the electron transport algorithm in the geant4 Monte Carlo code, Phys. Med. Biol. 50 (2005) 681–694.

[92] O. Kadri, V. N. Ivanchenko, F. Gharbi, A. Trabelsi, Geant4 simulation of electron energy deposition in extended media, Nucl. Instr. Meth. B 258 (2007) 381–387.

[93] V. N. Ivanchenko, O. Kadri, M. Maire, L. Urbán, Geant4 models for simulation of multiple scattering, J. Phys.: Conf. Ser. 219 (032045).

[94] J. M. Fernández-Varea, R. Mayol, D. Liljequist, F. Salvat, Inelastic scattering of electrons in solids from a generalized oscillator strength model using optical and photoelectric data, J. Phys. 5 (1993) 3593–3610.

[95] J. G. Trump, K. A. Wright, A. M. Clarke, Phys. Rev. 21 (1950) 345.

[96] Y. Nakai, Jpn. J. Appl. Phys. 2 (1963) 743.

[97] H. Aiginger, E. Gonauser, Atomkernenergic 13 (1968) 33.

[98] D. Harder, in: H. G. Ebert (Ed.), 2^{nd} Symposium on Microdosimetry, Stresa, 1969., Euratom, Brussels, 1969, p. 567.

[99] H. E. Bishop, A Monte Carlo calculation on the scattering of electrons in copper, Proc. Phys. Soc. 85 (1965) 855–866.

[100] G. J. Lockwood, L. E. Ruggles, G. H. Miller, J. A. Halbleib, Electron energy and charge albedos - calorimetric measurement vs Monte Carlo theory, Tech. Rep. SAND80-1968, Sandia National Laboratories (February 1980).

[101] G. Nubert, S. Rogaschewski, Measurements of the back-scattering and absorption of 15–60 keV electrons for transparent solid films at various angles of incidence, J. Phys. D: Appl. Phys. 17 (1984) 2439–2454.

[102] P. J. Ebert, A. F. Lauzon, E. M. Lent, Transmission and backscattering of 4.0–12.0 MeV electrons, Phys. Rev. 183 (422–430).

[103] C. K. Ross, et al., Measurement of multiple scattering of 13 and 20 MeV electrons by thin foils, Med. Phys. 35 (2008) 4121–4131.

[104] J. F. Janni, Energy loss, range, path length, time-of-flight, straggling, multiple scattering, and nuclear interaction probability, Atomic Data and Nuclear Data Tables 27 (1982) 147–339.

[105] M. J. Boschini, et al., Nuclear and non-ionizing energy-loss for coulomb scattered particles from low energy up to relativistic regime in space nuclear and non-ionizing energy-loss for coulomb scattered particles from low energy up to relativistic regime in space radiation environment, Proceedings of the ICATPP Conference on Cosmic Rays for Particle and Astroparticle Physics (2010) 9–23.